

**Structural and Chemical Investigations of the
Thermal Behavior of B-H Based Materials
(NaBH_4 and NH_3BH_3) and their Oxidation
Metaborate By-products**

Von der Naturwissenschaftlichen Fakultät der
Gottfried Wilhelm Leibniz Universität Hannover

zur Erlangung des Grades

Doktorin der Naturwissenschaften (Dr. rer. nat.)

genehmigte Dissertation

von

Zeina Assi, M2R (Libanon)

geboren am 01.01.1987 in Ansar, Libanon

2016

Referent: Prof. Dr. rer. nat. Claus Henning Rücher

Korreferent: Prof. Dr. rer. nat. Josef-Christian Buhl

Korreferent: Prof. Dr. rer. nat. Thomas Bredow

Tag der Promotion: 16.09.2016

Acknowledgements

I thank God for making all things possible for me and giving me strength to go. A thesis journey is not always easy, but with the supervision, support and encouragement of many people, I have never regretted that I started it.

I would like to express my deep and sincere gratitude to my supervisor, Prof. Dr. C. H. Rüscher for his valuable advice and constant support during this thesis. He was not only an advisor but also a good listener and a friend who showed me just what I was able to achieve even when I did not see it myself. Thank you for allowing me to join your team and for your guidance. It has been a true pleasure and I hope that we continue our collaboration.

I owe my sincere gratitude to Prof. Dr. J.-Ch. Buhl for his support and numerous suggestions, Prof. Dr. T. Bredow and A. G. Schneider for the collaboration and the interesting discussions.

I am also grateful to A. Schulz for the in-situ X-ray measurements and Dr. L. Schomborg for his support in the work in the lab. Thank you for the work group Crystallography and office 329.

I gratefully acknowledge the Deutscher Akademischer Austauschdienst DAAD for their financial assistance for four years.

I am forever thankful to my family: my father, my mother, my husband, my sister and my brothers who were always there for me. Thank you for your encouragement in all of my pursuits, believing in me, and inspiring me to follow my dreams. This made me go forward and made me want to succeed.

My deepest and sincerest thanks go to my little princess Batoul. It is not easy to become a mother in the first year of a PhD thesis, but you've learned me that mother can do anything! You supported and inspired me to get through the most difficult times without even you know it!

Abstract

The thermal behavior of solid sodium borohydride NaBH_4 , ammonia borane NH_3BH_3 and NH_3BH_3 embedded in an aluminosilicate geopolymer type matrix ($\text{NH}_3\text{BH}_3\text{-G}$) was studied between 25 and 400°C under different conditions. New results are obtained in TG/DTA and temperature dependent infrared absorption (TIR) experiments, where the different materials were diluted in KBr and NaCl and pressed in pellets. Hydrogen release could be followed using the reduction reaction of nitrate tracer added to the pressed pellet.

NaBH_4 slightly subjected to ambient conditions forms $\text{NaBH}_4\cdot 2\text{H}_2\text{O}$. Crystalline water is released between 40 and 60°C without reaction with NaBH_4 . Under inert He atmosphere, NaBH_4 is stable to 400°C. In presence of traces of $\text{H}_2\text{O}/\text{O}_2$, a thermal oxidation to anhydrous sodium metaborate NaBO_2 is observed between 300 and 400°C releasing H_2 . The oxidation reaction with O_2 produces H_2O which is further consumed for H_2 release. TIR of NaBH_4 in presence of NaNO_3 indicates some H_2 release between 200 and 300°C without decomposition of NaBH_4 . In this temperature range, a weak but significant peak is observed at about 1575 cm^{-1} indicating a possible transient state.

$\text{NH}_3\text{BH}_3\text{-G}$ could be better handled than pristine NH_3BH_3 salt. Foaming and liberation of undesirable B, N-containing gases could be suppressed. $\text{NH}_3\text{BH}_3\text{-G}$ decomposes similarly to NH_3BH_3 but at slightly lower temperatures. The dehydrogenation could be described by series of condensation reactions yielding poly-aminoborane $(-\text{H}_2\text{N}-\text{BH}_2-)_n$ and poly-iminoborane $(-\text{HN}=\text{BH}-)_n$ at about 140 and 170°C, respectively. TIR using KBr matrix shows IR features of BH_4^- substituted for Br^- in KBr, at 105°C for $\text{NH}_3\text{BH}_3\text{-G}$ and at 115°C for NH_3BH_3 , as indirect evidence of the formation of DADB ($[(\text{NH}_3)_2\text{BH}_2]\text{BH}_4$) intermediate.

The ionic exchange between NaBH_4 and halide matrices is facilitated for the case where the ionic radii of the anions are similar. The dissolution is accompanied by shifting of the IR frequencies of BH_4^- . The IR frequencies of BH_4^- isolated ($i\text{-BH}_4^-$) in different halide AX matrices with $A = \text{Na, K, Rb}$ and $X = \text{Cl, Br, I}$ are used to discuss the interactions of BH_4^- anion with ionic surroundings. Correlations between $\nu_3(i\text{-BH}_4^-)$ and different structural parameters of the halides are defined. The IR frequencies are governed by the repulsive interactions with the nearest neighbors.

The thermal dehydration of sodium metaborate tetrahydrate $\text{NaBO}_2\cdot 4\text{H}_2\text{O}$ is investigated between 20 and 500°C using principally TG/DTA, TIR and in-situ X-ray diffraction. The thermal dehydration occurs in five main endothermic steps. The dehydration products $\text{NaBO}_2\cdot 2\text{H}_2\text{O}$, $\text{NaBO}_2\cdot 1/3\text{H}_2\text{O}$ and NaBO_2 were isolated and characterized. A new gel-like phase is observed about 120°C during the dehydration-condensation of $\text{B}(\text{OH})_4^-$ of $\text{NaBO}_2\cdot 2\text{H}_2\text{O}$ to the six-membered rings of $\text{NaBO}_2\cdot 1/3\text{H}_2\text{O}$. The role of the metaborate by-products including the gel phase in the hydrolysis reaction of NaBH_4 is discussed.

Keywords: hydrides, hydrogen, metaborates

Zusammenfassung

Das thermische Verhalten von polykristallinem Natriumborhydrid NaBH_4 , Amminboran NH_3NH_3 und NH_3BH_3 rekristallisiert in einer aluminosilikatischen Geopolymer-Matrix ($\text{NH}_3\text{BH}_3\text{-G}$) wurde zwischen 25 und 400°C unter verschiedene Bedingungen untersucht. Neben der thermogravimetrischen Analyse (TG) wurden dazu umfangreiche temperaturabhängige Infrarot (TIR) Untersuchungen der Proben in gepressten KBr- und NaCl-Pellets durchgeführt. Dabei wurde die Wasserstofffreisetzung mithilfe der Nitrat-Reduktionsmethode beobachtet.

NaBH_4 bildet bereits nach sehr kurzer Zeit $\text{NaBH}_4\cdot 2\text{H}_2\text{O}$ unter Normalbedingungen. Das Kristallwasser wird zwischen 40 und 60°C ohne Reaktion mit dem NaBH_4 freigesetzt. Unter inerter He Atmosphäre ist NaBH_4 bis zu 400°C stabil. In Gegenwart von Spuren von $\text{H}_2\text{O}/\text{O}_2$ wird eine Oxidation zu NaBO_2 zwischen 300 und 400°C beobachtet, bei dieser Reaktion wird Wasserstoff freigesetzt. Die Reaktion mit O_2 erzeugt H_2O , das weiter zur Wasserstofffreisetzung verbraucht wird. TIR vom NaBH_4 mit Nitrat zeigt einige H_2 Freisetzung zwischen 200 und 300°C ohne Zersetzung von NaBH_4 . In diesem Temperaturbereich wird ein schwacher aber signifikanter Peak bei etwa 1575 cm^{-1} beobachtet, dies kann einen möglichen Übergangszustand andeuten.

Bei der thermischen Zersetzung von NH_3BH_3 entstehen unerwünschte Schäume und B, N-enthaltende Gase, während diese bei $\text{NH}_3\text{BH}_3\text{-G}$ unterdrückt werden. Die Zersetzung von $\text{NH}_3\text{BH}_3\text{-G}$ ähnelt der von NH_3BH_3 , findet aber bei etwas niedrigeren Temperaturen statt. Die Dehydrierung erfolgt durch Kondensationsreaktionen zu poly-Aminoboran ($-\text{H}_2\text{N-BH}_2-$) $_n$ bei etwa 140°C und zu poly-Iminoborane ($-\text{HN}=\text{BH}-$) $_n$ bei 170°C . TIR mittels KBr-Matrix zeigt IR Peaks von BH_4^- Anionen bei 105°C für $\text{NH}_3\text{BH}_3\text{-G}$ und bei 115°C für NH_3BH_3 , dies kann als indirekter Beweis für die Bildung vom DADB ($[(\text{NH}_3)_2\text{BH}_2]\text{BH}_4$) betrachtet werden.

Der Ionenaustausch zwischen NaBH_4 und Halogeniden findet leicht statt, wenn die Ionenradien der Anionen ähnlich sind. Die Auflösung vom NaBH_4 bewirkt die Verschiebung der IR-Frequenzen der BH_4^- Anionen. Die IR-Frequenzen von BH_4^- Anionen isoliert ($i\text{-BH}_4^-$) in verschiedenen Halogeniden AX (A = Na, K, Rb und X = Cl, Br, I) werden verwendet, um die Wechselwirkungen vom BH_4^- Anion mit seiner ionischen Umgebung zu beschreiben. Eindeutige Korrelationen zwischen $\nu_3(i\text{-BH}_4^-)$ und verschiedenen Strukturparametern der Halogenide wurden festgestellt. Die IR-Frequenzen sind von den abstoßenden Wechselwirkungen mit ihren nächsten Nachbarn stark beeinflusst.

Die thermische Zersetzung vom Natriummetaborat-Tetrahydrat $\text{NaBO}_2\cdot 4\text{H}_2\text{O}$ wurde zwischen 20 und 500°C mittels TG, TIR und in-situ Röntgenbeugung untersucht. Die Dehydratisierung erfolgt hauptsächlich in fünf endothermen Schritten. Die dabei entstehenden Produkte $\text{NaBO}_2\cdot 2\text{H}_2\text{O}$, $\text{NaBO}_2\cdot 1/3\text{H}_2\text{O}$ und NaBO_2 wurden isoliert und charakterisiert. Eine neue gelartige Phase wurde bei etwa 120°C während der Dehydratisierungs-Kondensations-Reaktion von $\text{B}(\text{OH})_4^-$ des $\text{NaBO}_2\cdot 2\text{H}_2\text{O}$ Phase zu der Ring-Struktur vom $\text{NaBO}_2\cdot 1/3\text{H}_2\text{O}$ beobachtet. Die Rolle der Metaborat Nebenprodukte einschließlich der Gelphase in der Hydrolysereaktion von NaBH_4 ist diskutiert.

Schlagwörter: Hydride, Wasserstoff, Metaborat

I. Table of Contents

II. List of Figures.....	8
III. List of Tables.....	15
IV. List of Abbreviations	17
1. Introduction.....	18
2. Experimental Methods	23
2.1 Samples.....	23
2.2 Methods	24
2.2.1 Thermogravimetry / Differential Thermal analyses (TG/DTA).....	24
2.2.2 Powder X-ray diffraction (XRD)	24
2.2.3 Fourier Transformation Infrared Spectroscopy (FTIR).....	25
2.2.4 Raman spectroscopy.....	30
2.2.5 Volumetric Acid catalyzed hydrolysis release (ACHR) method	31
2.2.6 Imaging method: Scanning Microscope Electron (SEM)	33
3. H ₂ Release from Solid State Sodium Borohydride NaBH ₄	34
3.1 State of the art.....	34
3.1.1 Synthesis and structure.....	34
3.1.2 H ₂ release by NaBH ₄ hydrolysis	36
3.1.3 Thermal decomposition of NaBH ₄	46
3.2 Results and discussion	49
3.2.1 The reaction of NaBH ₄ with neutral H ₂ O _(l)	49
3.2.2 Thermal behavior of NaBH _{4(s)} up to the melting point: TG/DTA analysis.....	55
3.2.3 Temperature dependent Raman (TRam) analyses	58
3.2.4 Temperature dependent Infrared (TIR) analyses.....	62
4. H ₂ release from Ammonia Borane NH ₃ BH ₃ and NH ₃ BH ₃ -Geopolymer (NH ₃ BH ₃ -G).....	73
4.1 State of the Art.....	73
4.1.1 Synthesis and structure.....	73
4.1.2 H ₂ release from NH ₃ BH ₃	75
4.1.3 Confinement of NH ₃ BH ₃ in porous scaffolds	79
4.2 Results and discussion	80
4.2.1 Characterization of NH ₃ BH ₃ and NH ₃ BH ₃ -G by XRD, SEM/EDX and IR	80
4.2.2 Stability in neutral water	85
4.2.3 Total hydrogen release using HCl solution	86
4.2.4 Alkaline solutions of NH ₃ BH ₃ and NH ₃ BH ₃ -G	89

4.2.5	Aging of $\text{NH}_3\text{BH}_3\text{-G}$	91
4.2.6	Stability at 80°C	92
4.2.7	TG/DTA analyses.....	94
4.2.8	TIR using KBr matrix	96
4.2.9	TIR using NaCl matrix	103
4.2.10	Thermolysis under open conditions	105
4.2.11	Characterization of the dehydrogenation products.....	108
4.3	Summary: thermal decomposition routes of $\text{NH}_3\text{BH}_3\text{-G}$ and NH_3BH_3 in KBr and NaCl matrices	110
5.	Solid Solutions of BH_4^- in Different Halide AX Matrices (A = Na, K, Rb; X = Cl, Br, I).....	114
5.1	State of the art.....	114
5.2	Results and discussion	117
5.2.1	Solid solution formation in equimolar NaBH_4 : AX pressed pellets.....	117
5.2.2	Spectra of $\text{NaBH}_4/\text{KBH}_4$ in ATR and pressed in various halides	123
5.2.3	TIR of $\text{NaBH}_4/\text{NaCl}$ pellet	126
5.2.4	BH_4^- -frequency variations dependences on halide parameters	129
5.2.5	BH_4^- -frequency variations using empirical experimental models.....	136
6.	Thermal dehydration of Sodium Metaborate Tetrahydrate $\text{NaBO}_2\cdot 4\text{H}_2\text{O}$	139
6.1	State of the art.....	139
6.1.1	Borates and sodium metaborate compounds	139
6.1.2	Role of $\text{NaBO}_2\cdot y\text{H}_2\text{O}$ in H_2 release from NaBH_4 and NH_3BH_3	142
6.2	Results and discussion	145
6.2.1	Characterization of the commercial $\text{NaBO}_2\cdot 4\text{H}_2\text{O}$ sample	145
6.2.2	TG/DTA analyses.....	146
6.2.3	In-situ X-ray diffraction	157
6.2.4	TIR	159
6.2.5	Characterization of the dehydration products	164
6.3	Summary: dehydration path of $\text{NaBO}_2\cdot 4\text{H}_2\text{O}$	173
7.	Conclusion and Outlook	180
V.	Literature	185
VI.	Curriculum Vitae.....	202
VII.	List of Publications	203

II. List of Figures

Figure 2.1: Scheme of the path of IR beam in the ATR system (the figure is taken from ref. [29]).....	25
Figure 2.2: The sample holder used for TIR experiments including the Ag holder and the two silver nets with a pellet.....	26
Figure 2.3: TIR of a KBr pellet.....	27
Figure 2.4: TIR of NaNO ₃ in KBr. (a) TIR spectra. Inset graph is zoomed for $\nu_3(\text{NO}_3^-)$. Variation of the peak position of (b) ν_2 and (c) $\nu_1+\nu_4$ in function of temperature. Gray lines are guide for eyes.....	29
Figure 2.5: Energy levels and transitions involved in IR and Raman spectroscopy.....	30
Figure 2.6: Scheme of the setup used for TRam measurements under N ₂ loaded with water vapor (A: heating plate, B and B': washing flask, C: Linkam stage, D: Raman microscope).	31
Figure 2.7: The glass apparatus used for ACHR experiments.....	32
Figure 3.1: The room temperature structure of (a) NaBH ₄ (Fm-3m) and (b) NaBH ₄ ·2H ₂ O according to the crystallographic data of ref. [49] (Na: blue, B: red, O: purple, hydridic hydrogens H ^{δ-} of BH ₄ ⁻ : gray, H ^{δ+} protonic hydrogens of H ₂ O: pink).....	36
Figure 3.2: The effect of NaBH ₄ concentration on (a) hydrogen generation and (b) hydrogen yield. The concentration of NaBH ₄ (in wt%) is indicated on the curves (the figure is taken from ref. [59]).....	38
Figure 3.3: The two possible activated complexes of the hydrolysis of NaBH ₄ in D ₂ O as given by Davis et al. [63].....	40
Figure 3.4: Schemes of the Hydrolysis of NaBH ₄ in D ₂ O: (a) in presence of D ⁺ according to ref. [65, 66, 67] and (b) in presence of Pd or Pt catalyst according to ref. [73, 74].....	43
Figure 3.5: ¹¹ B NMR spectrum of 84 mM solution of NaBH ₄ in 4:1 H ₂ O:D ₂ O showing the signals for BH ₄ ⁻ ($\delta = -40.24$ ppm), BH ₃ (OH) ⁻ ($\delta = -11.46$ ppm) and borates ($\delta = 3.01$ ppm) (the figure is taken from ref. [72]).	45
Figure 3.6: Scheme of the main steps of the mechanism of hydrolysis of BH ₄ ⁻ to B(OH) ₄ ⁻ as proposed in ref. [68]. (*)In basic solution the main product of the hydrolysis reaction is B(OH) ₄ ⁻ ; the reaction of BH(OH) ₃ ⁻ to B(OH) ₄ ⁻ may proceed through the	

dehydrogenation of $\text{BH}(\text{OH})_3^-$ to $(\text{OH})_2\text{B}=\text{O}^-$ followed by the hydrolysis of the latter to $\text{B}(\text{OH})_4^-$	46
Figure 3.7: TDA signal for H_2 and H_2O as a function of temperature for solid NaBH_4 heated under vacuum up to 600°C (the figure is taken from ref. [21]).	48
Figure 3.8: Raman spectra of (a) NaBH_4 powders and (b) in contact with a droplet of water of approximately 3 mm diameter. The Raman fundamentals of NaBH_4 are indicated.	50
Figure 3.9: Raman spectra of (a) as-received NaBH_4 and (b) after few minutes at ambient conditions	51
Figure 3.10: IR spectra of NaBH_4 , $\text{NaBH}_4 + \text{H}_2\text{O}$ (I and II) and $\text{NaBH}_4 + \text{D}_2\text{O}$ (III) solutions dried at 80°C in open conditions for different times (see Table 3.1 for more clarifications of the denotations I-, II-, and III-1-2). Circles denote the IR fundamentals of BH_4^- anion at $1125 (\nu_4)$ and $2290 (\nu_3) \text{ cm}^{-1}$	53
Figure 3.11: TG/DTA of NaBH_4 heated to 400°C at $5^\circ\text{C}/\text{min}$ under (a) He and (b) synthetic air (solid lines and dashed lines are for pre-evacuated and non-pre-evacuated samples, respectively). TG: red, dTG: blue and heat flow: green lines. The inset graph is zoomed for the TG curves between 0 and 250°C . (c) IR spectra of the solid residues after TG.	56
Figure 3.12: TRam of $\text{NaBH}_4 \cdot 2\text{H}_2\text{O}$ from room temperature to 400°C	59
Figure 3.13: TRam of NaBH_4 powder under (a) inert N_2 flowing and (b) N_2 loaded with water for temperatures above 300°C . Asterisks denote the Raman peaks assigned to $\text{Na}_3\text{B}_3\text{O}_6$	61
Figure 3.14: TIR of NaBH_4/KBr from room temperature to 400°C (at the left side). At the right side, the corresponding spectra are zoomed in the spectral range between 1200 and 1700 cm^{-1} . Asterisks are used to follow the intermediary peak at 1575 cm^{-1} . (<i>RT: room temperature</i>)	63
Figure 3.15: IR spectra $\text{NaBH}_4/\text{NaCl}$, NaBH_4/KCl and KBH_4/KBr pellets after thermal treatment to 450°C in comparison with of NaBH_4/KBr . Spectral region of $\text{B}_3\text{O}_6^{3-}$ (650 - 800 cm^{-1}) and BH_4^- (1000 - 1200 cm^{-1}) are shown. Dashed vertical lines are used to show the peak positions of $\text{B}_3\text{O}_6^{3-}$	64
Figure 3.16: Time dependence of the integrated intensities (Int. I) at 400°C of (a) $\text{Na}_3\text{B}_3\text{O}_6$ (677 - 775 cm^{-1}) and (b) NaBH_4 (2065 - 2700 cm^{-1}). Red lines are the regressions using a logarithmic function of the form $y = y_0 + a \ln(x-x_0)$	66
Figure 3.17: TIR spectra of NaBH_4/KBr in presence of NaNO_3 tracer	67
Figure 3.18: Temperature dependence of the integrated intensities of (a) NaBH_4 and (b) $\text{Na}_3\text{B}_3\text{O}_6$ for TIR of NaBH_4/KBr pellets with and without NaNO_3 tracer. (c) Integral intensities of ν_2 of NaNO_3 tracer used in NaBH_4/KBr pellet compared to a reference	

- NaNO₃/KBr pellet. Integrated intensities are calculated for the TIR spectra during the heating up run (left) and at 25°C when cooled down from T as denoted (T=>25°C) at the right side. Lines are only guide for eyes. 69
- Figure 3.19: IR spectra of NaBH₄/KBr pellets before and after the isotherms (a) at 250°C for 15 min and (b) at 270°C for 30 min under N₂ atmosphere loaded with water vapor. Experiments were performed on pellets without and with KNO₃ tracer. At the right side, the graphs are zoomed between 650 and 1700 cm⁻¹..... 71
- Figure 4.1: (a) Room temperature structure of NH₃BH₃ showing the rotational disorder of hydrogen atoms (white) around each B (pink) and N (purple) atoms (the figure is taken from ref. [104]). (b) The chemical bond between B (blue) and nitrogen N (red) atoms in NH₃BH₃. 74
- Figure 4.2: The mechanisms proposed for the acid catalyzed H₂ release of NH₃BH₃ according to ref. [115]. Scheme (a): protonation of the borohydride group. Scheme (b): protonation of the amino group. 76
- Figure 4.3: Chemical structure of some possible products of the thermal decomposition of NH₃BH₃ (the figure is taken from ref. [8])..... 77
- Figure 4.4: Temperature dependence of the ion intensity assigned to hydrogen (...), H₂N=BH_{2(g)} (---) and B₃N₃H_{6(g)} (—) from two different runs at 5°C/min (the figure is taken from ref. [121]). 78
- Figure 4.5: Mechanism of the release of the first mol H₂ of NH₃BH₃ at T=88°C. AB denotes ammonia borane NH₃BH₃ (the figure is taken from ref. [120])..... 78
- Figure 4.6: X-ray powder diffractograms of NH₃BH₃-G1 (green) and NH₃BH₃-G2 (blue). X-ray pattern of NH₃BH₃ is also shown for comparison. Inset graph is zoomed for the two main indexes between 23 and 25°2θ. S denotes the peaks indexed to sodalite phase. Circles indicate the peaks due to the sample holder. (Bruker D8, 5-90°2θ, step width of 0.01°2θ and 12 s/step). 81
- Figure 4.7: SEM pictures of NH₃BH₃ (left side) and NH₃BH₃-G1 (right side)..... 82
- Figure 4.8: IR and Raman spectra of as-received NH₃BH₃. Squares denote unassigned bands (see text for more clarifications). 83
- Figure 4.9: IR spectra of NH₃BH₃-G1 (green) and NH₃BH₃-G2 (blue) in comparison with NH₃BH₃ (black). S denotes the IR triplicate related to the sodalite phase..... 85
- Figure 4.10: IR spectra of NH₃BH₃ and NH₃BH₃-G1 and the solid residues of their aqueous solutions dried at 80°C under open conditions for 20 h..... 86

- Figure 4.11: (a) Experimental values of $V(\text{H}_2)$ released as a function of sample masses used for $\text{NH}_3\text{BH}_3\text{-G2}$ (squares) in comparison with NH_3BH_3 (triangles) and NaBH_4 (circles). Dashed lines are the linear regressions. (b) Predicted values for $V(\text{H}_2)/(100 \text{ mg sample})$. Bars represent the errors calculated as described in 2.2.5..... 87
- Figure 4.12: IR of $\text{NH}_3\text{BH}_3\text{-G2}$ and NH_3BH_3 and the solid residues after ACHR. IR spectra of NH_4Cl and H_3BO_3 are overlaid for comparison..... 89
- Figure 4.13: IR spectra of NH_3BH_3 and $\text{NH}_3\text{BH}_3\text{-G1}$ and the solid residues after treatment with NaOH solution (1M). Squares denote the IR peaks related to BH_4^- 90
- Figure 4.14: Possible decomposition pathways for the decomposition of NH_3BH_3 in NaOH solutions 91
- Figure 4.15: IR spectra of fresh prepared $\text{NH}_3\text{BH}_3\text{-G1}$ and after 4 months. IR spectrum of $\text{NaB}(\text{OH})_4$ is shown for comparison. 92
- Figure 4.16: IR spectra of (a) NH_3BH_3 and (b) $\text{NH}_3\text{BH}_3\text{-G1}$ kept at 80°C under open conditions for different heating times: 20, 43 and 64 h. IR spectra of NH_3BH_3 and $\text{NH}_3\text{BH}_3\text{-G1}$ are shown for comparison. 93
- Figure 4.17: (a) TG and (b) DTA results of NH_3BH_3 (dashed blue line) and $\text{NH}_3\text{BH}_3\text{-G1}$ (solid green line). The inset graph reproduces TG results of NH_3BH_3 according to Frueh et al. [118]. 95
- Figure 4.18: TIR spectra of (a) NH_3BH_3 and (b) $\text{NH}_3\text{BH}_3\text{-G1}$ in KBr matrix in the heating run to 400°C . IR modes of BH_4^- are indicated. 97
- Figure 4.19: TIR spectra of (a) NH_3BH_3 and (b) $\text{NH}_3\text{BH}_3\text{-G1}$ in KBr in presence of NaNO_3 tracer from room temperature to 180°C in the spectral range between 600 and 1800 cm^{-1} . Asterisks indicate the BH_4^- peak at 1123 cm^{-1} and the NH_2 deformation mode at 1566 cm^{-1} 99
- Figure 4.20: Variation of the integral intensity of $\nu_2(\text{NO}_3^-)$ of NaNO_3 tracer for NH_3BH_3 (stars) and $\text{NH}_3\text{BH}_3\text{-G}$ (square) in function of temperature in the TIR experiments in presence of NaNO_3 tracer, in comparison to the thermal behavior of NaNO_3/KBr reference pellet (open circles). Heat flow curves of NH_3BH_3 and $\text{NH}_3\text{BH}_3\text{-G}$ (dashed line) are overlaid for comparison. 100
- Figure 4.21: Integral intensity of $\nu_2(\text{NO}_3)$ of NH_3BH_3 (stars), $\text{NH}_3\text{BH}_3\text{-G1}$ (squares) in comparison with NaBH_4 (diamonds) as a function of thermal treatment temperature. $\nu_2(\text{NO}_3)$ of NaNO_3/KBr (circles) is taken as reference. Values are given for TIR spectra cooled down from temperature T as indicated ($T \Rightarrow \text{RT}$). Dashed lines are only guide for eyes..... 102

- Figure 4.22: TIR spectra of (a) NH_3BH_3 and (b) $\text{NH}_3\text{BH}_3\text{-G2}$ in NaCl (dry) from room temperature to 500°C . (c) IR spectrum of commercial boron nitride BN, for comparison. 104
- Figure 4.23: IR results of the heating of (a) NH_3BH_3 and (b) $\text{NH}_3\text{BH}_3\text{-G1}$ under open conditions to different temperatures as denoted. IR spectra of NH_3BH_3 and $\text{NH}_3\text{BH}_3\text{-G1}$ are shown for comparison. 106
- Figure 4.24: Reaction scheme of the decomposition of NH_3BH_3 and $\text{NH}_3\text{BH}_3\text{-G}$ in KBr and formation of BH_4^- anions. * It can be hard said whether the conversion of NH_3BH_3 to DADB is total or partial and whether H_2 is liberated from DADB or from a bimolecular reaction of NH_3BH_3 with DADB. ** $\nu_4(\text{BH}_4^-)$ appears for $\text{NH}_3\text{BH}_3\text{-G}$ at slightly lower temperatures compared to NH_3BH_3 112
- Figure 4.25: Reaction scheme of the thermal decomposition of $\text{NH}_3\text{BH}_3\text{-G}$ composite. 113
- Figure 5.1: Linear correlation between the decomposition temperature (T_d) of the complex hydride (borohydrides and alanates, respectively) and the Pauling electronegativity (χ_P) of the cation (the figure is taken from ref. [170])..... 115
- Figure 5.2: XRD patterns of the equimolar mixtures of $\text{NaBH}_4\text{:NaBr}$, $\text{NaBH}_4\text{:NaCl}$ and $\text{NaBH}_4\text{:KBr}$ pressed pellets in the range of the (2 2 0) reflections of the pristine NaBH_4 , NaBr, NaCl and KBr salts 118
- Figure 5.3: X-ray diffractograms of B-0.5-300°-20h in comparison with the diffractograms of the mixture before heating and NaBH_4 and NaBr pristine salts. The reflexes of NaBH_4 are indexed. Inset graph is zoomed for the (2 0 0) reflection between 41.4 and $43.8^\circ 2\theta$. Circles denote $\text{Na}(\text{BH}_4)_{(x-1)}\text{Br}_x$ reflexes. 120
- Figure 5.4: X-ray diffractograms of the thermally treated $\text{NaBH}_4\text{:NaCl}$ mixtures. Diffractograms of NaBH_4 and NaCl are shown for comparison. Inset graph is zoomed for the (2 2 0) reflections. Circles and squares denote $\text{Na}(\text{BH}_4)_{(1-x)}\text{Cl}_x$ and $\text{Na}(\text{BH}_4)_y\text{Cl}_{(1-y)}$, respectively. Asterisks are for the by-products. 121
- Figure 5.5: FTIR-ATR spectra of the as-received NaBH_4 and KBH_4 samples..... 123
- Figure 5.6: Room temperature transmission IR spectra of as-received NaBH_4 in (a) NaCl, in KBr (b) short pressed and (c) long pressed, in (d) NaBr and in (e) KI 125
- Figure 5.7: IR spectra of NaBH_4 diluted in (a) NaCl and (b) KCl pellets before (black dashed lines) and after the thermal treatment to 450°C (red solid lines) 126
- Figure 5.8: TIR spectra of $\text{NaBH}_4\text{/NaCl}$ pellet. The graph at the left side is zoomed for ν_4 127
- Figure 5.9: TIR spectra of (a) $\text{NaBH}_4\text{/NaCl}$ for ν_4 and their second derivatives Ψ'' . Results of (b) $\text{NaBH}_4\text{/KBr}$ are shown for comparison. 128

- Figure 5.10: Graphical representations of $v_3(i\text{-BH}_4^-)$ in function of (a) cell parameter a_0 and (b) radius ratio ($R = r^+/r^-$) of the corresponding AX halide. Solid lines represent common cation A-series and dashed lines are for the common anion X-series..... 131
- Figure 5.11: Graphical representations of $v_3(i\text{-BH}_4^-)$ in function of (a) exothermicity $-\Delta H$ of AX and (b) ionic character I_c of the bond for AX halides. Solid lines are for A-series and dashed lines are for X-series. 134
- Figure 5.12: Graphical representation of $v_3(i\text{-BH}_4^-)$ as a function of the contribution of the short range interaction energies in the corresponding AX. Dashed line is the linear regression. 137
- Figure 6.1: Crystal structures of sodium metaborate tetrahydrate and dihydrate (projection along c-axis). I and II denote the two distinct crystallographic molecules of water of the tetrahydrate (Na: orange, B: blue, O: green, H of $\text{B}(\text{OH})_4^-$: gray and H_2O molecules: dark red). I and II denote the two types of crystalline molecular water of the tetrahydrate. 140
- Figure 6.2: Role of the excess hydration factors α and β in the hydrogen storage capacity of $\text{NaBH}_4\text{-H}_2\text{O}$ (black) and $\text{NH}_3\text{BH}_3\text{-H}_2\text{O}$ (gray) systems according to reactions (6.2) and (6.3), respectively (α and β equal to 0, 2 and 4)..... 144
- Figure 6.3: Characterization of the commercial sample of $\text{NaBO}_2\cdot 4\text{H}_2\text{O}$. (a) IR spectrum and (b) X-ray patterns for two measurements. For comparison reflexes of $\text{NaBO}_2\cdot 4\text{H}_2\text{O}$ (black bars) and $\text{NaBO}_2\cdot 2\text{H}_2\text{O}$ (gray bars) references are shown. 146
- Figure 6.4: TG (solid blue lines), dTG (dashed red lines) and DTA (green solid lines) results for (a) He//vac//5 and (b) He//novac//5. The phases of the plateaus of the TG curves and the endotherms (E1-E5) are indicated. 148
- Figure 6.5: TG/DTA results of He//vac//2 and He//vac//1 in comparison with He//vac//5 153
- Figure 6.6: TG, dTG and DTA results of (a) air//vac//5 (red lines) in comparison with He//vac//5 (black) and (b) air//vac//1 (green) in comparison with He//vac//1 (black)..... 156
- Figure 6.7: In-situ X-ray patterns of the thermal dehydration of $\text{NaBO}_2\cdot 4\text{H}_2\text{O}$ using 0.12 s per step from room temperature to 400°C 158
- Figure 6.8: In-situ X-ray patterns obtained from the thermal dehydration of $\text{NaBO}_2\cdot 4\text{H}_2\text{O}$ using 0.7 s per step between 90 and 200°C . The main reflexes of $\text{NaB}(\text{OH})_4$, $\text{NaBO}_2\cdot (1/3)\text{H}_2\text{O}$ ($I \geq 30\%$, black bars) and $\text{NaBO}_2\cdot (2/3)\text{H}_2\text{O}$ ($I \geq 50\%$, pink bars) are overlaid for comparison. 159
- Figure 6.9: TIR of $\text{NaBO}_2\cdot 4\text{H}_2\text{O}$ from room temperature to 90°C 160
- Figure 6.10: TIR of $\text{NaB}(\text{OH})_4$ linearly heated from room temperature to 420°C 162
- Figure 6.11: TIR of $\text{NaB}(\text{OH})_4$ to 400°C using isothermals conditions at 160°C 163

- Figure 6.12: X-ray patterns of the end-products of exp.a-e. When necessary, a comparison with a reference pattern is given (vertical bars). 166
- Figure 6.13: IR spectra of the end-products of exp.a-e 167
- Figure 6.14: Raman spectra of the dihydrate (exp.a), the one-third (exp.d) and the anhydrous (exp.e) phases. The peak positions of the primary peak of each phase are indicated. 168
- Figure 6.15: TIR spectra of the decomposition of the metaborate ring (B_3O_6)³⁻ to the linear BO_2^- molecule 173
- Figure 6.16: The thermal dehydration path of $NaBO_2 \cdot 4H_2O$ according to this work (red path) in comparison with those reported previously in the literature (gray paths). The dehydration temperatures are given according to TG He//vac//5. For each metaborate phase, the hydration degree y and the content of water (wt% H_2O) are given. ^(a) ref. [202], ^(b) ref. [85], ^(c) ref. [207], ^(d) ref. [206]. 174
- Figure 6.17: Coordination of $B(OH)_4^-$ anion in (a) $NaB(OH)_4 \cdot 2H_2O$ and (b) $NaB(OH)_4$ crystals including sodium atoms and hydrogen bonds. The hydrogen bonding network in $NaB(OH)_4 \cdot 2H_2O$ is traced between oxygen atoms. (Na: yellow, B: blue; O and H of $B(OH)_4^-$: green and gray, respectively; H_2O molecules: dark red) 176
- Figure 6.18: IR spectra of the anhydrous samples after TG analyses of pre-evacuated and non-pre-evacuated $NaBO_2 \cdot 4H_2O$ samples under He at 5 and 1°C/min (TG experiments are He//vac//5, He//novac//5, He//vac//1 and He//novac//1). 178
- Figure 7.1: The thermal path for H_2 release using $NaBH_4$ between 20 and 400°C (green arrows) in comparison with the dehydration path for $NaBO_2 \cdot 4H_2O$ (blue arrows), as obtained in this thesis. The net reaction of $NaBH_4$ with O_2 is considered. Further experiments are needed to verify whether the transient species at 1575 cm^{-1} may occur from the reaction of $NaBH_4$ with O_2 between 200 and 300°C. 182

III. List of Tables

Table 3.1: Thermal treatment of NaBH ₄ in H ₂ O and D ₂ O solvents.....	52
Table 3.2: IR peak positions of B ₃ O ₆ ³⁻ and BH ₄ ⁻ after the thermal treatment of NaBH ₄ /KBr, NaBH ₄ /KCl, NaBH ₄ /NaCl and KBH ₄ /KBr pellets in comparison with literature values of Na ₃ B ₃ O ₆ and K ₃ B ₃ O ₆	65
Table 4.1: IR and Raman fundamentals of NH ₃ BH ₃	84
Table 4.2: ACHR of NH ₃ BH ₃ -G2, NH ₃ BH ₃ and NaBH ₄ . Experimental single measurements and predicted V(H ₂)/100 mg sample with the corresponding errors calculated as described in 2.2.5.	88
Table 4.3: IR frequencies obtained in this work for PAB in comparison with literature values for polymers containing single bonds between B and N atoms. HEL (helicoidal) and COIL (coiled) are two possible conformers proposed for PAB.	109
Table 4.4: IR frequencies obtained in this work for PIB in comparison with literature values for compounds containing π-bonds between B and N atoms. Asterisks denote the peaks that were estimated by reproduction of the IR spectra.	110
Table 5.1: List of thermally treated samples	119
Table 5.2: ATR frequencies of NaBH ₄ and KBH ₄ compared to ATR values of Renaudin et al. [81] (values in brackets) in addition to the transmission IR frequencies of NaBH ₄ in KBr and NaCl pellets.	124
Table 5.3: IR frequencies of i-BH ₄ ⁻ in different AX lattices. Structural parameters of AX are also given.....	130
Table 5.4: Empirical constants (α and β) of the linear relationship $\nu_3(i\text{-BH}_4^-) = \alpha \cdot a_0(\text{AX}) + \beta$ for common cation A- series and common anion X-series	132
Table 5.5: Correlations found between $\nu_3(i\text{-BH}_4^-)$ and the different parameters of the AX halide (the cell parameter a ₀ , the effective radii of the cation (r ⁺) and the anion (r ⁻), the radius ratio R = r ⁺ /r ⁻ , the Pauling electronegativity χ_P , the fractional ionic character I _c and the standard enthalpy of formation ΔH). The effect on the stability of BH ₄ ⁻ is also indicated.	135
Table 5.6: Contribution of the short range forces of the alkali halides as given by the Born-Mayer equation (in kg.cal.mol ⁻¹) [189]	138

Table 6.1: Crystallographic data of $\text{NaBO}_2 \cdot y\text{H}_2\text{O}$ compounds as reported in the literature in addition to the molecular structure of the borate anion (B: blue, O: green, H: gray).	141
Table 6.2: Information about the thermal treatments of the commercial $\text{NaBO}_2 \cdot 4\text{H}_2\text{O}$ sample. $\text{ML}_{\text{tot-curv}}$ is the total loss indicated on the TG curve and y_i is the equivalent mol of water. $\text{ML}_{\text{tot-calc}}$ is the total loss obtained by subtracting the mass of the crucible and the sample after the thermal treatment from that before the thermal treatment.	147
Table 6.3: Thermal treatments of $\text{NaBO}_2 \cdot 4\text{H}_2\text{O}$ and end-products	165
Table 6.4: Experimental IR frequencies and Raman shifts of $\text{NaB}(\text{OH})_4 \cdot 2\text{H}_2\text{O}$ and $\text{NaB}(\text{OH})_4$ in comparison with literature.....	169
Table 6.5: IR frequencies and Raman shifts of $\text{Na}_3\text{B}_3\text{O}_5(\text{OH})_2$ in comparison with Raman results of the literature.....	171
Table 6.6: IR frequencies and Raman shifts of $\text{Na}_3\text{B}_3\text{O}_6$, in comparison with literature.....	172

IV. List of Abbreviations

ATR	Attenuated total reflectance
DSC	Differential scanning calorimetry
DTA	Differential thermal analysis
IR	Infrared
mol	mole
TG	Thermogravimetry
dTG	Derivative of TG
TIR	Temperature dependent Infrared
TRam	Temperature dependent Raman
XRD	X-ray diffraction
a.u.	area units
T _m	Melting temperature
T _d	Decomposition temperature
T=>25°C	used in TIR experiments for the IR spectra taken at room temperature after cooling down from temperature T as indicated
χ _P	Pauling electronegativity

1. Introduction

Worldwide energy consumptions are expanding rapidly while global production of energy struggles to keep pace. Petroleum and oils reservoirs will inevitably run out. This, in addition to the global warming caused by CO₂ produced by petroleum combustion, make significant concerns about seeking alternatives to burning fossil fuels [1, 2].

During the last decades, hydrogen has been targeted as a clean energy carrier for both transportation and stationary applications due to its high environmental abundance and friendliness [3]. Power can be generated either as mechanical power by burning hydrogen or as electrical power by using it in a fuel cell. In both cases, hydrogen is oxidized by oxygen to form water [1].

On earth, hydrogen exists primarily in combination with other chemical elements. Therefore, the development of a hydrogen economy requires an adequate and readily accessible source for the production of H₂ which should then be stored and transported in an effective and a safe form.

When compared to petroleum, hydrogen has a higher energy content per mass (120 MJ/kg for hydrogen versus 44 MJ/kg for petroleum [4]) but unfortunately a lower energy content per volume (0.01 kJ/L at standard temperature and pressure and 8.4 MJ/L for liquid hydrogen versus 32 MJ/L for petroleum [4]) making high pressurized tanks of hydrogen and liquefied hydrogen at cryogenic temperatures impractical for a viable hydrogen economy. This raises the necessity of seeking new efficient storage systems. Works in this field are numerous and go in many directions. Hydrogen can be stored physisorbed (Van der Waals forces) to porous materials as metal organic frameworks, zeolites and carbon nanostructures [5, 6]. Hydrogen can be also chemically bound within a solid in the form of a chemical hydride [5]. Chemical hydrogen storage materials are targeted as potential hydrogen sources for fuel cells due to their high hydrogen content [7]. Among these materials, the compounds containing boron B and nitrogen N atoms have attracted attention since B and N are light weight elements and capable to bond to multiple hydrogen atoms [8, 9]. For example, ammonium borohydride NH₄BH₄ has a very high content in hydrogen (24.5 wt%), but it decomposes slowly at room temperature and must be stored in liquid ammonia or at

temperatures below -40°C [10]. Other attractive hydrides are Sodium Borohydride NaBH_4 and Ammonia Borane NH_3BH_3 which constitute the main focus of this thesis.

NaBH_4 and NH_3BH_3 contain 10.6 wt% and 19.6 wt% hydrogen, respectively. Both have high potential in the energy field, are stable at room temperature and are considered as green materials not hazardous for a sustainable and safe energy technology [11]. They can be regarded as complexes of borane, X-BH_3 , constituted of the Lewis base donor (X) and the Lewis acid borane group (BH_3) [12]. In the case of NaBH_4 , X is an anionic monoatomic donor (H^-) charging the complex negatively, while for NH_3BH_3 , X is a polyatomic neutral Lewis base donor (NH_3) forming a dative bond with the borane group. The history of NaBH_4 is longer and could be decisive in the development of NH_3BH_3 hydrogen storage based systems [11].

Sodium borohydride is also called sodium tetrahydroborate as recommended by the IUPAC (*International Union of Pure and Applied Chemistry*) and contains tetrahedral BH_4^- units [13]. Ionic interactions lie between BH_4^- and Na^+ . Within the borohydride unit, the boron B and hydrogen H atoms are covalently bound [14]. It is widely used as reducing agent in organic syntheses [15]. The white crystalline powder is sensitive to moisture but not to oxygen. It is one of the least expensive metal hydrides commercially available (on a hydride equivalent basis) [13]. Since its discovery by Soldate in 1947 [16], a very large number of papers have been focused on the hydrolysis reaction of NaBH_4 producing $\text{H}_{2(\text{g})}$ and metaborate by-products. In November 2007, the U.S. Department of Energy, DOE [17], recommended a no-go decision for NaBH_4 for on-board automotive application because the aqueous solution of NaBH_4 does not fulfill the requirements sets in term of storage capacity, costs and inefficiency of recycling the metaborate by-products [18]. Since then, researchers on NaBH_4 have been more involved on hydrogen release from solid state NaBH_4 [19]. NaBH_4 melts at 497°C [20] and decomposes completely above 500°C to its elemental constituents liberating $\text{H}_{2(\text{g})}$ [21]. This thesis focuses on the thermal behavior of solid NaBH_4 and hydrogen release reactions between room temperature and 450°C , below the melt formation.

NH_3BH_3 -based materials are very promising in terms of the use as viable H_2 carrier for on-board applications [22, 23]. Commercially, NH_3BH_3 is less widespread as NaBH_4 and exhibits few applications in organic chemistry such as an air-stable derivative of diborane [11]. The thermal dehydrogenation of NH_3BH_3 has today great promise to work in the transportation sector. Researches on NH_3BH_3 are still in their initial development phase. Long and rich experiences with NaBH_4 could be beneficial for NH_3BH_3 [11]. The thermal behavior

of NH_3BH_3 between room temperature and 400°C is investigated in details in this thesis. NH_3BH_3 melts and releases its first mol H_2 at $110\text{-}112^\circ\text{C}$. Nonetheless, this thermal decomposition is harsh from chemical and technical points of view, since it is accompanied by foaming caused by the liberation of B, N-containing gases and voluminous swelling of the sample. The re-crystallization of NaBH_4 [24, 25] and NH_3BH_3 [26] in a geopolymer type framework as so called NaBH_4 -geopolymer ($\text{NaBH}_4\text{-G}$) and NH_3BH_3 -geopolymer ($\text{NH}_3\text{BH}_3\text{-G}$) offers a very simple route for a better handling of NaBH_4 and NH_3BH_3 , respectively. Preliminary results on the new $\text{NH}_3\text{BH}_3\text{-G}$ composite are presented in this thesis.

A part of this thesis is concerned with the mechanism of the thermal dehydration of sodium metaborate tetrahydrate, $\text{NaBO}_2\cdot 4\text{H}_2\text{O}$. The identification of metaborate dehydration products is of importance since metaborate compounds appear as by-products in the oxidation reactions of NaBH_4 and NH_3BH_3 for H_2 release. In these reactions, the hydridic hydrogen atoms on B serve as source of electrons and are oxidized.

Project aims and structure of the work

The aim of this thesis is focused on the investigation of the thermal behavior of boron-hydride materials NaBH_4 , NH_3BH_3 and $\text{NH}_3\text{BH}_3\text{-G}$ in the solid state using mainly spectroscopic and diffraction methods.

In a first approach, H_2 release of solid state NaBH_4 is investigated between room temperature and 450°C , below the melting point. The role of O_2 and H_2O in the oxidation of NaBH_4 to metaborate NaBO_2 is discussed. The thermal dehydrogenation mechanism of $\text{NH}_3\text{BH}_3\text{-G}$ in comparison to NH_3BH_3 salt is investigated in details, too. Comparisons with NaBH_4 salt are made when necessary.

The thermal treatment of NaBH_4 favors ionic exchanges with the halide surrounding. The dissolution mechanism of NaBH_4 is investigated and the impact of the halide on BH_4^- anion is discussed.

Sodium metaborate compounds ($\text{NaBO}_2\cdot y\text{H}_2\text{O}$) are investigated in details considering the thermal dehydration of the commercial sample $\text{NaBO}_2\cdot 4\text{H}_2\text{O}$. Their role in the hydrolysis reaction of NaBH_4 for H_2 release is discussed.

The structure of the work is as follows:

Chapter 2 concerns the experimental techniques used in this work including principally thermogravimetric, spectroscopic and X-ray diffraction methods. Temperature dependent Infrared spectroscopy was conducted combined to nitrate tracer to follow H_2 release reactions of $NaBH_4$, NH_3BH_3 and NH_3BH_3 -G composites.

Chapter 3 entitled **H_2 Release from Solid State Sodium Borohydride $NaBH_4$** is focused on H_2 release of solid state $NaBH_4$ between room temperature and $450^\circ C$, below the melting point. Thermogravimetric analyses were conducted to check the thermal stability of $NaBH_4$ under He and under synthetic air. In-situ Raman experiments were carried out under air, N_2 and N_2 loaded with water vapor, to study the role of $H_2O_{(g)}$ and $O_{2(g)}$ in the oxidation reaction of $NaBH_4$ to metaborate. Temperature dependent Infrared experiments were also performed under vacuum using $NaBH_4/KBr$ pellet. H_2 release was followed using nitrate tracer method.

Chapter 4 is entitled **H_2 Release from Ammonia Borane NH_3BH_3 and NH_3BH_3 -Geopolymer (NH_3BH_3 -G)** and investigates the thermal dehydrogenation of NH_3BH_3 and its re-crystallization within a geopolymer matrix (NH_3BH_3 -G) for a better handling. NH_3BH_3 -G was characterized using different methods including X-ray diffraction, Infrared and Raman spectroscopy and imaging SEM/EDX. H_2 content in NH_3BH_3 -G was evaluated using a specific volumetric method (ACHR). The stability of NH_3BH_3 -G was checked under different operating conditions. The thermal decomposition of NH_3BH_3 and NH_3BH_3 -G from 25 to $400^\circ C$ is investigated basing principally on thermogravimetric and temperature dependent Infrared experiments using KBr and NaCl matrices. H_2 release was followed using nitrate tracer method. Comparisons with $NaBH_4$ are made when necessary.

Chapter 5 is entitled **Solid Solutions of BH_4^- in Different Halide AX Matrices (A = Na, K, Rb; X = Cl, Br, I)** and focuses on the ionic exchange between $NaBH_4$ and halides AX. Firstly, the mechanism of formation of the solid solutions of $NaBH_4$ and NaCl and NaBr salts, respectively, is investigated. Equimolar mixtures of $NaBH_4:NaCl$ and $NaBH_4:NaBr$ were pressed into pellets and annealed to different temperatures for different annealing times. End-products were characterized by X-ray diffraction, Infrared and Raman spectroscopy. The variation of the IR frequencies of BH_4^- anion during dissolution is followed using TIR spectroscopy. Secondly, the IR spectra of BH_4^- in NaX and KX halides are reported and compared to literature. Some of the used halides revealed the formation of solution of BH_4^- in AX during the classical pellet preparation method usually used in IR spectroscopy which consists of the dilution of low amounts of the sample in AX matrix. For some other AX matrices, the dissolution of $NaBH_4$ required a further thermal treatment of the pellet to $450^\circ C$.

Literature values for BH_4^- highly diluted in RbX matrix are taken. The high dissolution of NaBH_4 in AX is related to an isolation of BH_4^- in AX. Correlations between the stretching mode (ν_3) of BH_4^- and different structural parameters of the alkali halides are found and are discussed using some graphical demonstrations.

Chapter 6 is entitled **Thermal Dehydration of Sodium Metaborate Tetrahydrate $\text{NaBO}_2 \cdot 4\text{H}_2\text{O}$** and focuses on the detailed mechanism of the thermal dehydration of a commercial sample of $\text{NaBO}_2 \cdot 4\text{H}_2\text{O}$ between 25 and 500°C. The commercial sample contains traces of $\text{NaBO}_2 \cdot 2\text{H}_2\text{O}$ (2.4 - 4.3 %). Thermogravimetric analyses were performed considering slow (1 and 2°C/min) and fast (5°C/min) heating rates under two different flowing gases, He and synthetic air. The individual dehydration steps were followed in-situ using in-situ X-ray diffraction and temperature dependent Infrared spectroscopy. Dehydration products were isolated and characterized using X-ray diffraction, Infrared and Raman spectroscopy. Their role in the hydrogen release by NaBH_4 hydrolysis is discussed.

2. Experimental Methods

2.1 Samples

Commercial samples of sodium metaborate tetrahydrate $\text{NaBO}_2 \cdot 4\text{H}_2\text{O}$ ($137.86 \text{ g}\cdot\text{mol}^{-1}$, Riedel-de-Haën, > 98 %), sodium borohydride NaBH_4 ($37.83 \text{ g}\cdot\text{mol}^{-1}$, Merck, ≥ 98 %), ammonia borane NH_3BH_3 ($30.87 \text{ g}\cdot\text{mol}^{-1}$, Aldrich, 90 %), potassium borohydride KBH_4 ($53.94 \text{ g}\cdot\text{mol}^{-1}$, Aldrich, 99.9 %), sodium nitrate NaNO_3 ($85.01 \text{ g}\cdot\text{mol}^{-1}$, Fluka, ≥ 99 %), potassium nitrate KNO_3 ($101.11 \text{ g}\cdot\text{mol}^{-1}$, Merck, 99.0-100.05 %), sodium chloride NaCl (Merck, ≥ 9.5 %), sodium bromide NaBr (Fluka, ≥ 99.0 %), sodium iodide NaI (Fluka, ≥ 99.0 %), potassium chloride KCl (Merck, ≥ 99.5 %), potassium bromide KBr (Roth) and potassium iodide KI (Riedel-de Haën, 99-100.5 %) were used in this thesis without further manipulation.

NH_3BH_3 -Geopolymer (NH_3BH_3 -G) composite was prepared by a re-crystallization of NH_3BH_3 in sodium aluminate and sodium metasilicate solutions [26]. The same procedure was used for NaBH_4 -geopolymer composites [24, 25]. It consists of the dissolution of definite amounts of NH_3BH_3 in aluminate and silicate solutions. Afterwards, bringing these solutions together induces the polymerization in an aluminosilicate porous framework with very low crystallinity. Firstly, two homogeneous solutions of sodium aluminate (250 mg of $\text{NaAlO}_2 + 1.5 \text{ ml H}_2\text{O}$) and sodium silicate (310 mg $\text{Na}_2\text{SiO}_3 + 1.5 \text{ ml H}_2\text{O}$) were prepared. The total dissolution of sodium metasilicate in water was obtained by mild heating to 60°C . Therefore, it was necessary to cool down this solution to room temperature before adding the same amounts of NH_3BH_3 (250 mg) to the aluminate and metasilicate solutions under stirring. Afterwards, NH_3BH_3 -solutions were mixed together. This induced the gel precipitation and a pasty white liquid is obtained. At last, the gel was dried at 80°C for 4 h. Two different syntheses were made. The corresponding obtained products are denoted NH_3BH_3 -G1 and NH_3BH_3 -G2, respectively. For NH_3BH_3 -G2, NH_3BH_3 -aluminate and NH_3BH_3 -silicate solutions were longer stirred.

The synthesis procedure used for NH_3BH_3 -G and NaBH_4 -G composites differ from that usually used for the traditional geopolymer which is based on the incorporation of a high alkaline solution of alkali hydroxide or silicate (water glass) with source materials rich in SiO_2 and Al_2O_3 such as metakaolin or fly ash [27, 28] followed by the reorientation of free ion clusters and the polycondensation [28].

2.2 Methods

2.2.1 Thermogravimetry / Differential Thermal analyses (TG/DTA)

Thermogravimetric (TG) and differential thermal analyses (DTA) measure the changes in weight and in heat content in function of temperature, respectively. The two methods are complementary and are used to provide information about the structural transformations and chemical reactions of the sample during heating.

During the sample measurements, two crucibles are introduced. One contains the sample and the other is empty used as a correction curve to record the actual changes occurring in the sample.

TG/DTA analyses were conducted on the Setaram SetSys Evolution 1750 equipped with a combined measuring head TGA-DTA 1600. Heating-cooling runs were performed under two flowing gases: synthetic air (80 vol.% N₂ and 20 vol.% O₂) and He (99.9999 vol.%) at 20 ml/min. Different measurement programs were performed with heating/cooling rates varying between 1 and 5°C/min, and temperatures up to 400°C. In some cases, the samples were purged before heating up. The evacuation was completed at 10⁻⁵ mbar for 15 min before filling with the flowing gas. Before each sample measurement, a reference measurement was made exactly in the same way as the sample measurement using the crucible without the sample for baseline corrections.

TG/DTA methods were used to check the thermal stability and decomposition of NaBH₄ (chapter 3), NH₃BH₃ and NH₃BH₃-G (chapter 4) composites. This method was also used to study the thermal dehydration steps of NaBO₂·4H₂O to NaBO₂ (chapter 6).

2.2.2 Powder X-ray diffraction (XRD)

X-ray diffraction constitutes the fingerprint of a crystalline solid and gives information about the periodic arrangement of atoms and ions.

X-ray powder diffraction patterns were taken on the Philips PW-1800 and the Bruker D8 Advantage. The diffraction data were evaluated using STOE WinXpow software.

With X-ray diffraction, the less or more ionic exchange between different mixtures of NaBH_4 and halide (NaCl , KBr and NaBr) was determined (chapter 5).

In-situ powder X-ray diffraction using Bruker D8 Advance equipped with a hot stage PXD was carried out to follow in-situ the thermal dehydration of $\text{NaBO}_2 \cdot 4\text{H}_2\text{O}$ (chapter 6). Measurements were made under N_2 flowing.

2.2.3 Fourier Transformation Infrared Spectroscopy (FTIR)

IR spectroscopy is based on the absorbance of specific frequencies characteristic of the vibrations of atoms in the molecule. When a sample is subjected to IR radiation, it absorbs particular energies matching the frequencies of vibrations of its molecule. For a molecule to absorb IR radiation, the vibration must cause a net change in the dipole moment of the molecule.

Attenuated total reflectance ATR-FTIR spectroscopy

Attenuated total reflectance ATR-FTIR spectroscopy was used in this thesis to compare the IR frequencies of NaBH_4 and KBH_4 in the absence of any matrix effect (chapter 5). The ATR method does not require sample preparation. The IR beam is directed onto the ATR crystal of high refractive index and is totally reflected from the internal surface of the crystal creating an evanescent wave which emerges only a few microns into the sample. In the spectral regions where the sample absorbs energy, the evanescent wave is attenuated. After one or several internal reflections, the IR beam exits the ATR crystal and is directed to the IR-detector. Its penetration depth depends on the wavelength, the refractive indices of the ATR crystal and the sample and the angle of the entering light beam [29]. ATR-IR spectra were recorded on the Bruker IFS 66v/S FTIR spectrometer.

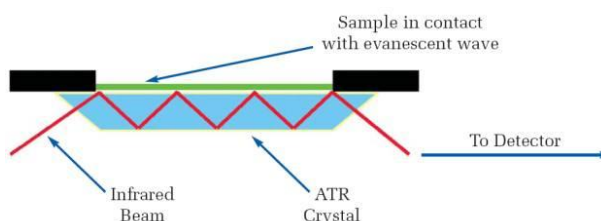


Figure 2.1: Scheme of the path of IR beam in the ATR system (the figure is taken from ref. [29])

Transmission FTIR spectroscopy

Transmission FTIR spectroscopy was used in this work unless stated otherwise. The IR spectra were recorded on the Bruker Vertex 80v spectrometer using the pressed pellet (disk) method. Typically 1 mg of the sample was finely grinded and diluted in 200 mg matrix and then pressed under 100 kN for approximately 2 min. The diameter of the pellet is 13 mm. Alkali halides as KBr and NaCl are usually used as matrices due to their excellent transmission in IR and the simple structure of their lattices. In this thesis KBr is chosen unless stated otherwise. Sample pellets were measured relatively to a reference-pellet constituted of 200 mg of the same alkali halide used for the sample-pellet. Data were recorded between 370 and 4000 cm^{-1} with a resolution of 2 cm^{-1} and 32 scans.

Temperature dependent FTIR spectroscopy

Temperature dependent Infrared (TIR) measurements were carried out using the Bruker IFS 66v/S FTIR spectrometer equipped with an in-house build furnace and a manually adjustable temperature controller (Eurotherm 810) [30]. For the measurements the samples were pressed in KBr- or NaCl-pellets. The sample holder consists of Ag cylinder with two silver nets used in contact of the sample-pellet to provide homogeneous and fast thermal distribution (**Figure 2.2**). The heating/cooling runs were accomplished under vacuum. TIR spectra were taken between 370 and 4000 cm^{-1} using a resolution of 2 cm^{-1} and 40 scans.

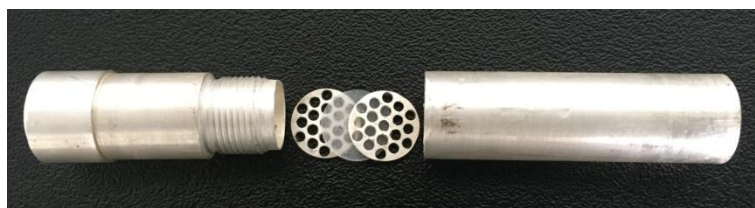


Figure 2.2: The sample holder used for TIR experiments including the Ag holder and the two silver nets with a pellet

Data were evaluated using the Bruker Opus 6.5 software. TIR bands were integrated to calculate the variations in the areas under the IR peaks in function of temperature. This gives particular results about increase or decrease of the concentration of the considered species in the sample compartment. For a given IR band, the integration limits were maintained the same throughout the calculations at different temperatures.

TIR spectroscopy was considered as in-situ method to study the thermal behavior and dehydrogenation of NaBH_4 (chapter 3), NH_3BH_3 and $\text{NH}_3\text{BH}_3\text{-G}$ (chapter 4), the ionic exchange between NaBH_4 and AX salts (chapter 5) and the dehydration of $\text{NaBO}_2\cdot 4\text{H}_2\text{O}$ (chapter 6).

TIR of a pellet constituted of only KBr was made between 25 and 500°C and taken as reference for TIR measurements of the sample-pellets (**Figure 2.3**).

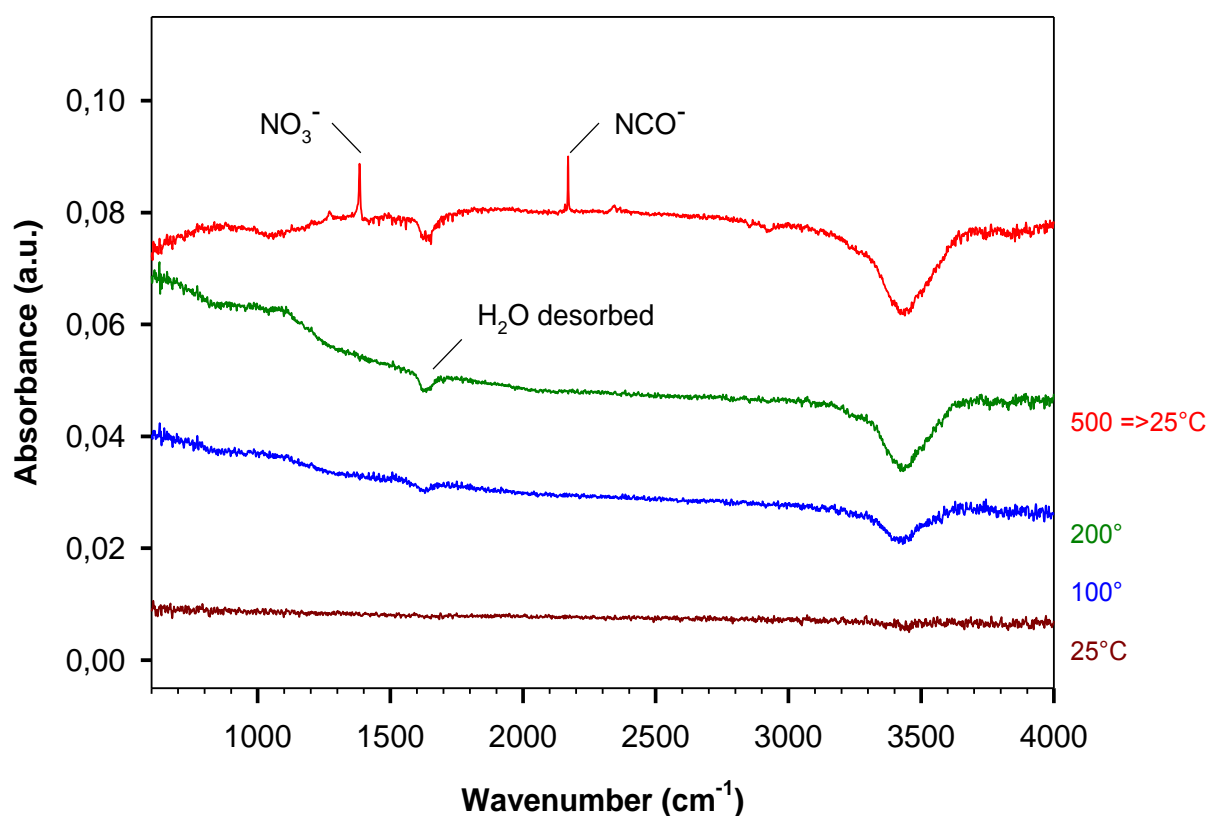


Figure 2.3: TIR of a KBr pellet

The KBr matrix contains traces of H_2O which becomes desorbed at 200°C as can be concluded from the negative IR bands for H_2O bending (1600-1680 cm^{-1} [31]) and O-H stretching (3300-3600 cm^{-1} [31]) modes. The TIR spectrum cooled down from 500°C shows very sharp IR peaks at 1384 and 2170 cm^{-1} assigned to NO_3^- [32, 33] and cyanate NCO^- [34, 35] isolated in KBr matrices, respectively. These are shifted in NaCl matrix to 1422 [32, 33] and 2211 cm^{-1} [34], respectively. Anions dispersed in very low amounts in halides are called “impurities” and give rise to very sharp and intense IR bands even at very low concentrations

[36]. NCO^- impurity may originate from a reaction between ammonium NH_4^+ ion (or trapped ammonia) and the carbonate-bicarbonate ion (or trapped carbon dioxide) [35].

Nitrate reduction method

TIR experiments were performed in presence of nitrate tracer to follow H_2 release from NaBH_4 (chapter 3), NH_3BH_3 and $\text{NH}_3\text{BH}_3\text{-G}$ (chapter 4) samples. Similar experiments have been previously described for the hydrogen release reaction of NaBH_4 -sodalite and NaBH_4 -geopolymer for temperatures above 250°C [37, 38]. Approximately 0.4 mg of NaNO_3 was grinded and distributed homogeneously in the sample/matrix mixture and then pressed in pellet. H_2 released of the sample reduces NO_3^- ions to NO_2^- (reaction 2.1).



The nitrite ion was indicated by the sharp peak assigned to the asymmetrical stretching mode (ν_3) at 1270 cm^{-1} in KBr [34, 39] and at 1300 cm^{-1} in NaCl [39]. H_2 release could also be followed considering the variation of the integrated intensities of NO_3^- tracer in function of temperature in comparison with a reference pellet constituted only of approximately 0.4 mg NaNO_3 diluted in the appropriate matrix.

TIR spectra of NaNO_3/KBr reference pellet are shown in **Figure 2.4**. The IR spectrum of NaNO_3 possesses peaks at 836 (out-of-plane bending ν_2), 1380 (broad, asymmetric stretching ν_3), 1447 (shoulder, $2\nu_4$) and 1789 cm^{-1} ($\nu_1+\nu_4$) in agreement with literature values reported for NaNO_3 [40]. At temperatures higher than 250°C , $\nu_3(\text{NO}_3^-)$ is strongly sharpened and peaked at 1383 cm^{-1} indicating the formation of solid solution of NO_3^- in KBr. This was accompanied by a peak shifting of ν_2 and $\nu_1+\nu_4$ between 200 and 240°C . At the end of the thermal treatment ν_2 is peaked at 839 cm^{-1} and $\nu_1+\nu_4$ at 1768 cm^{-1} .

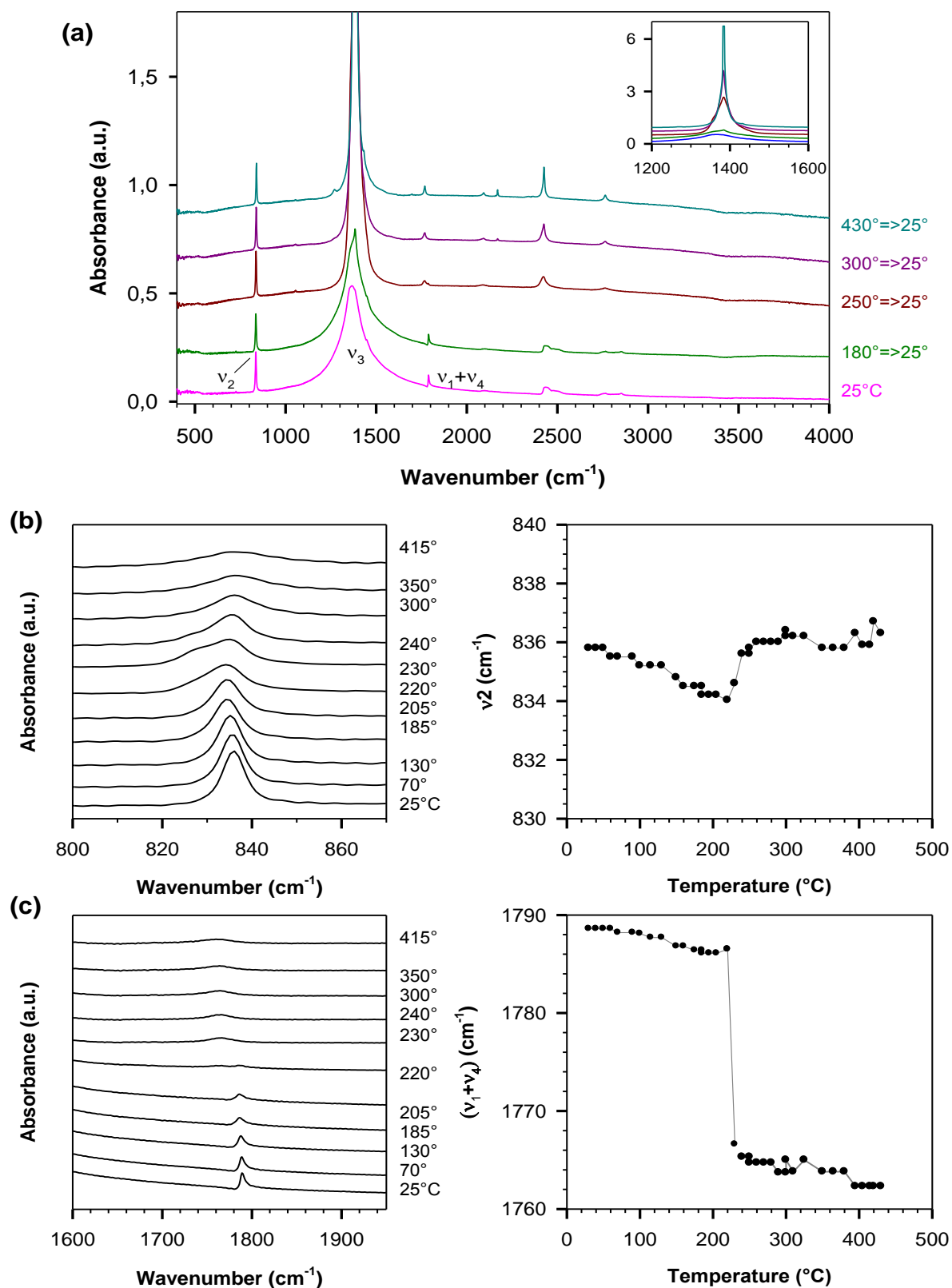


Figure 2.4: TIR of NaNO_3 in KBr. (a) TIR spectra. Inset graph is zoomed for $\nu_3(\text{NO}_3^-)$. Variation of the peak position of (b) ν_2 and (c) $\nu_1+\nu_4$ in function of temperature. Gray lines are guide for eyes.

2.2.4 Raman spectroscopy

Raman spectroscopy is a scattering technique where the sample is illuminated with a monochromatic laser beam. The majority of the light is scattered with the same frequency of that of the incident radiation and constitutes Rayleigh scattering. Only a small amount of the light (1×10^{-7}) is scattered with a frequency different from that of the incident radiation and constitutes Raman scattering. Scattered light with frequencies below the incident light frequency are known as Stokes frequencies; frequencies above the incident light frequency are called anti-Stokes frequencies. Stokes Raman frequencies involve the transitions from lower to higher energy vibrational levels and are more intense than the anti-Stokes. Therefore, it is Stokes frequencies which are measured in conventional Raman spectroscopy [41]. (See **Figure 2.5** for comparison between IR and Raman spectroscopy).

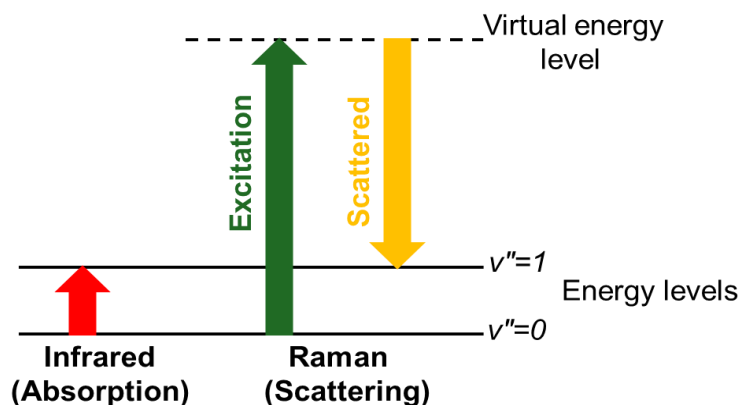


Figure 2.5: Energy levels and transitions involved in IR and Raman spectroscopy

Raman measurements were carried out on the Bruker Senterra dispersive Raman microscope using a laser excitation wavelength of 532 nm using the objective Olympus 50xLWD. Raman spectra were recorded using Opus Software in the range of 70 to 4455 cm^{-1} with a resolution of $\pm 9 \text{ cm}^{-1}$.

Temperature dependent Raman (TRam) spectroscopy

This method was used to study the thermal behavior of NaBH_4 from room temperature to 400°C under different atmospheres in order to determine the role of $\text{H}_2\text{O}_{(g)}$ and $\text{O}_{2(g)}$ in the oxidation reaction to metaborate (chapter 3). Samples were introduced in a Linkam stage coupled to a Linksys32 temperature controller and a cooling water system. TRam spectra were collected on the Bruker Senterra dispersive Raman microscope. Measurements were

performed under air, N_2 flowing and N_2 loaded with water vapor ($N_2 + H_2O$). For (N_2+H_2O) stream, a washing flask (denoted B) was filled with water and placed on a heating plate (A) heated to approximately $80^\circ C$ to increase water vapor. The N_2 flowing passing through the washing flask is then loaded with water vapor which is further transported to the entire system including the sample (**Figure 2.6**). The temperature of the sample must not go down below $120^\circ C$ to prevent the condensation of the vapor on the powder sample. To control N_2 flowing, the downstream gas was connected to a washing flask filled with distilled water that serves as a bubbles counter (B').

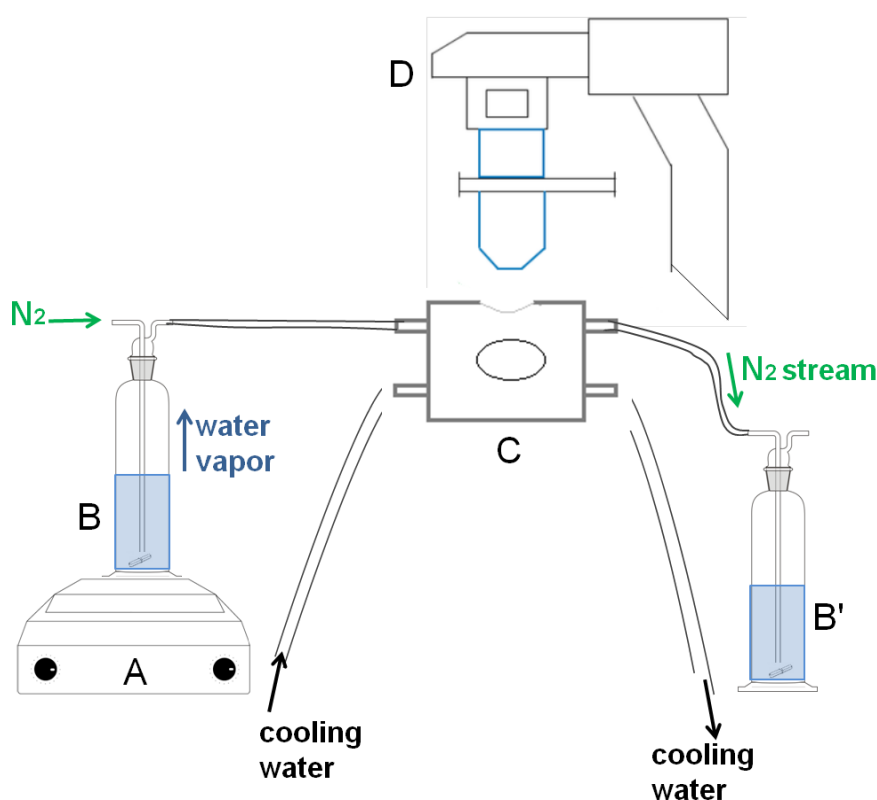


Figure 2.6: Scheme of the setup used for TRam measurements under N_2 loaded with water vapor (A: heating plate, B and B': washing flask, C: Linkam stage, D: Raman microscope).

2.2.5 Volumetric Acid catalyzed hydrolysis release (ACHR)

method

Acid catalyzed H_2 release reactions from NH_3BH_3 , NH_3BH_3 -G were conducted using the apparatus shown in **Figure 2.7** in comparison with $NaBH_4$ salt (chapter 4). The method was previously used to evaluate hydrogen content in $NaBH_4$ -geopolymer composites [25, 38]. Same experimental setup and back calculations are used here.

Specific amounts of the dry solid sample were introduced in a two-neck bulb surmounted by a gas-syringe. Definite volumes of hydrochloric acid (3 %) were injected with an injection needle through a pierceable rubber plug to make sure that the apparatus remains gastight. The added volume of acid was then subtracted from the shown volume at the gas syringe to register only the amount of released gas. Higher concentrations of acid result in too fast hydrogen release reactions.



Figure 2.7: The glass apparatus used for ACHR experiments

As the acid solution and the samples come in contact, bubbles of gas evolve rapidly from the samples. Oxyhydrogen-test carried out for several samples confirms that the released gas consists of hydrogen or at least mainly of hydrogen. Additionally, the released gas was checked with a gas detector suggesting the absence of CO_2 (detection limit < 1000 ppm). For each sample, three measurements with different masses in a wide range from 10 to 40 mg were investigated. Using linear regression, the amount of gas released per 100 mg sample was calculated for each hydride. A factor of 1.0118 that represents the influence of the additional weight of the plunger in the vertical assembling of the gas syringe was added to the results.

The calculated data were evaluated by considering the possible errors. These errors may rise from practical inaccuracies during each H_2 release experiment or from the linear regression. The equation (2.2) represents the absolute error for each single measurement. The reading error at the gas syringe is equal to the graduation of the scale, 1 ml (corrected with the

piston load). The injection needle has an absolute error of ± 0.02 ml. A factor of 2 was necessary to reproduce the intervention of the added volume of acid twice in the determination of the volume of released H_2 , respectively during the injection and the subtraction.

The uncertainties in the slope were estimated using the Excel function LINEST. The overall error (equation 2.3) consists of a combination of the average of the relative errors from the single measurements (equation 2.2) and the given error from LINEST-gradient.

$$\Delta V_{\text{single measurement}} = \sqrt{\left[\left(\left(\frac{V_{\text{acid}}}{V_{\text{gas}}} \right)^2 \cdot 0.02^2 \right) \cdot 2 + \left(\frac{V_{\text{gas}}}{V_{\text{gas}}} \right)^2 \cdot 1^2 \right]} \quad (2.2)$$

$$\Delta V_{\text{total}} = \sqrt{\left[(\text{rel.error}_{\text{LINEST-gradient}})^2 + (\text{av.rel.error}_{\text{single measurement}})^2 \right]} \quad (2.3)$$

2.2.6 Imaging method: Scanning Microscope Electron (SEM)

SEM images of NH_3BH_3 -G in comparison with NH_3BH_3 (chapter 4) were taken using a JOEL JSM-6390A equipped with a Bruker XFlash detector 410-M-200. The sample is scanned with a focused beam of electrons which interact with atoms of the sample producing secondary electrons that are used to give information of the topography and the composition of the sample. A low-vacuum sputter coating of the samples with gold was necessary to create a conductive layer that inhibits charging, reduces thermal damage and improves the secondary electron signal.

3. H₂ Release from Solid State Sodium Borohydride NaBH₄

3.1 State of the art

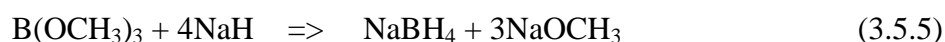
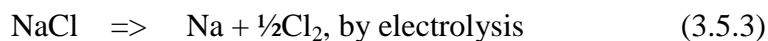
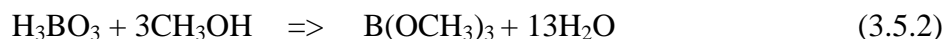
3.1.1 Synthesis and structure

The first reported synthesis of NaBH₄ was in 1949 by Kasper et al. [42] by shaking a sodium amalgam in the presence of diborane gas for 4 days. The compound was thought to be Na₂B₂H₆, but more diborane was adsorbed than that required to form disodium diborane and the CuK α -ray diffraction of the sample gave a pattern similar to that reported by Soldate [16] for NaBH₄ (1947).

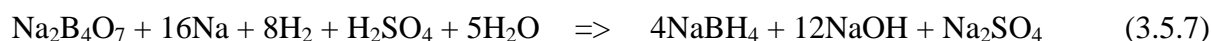
Later on, Schlesinger et al. [43] found that the reaction of trimethoxyborohydride NaBH(OCH₃)₃ and diborane B₂H₆ proceeds very rapidly to give NaBH₄ according to reaction (3.1). The reactions (3.2), (3.3) and (3.4) are other synthetic modifications for NaBH₄.



Commercially, NaBH₄ is produced via the Schlesinger process: a multi-step processing based on the reduction of the trialkylborate B(OCH₃)₃ with NaH (reaction 3.5.5) [44]. The synthetic pathway follows the chemical reactions (3.5.1-3.5.6) and provides high purity of NaBH₄, but it requires further optimization for energy efficiency [45].



The overall reaction is:



At room temperature, NaBH_4 adopts a rock salt, face centered cubic structure with $a_0 = 6.1635 \text{ \AA}$ [46]. At -83°C the structure undergoes a transition from the cubic to the tetragonal ordered phase caused by reorientations of the tetrahedra. The tetragonal phase has been described within the space group $\text{P4}_2/\text{nmc}$ ($a = 4.332 \text{ \AA}$ and $c = 5.869 \text{ \AA}$ for NaBD_4) [47]. The tetragonal modification appears also upon compression to 6 GPa and transforms at pressures higher than 8 GPa to the orthorhombic Pnma phase [48].

The cubic structure has been described either in Fm-3m [46, 49] or F-43m [50] space groups. Basing on the diffraction data alone, both groups could be considered. The only difference between them is that F-43m lacks an inversion center yielding a fully or partly order of BH_4^- units. Whereas, in the centrosymmetric Fm-3m , the B atoms are situated on the center of inversions and each B is coordinated to eight half occupancy hydrogen atoms yielding an intrinsically disordered structure. The peak of heat capacity is observed at approximately -83°C , consistent with an order-disorder transition. Therefore, for thermodynamic considerations the fully disordered Fm-3m has to be assumed [49, 51].

Single crystals of sodium borohydride dihydrate $\text{NaBH}_4 \cdot 2\text{H}_2\text{O}$ were obtained by re-crystallization of NaBH_4 from an aqueous solution of NaOH . The dihydrate crystallizes in the Pbca space group ($a = 10.2870$, $b = 6.8759$ and $c = 12.0651 \text{ \AA}$). The BH_4^- anion has a nearly ideal tetrahedral geometry with an average B–H bond length of approximately 1.12 \AA . The

structure involves strong dihydrogen bonds of 1.77-1.95 Å. The crystals can be stored in a closed vessel at 0°C. In open air, they take up water from atmosphere and dissolve [49].

The structures of the room temperature phase of NaBH₄ and NaBH₄·2H₂O are shown in **Figure 3.1**.

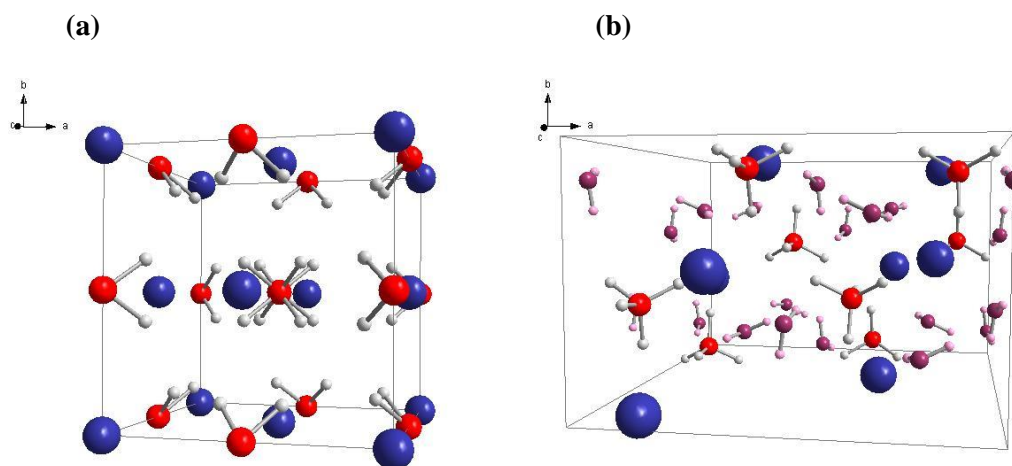
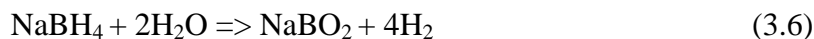


Figure 3.1: The room temperature structure of (a) NaBH₄ (Fm-3m) and (b) NaBH₄·2H₂O according to the crystallographic data of ref. [49] (Na: blue, B: red, O: purple, hydridic hydrogens H^{δ-} of BH₄⁻: gray, H^{δ+} protonic hydrogens of H₂O: pink).

H₂ can be released from NaBH₄ either by thermal decomposition or by hydrolysis. The thermal desorption of hydrogen atoms from NaBH₄ requires high temperatures (approximately 500°C) owing the strong covalent character of the B-H bonds. The hydrolysis reaction can be performed at moderated temperatures (30 – 80°C) using a catalyst. A large amount of water is required to hydrolyze the total amount of NaBH₄.

3.1.2 H₂ release by NaBH₄ hydrolysis

The reaction of NaBH₄ with H₂O produces pure hydrogen gas. It is an oxidation-reduction (*redox*) reaction, where NaBH₄, or more precisely the hydridic H on the B atoms, reduce H₂O to H₂. In turn, NaBH₄ gain O atoms and is oxidized to metaborates (NaBO₂). In an ideal way, 1 mol NaBH₄ reacts with 2 mol H₂O to produce 4 mol H₂ (reaction 3.6). Nevertheless, this reaction is a very simple representation which does reflect neither the challenges on the practical level nor the complexity of the mechanism on the molecular level.



In practical systems, the number of mol H_2O per 1 mol_(NaBH₄) exceeds largely the ideal stoichiometry because of the low solubility of each of the sodium borohydride reactant ($55\text{g}_{(\text{NaBH}_4)}/100\text{g}_{(\text{H}_2\text{O})}$ [11]) and the metaborate by-product ($28\text{g}/100\text{g}_{(\text{H}_2\text{O})}$ [11]), reducing the effective hydrogen storage capacity of the system. The formation of basic metaborate by-product increases the pH of the solution decreasing, thus, the rate of hydrogen evolution. Basic solutions of NaBH_4 are chemically stable and do not release significant amounts of H_2 under ambient conditions. The degree of hydrolysis of an aqueous solution of NaBH_4 is 0.01 % NaBH_4/h in 1 N NaOH meeting the stability requirements for the borohydride solutions [52].

The hydrolysis reaction of NaBH_4 can be greatly accelerated by rise of temperature or by adding acidic substances. Many efforts have been devoted to improve the storage capacities and hydrogen release by NaBH_4 hydrolysis. For example, the use of catalysts as PtRu-LiCoO_2 and Co-C has shown a remarkable improved H_2 release of NaBH_4 by hydrolysis. The remaining challenge today is raising the efficacy and the durability of the catalyst [11]. Other numerous strategies have been reported [53, 54, 55, 56, 57] and are actually beyond the scope of this thesis.

Mechanistic studies on the reaction between NaBH_4 and H_2O are copious. Nonetheless, suggested models were neither conclusive nor satisfactory with one another [58]. For a better understanding of the $\text{NaBH}_4\text{-H}_2\text{O}$ system, the reaction of NaBH_4 with H_2O is investigated in this review according to different criteria:

- (a) The external (experimental) parameters affecting the hydrogen release
- (b) The metaborate by-product
- (c) The interactions between NaBH_4 and H_2O
- (d) The hydrolysis reaction path

These are discussed in more details in the next paragraphs.

(a) The external (experimental) parameters affecting the hydrogen release

The rate of hydrogen generation is dependent on the temperature at which the reaction is performed and on the pH of the solution. The relation (3.7) of Kreevoy and Jacobson (1979) is a simple empirical representation of the reaction rate [58].

$$\log(t/2) = \text{pH} - (0.034T - 1.92) \quad (3.7)$$

$t/2$ is the half-life, the time required for one-half of NaBH₄ in solution to decompose, and is given in minutes, and T is the temperature in K. Accordingly, low temperatures and high values for pH slacken the hydrolysis of aqueous solution of NaBH₄.

Moon et al. [59] suggested that the rate is initially linear (zero order) then changes to non-linear after several hours of reaction time. They also found that the hydrogen generation rate increases with increase of NaBH₄ concentration ranging from 5 to 20 wt% and then decreases with 25 wt% NaBH₄. A similar pattern was also observed for the hydrogen yield which increases with increase of NaBH₄ concentration, reaches a maximum at 10 wt% NaBH₄ and then decreases (**Figure 3.2**). The reduced hydrogen amount generated from highly concentrated solution of NaBH₄ was referred to the reduction of water activity as the solution viscosity increases. The authors reported also that NaBO₂ particles formed in the course of the reaction hinder the hydrolysis of NaBH₄.

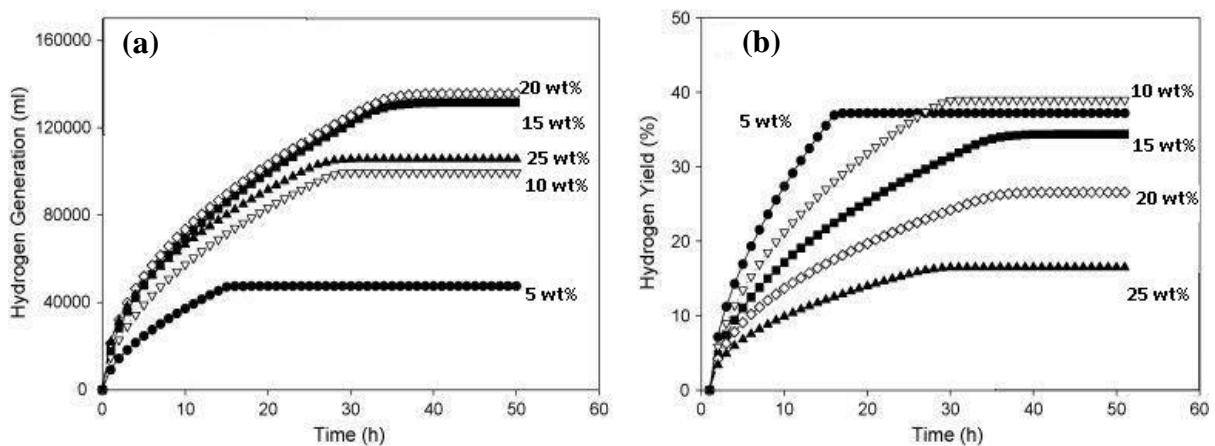
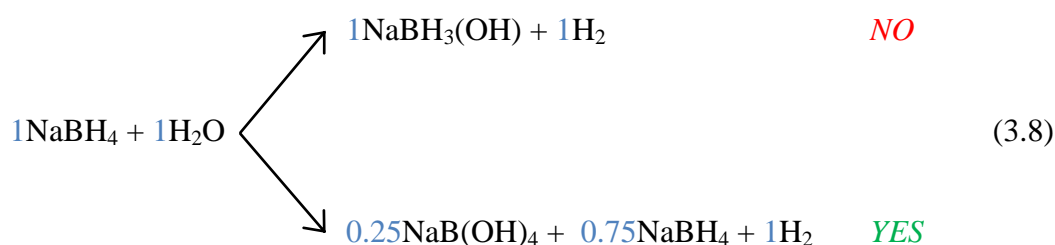


Figure 3.2: The effect of NaBH₄ concentration on (a) hydrogen generation and (b) hydrogen yield. The concentration of NaBH₄ (in wt%) is indicated on the curves (the figure is taken from ref. [59]).

(b) Identification of the metaborate by-product

Marrero-Alfonso et al. [60, 61] obtained NaB(OH)_4 by-product from the hydrolysis of solid NaBH_4 with H_2O steam regardless of the $\text{H}_2\text{O}/\text{NaBH}_4$ ratio used. Therefore, they concluded that the degree of hydration of the metaborate by-product does not appear to be a direct function of $\text{H}_2\text{O}/\text{NaBH}_4$ ratio originally present in the system. This was further supported by Andrieux et al. [62] basing on quenching an aqueous solution of NaBH_4 ($\text{NaBH}_4:\text{H}_2\text{O}$ 1:1) at a conversion of 25 %. The authors do not observe $\text{NaBH}_3(\text{OH})$ intermediate and obtained NaB(OH)_4 and un-reacted NaBH_4 . In other words, if water supplied for the hydrolysis is not enough to produce NaB(OH)_4 by-product, the reaction pursues the path to a final state of NaB(OH)_4 and un-reacted NaBH_4 (3.8).

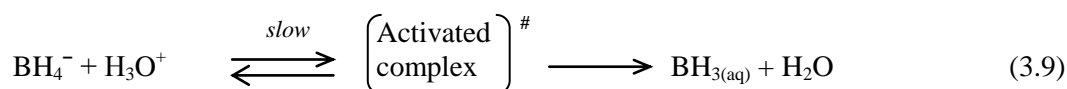


(c) The interactions between NaBH_4 and H_2O

Numerous kinetic studies were performed on the hydrolysis of NaBH_4 in aqueous media. The most important and common conclusion is that the hydrolysis reaction occurs in a stepwise fashion where the release of the first of the four H_2 is the rate determining step of the whole hydrogen release process. This assumption was made for hydrolysis reactions in alkaline to strongly alkaline solutions and over the pH range of 4 - 13 [12].

The first H_2 generation step involves a protonation of BH_4^- anion [63, 64, 65, 66, 67, 68]. The hydrolysis of NaBD_4 is faster than NaBH_4 [63, 65, 69] and BH_4^- hydrolyzes faster in H_2O than in D_2O [65]. Therefore, assuming the weaker basicity of D_2O with respect to H_2O , the interacting borohydride and water molecules might result in a weakening of an OH bond and a strengthening of a BH bond [65].

Davis et al. [63, 64] suggested the formation of BH_3 according to:



The reaction between BH₄⁻ and hydronium ion H₃O⁺ is general acid catalysis and is unity in the borohydride concentration and unity in the concentration of the acid. The rate expression is:

$$-d\frac{[\text{NaBH}_4]}{dt} = [\text{BH}_4^-] \sum_i \sum k_i [\text{HA}_i] \quad (3.10)$$

HA_i is general acid (for e.g. H₃O⁺, H₂O, H₃BO₃...).

When only [H₃O⁺] contributes significantly to hydrolysis, the equation (3.10) is reduced to:

$$-d\frac{[\text{NaBH}_4]}{dt} = k[\text{BH}_4^-][\text{H}_3\text{O}^+] \quad (3.11)$$

k is the second order rate coefficient and is given in mol.l⁻¹.s⁻¹. The authors claimed that the reaction of NaBH₄ with D₂O gives over 90 % HD. Therefore, they assumed that no exchange occurs between the hydride and the solvent and excluded the formation of a trigonal bipyramidal penta-coordinated complex as BDH₃ which would decompose to both H₂ and HD and speculated two possible activated complexes **I** and **II** (**Figure 3.3**). A four-center activated complex could also occur.

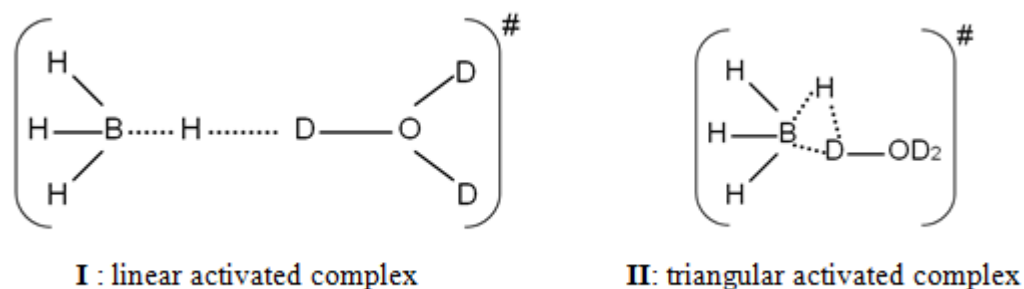
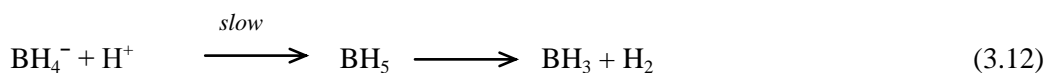


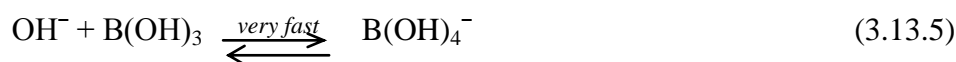
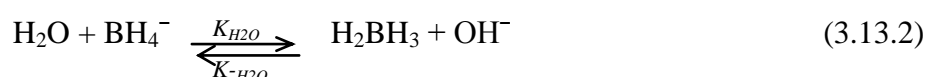
Figure 3.3: The two possible activated complexes of the hydrolysis of NaBH₄ in D₂O as given by Davis et al. [63]

Mesmer and Jolly [65] performed a kinetic study of NaBH₄ hydrolysis in water solution in the pH range of 3.8–14 for different temperatures (10–50°C) and concluded the existence of a molecular pentahydroboron complex BH₅ which decomposes to BH₃ and H₂ (3.12).



The fact that the hydrolysis reaction of BH_4^- in D_2O yields about 4 % H_2 and the hydrolysis of BD_4^- in H_2O gives about 1 % D_2 , indicates the formation of BDH_4 or BHD_4 complexes, which mainly decompose to HD and BH_3 or BD_3 and at a lower rate to H_2 and BDH_2 or D_2 and BHD_2 , respectively.

Kreevoy and Hutchins [66] supported the existence of BH_5 intermediate. They found that the experimental models based on general acid catalysis failed to correlate the rate of the hydrolysis of NaBH_4 in basic solutions, in particular at $\text{pH} > 13$. Furthermore, ^{11}B NMR studies reveal an uptake of deuterium by un-hydrolyzed BH_4^- in basic D_2O (1 M NaBH_4 + 1M NaOD at 25°C for two years and 1 M NaBH_4 + 4.4 M NaOD at 100°C for one month). Deuterium uptake by un-reacted BH_4^- occurs in stepwise; one deuterium is taken up at a time. The exchange with D_2O becomes faster than hydrolysis in strongly basic solutions. The authors considered these observations as indirect evidence of the existence of a reaction intermediate which can react with OH^- to regenerate BH_4^- . This should be BH_5 with the incoming proton is equivalent to only one of the original four protons. Therefore, it could be preferentially written as H_2BH_3 because it has two relatively long and three normal B-H bond lengths. The developed kinetic model is:



The BH_5 complex is a metastable species, isoelectronic and isosteric to the methonium ion, CH_5^+ , and has the C_s symmetry [66, 67, 68]. A similar pentahydroaluminium intermediate was proposed for the hydrolysis of alanate AlH_4^- [67].

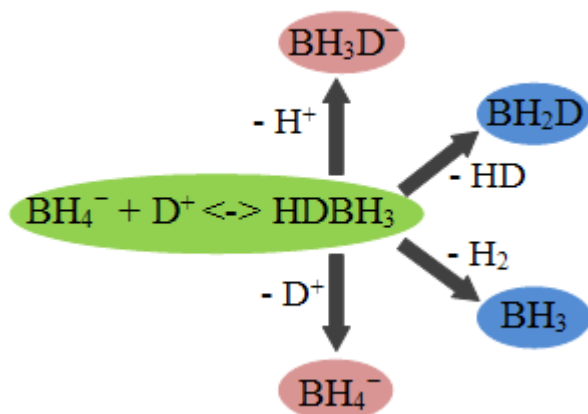
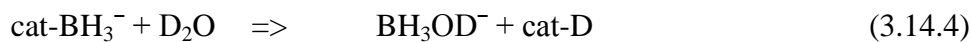
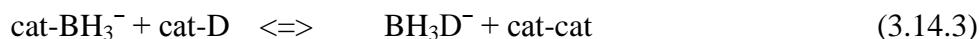
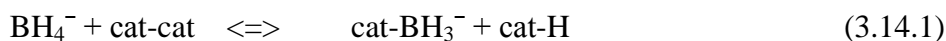
In the case of BDH_4 or better represented as HDBH_3 , the presence of H_2 in the evolved gas phase indicates a subsequent bond-bond rearrangement in the molecule resulting in a

cleavage of H₂ and formation of BH₂D [67]. HDBH₃ may hydrolyze or exchange. The loss of HD or H₂ results in hydrolysis, while the loss of H⁺ gives rise to exchange and appearance of BH_(4-n)D_n scrambled products.

The H-D scrambling in the D₂O solutions of NaBH₄ takes place by two different paths [70]. The first path occurs in highly basic solution (pH ≈ 14) and at elevated temperatures (70-100°C). In this case the rate is independent of pH (the exchange is first order in BH₄⁻ and zero in HO⁻). The second path involves D⁺ catalyzed exchange at ordinary temperatures (pH = 7-9) (the exchange rate is suggested to be first order on the concentrations of each of H⁺ and BH₄⁻). The scheme of the hydrolysis of NaBH₄ in D₂O in presence of D⁺ is simplified in **Figure 3.4a**. In pure D₂O and at moderated pH, NaBH₄ does not undergo significant H-D scrambling [71, 72]. Grice et al. [72] showed that NaBH₄ solution left 1 day in pure D₂O contains mainly BH₄⁻ and borates. Only traces of BH₃D⁻ were detectable.

Guella et al. [73] observed deuterium incorporation in BH₄⁻ affording BH_(4-n)D_n⁻ (n = 1, 2, 3, 4) in their investigation of the Pd-catalyzed hydrolysis of NaBH₄ in alkaline media. This occurred in competition with the hydrolysis reaction. Moreover, in contrast to the acid-catalyzed hydrolysis, the exchange rate constants of the Pd-catalyzed process were found to be higher than those of the corresponding hydrolysis reactions. For the Pt-catalyzed hydrolysis of NaBH₄ [74], ¹¹B NMR analyses indicate that the main reaction products are the tetrahydroxoborate species D_nH_(4-n)BO₄⁻ (n = 1, 2, 3, 4) and only a minor amount of the partially scrambled BH₃D⁻ is formed. The mechanism of the catalyzed hydrolysis of NaBH₄ in D₂O as proposed by Guella et al. is presented in **Figure 3.4b**. The first step is a fast, reversible and dissociative chemisorption of BH₄⁻ and the catalyst atoms and produces cat-BH₃⁻ and cat-H (3.14.1).

The exchange between NaBH₄ and D₂O facilitated in presence of D⁺ (**Figure 3.4a**) and that afforded in presence of Pd-catalyst (**Figure 3.4b**) confirm that the exchange path does not involve a direct exchange between D₂O and BH₄⁻. It occurs in an indirect way via HDBH₃ intermediate (**a**) or via the reversible reaction between cat-BH₃⁻ + cat-D in the Pd- or Pt-catalyzed hydrolysis reaction (**b**, reaction 3.14.3). This is further supported by the reaction (3.14.4) between cat-BH₃⁻ and D₂O which yields hydrolysis rather than exchange corroborating that the H/D scrambling is induced by the catalyst.

(a) Hydrolysis of NaBH₄ in D₂O in presence of D⁺.**(b) Hydrolysis of NaBH₄ in D₂O in presence of catalyst.**

The overall exchange reaction is:



The hydrolysis reaction is:

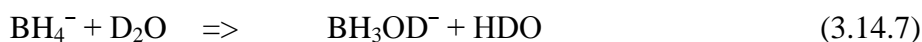


Figure 3.4: Schemes of the Hydrolysis of NaBH₄ in D₂O: (a) in presence of D⁺ according to ref. [65, 66, 67] and (b) in presence of Pd or Pt catalyst according to ref. [73, 74].

It can be concluded that the H on the B atoms have strong hydridic character ($\text{H}^{\delta-}$) and would combine preferentially to protonic hydrogen ($\text{H}^{\delta+}$) of the surrounding. The vacancy left on B might be plugged by an electron rich group possessing a lone electron pair or negative charge as the hydroxyl group HO^- in the case of water as will be shown in the next paragraph.

(d) The hydrolysis reaction path

The individual reaction steps of the reaction of BH₄⁻ (or BH₅) to NaB(OH)₄ in alkaline media (*in acidic media the hydrolysis of NaBH₄ leads to boric acid B(OH)₃*) are still not well established experimentally and the role of water molecule is still not fully understood.

The elementary steps can be described by series of conventional chemical reactions as the reductive eliminations and the nucleophilic substitution SN₂ reactions [68]. According to Mochalov et al., the hydrolysis of NaBH₄ in buffered solutions would occur in a stepwise fashion based on the substitutions of B–H by B–OH bonds [62, 68]. Proton magnetic studies of Mesmer and Jolly were not able to observe hydroxoborate intermediates [65]. Gardiner et al. [69, 75] made an allusion to the presence of the intermediate BH₃OH⁻ on the basis of ¹¹B NMR spectra and polarographic data. Goubeau and Kallfass [76] also suggested the formation of BH₃(OH)⁻ basing on IR data.

In a more recent study, Andrieux et al. [62] performed spectroscopic and kinetic studies of the spontaneous hydrolysis of NaBH₄ considering a wide range of concentrations (2.3-18.9 wt%) in the temperature range 30-80°C. They were able to demonstrate the presence of traces of a very short-lived intermediate BH₃(OH)⁻ using ¹¹B NMR spectroscopy. The monohydroxoborate intermediate exhibits a quartet at approximately δ = -10 ppm. The authors suggested a zero-order reaction versus the initial concentration of NaBH₄ (for T = 80°C, NaBH₄ solution concentrations: 2.3-18.9 wt%, at conversion of 20 and 40 %) at least within the conversion range 0-50 %, for which the apparent activation energy was constant and the hydrolysis is independent of NaBH₄ concentration.

Grice et al. [72] confirmed the presence of BH₃(OH)⁻ traces for concentrated NaBH₄ solutions (> 84 mM) (δ=-11.46 ppm, ¹J_{B-H} = 87.7 Hz) (**Figure 3.5**). The ¹H NMR of BH₃(OH)⁻ shows a broad quartet, δ=2.48 ppm, ¹J_{B-H} = 87.4 Hz, for NaBH₄ solutions highly concentrated (> 1 M).

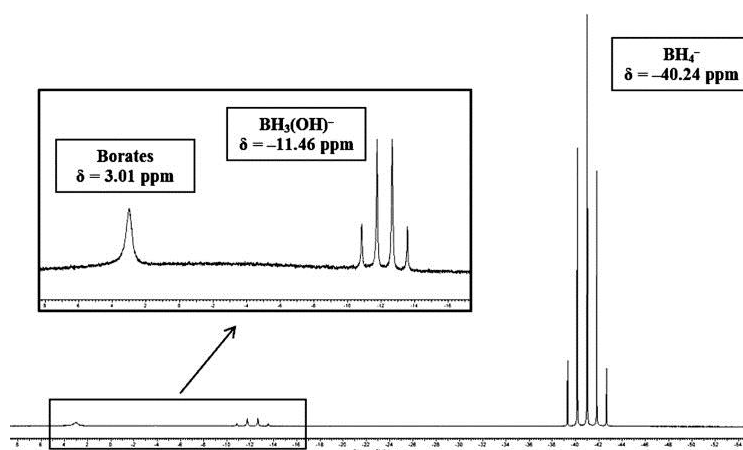
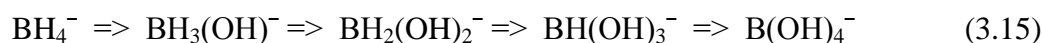


Figure 3.5: ^{11}B NMR spectrum of 84 mM solution of NaBH_4 in 4:1 $\text{H}_2\text{O}:\text{D}_2\text{O}$ showing the signals for BH_4^- ($\delta = -40.24$ ppm), $\text{BH}_3(\text{OH})^-$ ($\delta = -11.46$ ppm) and borates ($\delta = 3.01$ ppm) (the figure is taken from ref. [72]).

These results suggest that the un-catalyzed hydrolysis reaction of NaBH_4 occurs according to the following sequence:

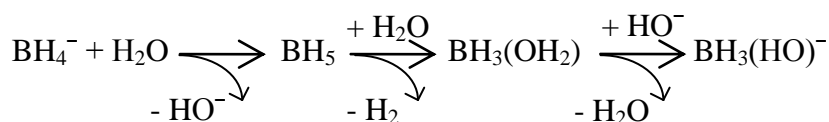


$\text{BH}_2(\text{OH})_2^-$ and $\text{BH}(\text{OH})_3^-$ are very reactive making their experimental observation very difficult [62]. Likewise, the theoretical calculations of Grice et al. [72] showed an increased hydridic reactivity of $\text{BH}_{(4-n)}(\text{OH})_n^-$ with increasing n . The calculated hydride donating abilities of BH_4^- , $\text{BH}_3(\text{OH})^-$, $\text{BH}_2(\text{OH})_2^-$, $\text{BH}(\text{OH})_3^-$ and $\text{B}(\text{OH})_4^-$ were 31, 14.8, 1.6 and -0.5 kcal.mol^{-1} , respectively.

Li et al. [68] performed theoretical ab-initio study of the un-catalyzed hydrolysis reaction of NaBH_4 and drew a comprehensive picture of the detailed mechanism. The identified elementary reactions gave evidence to the tetrahedral hydroxoborate $\text{BH}_{(4-x)}(\text{OH})_x^-$ ($x = 1, 2, 3$) and the planar three-coordinated boron $\text{BH}_{(3-y)}(\text{OH})_y$ ($y = 0, 1, 2$) intermediary species. The main steps of the mechanism are summarized in **Figure 3.6**. The initial step is a proton transfer from H_2O to BH_4^- yielding BH_5 , which in turn reacts with H_2O to give BH_3 and H_2 . BH_3 is not long-term stable in aqueous solution and bound rapidly to H_2O generating $\text{BH}_3(\text{OH}_2)$, which hydrolyses further to the monohydroxoborate, $\text{BH}_3(\text{OH})^-$ (**Figure 3.6i**). Hydrogen release from hydroxoborate is facilitated through direct dihydrogen bond between $\text{H}^{\delta-}$ of the hydroxoborate and $\text{H}^{\delta+}$ of water. The reaction yields also $\text{BH}_{(3-y)}(\text{OH})_y$ (**Figure 3.6ii**). None of the hydroxoborate is able to form five-coordinated metastable species with the

interacting environment, as do the borohydride anion. The identified reaction steps necessitate both protons and hydroxyls anions to proceed to completion.

i- Hydrogen release from BH₄⁻:



ii- Hydrogen release from hydroxoborates:

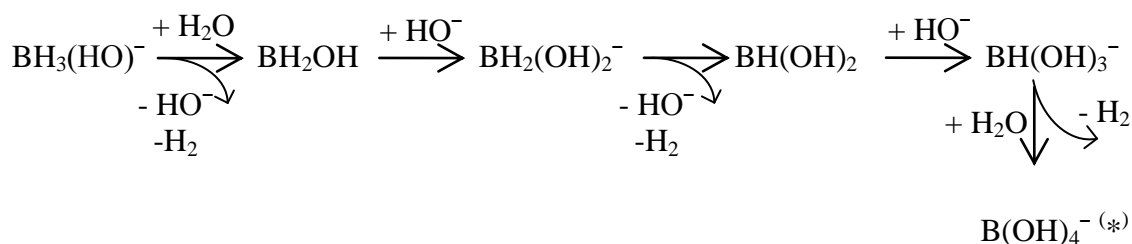


Figure 3.6: Scheme of the main steps of the mechanism of hydrolysis of BH₄⁻ to B(OH)₄⁻ as proposed in ref. [68]. (*) In basic solution the main product of the hydrolysis reaction is B(OH)₄⁻; the reaction of BH(OH)₃⁻ to B(OH)₄⁻ may proceed through the dehydrogenation of BH(OH)₃⁻ to (OH)₂B=O⁻ followed by the hydrolysis of the latter to B(OH)₄⁻.

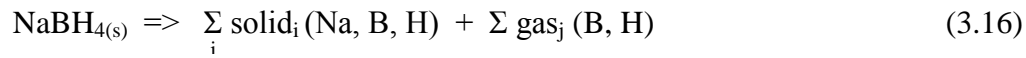
At last, it is worth to mention that there is no single kinetic law able to describe the hydrolysis reaction in the pH range from -1 to 14 since different mechanisms are thought to occur, particularly in the strongly acid (pH < 1) and strongly basic (pH > 13) solutions. Under strong acidic conditions (for e.g. the hydrolysis in acidic water-methanol at temperatures lower than -78°C [77], the reaction intermediates proposed are H₂O-BH₃, (H₂O)₂BH₂⁺ and H₂O-BH(OH)₂ which give by deprotonation the anionic species HO-BH₃⁻, HO-BH₂OH⁻ and HO-BH(OH)₂⁻, respectively. In this case, the loss of the first of the four H₂ is the fastest step and the rate is controlled by one of the intermediates [12]).

3.1.3 Thermal decomposition of NaBH₄

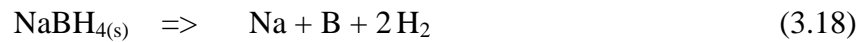
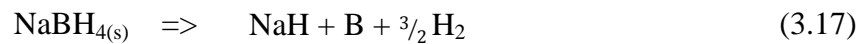
The thermal desorption of hydrogen from complex hydride leads to a complete decomposition of the complex hydride and a mixture of at least two phases is obtained [13].

The melting temperature (T_m) of borohydrides could be considered as an index for their thermal stability [20]. T_m of NaBH₄ was reported at 497°C basing on DSC measurement performed under 0.1 MPa hydrogen.

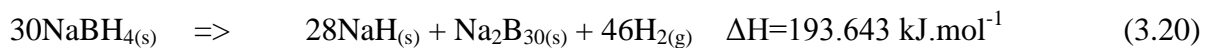
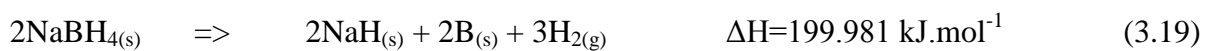
In a very general way, the thermal decomposition of NaBH₄ could be represented as follows [78]:



The decomposition pathway is thought to be the sum of the reactions (3.17) and (3.18) [13, 21].



The decomposition temperature (T_d) is defined as the temperature at which hydrogen gas with a pressure of 1 bar would be in equilibrium with the solid hydride ($T_d = \Delta H / \Delta S$) [13]. Martelli et al. [78] reported T_d of NaBH₄ at $534 \pm 10^\circ\text{C}$ under 0.1 MPa H₂. The desorbed material consists of a soft, gray metallic material, identified as Na, and a black powder with a more complex structure. The black powder could not be straightforwardly identified. The corresponding X-ray pattern shows broad features indicative of the presence of one or more amorphous phases in addition to NaOH and traces of NaH. The weight ratio of the two phases is about 2:1, equal to the ratio of the atomic weights of Na to B suggesting that the second phase might correspond to a boron-rich material. The presence of NaH in the solid residue indicates that the decomposition proceeds at least partially via NaH, which decomposes above 425°C to its elementary constituents. The authors performed theoretical calculations using density functional approach to get more insight into the thermal decomposition path. Similar reaction enthalpies are obtained for the decomposition path proceeding via NaH and elemental B (3.19) and that involving borides as Na₂B₃₀ (3.20) suggesting that the decomposition of NaBH₄ may involve elemental Na and B as well as Na-H and Na-B binary compounds.



Urgnani et al. [21] observed a multi-step thermal desorption of hydrogen from solid NaBH₄ in both isothermal and heating experiments. Some small but significant H₂ release could be observed at temperatures between 200 and 300 and at about 350°C. The main H₂ release starts at 450°C centered at about 500°C (**Figure 3.7**). However, XRD patterns taken after the thermal treatments below 450°C reveal only un-reacted NaBH₄ making further spectroscopic investigations desirable to clarify the intermediary stages. Undesirable emission of gases as B₂H₆ has not been observed.

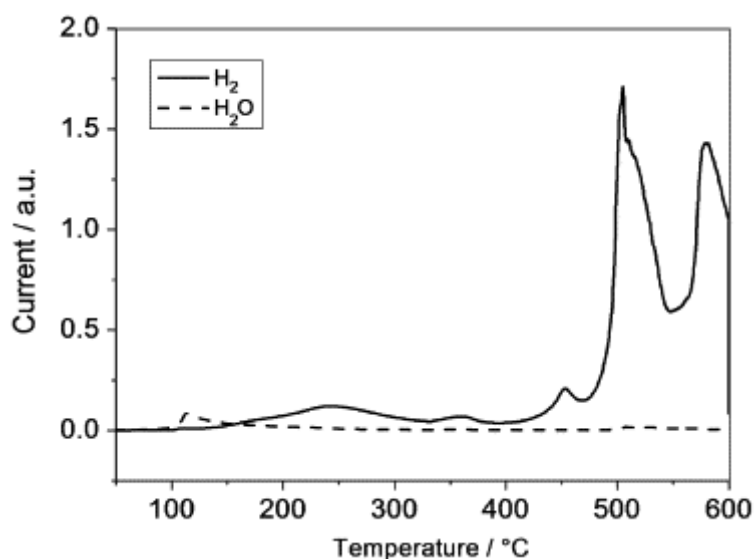


Figure 3.7: TDA signal for H₂ and H₂O as a function of temperature for solid NaBH₄ heated under vacuum up to 600°C (the figure is taken from ref. [21]).

Theoretical calculations based on density functional theory suggested that the thermal decomposition of NaBH₄ is based on a mass transport through point defects of missing Na⁺ and BH₄⁻. The transport proceeds via self-diffusion, i.e. creation and subsequent diffusion. At the surface BH₄⁻ is decomposed into BH₃ and H⁻. The H⁻ ions remain in the lattice converting NaBH₄ to NaH. BH₃ are not easily incorporated in the lattice and can escape to the gas phase and form B₂H₆, or they may alternatively decompose immediately to B and H [79]. NaH_(s) and B₂H_{6(g)} are not stable under the decomposition conditions of NaBH₄ and may decompose into the elements. This would explain the experimental results of Urgnani et al. [21], who do not observe B₂H₆ in the gas phase [19].

Na₂B₁₂H₁₂ was seen during the thermal decomposition of NaBH₄-composites. Nonetheless, its mechanism of formation is still unclear and may be the result of a reaction between evolved borane and un-reacted NaBH₄ rather than being a decomposition product of the thermolysis of NaBH₄ [19]. A similar case is the formation of Li₂B₁₂H₁₂ cluster during the

thermal hydrogen desorption of LiBH_4 , which was recently demonstrated by a reaction of B_2H_6 and un-reacted LiBH_4 at 200°C [80].

Since the US DOE recommended a no-go for NaBH_4 -hydrolysis for automotive applications [18], solid-state thermal decomposition has become more attention. Several approaches have been developed to ameliorate the kinetics and thermodynamics of hydrogen release and uptake of NaBH_4 . The catalytic doping is found to reduce notably the activation barrier for diffusion facilitating hydrogen dissociation. The use of reactive additives (as fluorographite FGi, MgH_2 , Mg_2NiH_4 ...) offers the opportunity to promote the kinetics and to tune the thermodynamics through an effective destabilization of NaBH_4 by creating alternative reaction pathways for uptake and release and making the dehydrogenation and even more the hydrogenation possible at moderated temperatures and pressures. The infiltration of NaBH_4 into a porous host matrix (SBA-15, CMK-3, C...) promotes the dehydrogenation of NaBH_4 , but it reduces the hydrogen storage capacity of the system [19].

3.2 Results and discussion

3.2.1 The reaction of NaBH_4 with neutral $\text{H}_2\text{O}_{(l)}$

The reaction of NaBH_4 with $\text{H}_2\text{O}_{(l)}$ was investigated in neutral water and for temperatures up to 80°C .

In a first step, a droplet of water (of approximately 3 mm diameter) was added to NaBH_4 powder (2-3 mg). Raman spectra taken at room temperature are shown in **Figure 3.8**.

Theoretically, the BH_4^- anion has a tetrahedral symmetry and exhibits four normal modes of vibration, the symmetric stretching of B-H $\nu_1(\text{A}_1)$, the in-plane bending or deformation of HBH $\nu_2(\text{E})$, the asymmetric stretching of B-H $\nu_3(\text{F}_2)$ and the in-plane bending or deformation of HBH $\nu_4(\text{F}_2)$. All four vibrations are Raman active, whereas only F_2 vibrations are IR active [31]. The room temperature Raman spectrum of NaBH_4 (**Figure 3.8a**) shows peaks at 1277 (ν_2), 2198 ($2\nu_4$, A_1), 2227 cm^{-1} ($2\nu_4$, F_2), 2333 (ν_1), 2400 ($\nu_2+\nu_4$) and 2538 cm^{-1} ($2\nu_2$) in agreement with previous works [81, 82]. The asymmetric bending mode ν_4 appears in the Raman spectrum as a weak band at 1124 cm^{-1} [83]. The Raman spectrum is characterized by the A_1 resonance of ν_1 with $2\nu_4$ (strong) and to a much lesser extent with $2\nu_2$ (weak) [83, 84].

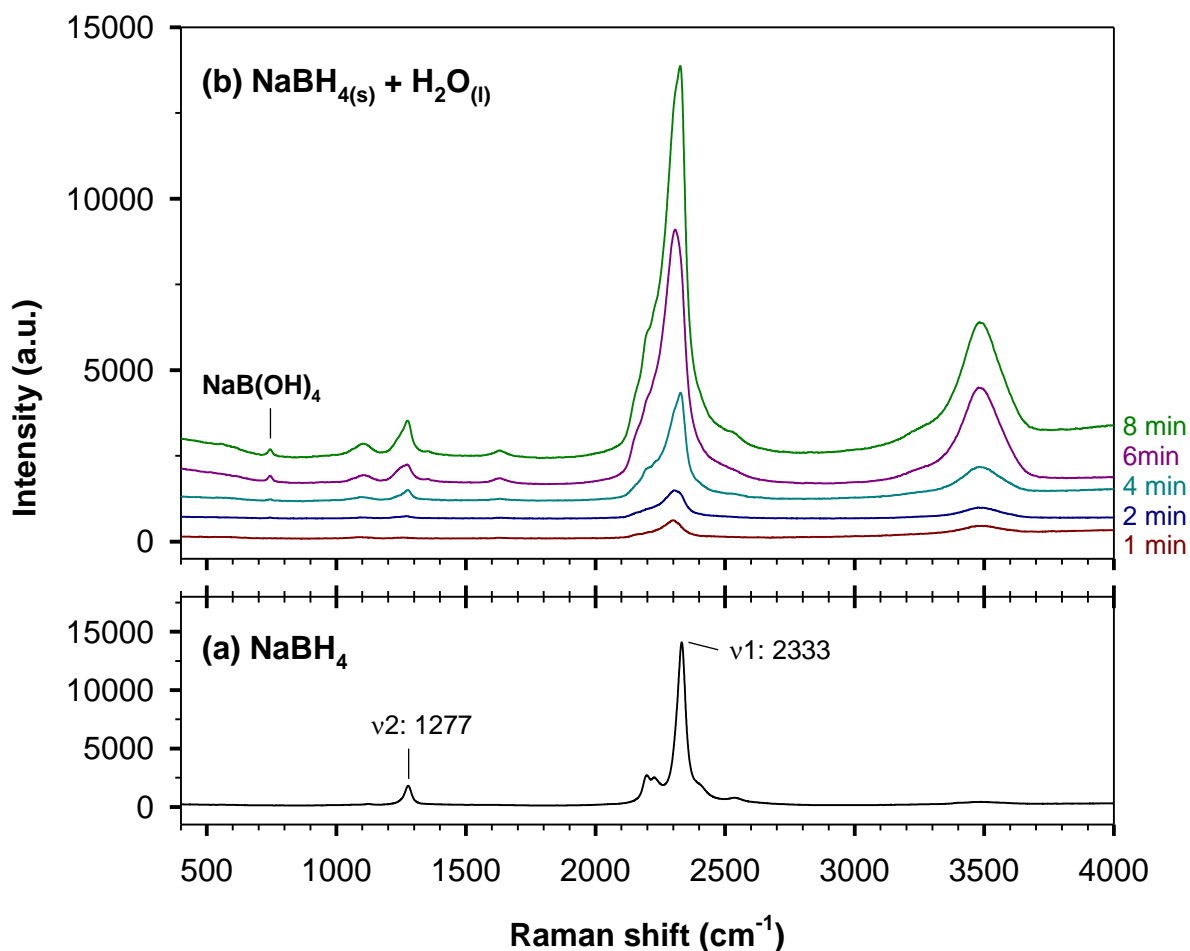


Figure 3.8: Raman spectra of (a) NaBH₄ powders and (b) in contact with a droplet of water of approximately 3 mm diameter. The Raman fundamentals of NaBH₄ are indicated.

The first two Raman spectra recorded just after adding water (after 1 and 2 min) show unresolved broad BH₄⁻-related bands (**Figure 3.8b**). These bands evolve to peaks after few minutes (6 min). The Raman fundamentals ν_2 and ν_1 are peaked in the Raman spectrum taken after 8 minutes at 1275 and 2325 cm⁻¹, respectively. Shoulders are detected at 1258 and 2316 cm⁻¹, respectively. For comparison, as-received NaBH₄ powders were slightly kept at ambient conditions. The corresponding Raman spectra are showed in **Figure 3.9**. NaBH₄ take up H₂O molecule from the atmosphere resulting in a slight shifting of the Raman bands toward lower frequencies. The spectrum corresponds to NaBH₄·2H₂O as can be deduced from a comparison between the obtained Raman shifts and those reported by Filinchuck and Hagemann for NaBH₄·2H₂O [49]. The ν_2 mode appears at 1259 cm⁻¹ with a shoulder at 1245 cm⁻¹ and ν_3 at 2316 cm⁻¹ with a shoulder about 2299 cm⁻¹. The weak peak at 1102 cm⁻¹ is related to ν_4 . The authors suggested an almost tetrahedral symmetry for the BH₄⁻ anion

since the deformation mode is slightly split. In addition, the Raman spectrum shows the vibrational modes of crystalline H₂O. The H-O-H bending mode is at 1641 cm⁻¹ and the O-H stretching modes appear as a single peak at 3564 cm⁻¹ and a much stronger band peaked at 3480 cm⁻¹ with shoulders at 3500 and 3469 cm⁻¹. These are consistent with the literature IR and crystallographic data of NaBH₄·2H₂O revealing strong dihydrogen bonds for three OH groups (strong Raman band) and the absence of dihydrogen bonding for the fourth one (single Raman peak). Filinchuck and Hagemann obtained NaBH₄·2H₂O by re-crystallization of NaBH₄ from an aqueous solution of NaOH. The dihydrate crystals were stored at 0°C in closed box. Under open conditions the crystals take up water from the atmosphere and dissolve.

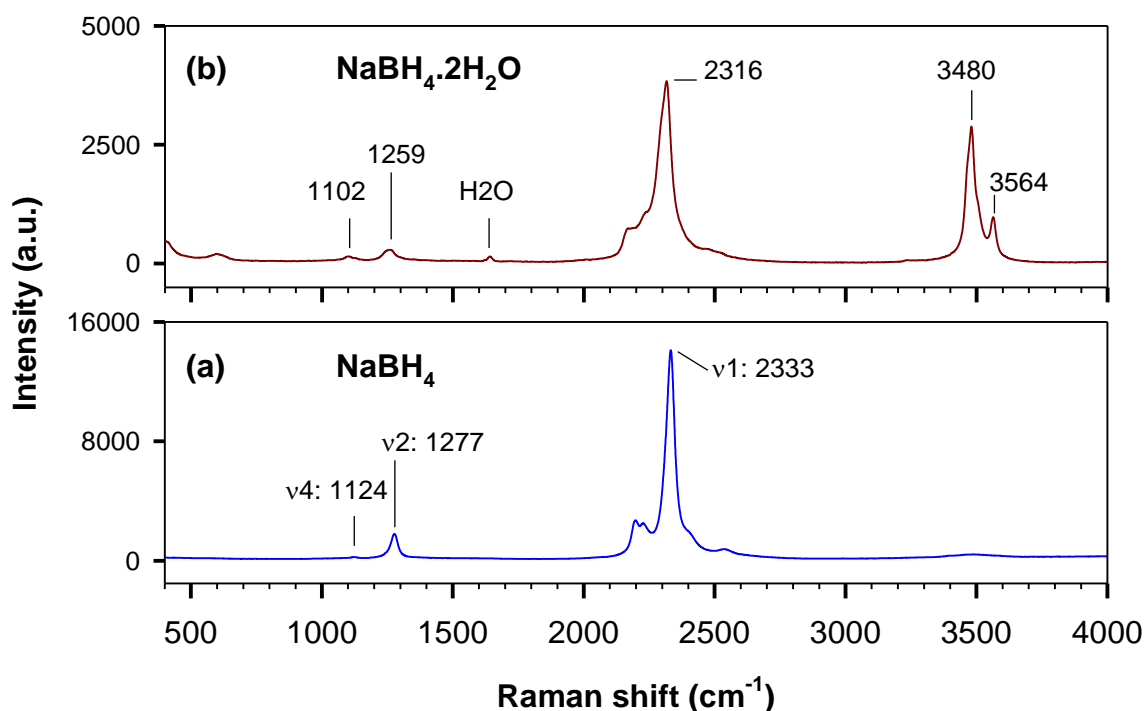


Figure 3.9: Raman spectra of (a) as-received NaBH₄ and (b) after few minutes at ambient conditions

According to these observations, the shoulders at 1258 and 2316 cm⁻¹ in the Raman spectrum taken after 8 minutes (**Figure 3.8b**) are due to NaBH₄·2H₂O. Therefore, it can be concluded that some re-crystallization occurred in the sample yielding NaBH₄·2H₂O. Nonetheless, the dissolution of NaBH₄ in water was not complete and the sample still contains NaBH₄ residuals. The thermal behavior of NaBH₄·2H₂O is considered later in section 3.2.3. It may also be noted that a weak peak is observed at 745 cm⁻¹ which can be assigned to

NaB(OH)₄ [85]. This indicates that a reaction of NaBH₄ with H₂O occurred releasing hydrogen, too. This reaction is however minor.

The reaction with water was further investigated using IR spectroscopy. Few mg of NaBH₄ were dissolved in 5-10 ml water. Three experiments were performed denoted I, II and III, respectively. I and II use H₂O whereas III uses D₂O solvents. The solutions were dried at 80°C under open conditions for different times. Residues were then pressed into KBr pellets and characterized by IR spectroscopy. In some cases, the pellets after the IR measurements were further dried. The different thermal treatments are summarized in **Table 3.1**. Solution I was dried for 24 h. The obtained solid residue was pressed in KBr pellet and characterized using IR spectroscopy (thermal treatment I-1). Afterwards, the pellet was further dried at 80°C for 24 h (I-2). Solution II was dried for 24 h (II-1) and 72 h (II-2), respectively. Residues were characterized using IR spectroscopy. Solution III was dried for 24 h and the residue was then pressed in KBr pellet (III-1). The pellet was further dried for 2 h (III-2). The IR results are shown in **Figure 3.10** in comparison to the IR spectrum of NaBH₄ in KBr pellet.

Table 3.1: Thermal treatment of NaBH₄ in H₂O and D₂O solvents

Experiment	Solvent	Thermal treatment at 80°C under open conditions	Pellet composition
I	H ₂ O	I-1: solution dried for 24 h, then pressed in pellet	NaBH ₄ , NaB(OH) ₄ , H ₂ O
		I-2: Pellet of I-1 dried for 24 h	NaBH ₄ , NaB(OH) ₄
II	H ₂ O	II-1: solution dried for 24 h	NaBH ₄ , Phase “n”
		II-2: solution dried for 72 h	NaBH ₄ , NaB(OH) ₄
III	D ₂ O	III-1: solution dried for 65 h, then pressed in pellet	NaBH ₄ , Phase “n”, H ₂ O, DOH
		III-2: Pellet of III-1 dried for 2 h	NaBH ₄ , NaB(OH) ₄ , NaB(OD) ₄ , H ₂ O, DOH

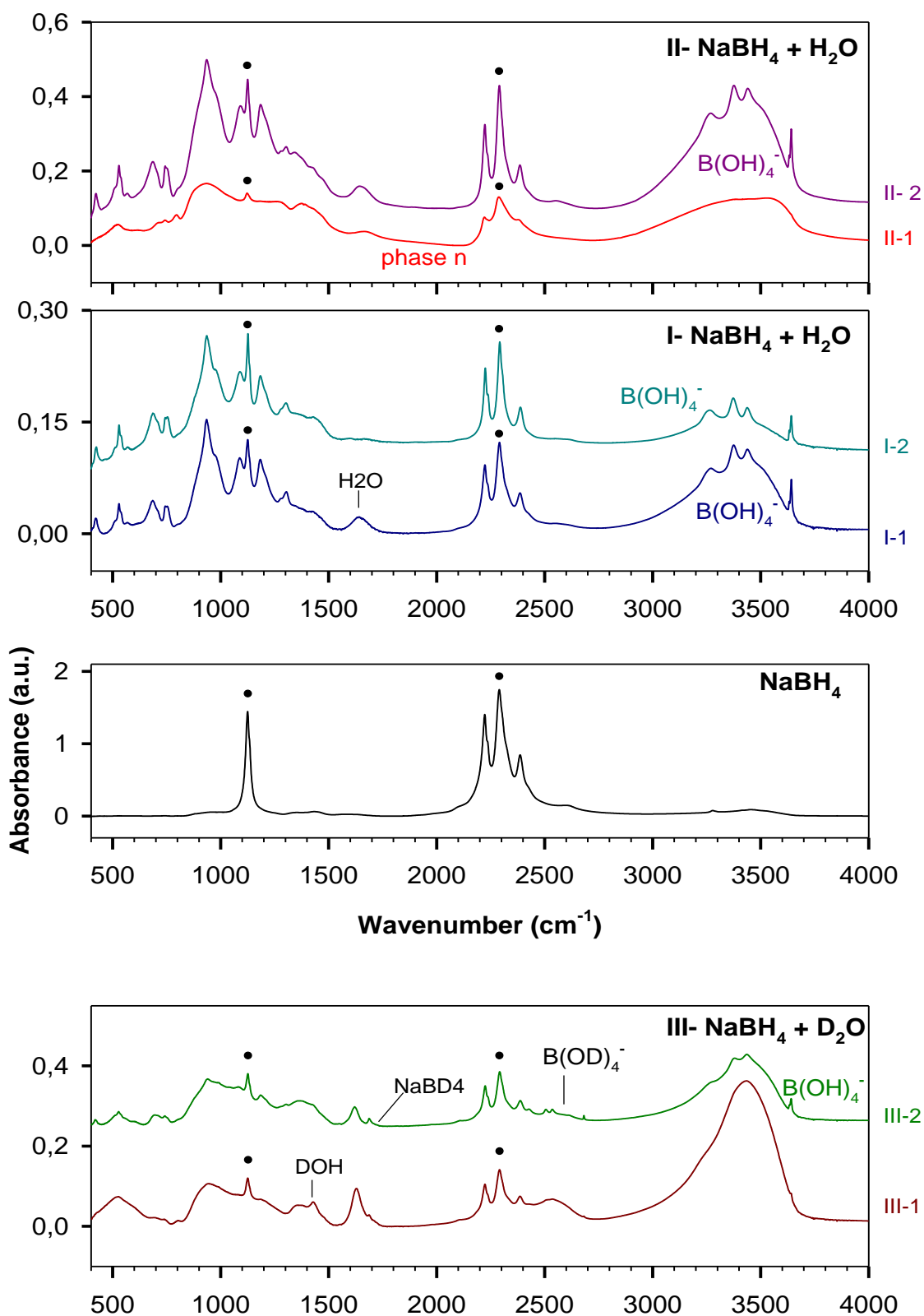


Figure 3.10: IR spectra of NaBH_4 , $\text{NaBH}_4 + \text{H}_2\text{O}$ (I and II) and $\text{NaBH}_4 + \text{D}_2\text{O}$ (III) solutions dried at 80°C in open conditions for different times (see Table 3.1 for more clarifications of the denotations I-, II-, and III-1-2). Circles denote the IR fundamentals of BH_4^- anion at 1125 (ν_4) and 2290 (ν_3) cm^{-1} .

The IR spectrum of NaBH₄/KBr pellet shows peaks at 1125, 2223, 2290 and 2386 cm⁻¹, which can be assigned to ν_4 , $2\nu_4$, ν_3 and $\nu_2+\nu_4$ modes, respectively [81]. Each peak reveals a shoulder at higher frequency attributed to the isotope distribution ¹⁰B/¹¹B in natural abundance [24]. The bending mode occurs about the half the stretching frequency giving rise to multiple Fermi resonances between the combination, the overtone and the stretching fundamental [83, 84, 86, 87]. The resonance redistributes the intensities and changes the frequencies. As a result, the overtone and the combination modes appear with much greater intensity than would have been expected and the IR frequencies are shifted from the values at which they would otherwise have appeared [83].

All experiments reveal more or less significant amounts of un-reacted NaBH₄ as indicated on the IR spectra by ν_4 and ν_3 peaks. Thus, a partial decomposition of NaBH₄ with H₂O is observed showing that the hydrolysis reaction of NaBH₄ is self-inhibited in agreement with previous reports [15, 58]. The IR spectrum of I-1 can be assigned to NaB(OH)₄ basing on a comparison of the obtained IR frequencies with those reported by Kessler and Lehmann [88]. In addition, the IR spectrum shows molecular water at 1641 cm⁻¹ which disappears after drying the pellet at 80°C for 24 h (I-2). The IR spectrum of II-1 has broad IR bands at principally 940 and 1383 cm⁻¹ which can be assigned to the tetrahedral BO₄ and planar BO₃ units, respectively [89], in addition to a broad OH stretching band between 2850 and 3820 cm⁻¹. This metaborate phase (called phase “n”) is rather unknown and was not previously described in the literature. After a longer drying time of 72 h (II-2), NaB(OH)₄ is obtained. The IR spectrum III-1 shows also broad IR bands which can be referred to the phase “n”. Drying the pellet for 2 h yields NaB(OH)₄ (III-2). The origin of the phase “n” is further investigated in details in chapter 6. It is showed that NaB(OH)₄ decomposes above 85-90°C and yields in a first step a new gel-like phase reported for the first time. The gel was isolated at 120°C and exhibits broad IR bands similar to those observed for II-1 and III-1. In open conditions, the gel takes up water and re-hydrates back to NaB(OH)₄. Therefore, it can be assumed that the hydrolysis of NaBH₄ at 80°C yields the gel phase “n” of sodium metaborate.

The IR spectrum of III-2 shows a minor amount of NaB(OD)₄ as can be deduced from a comparison of the OD stretching region between 2470 and 2680 cm⁻¹ and the OH stretching region of NaB(OH)₄ between 3070 and 3670 cm⁻¹. Strong H/D exchange should have taken place between NaB(OD)₄ and H₂O molecules of the atmosphere to yield a large amount of NaB(OH)₄. It may also be noted that a very weak peak is observed at 1720 cm⁻¹ related to ν_3 of NaBD₄ [82]. This can be interpreted by a weak H/D exchange which might have taken

place during the long drying time at 80°C. It has been reported that H/D exchange is faster than hydrolysis in highly basic solutions of NaBH₄ at temperatures between 70 and 100°C since the H₂BH₃ intermediate or its isotopic analog reacts back to BH₄⁻ (see the hydrolysis path proposed by Kreevoy and Hutchins 3.13.1-3.13.5, page 41) and the rate of exchange (reaction 3.13.2) is almost equal the rate of protonation (reaction 3.13.1) [66, 70]. In the present case, the hydrolysis releasing H₂ occurs during the first few hours and produces basic metaborate NaB(OH)₄ by-product which makes the solution basic.

It is worth noting that in all investigated cases no BH_(4-n)(OH)_n (n = 1, 2 and 3) intermediates were not observed in agreement with previous reports [61, 62, 72]. Furthermore, in the non-catalyzed hydrolysis reaction of NaBH₄, no exchange occurs with the solvent at room temperature supporting ref. [72].

3.2.2 Thermal behavior of NaBH_{4(s)} up to the melting point:

TG/DTA analysis

TG/DTA analyses of NaBH₄ were conducted from room temperature to 400°C at 5°C/min under He flowing and synthetic air. Two experiments were performed under synthetic air considering pre-evacuated and non-pre-evacuated samples, respectively. The solid residues after TG were collected and characterized using IR spectroscopy (KBr pellet). Results are shown in **Figure 3.11**.

NaBH₄ sample heated under He is relatively stable to 400°C. It shows neither significant mass loss nor thermal effect. The IR spectrum of the solid residue after TG reveals principally the presence of only NaBH₄. The H-O-H bending modes at 1618 and 1637 cm⁻¹ and the O-H stretching band at 3100-3680 cm⁻¹ are due to the formation of NaBr.2H₂O. Its formation indicates some ionic exchanges between NaBH₄ and KBr matrix during the pellet preparation (discussed in details in chapter 5).

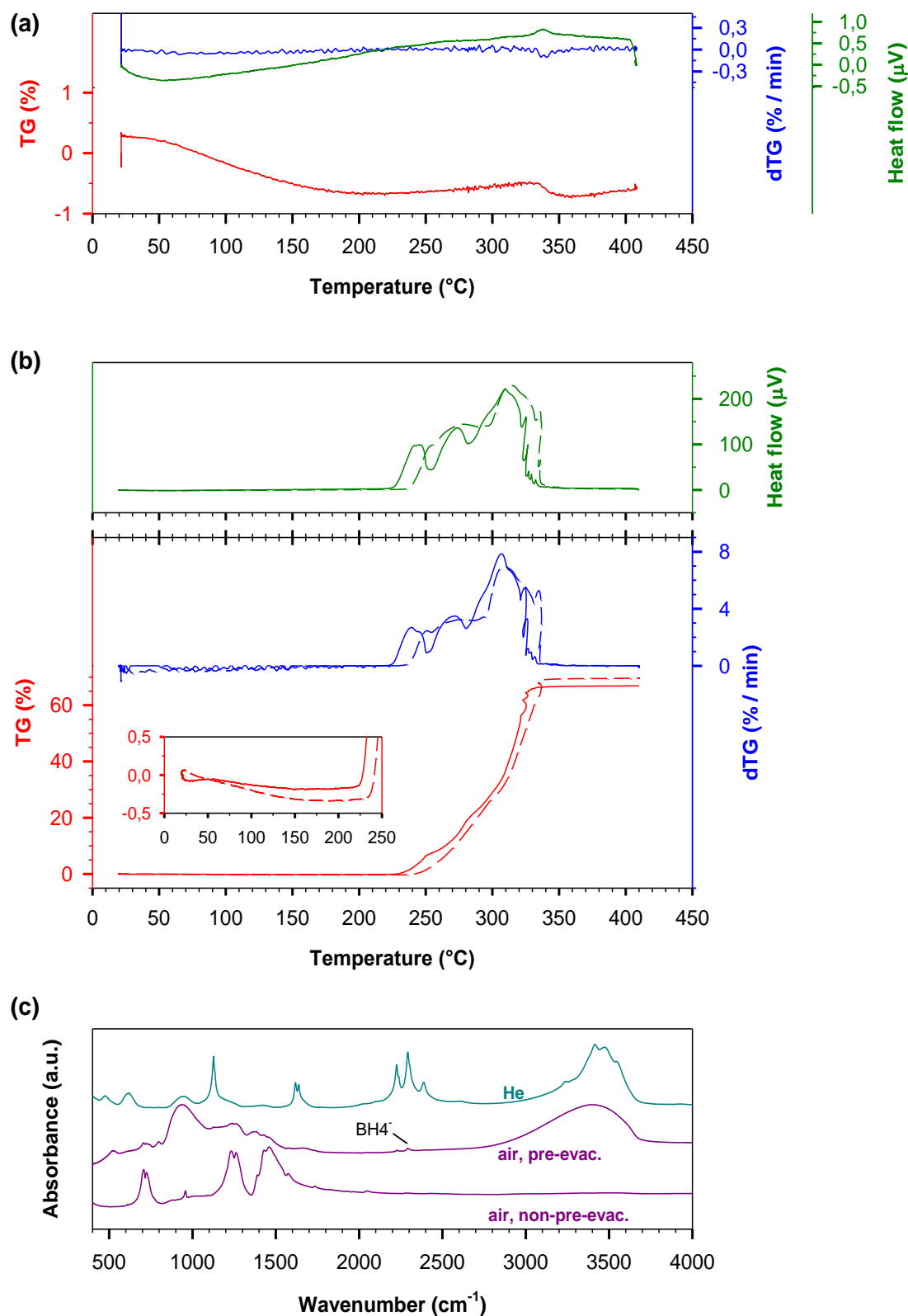


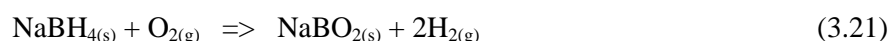
Figure 3.11: TG/DTA of NaBH₄ heated to 400°C at 5°C/min under (a) He and (b) synthetic air (solid lines and dashed lines are for pre-evacuated and non-pre-evacuated samples, respectively).

TG: red, dTG: blue and heat flow: green lines. The inset graph is zoomed for the TG curves between 0 and 250°C. (c) IR spectra of the solid residues after TG.

The thermal treatment under synthetic air shows high reactivity for NaBH_4 . Only traces of NaBH_4 are detected in the IR spectra of the residues after TG. This indicates an important role of $\text{O}_{2(\text{g})}$ in the thermal decomposition of solid NaBH_4 . The TG curves show total mass increase of approximately 67 % initiating at about 230°C for the pre-evacuated sample and a total mass increase of 69.92 % initiating at about 240°C for the non-pre-evacuated sample. Mass increase occurs in three main steps peaked on the dTG curve of the pre-evacuated sample at 240, 272 and 306°C, respectively. The mass increase during the first and the second steps between 219 and 288°C is about 22.79 % and becomes more pronounced in the third step (44 % between 290 and 350°C). All steps correspond principally to exothermic effects as can be concluded from the comparison of dTG and DTA curves. The DTA exotherms are broad suggesting that more or less strong endothermic effects could take place simultaneously.

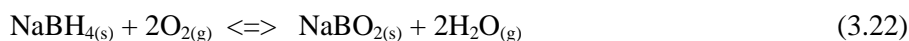
The IR spectra of the residues after TG under synthetic air reveal the formation of borates by-products due to the oxidation of B-H to the heavier B-O. The IR spectrum for the non-pre-evacuated sample shows $\text{Na}_3\text{B}_3\text{O}_6$. The difference of the IR spectra between the two residues is not related to the thermal treatment of the sample. It is simply due to the instability of $\text{Na}_3\text{B}_3\text{O}_6$ at room temperature as will be shown in chapter 6. For the pre-evacuated sample, the solid residue was kept longer at ambient conditions before pressing it in KBr pellet resulting in a partial hydration of $\text{Na}_3\text{B}_3\text{O}_6$ into hydrated borates. Thus, it can be assumed that the overall heating under synthetic air yields an almost total oxidation of NaBH_4 to $\text{Na}_3\text{B}_3\text{O}_6$. The total mass increases obtained (67 and 69.92 % for the pre-evacuated and non-pre-evacuated samples, respectively) are slightly lower than the theoretical loss of 73.93 % corresponding to the oxidation of NaBH_4 ($37.83 \text{ g}\cdot\text{mol}^{-1}$) to NaBO_2 ($65.7996 \text{ g}\cdot\text{mol}^{-1}$). This could be due to still unspecified additional contents in the starting materials as $\text{NaBH}_4\cdot 2\text{H}_2\text{O}$. These contributions may be indicated by the slight mass decreases up to 150°C in the inset graph of **Figure 3.11b** related to dehydration reactions in the sample.

The reaction of $\text{NaBH}_{4(\text{s})}$ with $\text{O}_{2(\text{g})}$ could release H_2 according to:

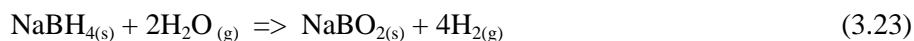


For the non-pre-evacuated sample, the reaction is slightly retarded and shifted about 10°C to higher temperatures in comparison with the non-pre-evacuated sample. For this sample, the mass decrease of the dehydration observed up to 150°C is higher (inset graph of **Figure**

3.11b). Therefore, the retarded reaction in the non-pre-evacuated sample can be referred to a higher water partial pressure at the surface of NaBH₄. The inverse correlation between the water partial pressure and the decomposition reaction with O₂ is more pronounced for the NaBH₄-geopolymer composites (NaBH₄-G) where the dehydration step is more intense [90]. The thermal decomposition of NaBH₄-geopolymer composites under synthetic air is retarded by 50°C for the non-pre-evacuated sample in comparison with the pre-evacuated sample. The geopolymer framework contains H₂O molecules which are desorbed at temperatures below 200°C. Pre-evacuating the sample is found to reduce the endotherm of dehydration on the DTA curves. Therefore, it can be concluded that the reaction of NaBH₄ with O₂ can be seen as equilibrium according to:



The reaction may form NaBO₂ or other intermediate. Water provided by the reaction of NaBH₄ with O_{2(g)} can be further consumed by NaBH_{4(s)} (or the intermediate) for hydrogen release (3.23).



The sum of the two reactions (3.22) and (3.23) leads to the global reaction (3.21). That is to say, the reaction of NaBH₄ with O_{2(g)} generates H_{2(g)} in an indirect way via the production of H₂O_(g) which reacts with NaBH₄ to release H_{2(g)}. The higher water partial pressure in the non-pre-evacuated sample suppresses to some extent the reaction with O_{2(g)} near 250°C (3.22) but would enhance H₂ release at 400°C with respect to the reaction (3.23). This could be indicated by the slightly higher mass increase (2-3 %) observed for the non-pre-evacuated sample at 400°C compared to the pre-evacuated sample and the presence of still traces of unreacted NaBH₄ in the IR spectrum of the pre-evacuated sample.

3.2.3 Temperature dependent Raman (TRam) analyses

The thermal behavior of solid NaBH₄ was further studied in-situ from room temperature to 400°C by mean of temperature dependent Raman (TRam) spectroscopy performed under different atmospheres (air, N₂ flowing and N₂ flowing loaded with water vapor). During heating, the image of the illuminated spot becomes grainy and blurry and required the microscope to be refocused.

Figure 3.12 shows TRam spectra of NaBH_4 heated from room temperature to 400°C under air. The room temperature Raman spectrum reveals a hydration of NaBH_4 powders to $\text{NaBH}_4 \cdot 2\text{H}_2\text{O}$. Crystalline water is upon slight heating to 40°C without being apparently consumed by NaBH_4 . The Raman spectrum at 60°C is related to anhydrous NaBH_4 . It is observed that NaBH_4 remains stable up to 350°C . At 375°C , traces of $\text{Na}_3\text{B}_3\text{O}_6$ are detected at 625 and about 1550 cm^{-1} [85]. The peaks increase during heating at 400°C together with a broad scattering background.

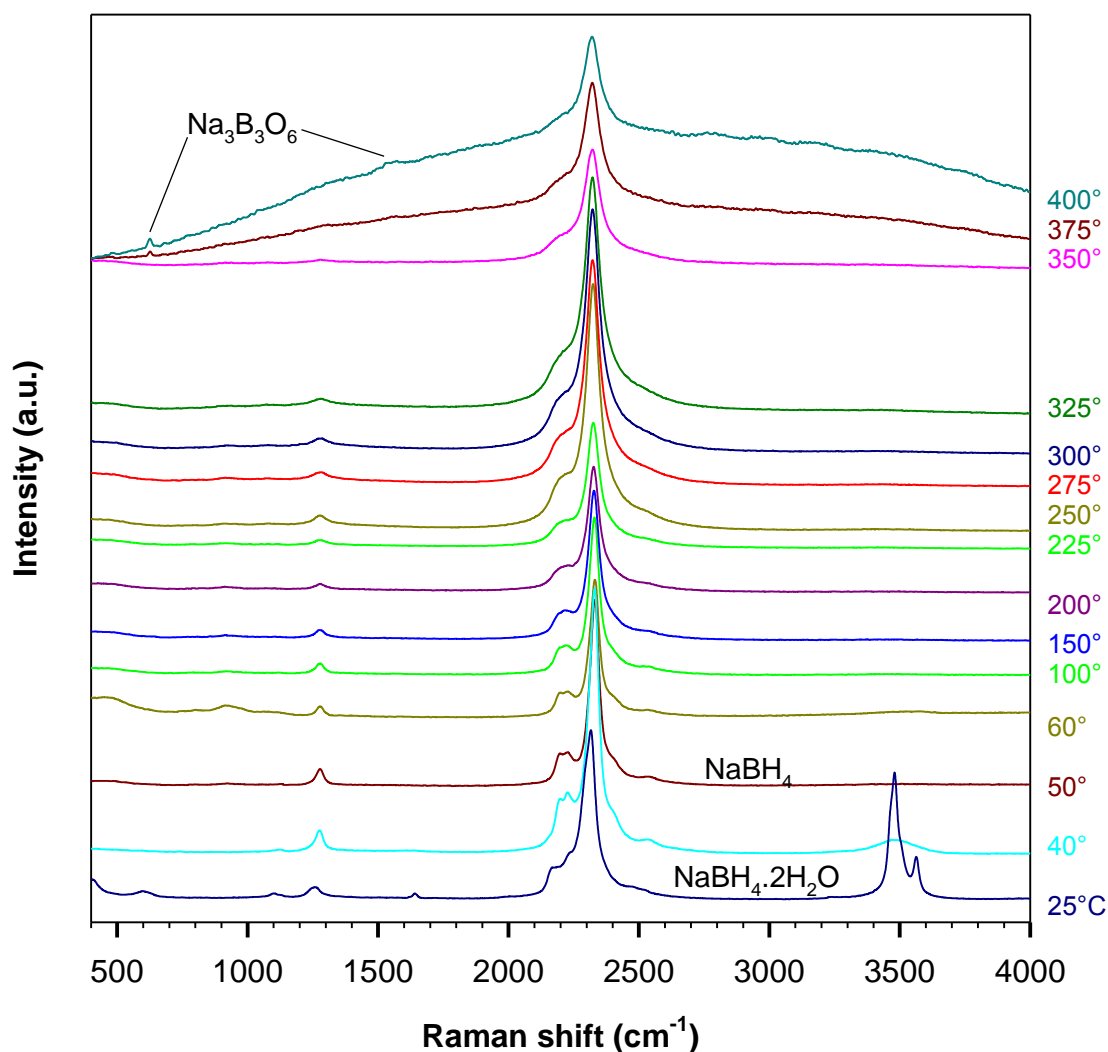


Figure 3.12: TRam of $\text{NaBH}_4 \cdot 2\text{H}_2\text{O}$ from room temperature to 400°C

For comparison, the decomposition of NaBH_4 in the TG experiment under synthetic air becomes visible at lower temperatures (near 250°C). This could indicate that the reaction of NaBH_4 with O_2 occurs at the surface and is dependent on the effective partial pressure of $\text{O}_{2(g)}$

which could be effectively lower in the TRam under open conditions shifting, thus, the reaction to higher temperatures. The difference may also be related to the sodium metaborate by-product. The detailed investigations of sodium metaborate compounds in chapter 6 indicate that the crystallization of Na₃B₃O₆ requires temperatures above 300°C. For temperatures between 200 and 300°C, the TIR spectra of the metaborates show broad IR bands indicating a poor crystallinity. Therefore, the reaction of NaBH₄ with O₂ between 200 and 300°C may yield NaBO₂ or other intermediate with very poor crystallinity difficult to be seen in the Raman spectra which are taken on a limited illuminated spot of the sample.

Further TRam experiments on the thermal behavior of NaBH₄ were performed under N₂ and N₂ flowing loaded with water vapor to check the role of H₂O in the decomposition reaction of NaBH₄. Results are shown in **Figure 3.13**. The formation of Na₃B₃O₆ was seen even under inert N₂ inert flowing. Na₃B₃O₆ peaks are detected at 375°C, similarly to TRam under air. This indicates that the reaction of NaBH₄ occurs with traces of H₂O and/or O₂ of the atmosphere. An increased reaction is observed at 350°C under N₂ loaded with water vapor. Thus, H₂O_(g) plays an important role in the oxidation of NaBH₄ to Na₃B₃O₆ above 350°C and have a minor role below 300°C since H₂O_(g) loaded in N₂ flowing decomposes NaBH_{4(s)} at temperatures above 350°C. Therefore, it can be concluded that the third step of the oxidation of NaBH₄ to Na₃B₃O₆ observed above 300°C in the TG experiments under synthetic air includes a reaction of NaBH₄ with H₂O releasing H₂ (reaction 3.23).

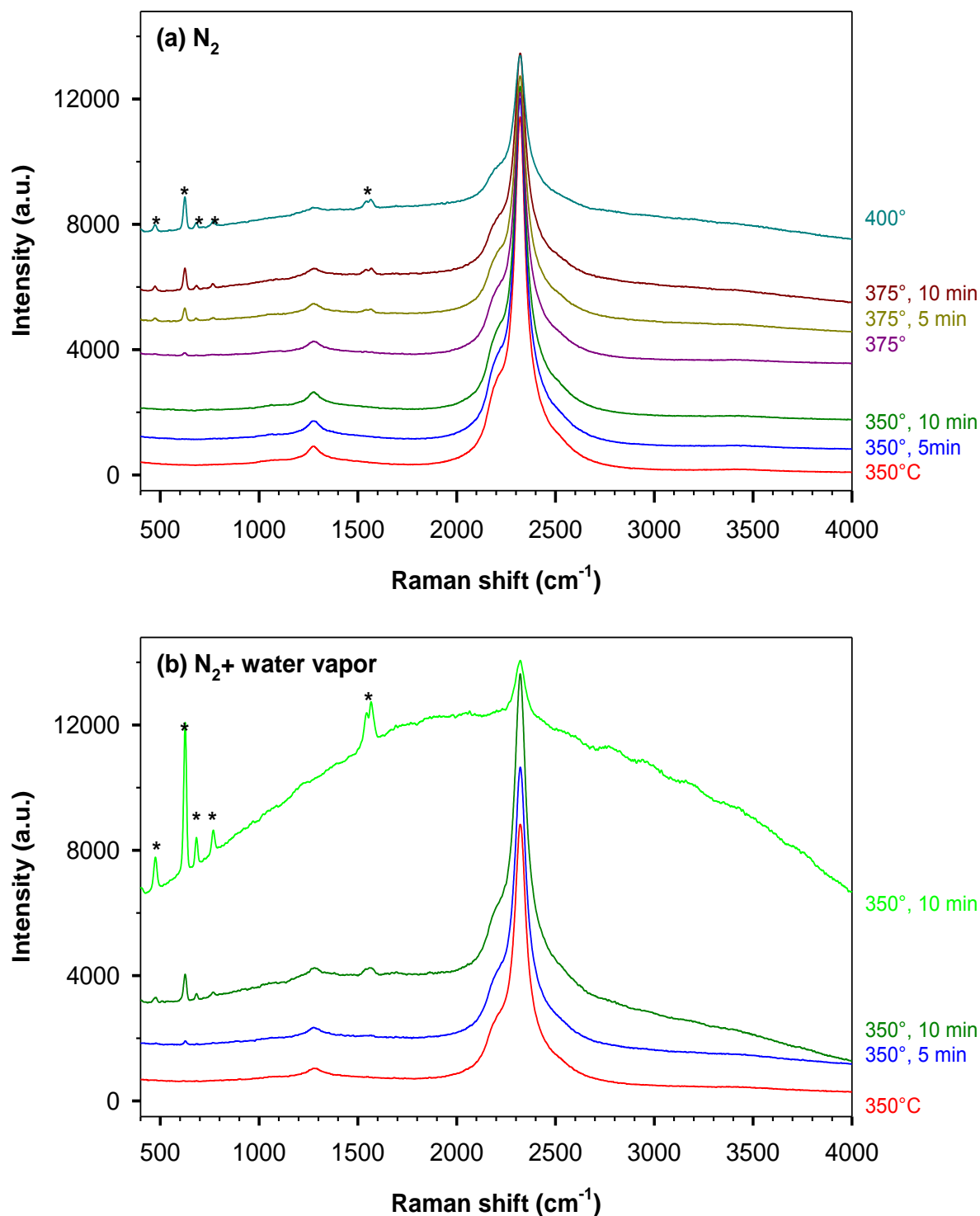


Figure 3.13: TRam of NaBH₄ powder under (a) inert N₂ flowing and (b) N₂ loaded with water for temperatures above 300°C. Asterisks denote the Raman peaks assigned to Na₃B₃O₆.

In order to check H₂ release, nitrate reduction method was conducted on a mixture of NaBH₄:NaNO₃ (50:50 wt%) pressed into pellet for a full homogeneity. TRam spectra were collected on a spot containing NaBH₄ and NaNO₃ together (*results not shown*). The sample

reveals a thermal stability up to 300°C, where an abrupt explosion occurred and prevented the completion of the experiment. The detonation could be interpreted by the use of a relatively high amount of the oxidizing nitrate agent in addition to a probable release of H_{2(g)} near 300°C.

3.2.4 Temperature dependent Infrared (TIR) analyses

TIR spectra of NaBH₄ using KBr matrix from room temperature to 400°C are shown in **Figure 3.14**. The room temperature IR spectrum shows peaks at 1125 cm⁻¹ (ν_4), 2223 cm⁻¹ ($2\nu_4$), 2291 cm⁻¹ (ν_3) and 2387 cm⁻¹ ($\nu_2+\nu_4$). These are close to those reported for BH₄⁻ anion in solid solution in KBr halide where BH₄⁻ substitute Br⁻ anions [91, 92]. Additionally, the IR spectrum shows weak bands at about 940 and 1350 cm⁻¹ which can be assigned to borates by-products due to a possible reaction of NaBH₄ with H₂O adsorbed from atmosphere during the pellet preparation. The pellet also contains traces of CO₃²⁻ and H₂O as can be concluded from the weak bands at 1435 and 3300-3600 cm⁻¹, respectively.

Above 300°C, new peak structures appear indicating some destruction products. These are resolved in the IR spectrum cooled down from 400°C into three doublets peaked at 708, 726 cm⁻¹, 1240, 1265 cm⁻¹ and 1438, 1460 cm⁻¹ respectively, in addition to a single weak but sharp peak at 959 cm⁻¹ that can be assigned to Na₃B₃O₆ [91].

The formation of Na₃B₃O₆ rather than K₃B₃O₆ confirms that the reaction does not take place in the KBr matrix, and it involves NaBH₄ crystal rather than BH₄⁻ in solid solution in KBr. It has been reported that the IR frequencies of B₃O₆³⁻ anions depend on the cation element [91]. If the reaction involved BH₄⁻ in solid solution in KBr, the resulting by-product would be K₃B₃O₆. This can be therefore ruled out. For comparison, NaBH₄ pellets using other halide matrices KCl and NaCl, and KBH₄ diluted in KBr were heated to 450°C, too. IR spectra are recorded after cooling down the pellets to room temperature. Results are shown in **Figure 3.15** in comparison with the IR spectrum of NaBH₄/KBr thermally treated in the same way.

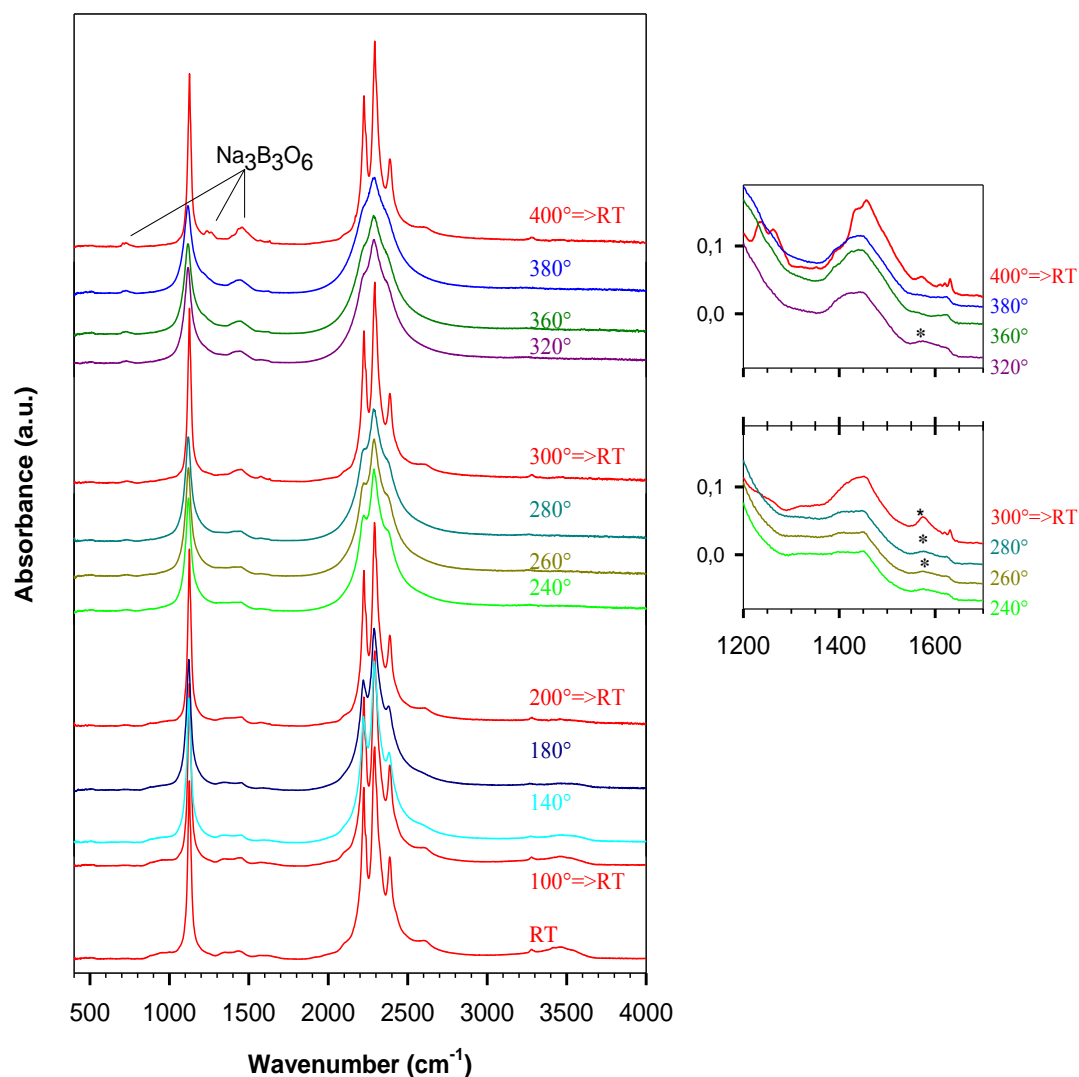


Figure 3.14: TIR of NaBH_4/KBr from room temperature to 400°C (at the left side). At the right side, the corresponding spectra are zoomed in the spectral range between 1200 and 1700 cm^{-1} . Asterisks are used to follow the intermediary peak at 1575 cm^{-1} . (*RT*: room temperature).

The IR peak maxima of BH_4^- (for e.g. for ν_4) after the different thermal treatments are not the same and are found to be similar to reported values for BH_4^- in solid solution in the halide matrix in use [91, 92]. These frequencies are governed by the halide matrix independently of the borohydride salt used. Indeed, NaBH_4/KBr and KBH_4/KBr pellets after the thermal treatment reveal the same frequencies for BH_4^- group which are related to the solid solution of BH_4^- in KBr . The solid solution of BH_4^- in different Na, K and Rb-halides are discussed in details in chapter 5. All pellets give evidence to the formation of the metaborate $\text{B}_3\text{O}_6^{3-}$ ring. The obtained frequencies are given in **Table 3.2**.

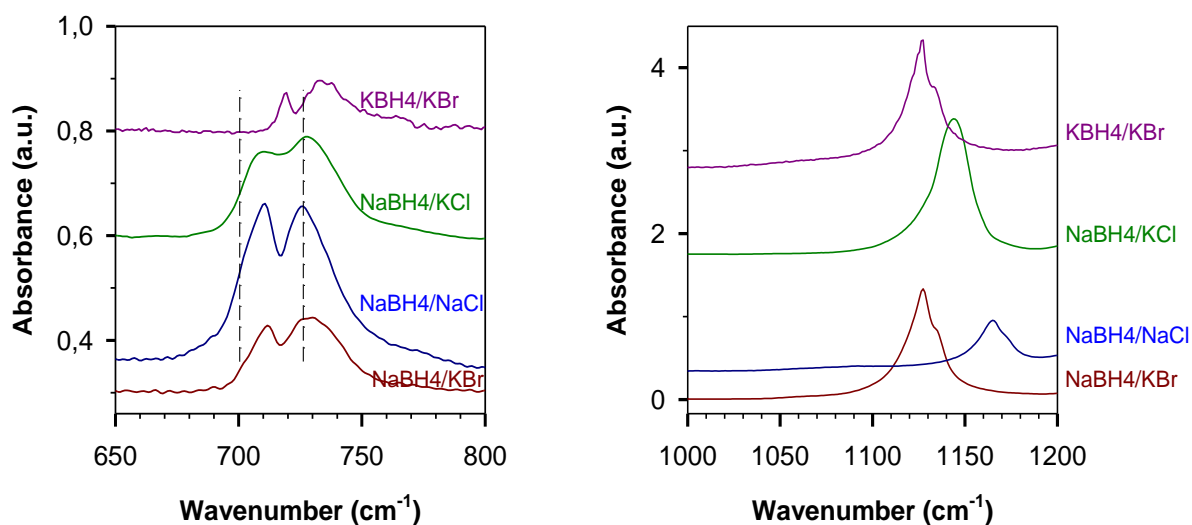


Figure 3.15: IR spectra NaBH₄/NaCl, NaBH₄/KCl and KBH₄/KBr pellets after thermal treatment to 450°C in comparison with of NaBH₄/KBr. Spectral region of B₃O₆³⁻ (650-800 cm⁻¹) and BH₄⁻ (1000-1200 cm⁻¹) are shown. Dashed vertical lines are used to show the peak positions of B₃O₆³⁻.

The IR frequencies of Na₃B₃O₆ and K₃B₃O₆ salts are also given. These are the average of the IR frequencies reported in ref. [91] for B₃O₆³⁻ in NaX and KX halides (X = Cl, Br and I), respectively. For NaBH₄ pellets, the IR frequencies of B₃O₆³⁻ are similar and close to those reported for Na₃B₃O₆. For KBH₄/KBr pellet, the IR frequencies of B₃O₆³⁻ are different and related to K₃B₃O₆. Therefore, it can be said that the metaborate by-product is related to the borohydride salt used rather than the solid solution of BH₄⁻ in the halide matrix. As a consequence, during the pellet preparation of NaBH₄ in KBr a large amount of BH₄⁻ forms solid solution in KBr. Only a minor amount of NaBH₄ remains unaffected by KBr and undergoes the reaction to Na₃B₃O₆ above 300°C. The BH₄⁻ anion in solid solution is stabilized in the matrix and decomposes at much higher temperature.

Table 3.2: IR peak positions of $B_3O_6^{3-}$ and BH_4^- after the thermal treatment of $NaBH_4/KBr$, $NaBH_4/KCl$, $NaBH_4/NaCl$ and KBH_4/KBr pellets in comparison with literature values of $Na_3B_3O_6$ and $K_3B_3O_6$

	$B_3O_6^{3-}$			BH_4^-
	Ring out-of-plane bend ν_{11}	Ring stretching ν_7	Ring stretching ν_6	ν_4
$NaBH_4/KBr$	712; 729	1240; 1265	1438; 1463	1127
$NaBH_4/KCl$	711; 728	1238; 1264	1440; 1463	1144
$NaBH_4/NaCl$	710; 726	1241; 1266	1437; 1468	1165
KBH_4/KBr	718; 735	1228; 1253	1405; 1441	1127
$Na_3B_3O_6$ [91]	707; 722	1240; 1263	1436; 1464	--
$K_3B_3O_6$ [91]	717; 734	1226; 1250	1405; 1440	--

The oxidation of $NaBH_4$ to $Na_3B_3O_6$ above $300^\circ C$ can be interpreted by the presence of H_2O and/or O_2 contaminations in the evacuated cell, similar to the case of TRam results under inert N_2 flowing. Detailed visualization of the TIR of $NaBH_4$ in KBr (**Figure 3.14**) reveals the presence of a weak but significant peak at 1575 cm^{-1} between 200 and $300^\circ C$ which could be tentatively described by a stretching mode involving a boron atom $B\text{ sp}^2$ hybridized vibrating with an oxygen atom [90, 93]. This peak vanishes above $320^\circ C$, concurrently with the formation of $Na_3B_3O_6$ (*this may be confused with the weak peak of $Na_3B_3O_6$ at about 1570 cm^{-1} which appears near $380^\circ C$*). Therefore, it can be referred to an intermediate or transient species which polymerizes above $300^\circ C$ to $Na_3B_3O_6$. Other plausible descriptions could not be excluded. Compounds containing boron double bonded to oxygen are generally not stable [94] due to the oxophilicity of the boron atom which favors the B-O-B linkage with ease compared to the B=O double bond [95]. Pietsch et al. [96] suggested $O=B(OH)_2^-$ as isolated species in the sodalite cages during the thermal dehydration of $B(OH)_4^-$ -sodalite to BO_2^- -sodalite. The corresponding asymmetric stretching of the threefold coordinated B atom to O was reported between 1400 and 1500 cm^{-1} .

The evolution of $Na_3B_3O_6$ at $400^\circ C$ was followed in function of time (*IR spectra not shown*). Integral intensities for $Na_3B_3O_6$ peak between 677 and 775 cm^{-1} and $NaBH_4$ between 2065 and 2700 cm^{-1} (corresponding to $2\nu_4$, ν_3 and $\nu_2+\nu_4$) were calculated and plotted against the holding time at $400^\circ C$ (**Figure 3.16**).

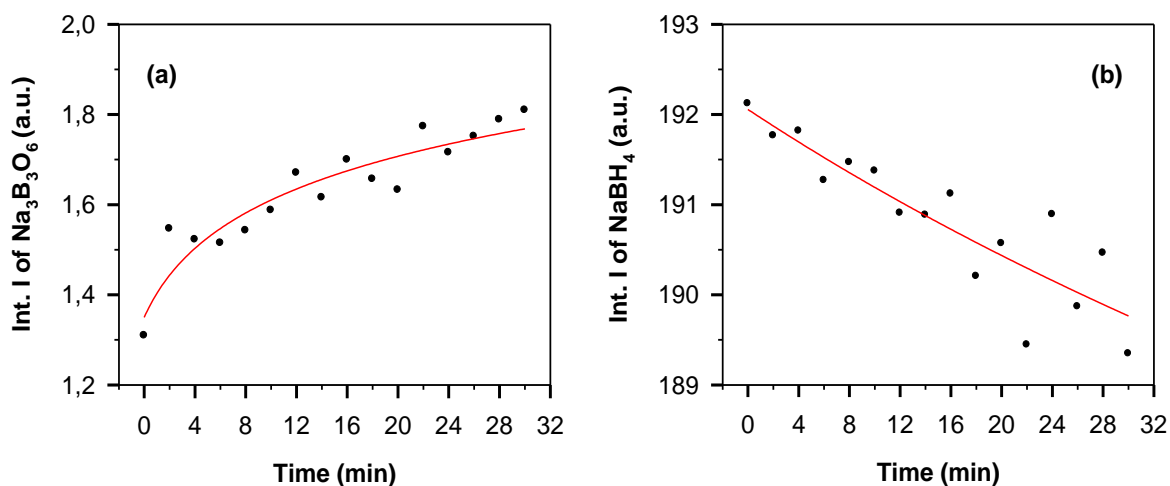


Figure 3.16: Time dependence of the integrated intensities (Int. I) at 400°C of (a) Na₃B₃O₆ (677-775 cm⁻¹) and (b) NaBH₄ (2065-2700 cm⁻¹). Red lines are the regressions using a logarithmic function of the form $y = y_0 + a \ln(x-x_0)$.

The variation of the integrated intensities in function of time can be described by a logarithmic function representing an increase for Na₃B₃O₆ and a decrease for NaBH₄. This confirms the oxidation reaction of NaBH₄ to Na₃B₃O₆ and indicates that the reaction proceeds rapidly in the first few minutes and then decelerates.

The oxidation of NaBH₄ to Na₃B₃O₆ is accompanied by H₂ release, as showed in the TIR experiment of NaBH₄ in KBr conducted in presence of nitrate tracer (NaNO₃) (**Figure 3.17**). Additional IR bands at room temperature at 836 cm⁻¹ (ν_2), 1380 cm⁻¹ (ν_3 , broad), 1447 cm⁻¹ ($2\nu_4$, shoulder) and 1789 cm⁻¹ ($\nu_1+\nu_4$) are for NaNO₃ [40]. The TIR spectrum taken after cooling down the pellet from 300°C shows a weak peak at 1270 cm⁻¹ which corresponds to $\nu_3(\text{NO}_2^-/\text{KBr})$ [34, 39]. The nitrite contribution in the TIR spectrum taken after the thermal treatment to 420°C appears superimposed to the doublet of Na₃B₃O₆ and is highly increased along with the oxidation reaction of NaBH₄⁻ to Na₃B₃O₆.

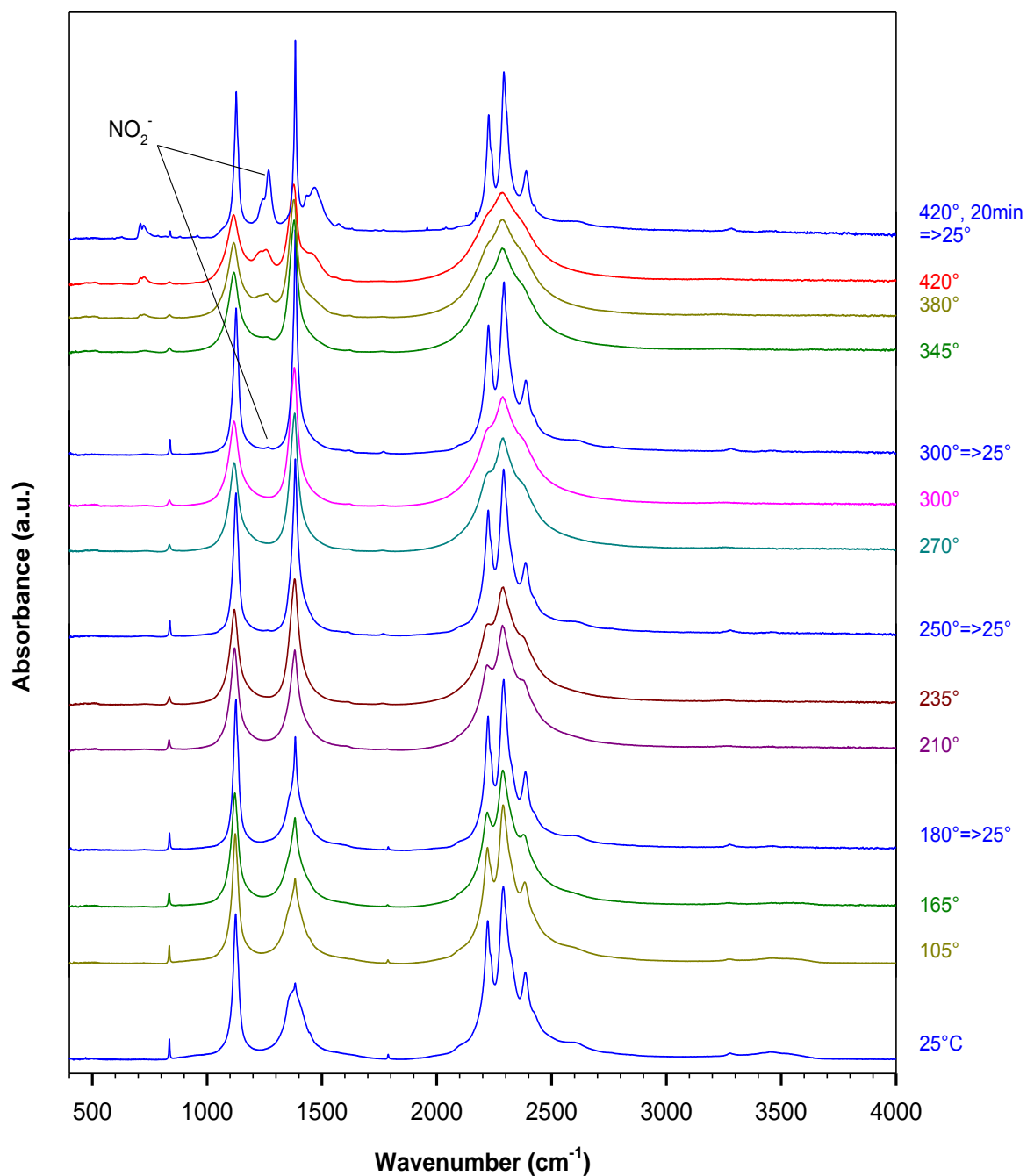


Figure 3.17: TIR spectra of NaBH₄/KBr in presence of NaNO₃ tracer

The IR spectrum cooled down from 420°C shows a slight decomposition of the cyclic B₃O₆³⁻ to the linear BO₂⁻ molecule as can be concluded from the pair of weak but sharp peaks about 2000 cm⁻¹. Additional weak peaks are observed at 2170, 1630 and 2426 cm⁻¹. The peak at 2170 cm⁻¹ is for NCO⁻ impurities in KBr and this at 2426 cm⁻¹ is related to N-based compounds originating from the thermal decomposition of the nitrate (see Chapter 2). The IR peak at 1630 cm⁻¹ corresponds to the formate ion HCO₂⁻ in solid solution in KBr [97, 98, 99,

100]. Its formation can be interpreted by the reaction of BH₄⁻ with CO₂ contaminations. Grice et al. [72] reported a hydride transfer from BH₄⁻ to CO₂ in aqueous solution and this occurs in competition with the hydrolysis reactions of NaBH₄ with H₂O releasing H_{2(g)}.

The NaBH₄/KBr pellets were generally much darker after being heated to temperatures between 400 and 500°C. This was referred to the presence of carbon in the thermally treated pellets. Its formation can be explained by the reduction of contaminations of CO₂ by NaBH₄ [101]. Likewise, the decomposition of HCO₂⁻ near 500°C can also make the pellet appear dark. It has been reported that HCO₂⁻ diluted in KBr decomposes to CO₃²⁻, CO and H₂. The disproportionation reaction of CO produces CO₂ and carbon [97].

The H₂ release reaction was followed using the variation of the integral intensities of ν₂(NO₃⁻) in function of temperature. Results are depicted in **Figure 3.18** and are compared to a reference pellet constituted of only NaNO₃ diluted in KBr. The variation of the integral intensities of Na₃B₃O₆ (677-775 cm⁻¹) and NaBH₄ (2065-2700 cm⁻¹) in presence of NaNO₃ tracer are also shown and are compared to the integral intensities of Na₃B₃O₆ and NaBH₄ for the pellet without NaNO₃ tracer. A decrease of the integral intensity may originate, in some cases, from a broadening of the IR peak at high temperatures (for e.g. for BH₄⁻ and NO₃⁻) since the integration limits for a given species were maintained the same overall the integrations. Therefore, integrated intensities of the TIR spectra after cooling down from a given temperature to room temperature (T => 25°C) were also considered.

The formation of Na₃B₃O₆ becomes significant above 300°C. This is accompanied simultaneously by a gradual decrease of the integral intensities of BH₄⁻ at high temperatures. A remarkable decrease of the integral intensities of BH₄⁻ is observed at relatively lower temperature (100-200°C), which cannot be related to any chemical reactions since the TIR spectra in this temperature range do not show additional IR decomposition bands. Therefore, this can be referred to structural changes within the borohydride as a re-crystallization in the KBr matrix.

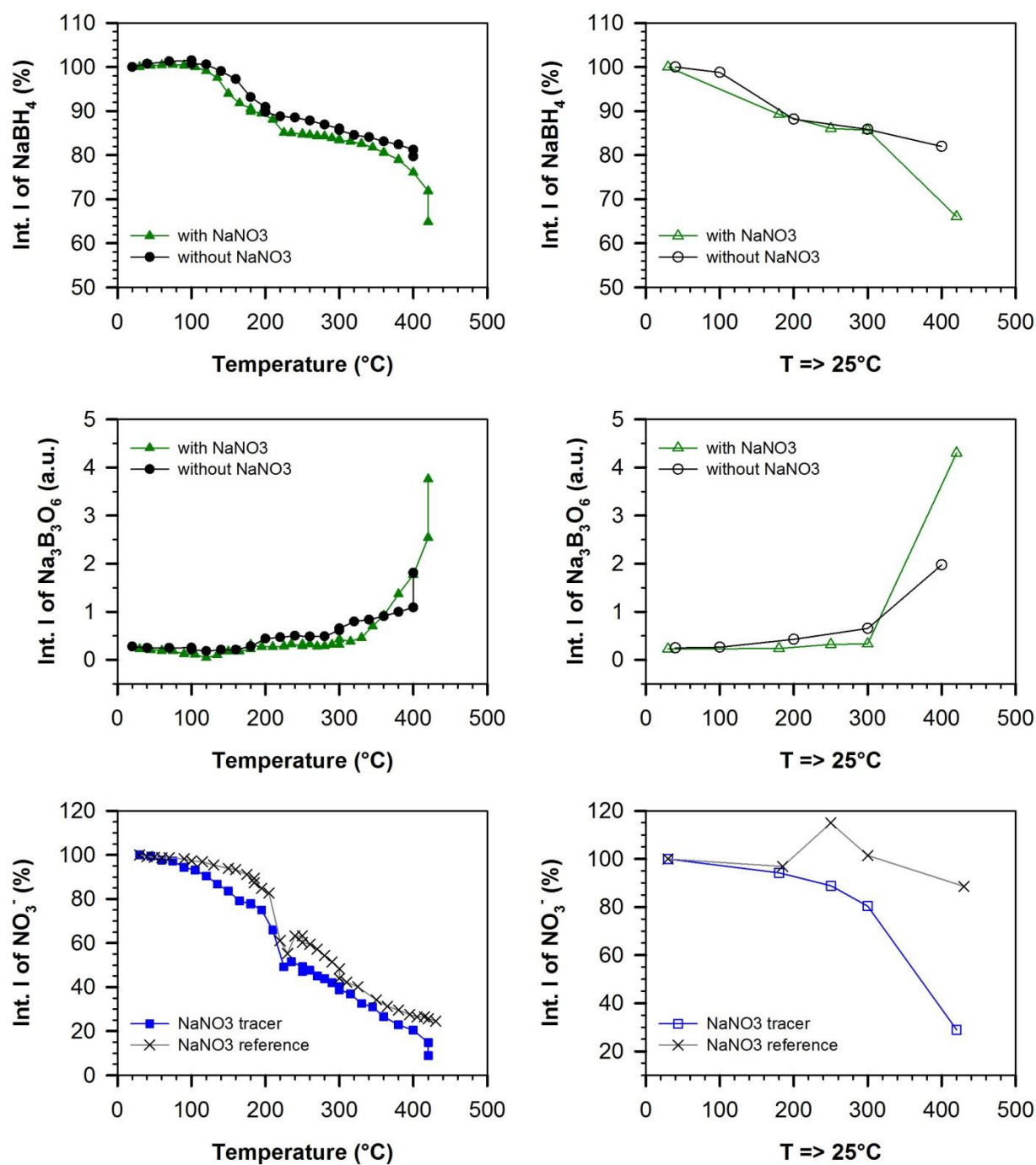


Figure 3.18: Temperature dependence of the integrated intensities of (a) NaBH_4 and (b) $\text{Na}_3\text{B}_3\text{O}_6$ for TIR of NaBH_4/KBr pellets with and without NaNO_3 tracer. (c) Integral intensities of ν_2 of NaNO_3 tracer used in NaBH_4/KBr pellet compared to a reference NaNO_3/KBr pellet. Integrated intensities are calculated for the TIR spectra during the heating up run (left) and at 25°C when cooled down from T as denoted (T=>25°C) at the right side. Lines are only guide for eyes.

The oxidation of NaBH_4 to $\text{Na}_3\text{B}_3\text{O}_6$ above 300°C produces strong decrease of $\nu_2(\text{NO}_3^-)$ confirming H_2 release. The percent of NaBH_4 decomposition in KBr , calculated from the decrease of the integral intensities of BH_4^- bands above 200°C, is about 23 % at

420°C after 20 min for the pellet containing NaNO₃ tracer and 7 % at 400°C after 30 min for the pellet without NaNO₃ tracer. Theoretically, conversions of 8.9 wt% and 4.5 wt% of NaBH₄, calculated according to the reaction (3.21) and the reaction (3.23), respectively, are enough to reduce the total amount of NaNO₃ used in the pellet. Therefore, a significant amount of H₂ is evacuated and goes out of the pellet without reducing NO₃⁻.

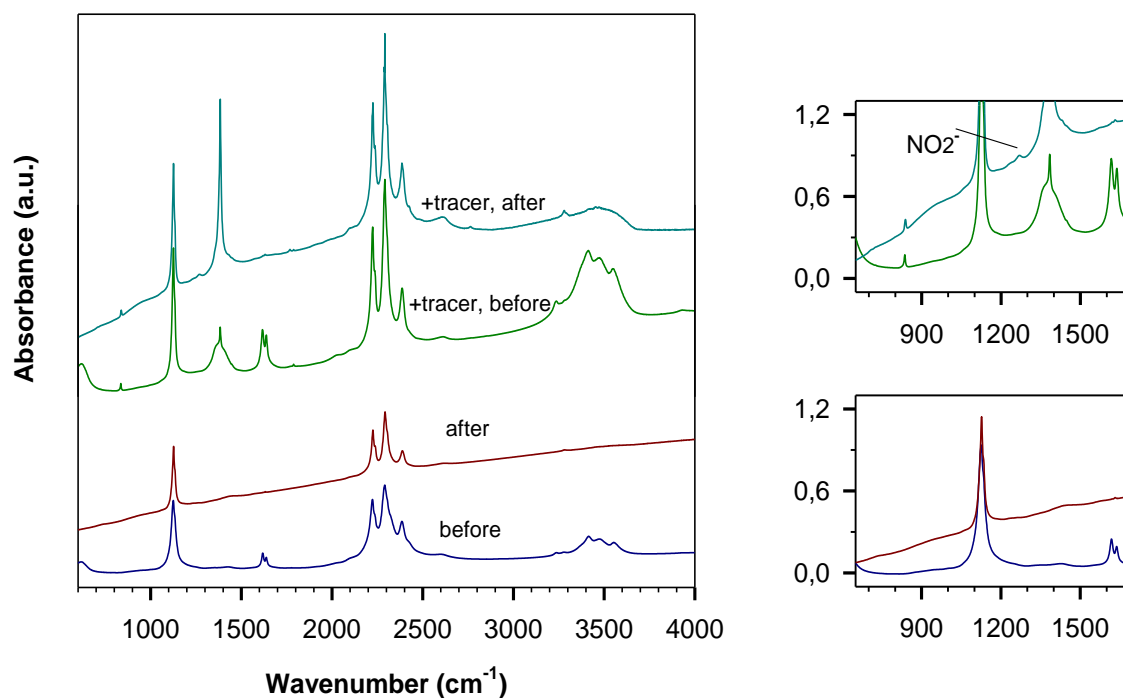
The TIR experiment performed in presence of NaNO₃ tracer shows an increased conversion of NaBH₄ to Na₃B₃O₆ compared to TIR without NaNO₃ tracer. This is explained by the reduction reaction of nitrate to nitrite which supplies “internal” water vapor to the system according to $\text{NO}_3^- + \text{H}_2 \Rightarrow \text{NO}_2^- + \text{H}_2\text{O}$.

An interesting observation is that, between 250 and 300°C, $\nu_2(\text{NO}_3^-)$ of NaNO₃ tracer decreases without a significant decrease of BH₄⁻ or increase of Na₃B₃O₆ integral intensities. In this same temperature range the weak IR band at 1575 cm⁻¹ is also observed (**Figure 3.14**). This indicates hydrogen release without significant consumption of NaBH₄. Urganani et al. [21] reported a small but significant H₂ release near 250°C during the thermal desorption of NaBH₄ under vacuum (**Figure 3.7**).

The origin of H₂ release between 200 and 300°C was further investigated using NaBH₄/KBr pellets with and without nitrate tracer (KNO₃). The pellets were heated under N₂ atmosphere loaded with water vapor to 250°C for 15 min and to 270°C for 30 min, respectively. IR spectra recorded before and after the thermal treatment are shown in **Figure 3.19**.

The room temperature IR spectra reveal the presence of NaBr·2H₂O indicated by the H₂O bending modes at 1618 and 1638 cm⁻¹ and the OH stretching modes at 3236, 3412, 3473 and 3551 cm⁻¹ [102]. The IR bands related to the nitrate ion are observed at 836 cm⁻¹ (ν_2), 1380 cm⁻¹ (broad, ν_3), 1447 cm⁻¹ (shoulder, $2\nu_4$) and 1789 cm⁻¹ ($\nu_1+\nu_4$). These correspond to NaNO₃ rather than KNO₃ [31, 40] and suggest an ionic exchange K⁺/Na⁺ during the pellet preparation. The IR spectrum cooled down from 250°C reveals the presence of two components for the combination mode $\nu_1+\nu_4$ peaked respectively at 1788 and 1768 cm⁻¹, in addition $\nu_3(\text{NO}_3^-)$ mode at 1384 cm⁻¹ is strongly sharpened. These variations indicate that most of NO₃⁻ anions did go in the KBr matrix.

(a) 250°C, 15 min



(b) 270°C, 30 min

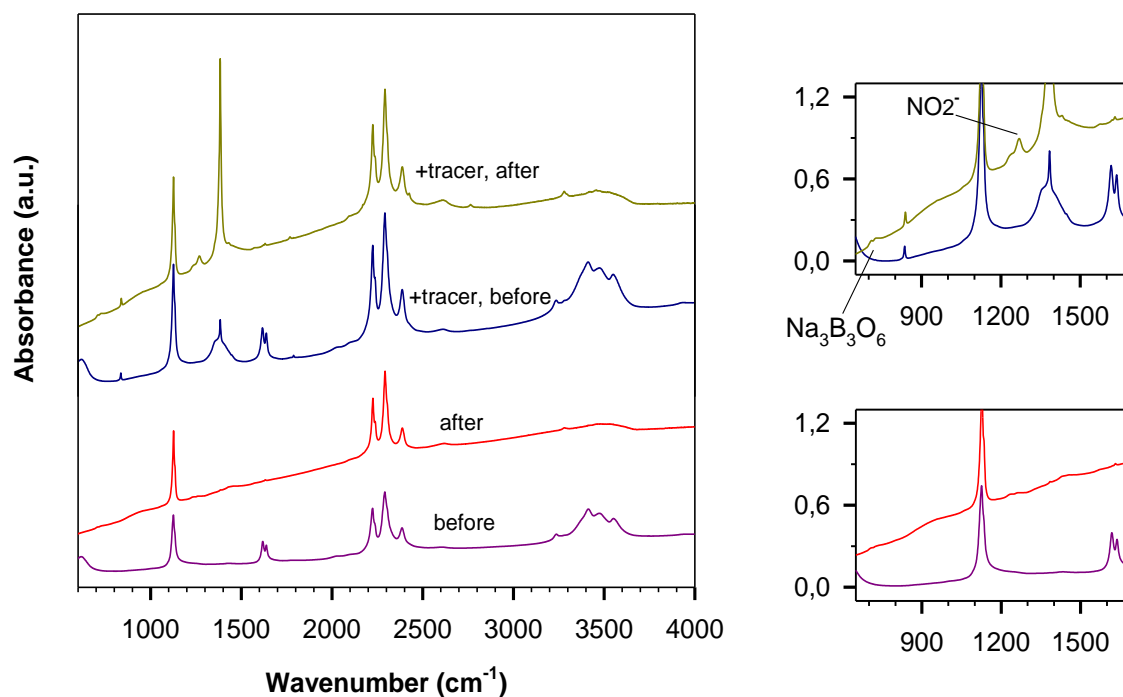


Figure 3.19: IR spectra of NaBH₄/KBr pellets before and after the isotherms (a) at 250°C for 15 min and (b) at 270°C for 30 min under N₂ atmosphere loaded with water vapor. Experiments were performed on pellets without and with KNO₃ tracer. At the right side, the graphs are zoomed between 650 and 1700 cm⁻¹.

The pellets without nitrate tracer do not reveal any decomposition of NaBH₄ to metaborate after the thermal treatment. This is in agreement with TG analyses and TRam

experiment under N₂ flowing loaded with water vapor suggesting that H₂O_(g) do not decompose NaBH₄ to NaBO₂ for temperatures below 300°C and could furthermore suppress the decomposition of NaBH₄ with O_{2(g)} between 200 and 300°C. Loading the atmosphere with H₂O did not increase the band at 1575 cm⁻¹ indicating that this peak is a metastable species which polymerizes readily to Na₃B₃O₆.

The above observations could imply new reaction path for H₂ release using NaBH₄ between 200 and 300°C. One approach, NaBH₄ could exhibit a poorly catalytic effect for the thermal production of hydrogen from water. In this case, the weak IR band at 1575 cm⁻¹ could indicate a transition state on the NaBH₄ surface in the reaction with water. O₂ released from water could adsorb on NaBH₄ and reacts further with NaBH₄ to Na₃B₃O₆ (reaction 3.21 and 3.22). Other reaction schemes could not be excluded.

The IR spectra after the thermal treatment in the presence of nitrate tracer show the nitrite peak at 1270 cm⁻¹ confirming H₂ release. The IR spectra indicate slight decomposition to Na₃B₃O₆, too. This could indicate that the nitrate reduction to nitrite (NO₃⁻ + H₂ => NO₂⁻ + H₂O) releases water in an “activated form” different from molecular H₂O of the atmosphere which is able to oxidize NaBH₄ to Na₃B₃O₆ at such temperatures. Furthermore, water provided by the reduction reaction of nitrate may increase the effective water partial pressure at NaBH₄ surface in comparison with H₂O_(g) of the atmosphere promoting thus the decomposition of NaBH₄ with H₂O to NaBO₂.

4. H₂ release from Ammonia Borane NH₃BH₃ and NH₃BH₃-Geopolymer (NH₃BH₃-G)

4.1 State of the Art

4.1.1 Synthesis and structure

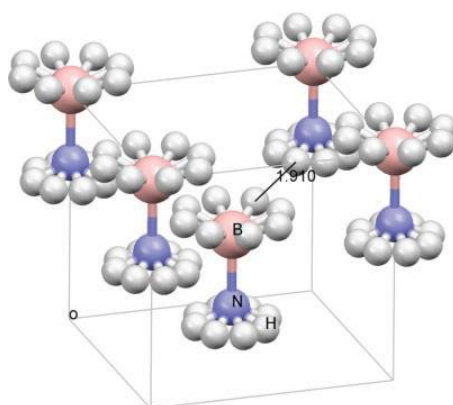
The room temperature structure of NH₃BH₃ has been described within the space group I4mm with the cell parameters $a = b = 5.2630 \text{ \AA}$ and $c = 5.0504 \text{ \AA}$ [103, 104]. The BH₃NH₃ molecules are located at the vertices and body-center of the unit cell and have their B-N bond oriented parallel to the four-fold c-axis. Boron and nitrogen atoms carry opposite formal charges and are distanced by 1.597 \AA according to the single crystal X-ray studies on NH₃BH₃ [104]. The structure exhibits halos of hydrogen atom occupancy around N and B atoms. Hydrogen disorder in tetragonal BH₃NH₃ arises from either rotations of higher than three-fold order or from random orientations of hydrogen-containing groups (**Figure 4.1a**).

An order-disorder phase transition occurs at -48°C [105]. The low temperature phase is orthorhombic with the space group Pmn2₁ and the cell parameters $a = 5.541 \text{ \AA}$, $b = 4.705 \text{ \AA}$ and $c = 5.0237 \text{ \AA}$ [104, 106]. The structure of NH₃BH₃ molecule is preserved in both phases.

A highly polarized dative bond is formed between the lone pair of electrons of nitrogen atom and the empty 2p orbital of boron atom as shown in **Figure 4.1b**. This results in a stabilization of NH₃BH₃ at ambient conditions compared to the isoelectronic molecule of ethane H₃C-CH₃ which melts at -181°C [107].

NH₃BH₃ salt contains dihydrogen bonding between the protonic hydrogen on N (N-H^(δ^+)) and the hydridic hydrogen on B (B-H^(δ^-)), with 2.02 \AA being the shortest H...H distance in the orthorhombic structure [106] and 1.91 \AA in the tetragonal structure [104]. The N-H bond has a more covalent character, whereas the B-H bond is more ionic [108].

(a)



(b)

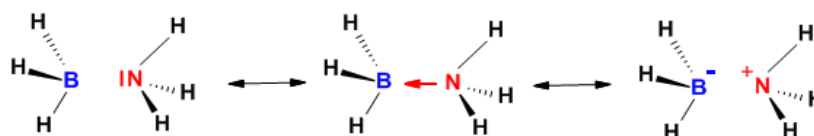
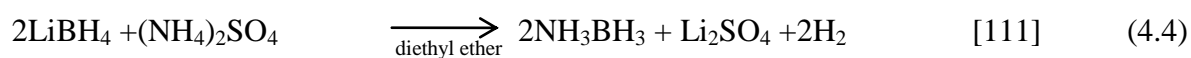
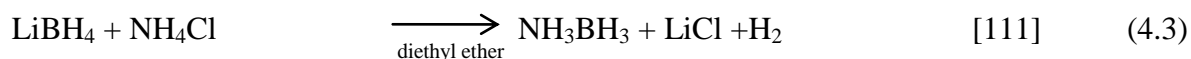
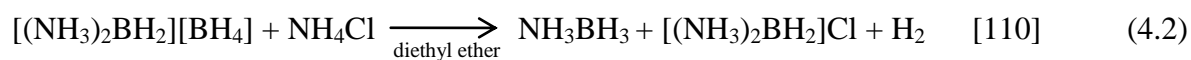
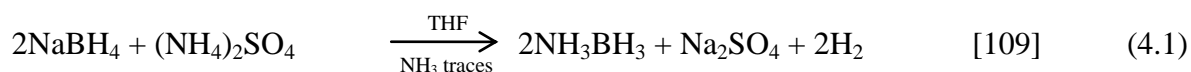


Figure 4.1: (a) Room temperature structure of NH₃BH₃ showing the rotational disorder of hydrogen atoms (white) around each B (pink) and N (purple) atoms (the figure is taken from ref. [104]). (b) The chemical bond between B (blue) and nitrogen N (red) atoms in NH₃BH₃.

Several synthetic routes of NH₃BH₃ were developed all based on chemical reactions between borohydride and ammonium salts. Some examples are reported in reactions (4.1) to (4.4).

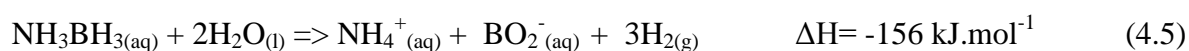


4.1.2 H₂ release from NH₃BH₃

Hydrogen can be released from NH₃BH₃ either by hydrolysis or by thermal dehydrogenation (thermolysis).

NH₃BH₃ is highly stable in water under inert atmosphere [112] unlike NaBH₄ which undergoes a self-hydrolysis reaction in aqueous solution. Aqueous solution of NH₃BH₃ hydrolyses slowly under air due to the catalytic effect of carbon dioxide [113].

The hydrolysis of NH₃BH₃ is an acid [113] or metal catalyzed reaction [112] and could be presented stoichiometrically according to reaction (4.5) [114].



The theoretical hydrogen storage capacity of NH₃BH₃-H₂O system is 15 wt%. The system loses unrecoverable hydrogen in the form of NH₄⁺. In practical system, the storage capacity of an aqueous solution of NH₃BH₃ does not exceed 4.9 wt% by reason of its low solubility (33.6 g_{(NH₃BH₃)/100g_(H₂O) [11]). For comparison, the aqueous solubility of NaBH₄ (55 g_{(NaBH₄)/100g_(H₂O) [11]) implies an aqueous storage capacity of 7.5 wt%.}}

Studies of the acid catalyzed hydrolysis of NH₃BH₃ suggested two mechanisms for H₂ release [115] (**Figure 4.2**). In scheme **a**, the rate determining step involves a proton transfer from HCl to the borohydride group in NH₃BH₃ resulting in the formation of a five-coordinated boron species. A similar penta-coordinated boron intermediate species has been reported for NaBH₄ (chapter 3, section 3.1.2). Analyses of isotope effects and reaction rates suggested a favorable protonation of the nitrogen atom (scheme **b**). In this model, an activated complex involving both the entering group (H⁺) and the leaving group (BH₃) is proposed. In a next step, H₂ is released via rapid hydrolysis of the highly reactive BH₃ solvated species.

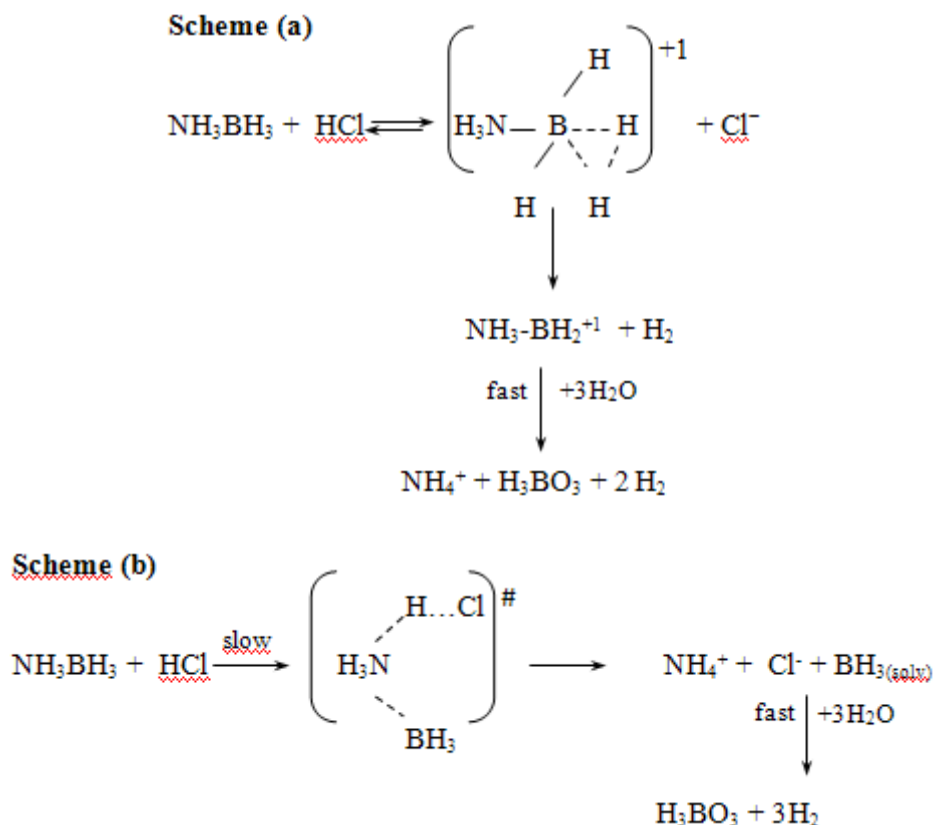


Figure 4.2: The mechanisms proposed for the acid catalyzed H₂ release of NH₃BH₃ according to ref. [115]. Scheme (a): protonation of the borohydride group. Scheme (b): protonation of the amino group.

The dehydrocoupling of NH₃BH₃ catalyzed by a strong Lewis acid or Brønsted acids (B(C₆F₅)₃, HOSO₂CF₃, HCl) at 60°C in glyme, diglyme or tetraglyme involves a hydride subtraction generating the boronium cation NH₃BH₂⁺ which could be obtained according to scheme a. NH₃BH₂⁺ reacts with NH₃BH₃ to liberate H₂. These reactions set between 0.6 and 1.2 equivalents H₂ free [116].

The thermal decomposition route can achieve a higher extent of H₂ than the hydrolysis process. Nevertheless, from a chemical point of view it is a harsh process since hydrogen release is accompanied with foaming and voluminous swelling of the material. Additive reagents as methyl cellulose and others have a foam suppression effect on the bulk material [117].

Hydrogen release is facilitated by the presence of hydridic B-H^(δ-) and protic N-H^(δ+) hydrogen [8]. NH₃BH₃ melts with decomposition at 110-114°C [107]. Two thermolysis steps were reported at about 110 and 150°C for the release of the first and the second mol H₂, respectively [8, 11]. The third mol H₂ is desorbed at much higher temperature, above 1100°C

[118]. ^{11}B magic angle spinning-nuclear magnetic resonance (^{11}B MAS-NMR) [119, 120] and vibrational spectroscopic studies [118, 121] confirmed the formation of poly-aminoborane (PAB) $(-\text{NH}_2-\text{BH}_2-)_n$ in the solid phase of the first decomposition step. The solid residue of the second decomposition step is formed in a broad range of temperature and is assigned to poly-iminoborane (PIB) $(-\text{NH}=\text{BH}-)_n$ structures which are characterized by π -bonded B and N atoms [118, 122]. The consumption of all hydrogen atoms yields hexagonal boron nitride as evidenced by ATR-FTIR spectroscopy [118]. The nature of PAB and PIB polymers is complex and is not well-defined since H_2 could be released via different routes involving linear as well as cyclic structures [108]. PAB compounds may include a diversity of linear, branched and cyclic compounds. Likewise, PIB may have undefined amounts of cross-linking and branching [4]. **Figure 4.3** shows some examples of PAB and PIB compounds.

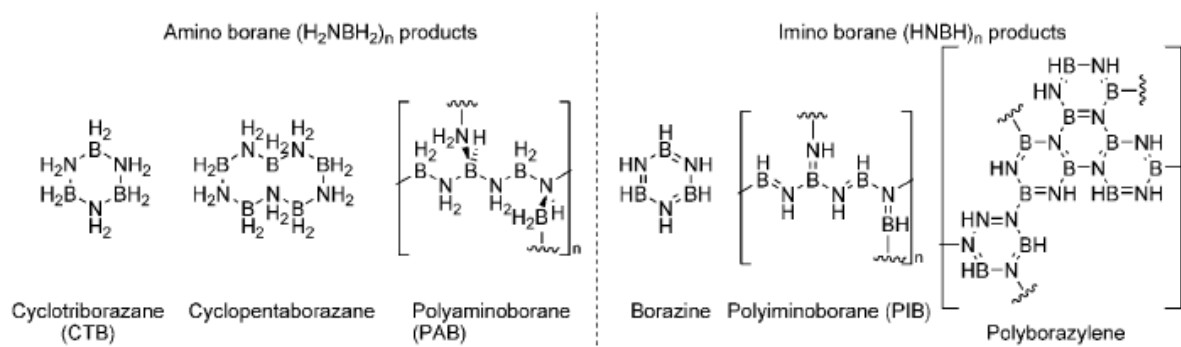


Figure 4.3: Chemical structure of some possible products of the thermal decomposition of NH_3BH_3 (the figure is taken from ref. [8]).

The release of the first and second mol H_2 overlap at high heating rates but could be separated at very slow heating rates ($0.05^\circ\text{C}/\text{min}$) or at stepwise rising temperatures [121, 123]. Wolf et al. [123] reported the release of the first mol H_2 after heating NH_3BH_3 at 90°C for 6 h.

Baitalow et al. [121] showed a constant hydrogen release of NH_3BH_3 between room temperature and 220°C and variable mass losses which increase with increasing the heating rate. Simultaneous TG/FTIR measurements [121, 123] and TG/MS analyses [121] demonstrated the presence of monomeric aminoborane $\text{H}_2\text{N}=\text{BH}_2(\text{g})$, borazine $\text{B}_3\text{N}_3\text{H}_6(\text{g})$ and traces of diborane $\text{B}_2\text{H}_6(\text{g})$ in the evolved gas phase (**Figure 4.4**). The release of B, N-containing gases becomes more significant at temperatures above 140°C . Zhu et al. [124] suggested that the gas phase may also contain traces of ammonia $\text{NH}_3(\text{g})$.

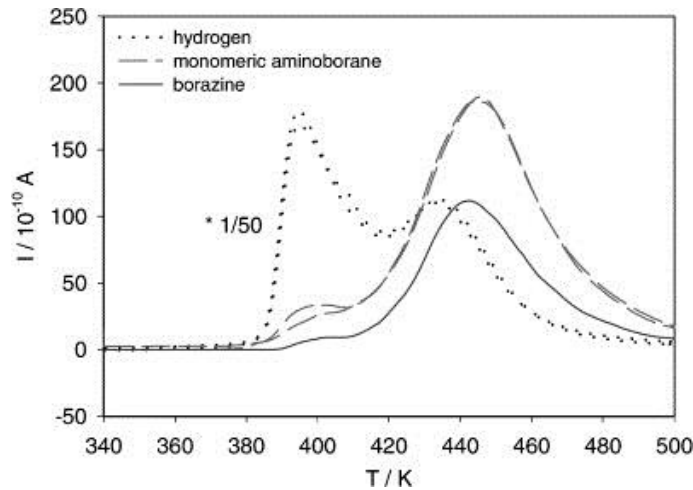


Figure 4.4: Temperature dependence of the ion intensity assigned to hydrogen (...), H₂N=BH_{2(g)} (---) and B₃N₃H_{6(g)} (—) from two different runs at 5°C/min (the figure is taken from ref. [121]).

Stowe et al. [120] proposed a mechanistic model for the first decomposition step of NH₃BH₃ at 88°C based on ¹¹B MAS-NMR studies. It consists of three principal steps: (i) an induction period leading to a mobile phase denoted NH₃BH₃*, (ii) nucleation and formation of the diammoniate of diborane (DADB) [(H₃N)₂BH₂][BH₄] and (iii) growth releasing H₂ through a reaction between DADB and NH₃BH₃ (**Figure 4.5**).

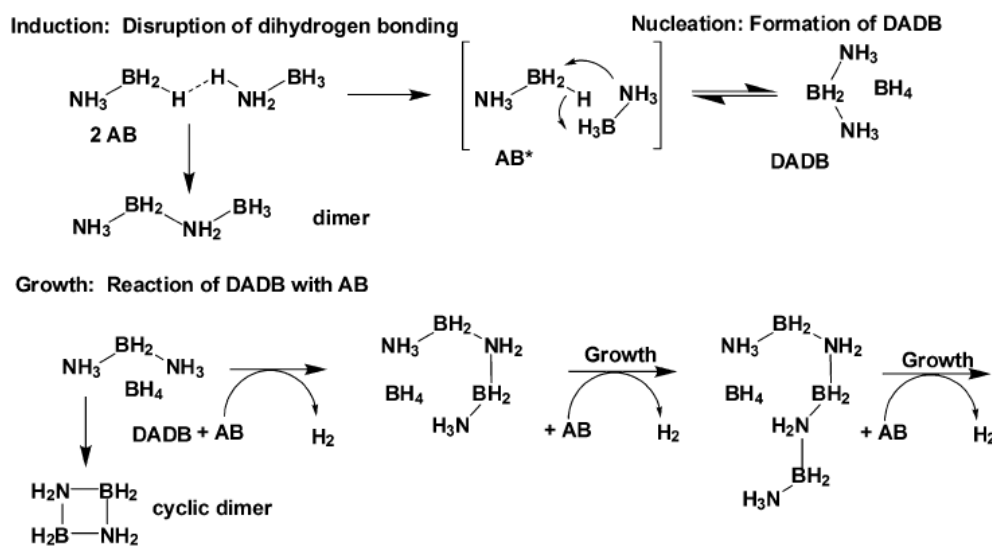


Figure 4.5: Mechanism of the release of the first mol H₂ of NH₃BH₃ at T=88°C. AB denotes ammonia borane NH₃BH₃ (the figure is taken from ref. [120]).

The thermal decomposition of NH₄BH₄ at 50°C yields DADB. The decomposition goes through the formation of NH₃BH₃ according to reactions (4.6) and (4.7) [10]. This

finding could be considered as an evidence of the formation of DADB intermediate from the thermal decomposition of NH_3BH_3 .



DADB is nowadays accepted as a borohydride salt $[(\text{H}_3\text{N})_2\text{BH}_2]^+[\text{BH}_4]^-$ [110, 125] after an ambiguity with $[\text{NH}_4]^+[(\text{BH}_3)_2\text{NH}_2]$ [126] and $[\text{NH}_4]^+\text{BH}_2\text{NH}_2[\text{BH}_4]^-$ [127]. The crystal structure of DADB can be described within the space group $I4/mcm$. Each BH_4^- tetrahedron is disordered between two orientations related by 90° rotation, as in the room temperature structure of NaBH_4 . There are two crystallographic distinct sites of BH_4^- which coordinate differently with neighboring $(\text{NH}_3)_2\text{BH}_2^+$ ions [128]. DADB undergoes solid-phase decomposition without melting and free of foaming with no appreciable induction period unlike NH_3BH_3 which has a long induction period for more than 10 h [128, 129].

Several strategies have been developed to improve the thermal dehydrogenation of NH_3BH_3 . For example, heating NH_3BH_3 in an ionic liquid as 1-butyl-3-methylimidazolium eliminates completely the induction period and enhances the rate and the extent of H_2 release [130, 131]. The pre-heating of NH_3BH_3 at 80°C for 2-4 h [132] or the use of chemical additives as DADB or ammonium chloride (NH_4Cl) reduce significantly the induction period. NaBH_4 additive has no significant role [133]. Catalytic activities using strong Lewis and Brønsted acids [116], basics [134, 135] and metal catalysts [136, 137, 138, 139] have been also widely investigated.

4.1.3 Confinement of NH_3BH_3 in porous scaffolds

One approach for a better handling of NH_3BH_3 consists of its incorporation in a porous framework. Confining NH_3BH_3 into a mesoporous graphitic carbon nitride (MGCN) improves the hydrogen release reaction afforded by the basic catalytic sites of the MGCN [140]. Mesoporous silica SBA-15 loaded with NH_3BH_3 lowers the activation barrier of H_2 release due to the catalysis activity of SiO-H groups within the silica scaffold [141]. Another example is the infiltration of NH_3BH_3 in silica hollow nanospheres SHNS, where new interactions of the type $\text{SiO-H}\dots\text{H-B}$ result in a remarkable decrease of the onset temperature of H_2 release

(70°C) [142]. Metal-organic framework MOF embedded with NH₃BH₃ offers also a relatively low operational temperature and a suppression of unwanted gas particularly NH₃ [124].

One approach for a better handling of hydridic materials consists of the re-crystallization of the salt in a geopolymer type matrix. Geopolymers are “inorganic polymers” possessing a mostly amorphous to semi-crystalline three-dimensional aluminosilicate framework. SiO₄ and AlO₄ tetrahedra are linked by oxygen bridges via sialate (Si-O-Al) and/or siloxo (Si-O-Si) bonding. Negative charges on tetrahedral sites are generally compensated with alkali cations (typically Na⁺ and /or K⁺). The structure is generally expressed by M_n[-(SiO₂)_z-Al₂O₃]_n.wH₂O where M is the alkaline cation, n is the degree of polycondensation, z is 1, 2, 3 or more and w is binding water [143]. Geopolymer technology is intended for sustainable concrete industry and green buildings. The geopolymer exhibits comparable performance to traditional concrete with a much smaller CO₂ footprint with the main advantage of consumption of industrial wastes that are produced in every country including mining, metallurgical, municipal, construction and demolition [27, 144]. NaBH₄ [24, 25, 38] and NH₃BH₃ [26] have been readily confined in geopolymer host matrices. The NaBH₄-geopolymer composite can be optimized releasing up to 80 % of the amount obtained for pure NaBH₄ [25]. In this thesis, preliminary results of the NH₃BH₃-geopolymer composite including its stability and dehydrogenation mechanism are presented and compared when necessary to NH₃BH₃ and NaBH₄ salts.

4.2 Results and discussion

4.2.1 Characterization of NH₃BH₃ and NH₃BH₃-G by XRD, SEM/EDX and IR

The synthesis of NH₃BH₃-G is described in details in chapter 2. Two syntheses batches were made. The corresponding obtained products are denoted NH₃BH₃-G1 and NH₃BH₃-G2, respectively. For NH₃BH₃-G2, NH₃BH₃-aluminate and NH₃BH₃-silicate solutions were longer stirred.

XRD

The XRD patterns of NH₃BH₃-G1 and NH₃BH₃-G2 are shown in **Figure 4.6**. All main reflections of NH₃BH₃ are also seen for NH₃BH₃-G. For both NH₃BH₃-G1 and NH₃BH₃-G2,

some additional reflections of low intensities are observed. For $\text{NH}_3\text{BH}_3\text{-G1}$, the additional peaks are assigned to minor amounts of the sodalite phase [26]. For $\text{NH}_3\text{BH}_3\text{-G2}$, the additional reflexes could be related to some decomposition of NH_3BH_3 due probably to the longer stirring time of $\text{NH}_3\text{BH}_3\text{-silicate}$ and $\text{NH}_3\text{BH}_3\text{-aluminate}$ solutions during the synthesis.

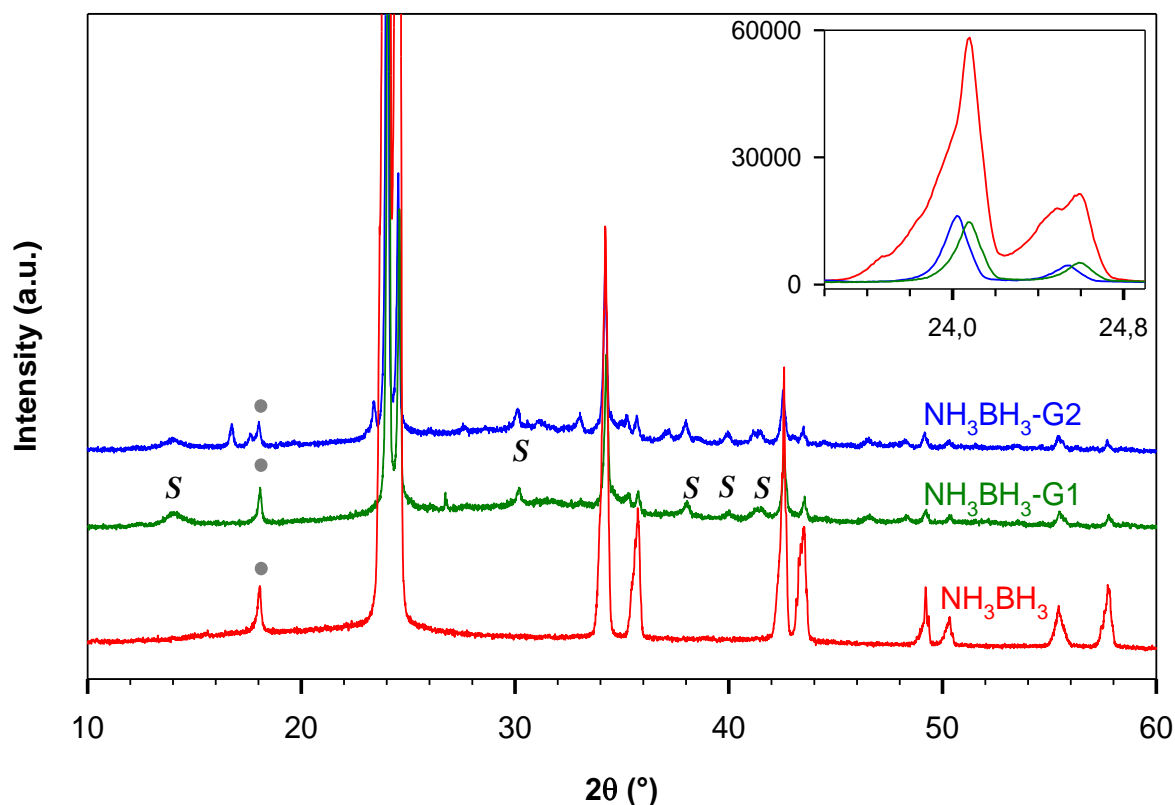


Figure 4.6: X-ray powder diffractograms of $\text{NH}_3\text{BH}_3\text{-G1}$ (green) and $\text{NH}_3\text{BH}_3\text{-G2}$ (blue). X-ray pattern of NH_3BH_3 is also shown for comparison. Inset graph is zoomed for the two main indexes between 23 and $25^\circ 2\theta$. S denotes the peaks indexed to sodalite phase. Circles indicate the peaks due to the sample holder. (Bruker D8, $5\text{-}90^\circ 2\theta$, step width of $0.01^\circ 2\theta$ and 12 s/step).

The broad bump between 20 and $40^\circ 2\theta$ centered about $30\text{-}32^\circ 2\theta$ is attributed to the geopolymer formed by the condensation of siloxo (Si-O-Si) and sialate (Si-O-Al) units by mixing the aluminate and silicate solutions [25].

The as-received NH_3BH_3 exhibits asymmetric peaks whereas for $\text{NH}_3\text{BH}_3\text{-G}$ the distribution tends to more symmetrical profile as shown in the inset of **Figure 4.6**. This indicates that the morphology of NH_3BH_3 crystals is improved upon its re-crystallization within the geopolymer.

SEM/EDX

Typical SEM pictures of NH₃BH₃ and NH₃BH₃-G using a magnification of 4000 and 10000, respectively, are displayed in **Figure 4.7**.

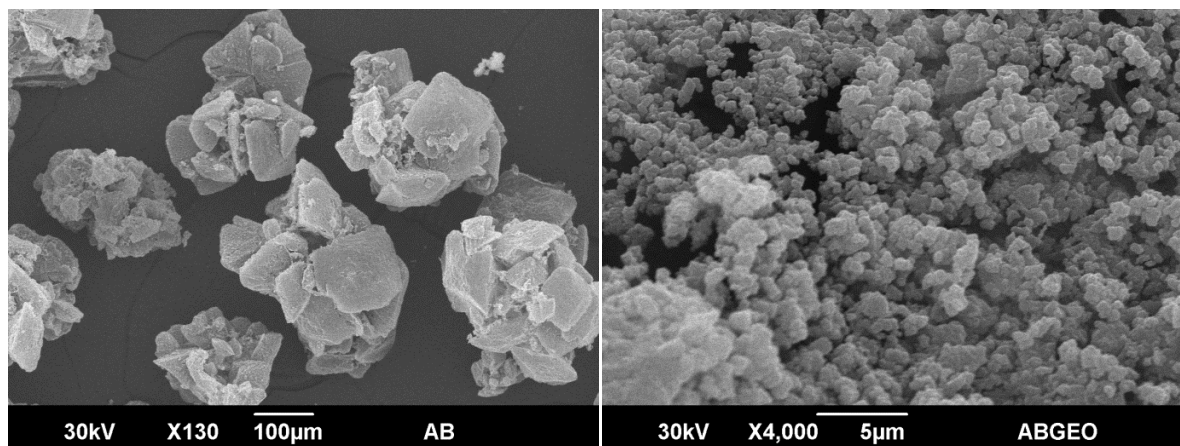


Figure 4.7: SEM pictures of NH₃BH₃ (left side) and NH₃BH₃-G1 (right side)

NH₃BH₃ crystals appear as birefringent elongated laths. The higher magnification was necessary for NH₃BH₃-G sample since the typical particle size was much finer distributed compared to those of the as-received NH₃BH₃ sample. This could be related to the dissolution and re-crystallization processes. For NH₃BH₃, only B and N were obtained by EDX analysis, whereas for NH₃BH₃-G very strong signals for Si, Al, and Na were seen compared to some weak identifications of B and N. This shows that NH₃BH₃ crystals are well covered by the geopolymer.

IR and Raman

IR and Raman spectra of the as-received NH₃BH₃ are shown in **Figure 4.8**. The vibrational spectrum of the room temperature tetragonal phase of NH₃BH₃ can be understood based on the symmetry of the free molecule. Isolated NH₃BH₃ molecule has C_{3v} symmetry. The irreducible representation is 5A₁+A₂+6E and corresponds to 18 degrees of freedom. Twelve of these are unique vibrational frequencies and 11 are both Raman and IR active [145, 146].

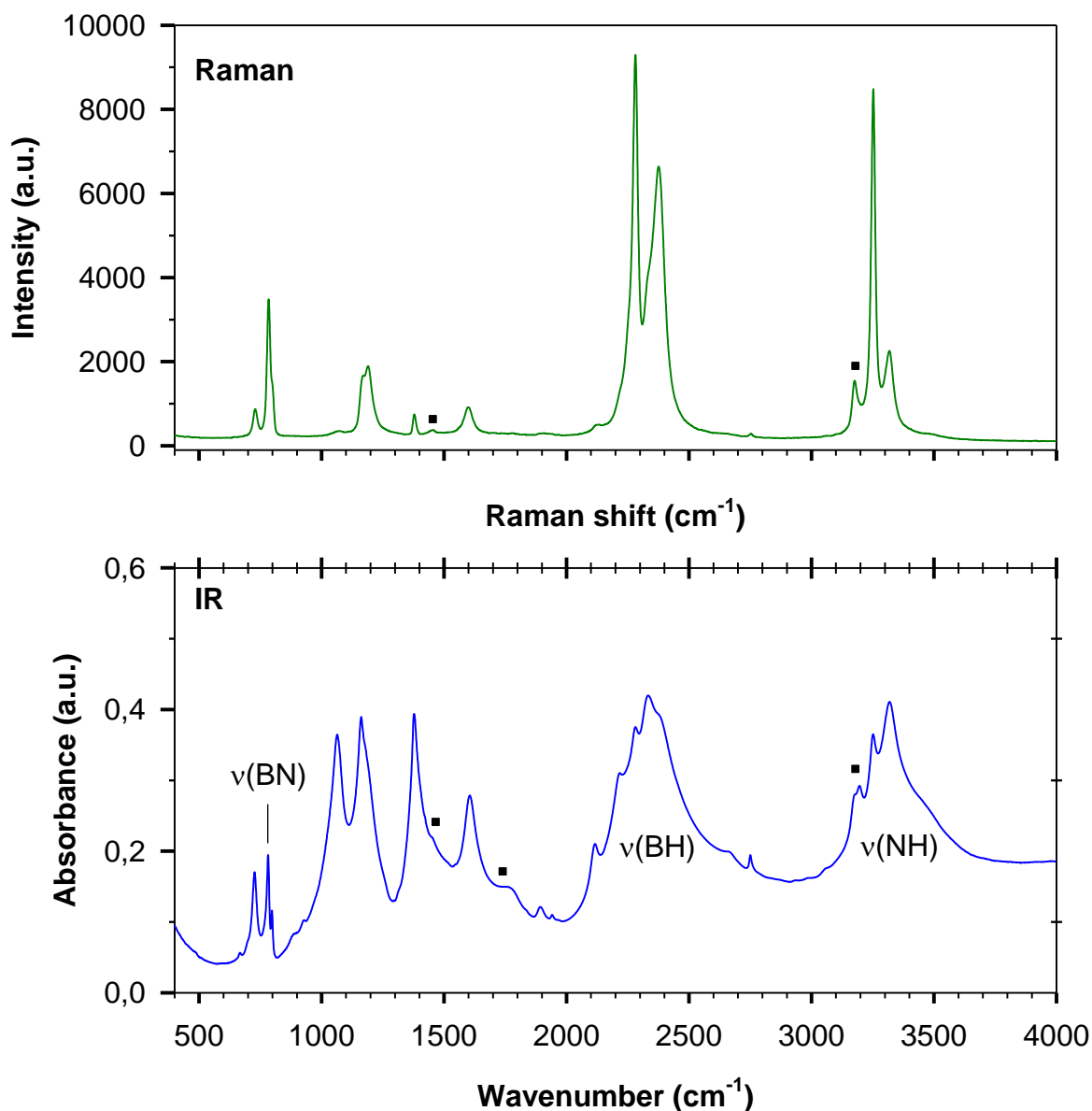


Figure 4.8: IR and Raman spectra of as-received NH_3BH_3 . Squares denote unassigned bands (see text for more clarifications).

The IR and Raman spectra of NH_3BH_3 could be divided into five regions: the lattice region at $50\text{-}600\text{ cm}^{-1}$ (not considered in this thesis), the B-N stretching, BH_3/NH_3 deformations and NBH rocking region at $700\text{-}1650\text{ cm}^{-1}$, the B-H stretching region at $2100\text{-}2600\text{ cm}^{-1}$ and the N-H stretching region at $3000\text{-}3500\text{ cm}^{-1}$. Similar descriptions can be made for the IR and Raman peaks at similar frequencies.

The IR and Raman fundamentals are summarized in (**Table 4.1**). The obtained results are in good agreement with previous works [147, 148, 149, 150].

Table 4.1: IR and Raman fundamentals of NH₃BH₃

IR (cm ⁻¹)	Raman (cm ⁻¹)	Assignment
3318	3315	N-H asym stretch N-H (v ₇)
3250	3253	N-H sym stretch N-H (v ₁)
2377 2332		B-H asym stretch B-H (v ₈)
2280	2282	B-H sym stretch B-H (v ₂)
1605	1598	NH ₃ deformation (v ₉)
1378	1379	NH ₃ deformation (v ₃)
1178, 1162	1185, 1165	BH ₃ deformation (v ₁₀ , v ₄)
1064	1065	NBH rocking (v ₁₁)
798	797	⁽¹⁰⁾ B-N stretch (v _{5'})
782	783	⁽¹¹⁾ B-N stretch (v ₅)
727	728	NBH rocking (v ₁₂)

The vibrational spectra show unassigned bands (indicated on **Figure 4.8** using square symbols) that could be interpreted as overtones and/or combination modes. For example in the Raman spectrum, Allis et al. [151] assigned the peak at 1450 cm⁻¹ to the overtone (2v₁₂) of the low frequency rocking mode. The peak at 3176 cm⁻¹ could be explained as the result of Fermi resonance of the overtone of the NH₃ deformation mode at 1600 cm⁻¹ (v₉) and the N-H symmetric stretching fundamental [146]. These two peaks are also observed in the IR spectrum, which shows more many unassigned peaks as those at 2751 and 2116 cm⁻¹ which may be assigned to 2v₃ and 2v₁₁, respectively. The IR band at 1750 cm⁻¹ is likely a combination of lattice and internal modes [147].

The main IR bands of NH₃BH₃ are also observed for NH₃BH₃-G (**Figure 4.9**). An additional broad band centered at 980 cm⁻¹ is related to the formation of Si-O-Al groups characteristic of the geopolymer [25]. The triplicate at 726, 703 and 666 cm⁻¹ and the two peaks at 460 and 432 cm⁻¹ indicate the presence of a type sodalite phase in its earlier crystallization stage due to the low intensities of these bands [38]. The peaks around 1450 and 878 cm⁻¹ are assigned to CO₃²⁻ which results from a reaction of CO₂ of the atmosphere and the

alkaline solutions through the handling under atmospheric conditions. The large IR band between 3500 and 3600 cm^{-1} is related to the stretching vibration of OH groups. The additional shoulders at 3615, 3558 and 3538 cm^{-1} for $\text{NH}_3\text{BH}_3\text{-G2}$ are mainly due to the partial destruction of NH_3BH_3 during the synthesis in agreement with XRD data.

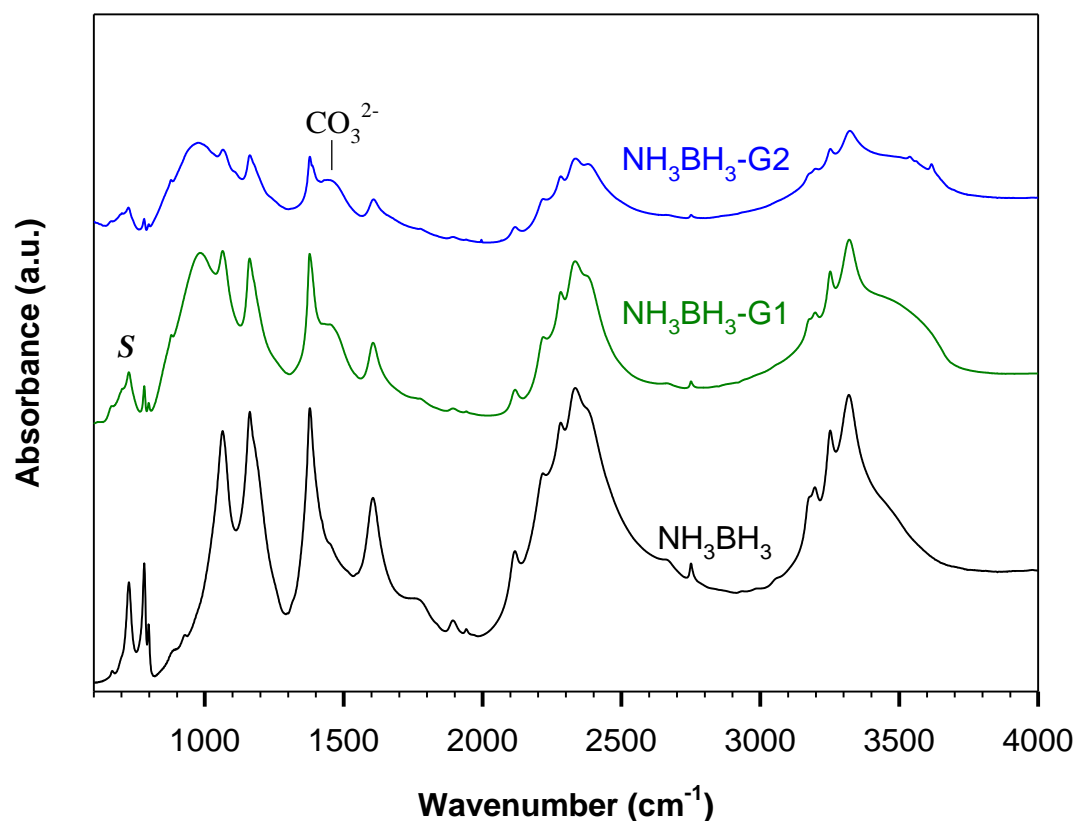


Figure 4.9: IR spectra of $\text{NH}_3\text{BH}_3\text{-G1}$ (green) and $\text{NH}_3\text{BH}_3\text{-G2}$ (blue) in comparison with NH_3BH_3 (black). S denotes the IR triplicate related to the sodalite phase.

4.2.2 Stability in neutral water

NH_3BH_3 and $\text{NH}_3\text{BH}_3\text{-G1}$ were dissolved in distilled water (50 mg sample in 1.2 ml H_2O). The obtained solutions were dried at 80°C under open conditions. After 20 h, white powders were obtained and were characterized using IR spectroscopy (**Figure 4.10**).

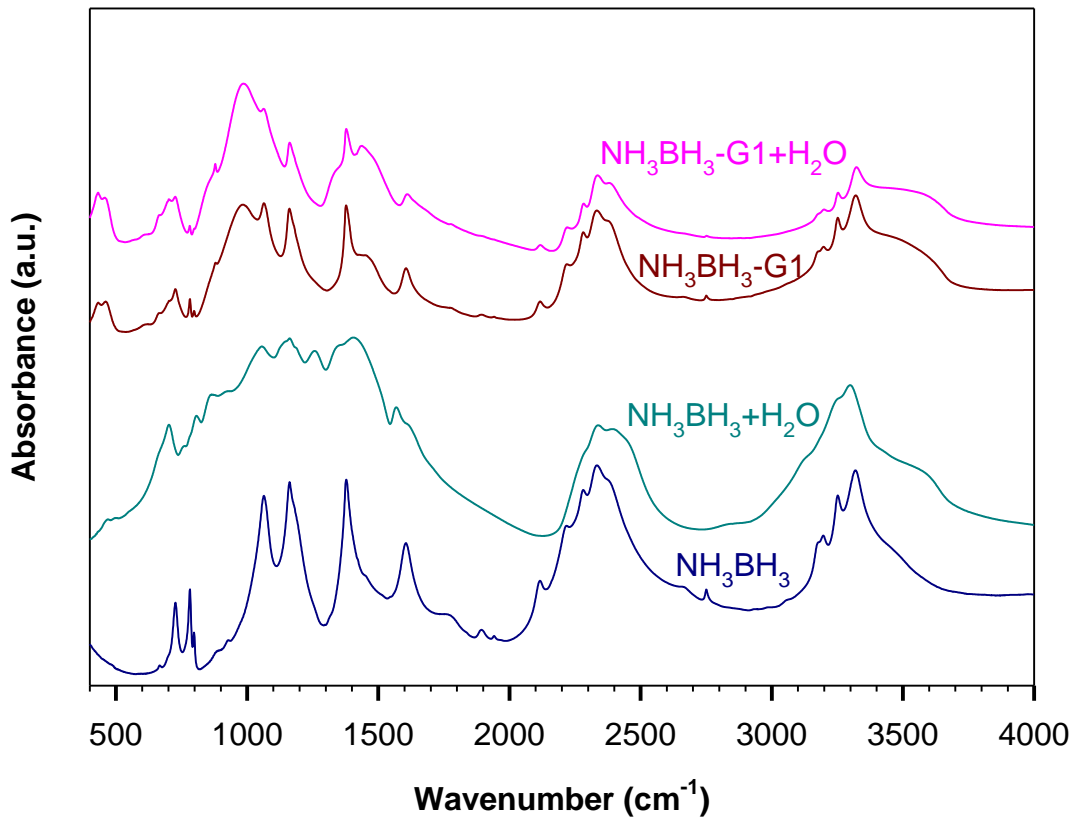
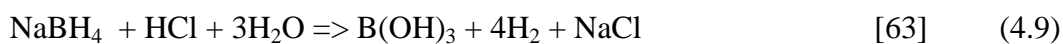


Figure 4.10: IR spectra of NH₃BH₃ and NH₃BH₃-G1 and the solid residues of their aqueous solutions dried at 80°C under open conditions for 20 h

NH₃BH₃ is totally decomposed whereas NH₃BH₃-G remains stable. This indicates that NH₃BH₃ molecules of NH₃BH₃-G composite are well covered and protected by the geopolymer.

4.2.3 Total hydrogen release using HCl solution

The amount of NH₃BH₃ re-crystallized within the geopolymer during the synthesis was evaluated considering the amount of H₂ released of NH₃BH₃-G in comparison with NH₃BH₃ salt. Acid-catalyzed hydrogen release reaction (ACHR) of NH₃BH₃ and NaBH₄ yields total decomposition with H₂ release according to reactions (4.8) and (4.9), respectively.



ACHR experiments were performed by adding diluted solutions of HCl (3 %) for series of $\text{NH}_3\text{BH}_3\text{-G2}$, NH_3BH_3 and NaBH_4 samples using the glass apparatus described in chapter 2. The results are shown in **Figure 4.11**. Regression analyses were used to predict the volume of H_2 liberated per 100 mg of the sample $V(\text{H}_2)/(100 \text{ mg sample})$. Relative errors of each single measurement and the total error of the predicted values of $V(\text{H}_2)/(100 \text{ mg sample})$ are given in **Table 4.2**.

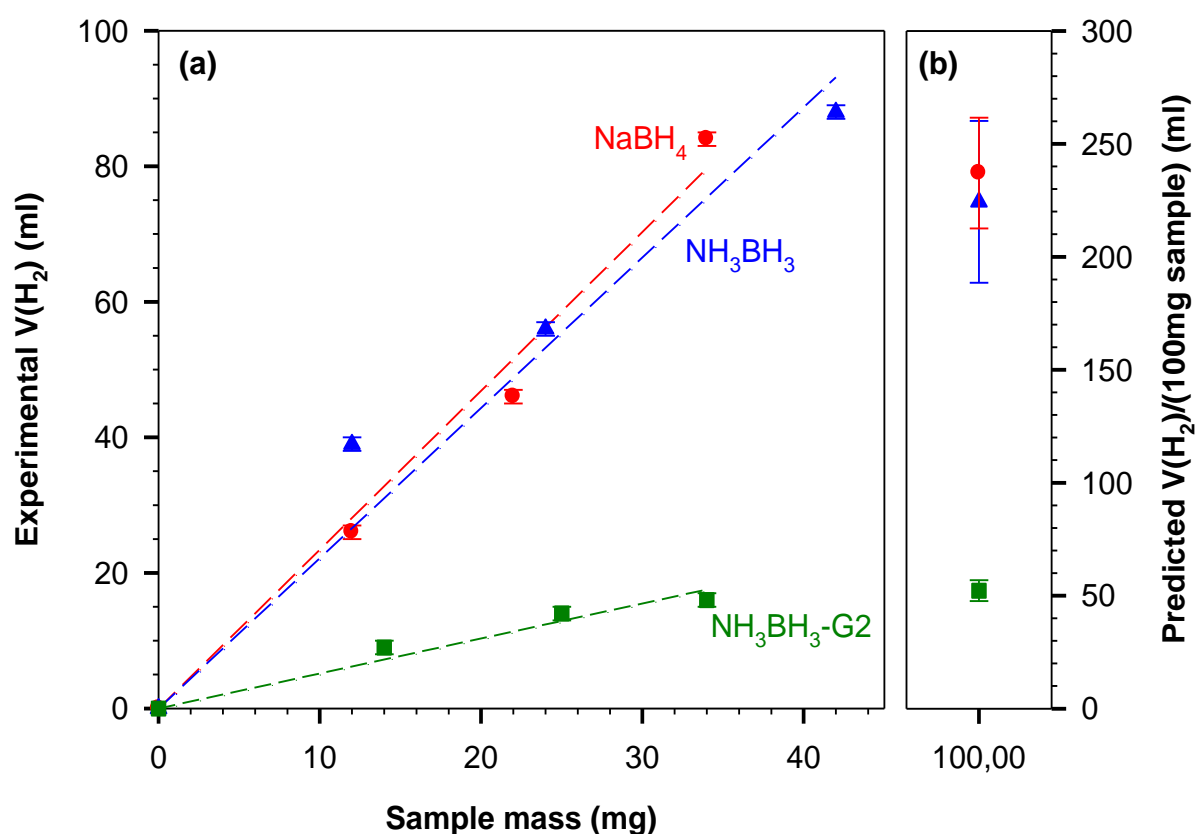


Figure 4.11: (a) Experimental values of $V(\text{H}_2)$ released as a function of sample masses used for $\text{NH}_3\text{BH}_3\text{-G2}$ (squares) in comparison with NH_3BH_3 (triangles) and NaBH_4 (circles). Dashed lines are the linear regressions. (b) Predicted values for $V(\text{H}_2)/(100 \text{ mg sample})$. Bars represent the errors calculated as described in 2.2.5.

The regression analyses predicted 224 ml H_2 per 100 mg NH_3BH_3 and 237 ml H_2 per 100 mg NaBH_4 . These values are close to those expected theoretically according to reactions (4.8) and (4.9), respectively. About 50 wt% hydrogen of NH_3BH_3 is lost in the form of NH_4^+ . For $\text{NH}_3\text{BH}_3\text{-G2}$, the analyses reveal 52 ml $\text{H}_2/(100 \text{ mg sample})$. Considering the mass ratio $\text{NH}_3\text{BH}_3/\text{solid}$ of 0.47 used in the syntheses and the fact that three mol H_2 could be released of the hydrolysis of 1 mol NH_3BH_3 (reaction 4.8), the obtained value implies that 50 % of NH_3BH_3 was effectively used for the hydrogen release reaction. For $\text{NH}_3\text{BH}_3\text{-G}$ samples with

less destruction products (as NH₃BH₃-G1 sample), at least 60 % of NH₃BH₃ is available for hydrogen release [26].

Table 4.2: ACHR of NH₃BH₃-G2, NH₃BH₃ and NaBH₄. Experimental single measurements and predicted V(H₂)/100 mg sample with the corresponding errors calculated as described in 2.2.5.

	Mass (mg)	V(HCl) (ml)	V(H ₂) (ml) (<i>experimental</i>)	relative error (<i>single measurement</i>)	V(H ₂)/(100mg sample) (<i>predicted</i>)	Absolute total error (ml)
NaBH ₄	12	2	26	0.0385	237	25
	22	2	46	0.0217		
	34	3	84	0.0119		
NH ₃ BH ₃	12	3	39	0.0256	224	35
	24	4	56	0.0178		
	42	4	88	0.0114		
NH ₃ BH ₃ -G2	14	5	9	0.1111	52	4
	25	6	14	0.0714		
	34	8	16	0.0625		

The solutions after ACHR were dried at 80°C in open conditions for 20 h. The solid residues were then characterized using IR spectroscopy. The main product was identified as boric acid H₃BO₃. Results are shown for NH₃BH₃-G2 and NH₃BH₃ samples in **Figure 4.12**. The residuals of NH₃BH₃ and NH₃BH₃-G2 show indications of NH₄Cl as can be deduced from a comparison with NH₄Cl reference spectrum. The geopolymer framework is broken in acidic medium. The mechanisms proposed for H₂ release of NH₃BH₃ in acidic solution are described in section 4.1.2 (page 76).

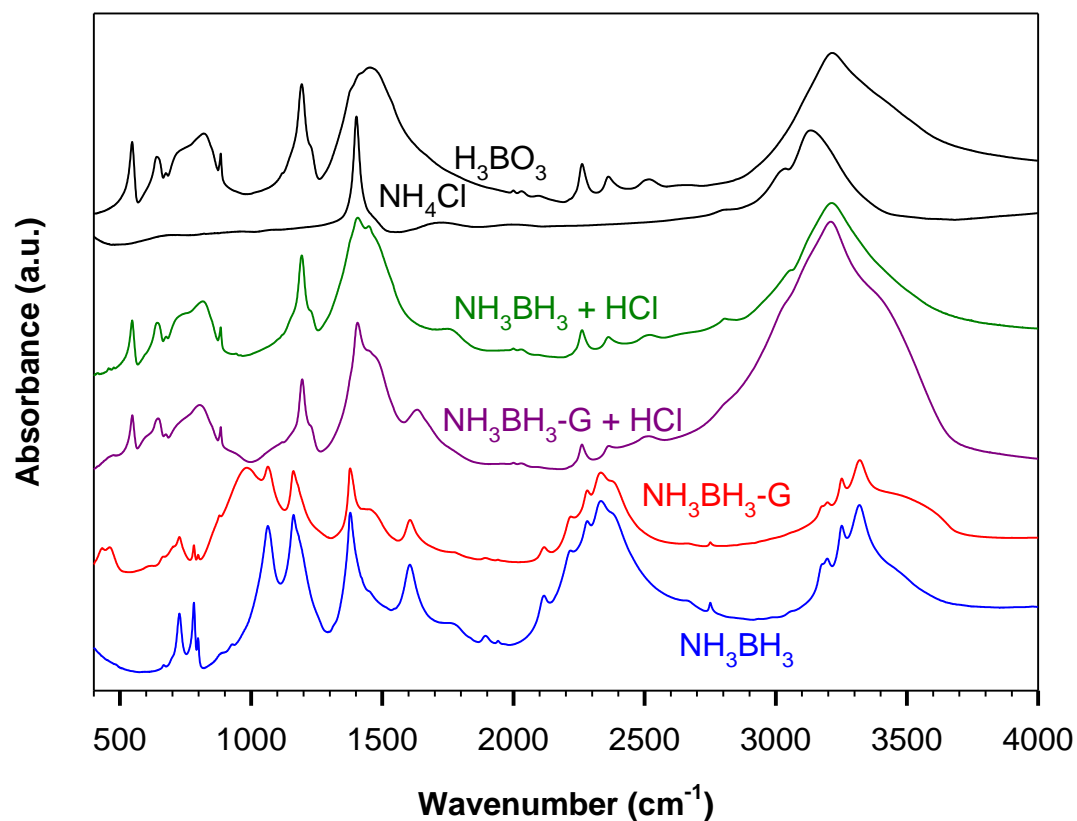


Figure 4.12: IR of $\text{NH}_3\text{BH}_3\text{-G2}$ and NH_3BH_3 and the solid residues after ACHR. IR spectra of NH_4Cl and H_3BO_3 are overlaid for comparison.

4.2.4 Alkaline solutions of NH_3BH_3 and $\text{NH}_3\text{BH}_3\text{-G}$

$\text{NH}_3\text{BH}_3\text{-G1}$ and NH_3BH_3 dissolved in a solution of sodium hydroxide NaOH (50 mg sample in 1.5 ml NaOH 1 M) reveal a total dissolution without any effervescence. The filtrates were dried at 80°C under open conditions for 18 h. The solid residues were then characterized using IR spectroscopy (**Figure 4.13**).

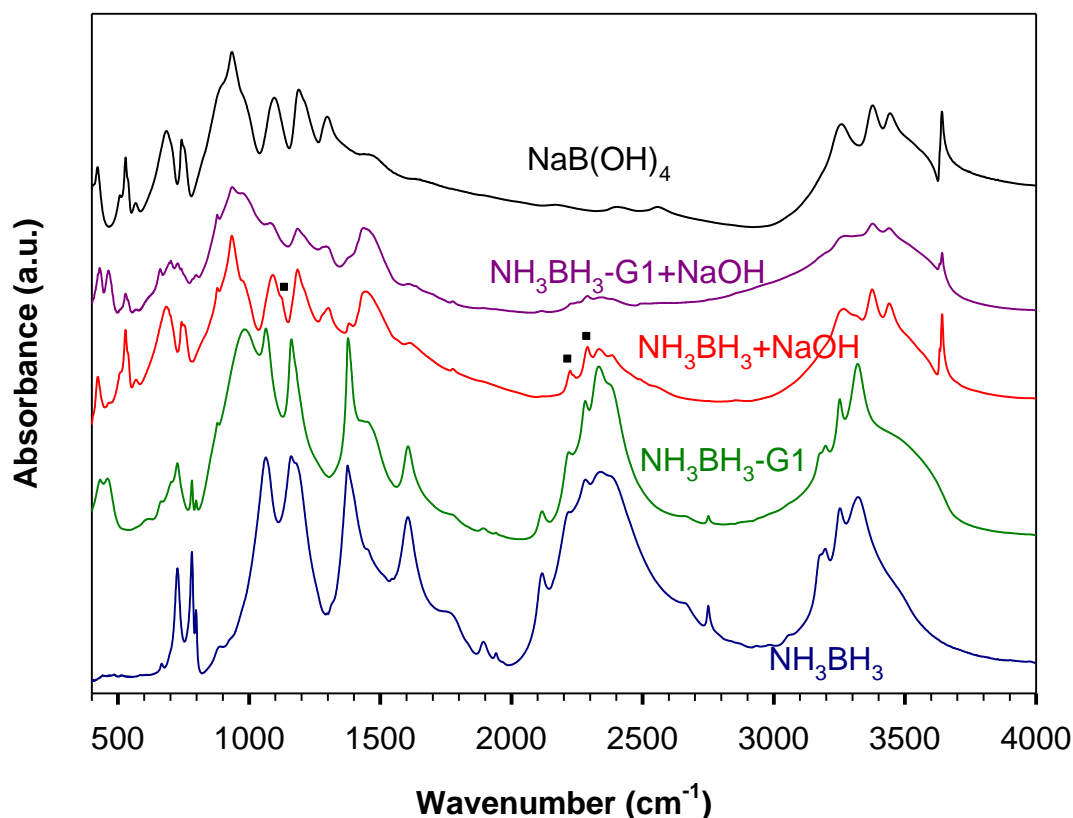


Figure 4.13: IR spectra of NH₃BH₃ and NH₃BH₃-G1 and the solid residues after treatment with NaOH solution (1M). Squares denote the IR peaks related to BH₄⁻.

The main IR bands for NH₃BH₃ and NH₃BH₃-G coincide principally with those of NaB(OH)₄. NaBH₄ is highly stable in NaOH solutions. It has been reported that NH₃BH₃ is stable in weak basic solutions [152]. In a relative strong basis solution as pyridine (C₅H₅N, pK_b=8-9), NH₃BH₃ is converted to C₅H₅NBH₃ and NH_{3(g)} [153]. This indicates an abstraction of protonic hydrogen by the solvent. Accordingly, the formation of NaB(OH)₄ could be referred to the formation of BH₃(OH)⁻ and NH_{3(g)}. BH₃(OH)⁻ is a very short-lived intermediate (see chapter 3, section 3.1.2) and could further reacts with NaOH to give NaB(OH)₄ and NaH. This is described in the scheme **a** of **Figure 4.14**.

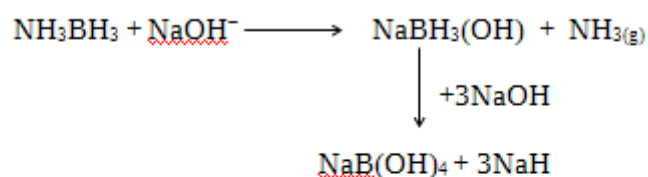
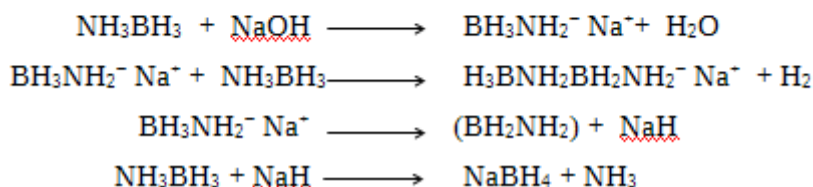
Scheme (a)**Scheme (b)**

Figure 4.14: Possible decomposition pathways for the decomposition of NH_3BH_3 in NaOH solutions

Further inspections of **Figure 4.13** show weak peaks at 1120, 2225 and 2289 cm^{-1} , which can be assigned to BH_4^- groups. The formation of BH_4^- could be referred to the reaction of NH_3BH_3 with NaOH upon drying at 80°C. Basic agents as bis(dimethylamino)naphthalene (proton sponge) [134] and Verkade's base ($\text{C}_{18}\text{H}_{39}\text{N}_4\text{P}$) [135] were shown to improve the dehydropolymerization of NH_3BH_3 at temperatures slightly higher than room temperature via the formation of intermediates of the type BH_3NH_2^- . The deprotonating agent LiNH_2 produces PAB and LiBH_4 , too [134]. Based on these results, the formation of BH_4^- in the present experiment could be interpreted by the reaction of NH_3BH_3 and NaH via the BH_3NH_2^+ intermediate. The suggested reactions are described in scheme **b** of **Figure 4.14**.

4.2.5 Aging of $\text{NH}_3\text{BH}_3\text{-G}$

The IR spectrum of $\text{NH}_3\text{BH}_3\text{-G1}$ held in closed glass bottle under standard conditions for four months is shown in **Figure 4.15**.

A partial decomposition of $\text{NH}_3\text{BH}_3\text{-G1}$ to $\text{NaB}(\text{OH})_4$ is observed. For comparison, NaBH_4 -geopolymer remained unaltered after 9 months [25]. This difference can be explained by the high stability of NaBH_4 in alkaline media compared to NH_3BH_3 .

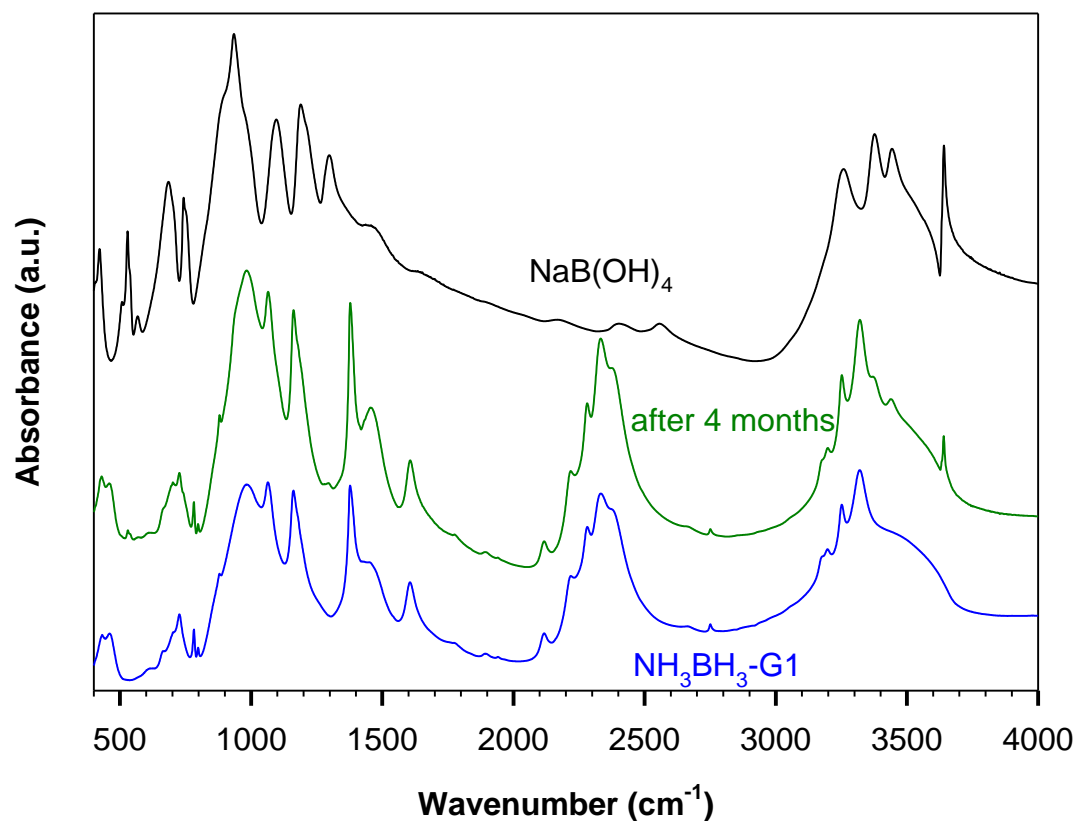


Figure 4.15: IR spectra of fresh prepared NH₃BH₃-G1 and after 4 months. IR spectrum of NaB(OH)₄ is shown for comparison.

4.2.6 Stability at 80°C

Different NH₃BH₃-G and NH₃BH₃ samples were kept in open conditions at 80°C for different times: 20, 43 and 64 h. IR spectra of the samples before and after the isotherms at 80°C are displayed in **Figure 4.16**.

NH₃BH₃ samples remain stable even after the isotherm for 64 h at 80°C. Wolf et al. [123] and Heldebrant et al. [133] detected H_{2(g)} from NH₃BH₃ within hours at 80°C. Their observations were made using principally calorimetric DSC method coupled to gas volumetric equipment, i.e. closed systems, and running under inert atmosphere. Zhang et al. [132] reported H₂ release at 80°C in less than an hour. They attributed the difference between their results and those of Heldebrant et al. [133] to the material of which the cell that holds NH₃BH₃ is made and to the pressure in the reaction chamber.

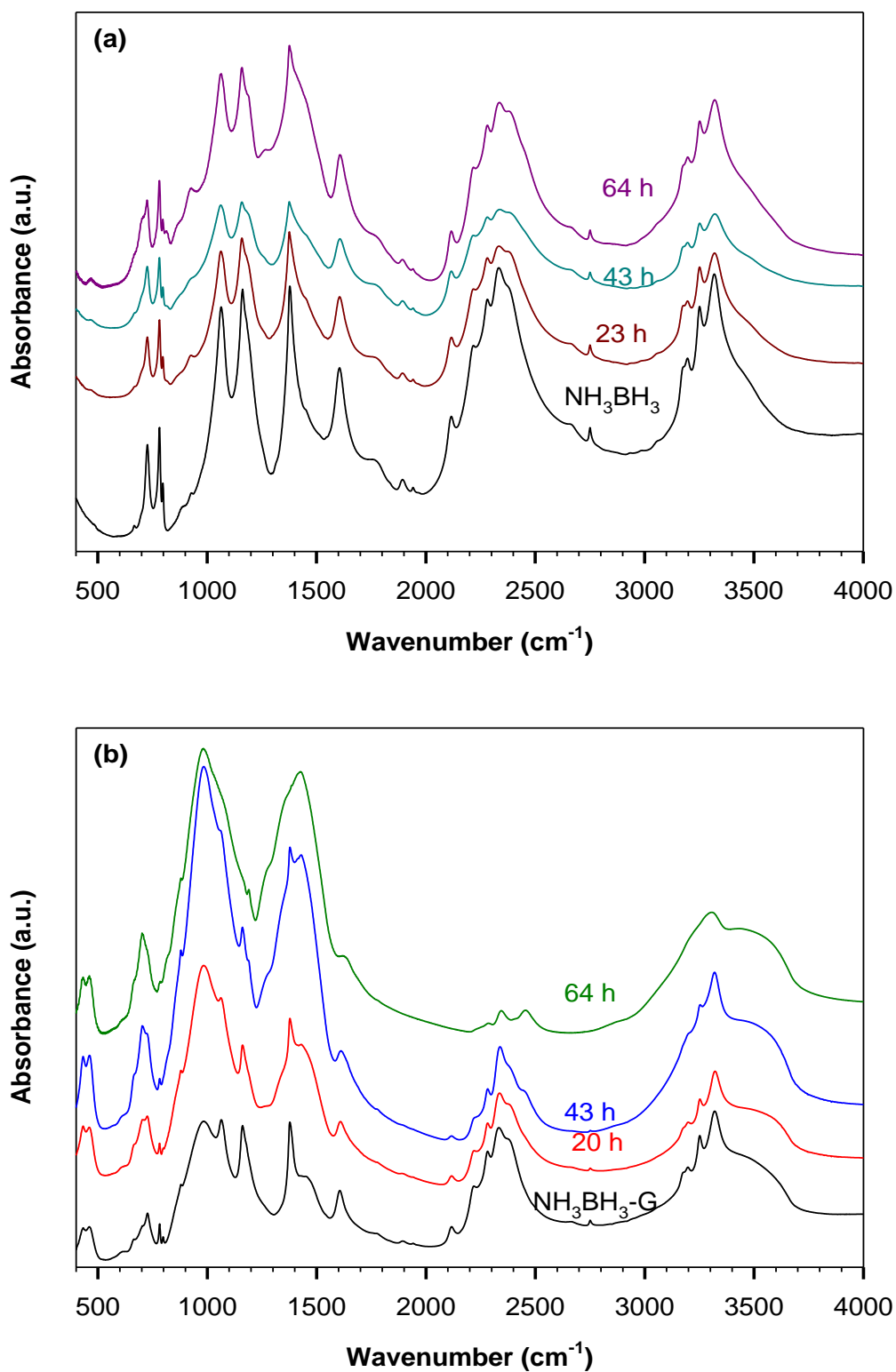


Figure 4.16: IR spectra of (a) NH_3BH_3 and (b) $\text{NH}_3\text{BH}_3\text{-G1}$ kept at 80°C under open conditions for different heating times: 20, 43 and 64 h. IR spectra of NH_3BH_3 and $\text{NH}_3\text{BH}_3\text{-G1}$ are shown for comparison.

In the present work, the different isotherms were performed under open conditions, i.e. open systems, using bottle of glass as sample holder. Further investigations are required to more explain the differences in the behavior of NH₃BH₃ at 80°C.

The IR spectrum of NH₃BH₃-G1 composite after 64 h at 80°C reveals high concentration of CO₃²⁻ due to the intense IR band at 1430 cm⁻¹. In addition, the IR spectrum shows broad IR bands and weak amount of NH₃BH₃ molecules.

4.2.7 TG/DTA analyses

TG and DTA of NH₃BH₃ and NH₃BH₃-G1 samples (pre-evacuated) were carried out to 300°C under synthetic air at 5°C/min. Results are shown in **Figure 4.17**. A voluminous swelling of the NH₃BH₃ sample near 120°C even for small sample size (2 mg) prevented the completion of the TG measurement. The DTA values for NH₃BH₃ above 120°C are only considered for qualitative analyses. This harsh aspect was suppressed for NH₃BH₃-G indicating a better handling.

For comparison, TG of NH₃BH₃ is reproduced in the inset of **Figure 4.17a** according to the results of Frueh et al. [118] using the same heating rate (5°C/min). The TG profile shows two mass loss steps which initiate near 110 and 150°C, respectively, and are accompanied by H₂ release as confirmed by mass spectrometric analyses. The total mass loss reported around 200°C is about 50 %, which greatly exceeds the theoretical value corresponding to the loss of two mol H₂ (13 %). Nonetheless, the authors were not able to detect other gas emissions due probably to the small sample size (1.5 mg). Several other authors [121, 123, 142] confirmed the evolution of other B, N-containing volatiles (H₂N=BH_{2(g)}, B₃N₃H_{6(g)}, NH_{3(g)} and B₂H_{6(g)}).

For NH₃BH₃-G1, the TG curve reveals a total mass loss of about 11.8 % at 300°C. A slight mass loss commences about 50°C and continues up to 110°C. This is estimated to be about 2-3 % and attributed to the dehydration of NH₃BH₃-G1. Afterwards two sharp decreases are observed in the temperature ranges 110-130 and 135-170°C and are accompanied with mass losses of 4 and 3 %, respectively. These coincide with the two exothermic peaks on the DTA curve centered at 120 and 155°C confirming the release of the first and the second mol H₂, respectively.

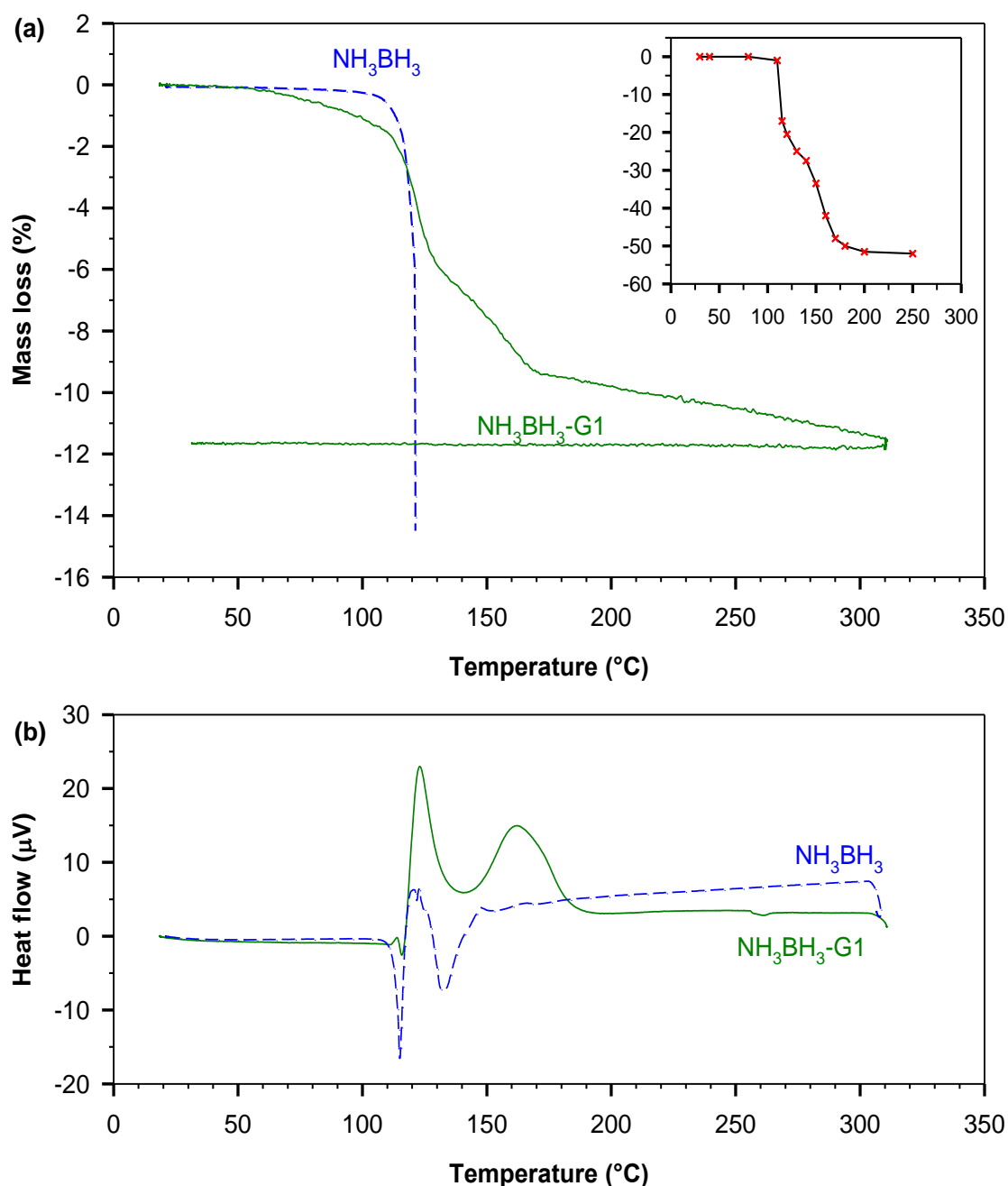


Figure 4.17: (a) TG and (b) DTA results of NH_3BH_3 (dashed blue line) and $\text{NH}_3\text{BH}_3\text{-G1}$ (solid green line). The inset graph reproduces TG results of NH_3BH_3 according to Frueh et al. [118].

Assuming the mass ratio $\text{NH}_3\text{BH}_3/\text{solid}$ of 0.47 used in the synthesis and that according to ACHR method at least 65 % of NH_3BH_3 is effectively embedded in the geopolymer [26], a minimal loss of 4 % is expected for the release of two mol hydrogen, the first and the second one. This suggests a significant suppression of unwanted B, N-containing volatiles for $\text{NH}_3\text{BH}_3\text{-G1}$ sample. Further elemental analyses of the gas phase are highly recommendable to confirm this result.

For NH₃BH₃, the two exotherms on the DTA curve about 120 and 130°-150°C are assigned to the release of the first and the second mol H_{2(g)}, respectively. The first exotherm is preceded by a crossover into an endotherm peaked at about 115°C. The sharp decrease is referred to the melting of NH₃BH₃. For NH₃BH₃-G1, the endothermic effect of the melt is less significant. The corresponding DTA curve shows a weak but significant exothermic effect, which becomes interrupted by a small endothermic peak before a steep exothermic peak evolves. That is to say, the heat desorbed during the first exotherm offsets the heat required for NH₃BH₃ melting indicating that hydrogen release from NH₃BH₃-G1 sample starts before the melt occurs, at slightly lower temperature compared to NH₃BH₃.

4.2.8 TIR using KBr matrix

TIR spectra of NH₃BH₃ and NH₃BH₃-G1 using KBr matrix during the heating run to 400°C are shown in **Figure 4.18**.

Near 130°C, the absorbance cross section of NH₃BH₃/KBr pellet increases abruptly. This is due to the melting of NH₃BH₃ as can be recognized by the disappearance of the B-N stretching mode at 780 cm⁻¹. It is also observed that this effect is accompanied by the appearance of B-H modes at 1123, 2221, 2287 and 2380 cm⁻¹ which could be assigned to BH₄⁻ substituted for Br⁻ in KBr [91, 92]. The BH₄⁻ anions persist in the pellet even at 400°C, the highest temperature reached in this experiment. The origin of BH₄⁻ anions is discussed later. Next to the IR bands of BH₄⁻, the IR spectrum at 150°C indicates the formation of a B, N(H)-polymer involving principally single bonds between B and N as can be concluded from the broad N-H stretching band centered at about 3200 cm⁻¹, the NH₂ deformation mode at 1562 cm⁻¹ and the IR peak at 1400 cm⁻¹ [118, 154, 155] (the denotation B, N(H) is usually used to describe a polymer formed of alternating B and N atoms which may carry one or two hydrogen atoms).

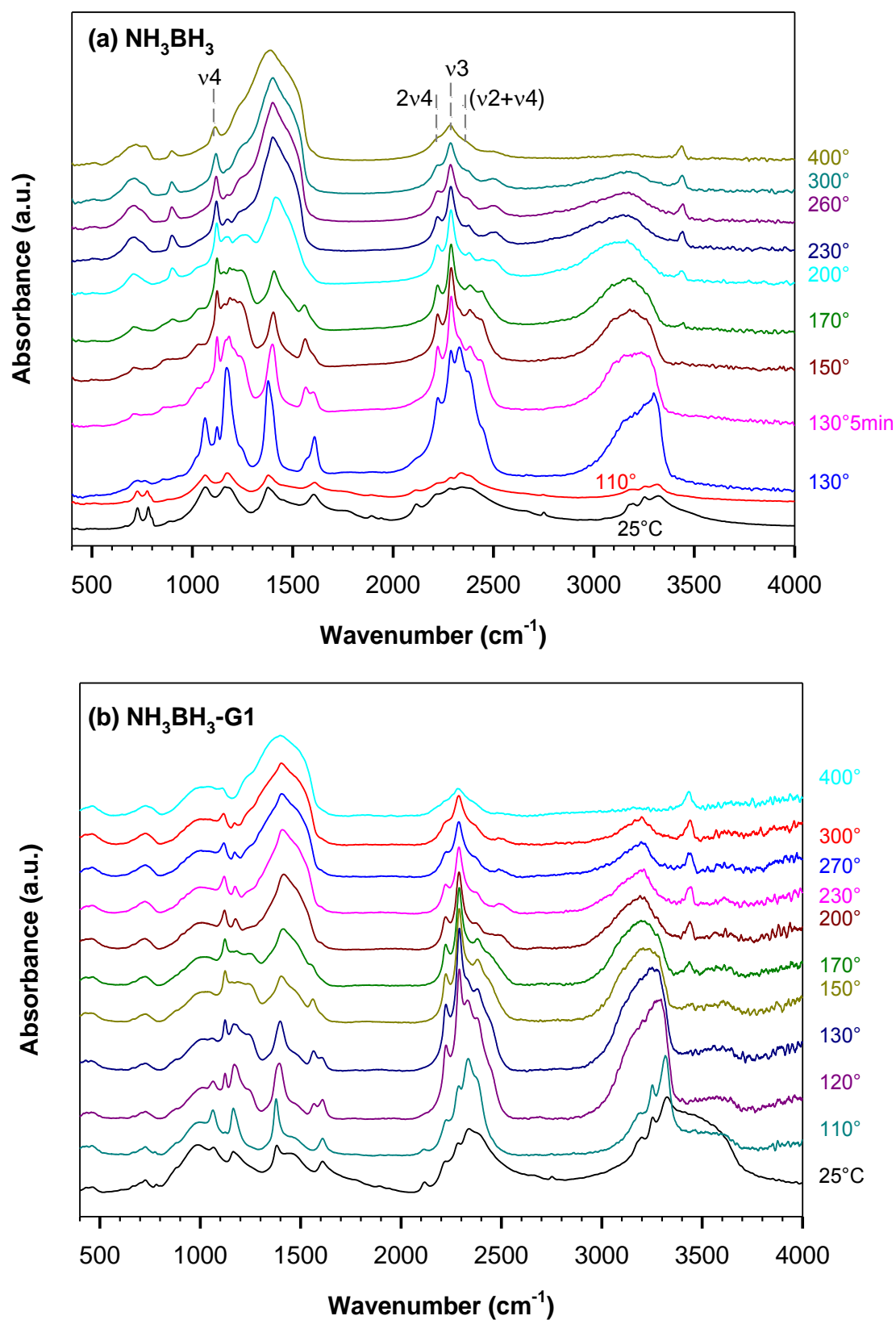


Figure 4.18: TIR spectra of (a) NH_3BH_3 and (b) $\text{NH}_3\text{BH}_3\text{-G1}$ in KBr matrix in the heating run to 400°C . IR modes of BH_4^- are indicated.

Above 200°C, new NH and BH stretching frequencies appear at higher wavenumbers, 3435 and 2500 cm⁻¹, respectively, indicating the formation of a more condensed structure containing B double bonded to N [118].

For NH₃BH₃-G, most water enclosed in the pores becomes desorbed at 120°C. The changes in the TIR spectra of NH₃BH₃-G upon annealing are very similar to those of NH₃BH₃ suggesting a similar thermal decomposition for both materials. Nonetheless, the BH₄⁻ peak at 1120 cm⁻¹ (ν₄) appears at about 110-120°C in the case of NH₃BH₃-G, a lower temperature compared to NH₃BH₃ (130°C).

The observations of B, N(H)-polymers with single and double bonds between B and N about 120-130 and 160°C, respectively, can be taken as indirect proof of the evolution of hydrogen in two consecutive steps in agreement with the two exothermic peaks observed in the DTA curve of NH₃BH₃-G centered at 120 and 155°C, respectively (**Figure 4.17**). In order to further investigate the release of hydrogen, nitrate tracer experiments were conducted as in-situ measurements in TIR. Particularly interesting are the profound spectral changes between 100 and 150°C. TIR spectra in presence of NaNO₃ tracer show principally the same variations as those without nitrate tracer, therefore only the spectral region between 600 and 1800 cm⁻¹ is presented in **Figure 4.19**.

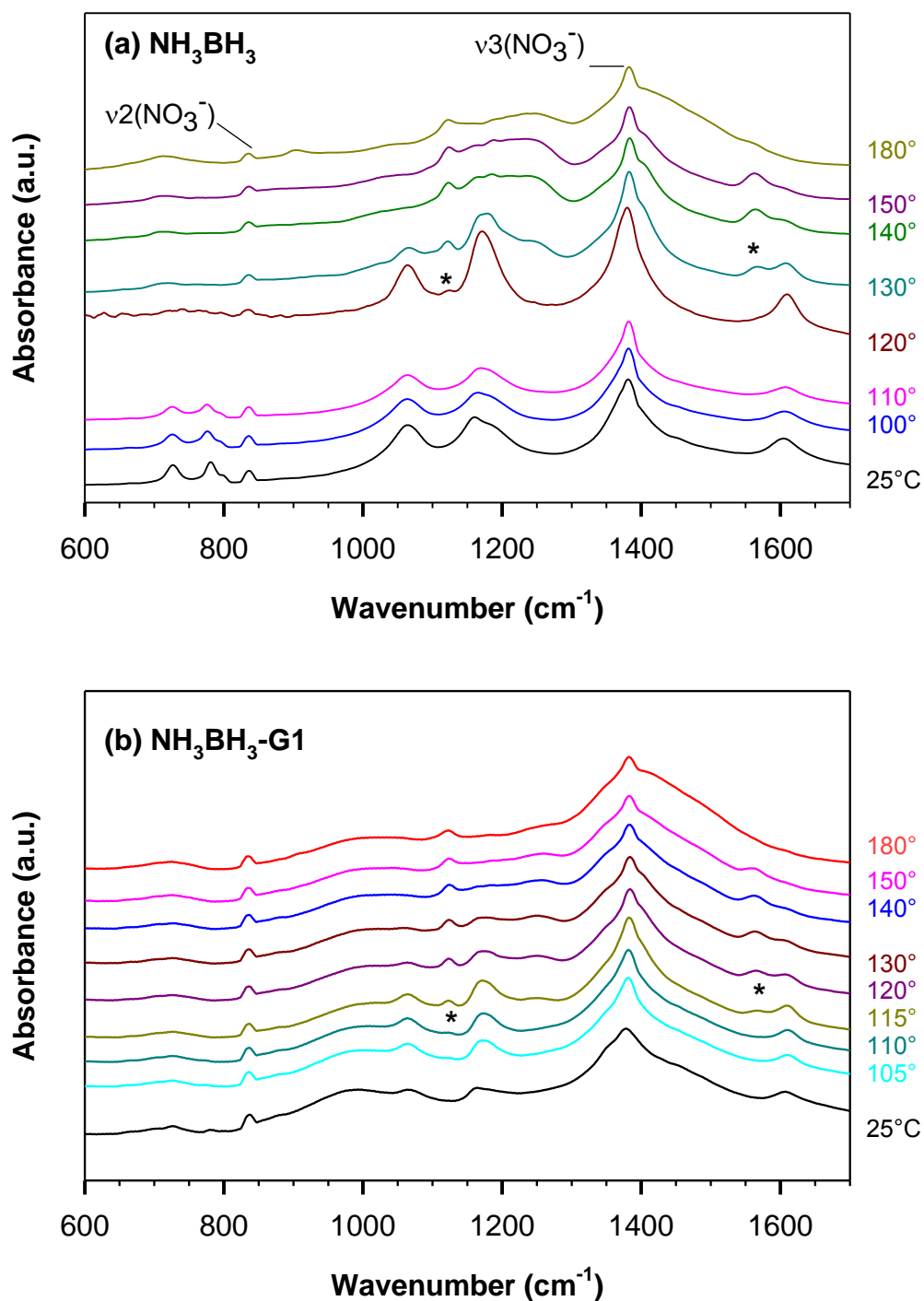


Figure 4.19: TIR spectra of (a) NH_3BH_3 and (b) $\text{NH}_3\text{BH}_3\text{-G1}$ in KBr in presence of NaNO_3 tracer from room temperature to 180°C in the spectral range between 600 and 1800 cm^{-1} . Asterisks indicate the BH_4^- peak at 1123 cm^{-1} and the NH_2 deformation mode at 1566 cm^{-1} .

The more intense peak of nitrite $\nu_3(\text{NO}_2^-/\text{KBr})$ appears at 1270 cm^{-1} [34, 39]. The absorbance of the decomposition products of NH_3BH_3 at the same frequencies as $\nu_3(\text{NO}_2^-)$ makes it difficult to identify low yield of nitrite. Therefore, the integrated intensities of

$\nu_2(\text{NO}_3^-)$ of (NH₃BH₃+NaNO₃)/KBr and (NH₃BH₃-G+NaNO₃)/KBr were followed in function of temperature in comparison with NaNO₃/KBr reference pellet. Results are shown in **Figure 4.20**.

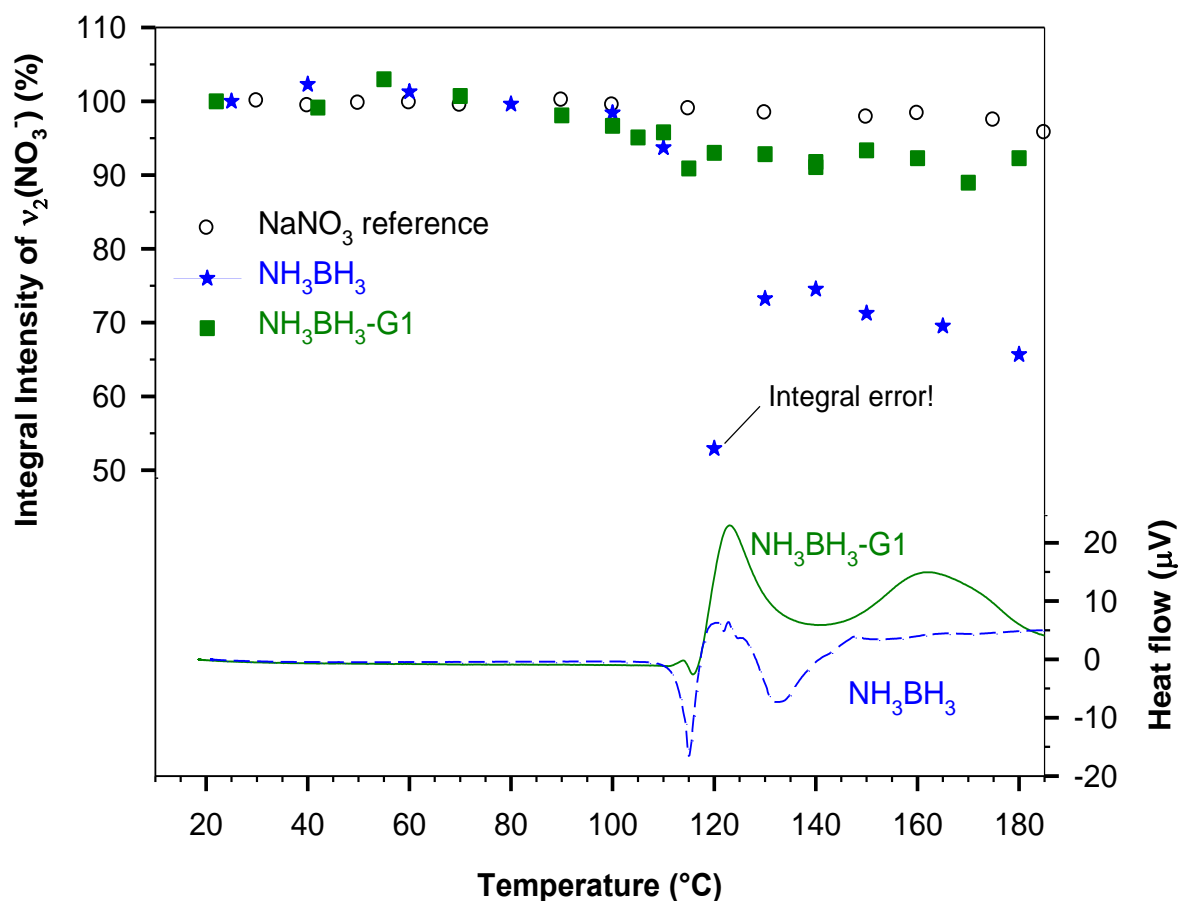


Figure 4.20: Variation of the integral intensity of $\nu_2(\text{NO}_3^-)$ of NaNO₃ tracer for NH₃BH₃ (stars) and NH₃BH₃-G (square) in function of temperature in the TIR experiments in presence of NaNO₃ tracer, in comparison to the thermal behavior of NaNO₃/KBr reference pellet (open circles). Heat flow curves of NH₃BH₃ and NH₃BH₃-G (dashed line) are overlaid for comparison.

The integrated intensities of NaNO₃/KBr are nearly the same between 20 and 180°C. For NH₃BH₃+NaNO₃, $\nu_2(\text{NO}_3^-)$ decreases clearly for $T > 110^\circ\text{C}$ with a minimum about 120°C in accordance to the first exothermic peak on the DTA curve. This experiment demonstrates also that the nitrate reduction method works as low as 110°C. The fact that the nitrate tracer method does not correlate with the second exothermic effect on the DTA curve could be referred to the fact that above 140°C the release of B, N-containing volatiles becomes more significant (**Figure 4.4**). That is to say the second mol H₂ released is “diluted” in a gas mixture containing also considerable amounts of NH₂=NH_{2(g)} and B₃N₃H_{6(g)} decreasing the

accuracy of the NaNO_3 tracer. It is worth to mention that in the case of KNO_3 tracer (*not shown*), the integrated intensities of $\nu_2(\text{NO}_3^-)$ decrease in the temperature range 100-150°C because of a structural phase transition occurring at 128°C making it not suitable to follow the release of the first mol H_2 of NH_3BH_3 .

Detailed observation of **Figure 4.19** shows that BH_4^- and NH_2 group characteristic of PAB structures are formed in $\text{NH}_3\text{BH}_3\text{-G}$ at slightly lower temperatures in comparison with NH_3BH_3 . Indeed, $\nu_4(\text{BH}_4^-)$ at 1123 cm^{-1} is detected at 110°C for $\text{NH}_3\text{BH}_3\text{-G}$ and at 120°C for NH_3BH_3 . Likewise, NH_2 deformation band at 1565 cm^{-1} is observed at about 115°C for $\text{NH}_3\text{BH}_3\text{-G}$ and at about 130°C for NH_3BH_3 . Moreover, the integrated intensities of $\nu_2(\text{NO}_3^-)$ of NaNO_3 tracer in **Figure 4.20** reveal the minima for $\text{NH}_3\text{BH}_3\text{-G}$ and NH_3BH_3 at 115°C and 120-130°C, respectively. These observations suggest a less thermal stability of $\text{NH}_3\text{BH}_3\text{-G}$ by at least 10-15°C in comparison with pristine NH_3BH_3 , which is in agreement with TG/DTA results of NH_3BH_3 and $\text{NH}_3\text{BH}_3\text{-G}$ samples.

The averaged decrease of $\nu_2(\text{NO}_3^-)$ between 110 and 180°C is about 30 % for $\text{NH}_3\text{BH}_3\text{+NaNO}_3$ sample and 8-9 % for $\text{NH}_3\text{BH}_3\text{-G+NaNO}_3$ sample. Considering the mass ratio $\text{NH}_3\text{BH}_3/\text{NH}_3\text{BH}_3\text{-G}$ of 0.47 used during the synthesis, obtained values suggest that approximately 60 % of NH_3BH_3 in $\text{NH}_3\text{BH}_3\text{-G}$ is used for H_2 release.

Comparison with NaBH_4 salt

Figure 4.21 shows the variation of the integral intensities of NH_3BH_3 , $\text{NH}_3\text{BH}_3\text{-G}$ in comparison with NaBH_4 salt for TIR using KBr matrix in presence of NaNO_3 tracer (see chapter 3, section 3.2.4 for more details about TIR of NaBH_4 in KBr in presence of NaNO_3). The integrated intensities are taken for the TIR spectra cooled down to room temperature from a given temperature since BH_4^- peaks broaden extremely at temperatures above 100°C. The thermal behavior of NaNO_3/KBr is taken as reference.

According to NaNO_3 tracer, the major H_2 release for NH_3BH_3 and $\text{NH}_3\text{BH}_3\text{-G}$ occurs between 100 and 150°C as could be concluded from the decrease of the integral intensities of $\nu_2(\text{NO}_3^-)$. Above 150°C, $\nu_2(\text{NO}_3^-)$ shows a comparable behavior to the reference pellet NaNO_3/KBr . For NaBH_4 , the nitrate tracer reveals the evolution of H_2 traces between 200 and 300°C. The decrease of $\nu_2(\text{NO}_3^-)$ becomes more significant above 300°C concurrently with the oxidation reaction of NaBH_4 to metaborate (chapter 3). That is to say, for temperatures above

200°C the H₂ release from NaBH₄ is more pronounced when compared to NH₃BH₃ and NH₃BH₃-G.

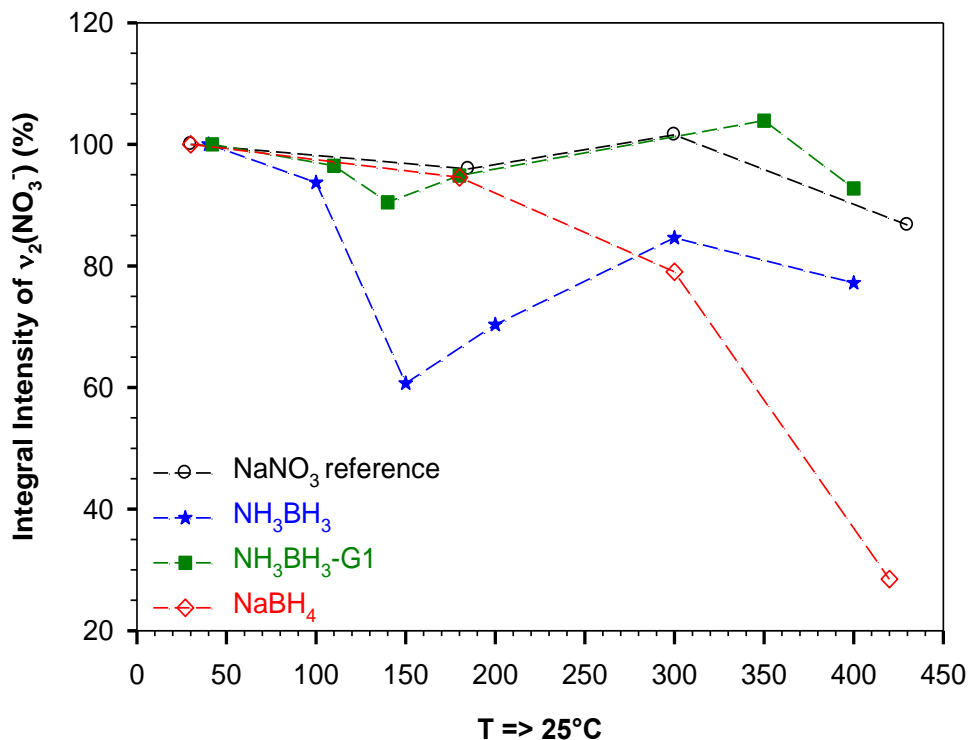


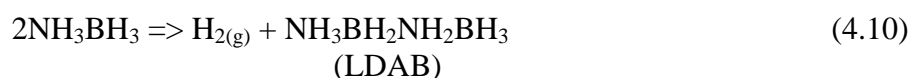
Figure 4.21: Integral intensity of $\nu_2(\text{NO}_3)$ of NH₃BH₃ (stars), NH₃BH₃-G1 (squares) in comparison with NaBH₄ (diamonds) as a function of thermal treatment temperature. $\nu_2(\text{NO}_3)$ of NaNO₃/KBr (circles) is taken as reference. Values are given for TIR spectra cooled down from temperature T as indicated (T=>RT). Dashed lines are only guide for eyes.

Further inspections of **Figure 4.21** suggest that the total amount of H₂ released from NH₃BH₃ is lower than that from NaBH₄ for the same sample size (1 mg). NH₃BH₃ releases about 6.5 wt% hydrogen pro decomposition step, whereas NaBH₄ provides a higher amount of H₂, 21.14 wt% hydrogen for the reaction $\text{NaBH}_4 + 2\text{H}_2\text{O}_{(\text{g})} \Rightarrow \text{NaBO}_2 + 4\text{H}_{2(\text{g})}$ and 10.6 wt% assuming the reaction $\text{NaBH}_4 + \text{O}_{2(\text{g})} \Rightarrow \text{NaBO}_2 + 2\text{H}_{2(\text{g})}$ (see chapter 3). Moreover, the NH₃BH₃/KBr and NH₃BH₃-G/KBr pellets lose considerable amount of hydrogen in the form of BH₄⁻ anions substituted for Br⁻ in the KBr matrix (**Figure 3.18**) reducing significantly the amount of H₂ released. The formation of BH₄⁻ is discussed in section 4.3.

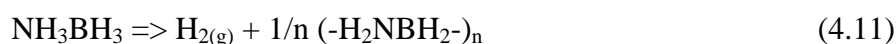
4.2.9 TIR using NaCl matrix

The role of the matrix on the thermal decomposition of NH_3BH_3 and $\text{NH}_3\text{BH}_3\text{-G}$ was checked using NaCl-pellets. TIR results are shown in **Figure 4.22**. Interestingly, there is no evidence of BH_4^- .

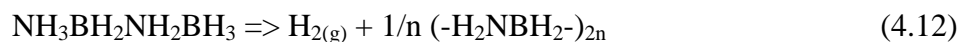
For NH_3BH_3 , at about 130°C , the absorbance cross section of the sample increases and the stretching mode of the dative B-N bond about 780 cm^{-1} disappears indicating the formation of the melt. The other IR modes of NH_3BH_3 are preserved in addition to a new weak peak at 1562 cm^{-1} characteristic of the bond bending mode of $-\text{NH}_2$ group. The spectrum differs from that of the polymeric species and could be attributed to aminoborane oligomers exhibiting short B, N(H)-chains as the linear dimer of aminoborane LDAB, $\text{NH}_3\text{BH}_2\text{NH}_2\text{BH}_3$ [132] (reaction 4.10):



Upon slight heating to 140°C , the IR bands of NH_3BH_3 disappears and new IR peaks are principally observed at 3285 and 3246 cm^{-1} for NH stretching, at 2380 and 2321 cm^{-1} for BH stretching and at 1560 cm^{-1} assigned to the NH_2 deformation mode. These coincide with the literature values reported for PAB structures [118, 122, 154, 155]. The formation of PAB structures can be described according to reaction (4.11).



Or according to reaction (4.12) considering LDAB



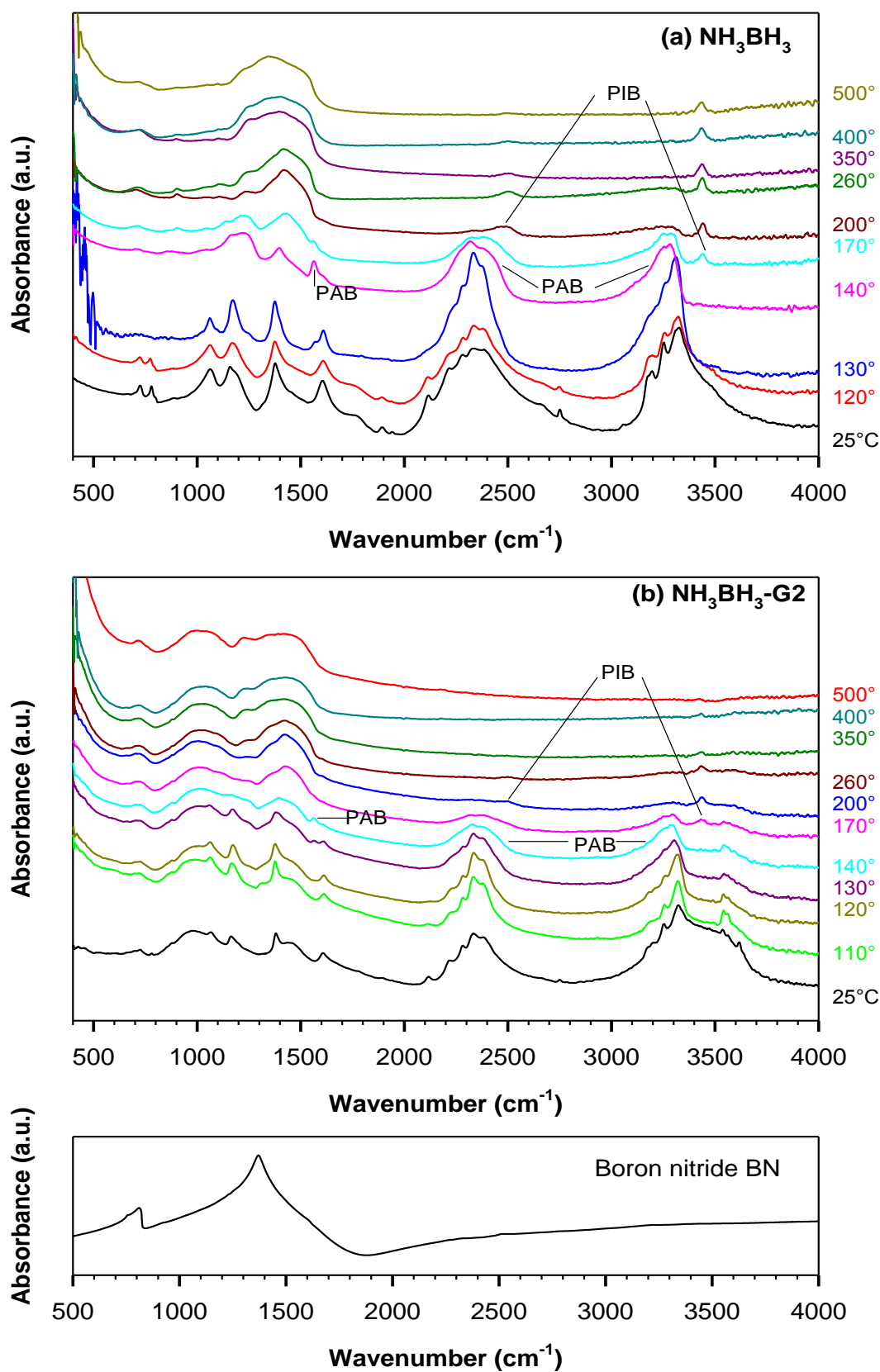
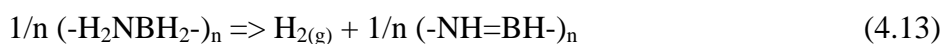


Figure 4.22: TIR spectra of (a) NH₃BH₃ and (b) NH₃BH₃-G2 in NaCl (dry) from room temperature to 500°C. (c) IR spectrum of commercial boron nitride BN, for comparison.

As the temperature further increases, NH and BH stretching modes on singly bonded N and B decrease and disappear totally around 260°C. The IR spectrum at 170°C shows NH and BH stretching modes at higher wave numbers, 3434 and 2495 cm^{-1} , respectively, which can be explained by the π -character between B and N atoms strengthening the bonds and resulting, thus, in absorbance at higher IR frequencies. These are close to those reported in ref. [118, 122] for PIB structures. Additionally, the broadening of the IR band between 1300 and 1550 cm^{-1} indicates the polymerization into a more condensed structure. The dehydrogenation of PAB to PIB can be represented according to:



TIR spectra of NH_3BH_3 -G2 in NaCl indicate that the decomposition steps and products of NH_3BH_3 -G2 are very similar to those of NH_3BH_3 . The room temperature IR spectrum of NH_3BH_3 -G2 shows additional OH stretching peaks at 3564 and 3541 cm^{-1} related probably to the partial decomposition of NH_3BH_3 during the longer stirring time of NH_3BH_3 -aluminate and NH_3BH_3 -silicate solutions during the synthesis as confirmed by X-ray diffraction. These peaks persist up to 200°C and do not show any additional effect on the thermal decomposition of NH_3BH_3 molecules.

4.2.10 Thermolysis under open conditions

The effect of heating on NH_3BH_3 -G and NH_3BH_3 to different temperatures was investigated ex-situ under open conditions. The samples were heated to 120, 120°C for 5 min, 150 and 300°C, respectively, using a heating rate of 5°C/min. End-products were pressed into KBr pellets and characterized using IR spectroscopy.

At 120°C, NH_3BH_3 melts vigorously with foaming. When heating a bit longer at 120°C (5 min) the sample forms a more voluminous soft white powder. Both sample forms, melt and soft white powder, were collected and characterized. Unlike NH_3BH_3 , the NH_3BH_3 -G1 sample does not show significant variations of the sample form at 120°C. IR results for NH_3BH_3 and NH_3BH_3 -G1 are depicted in **Figure 4.23**.

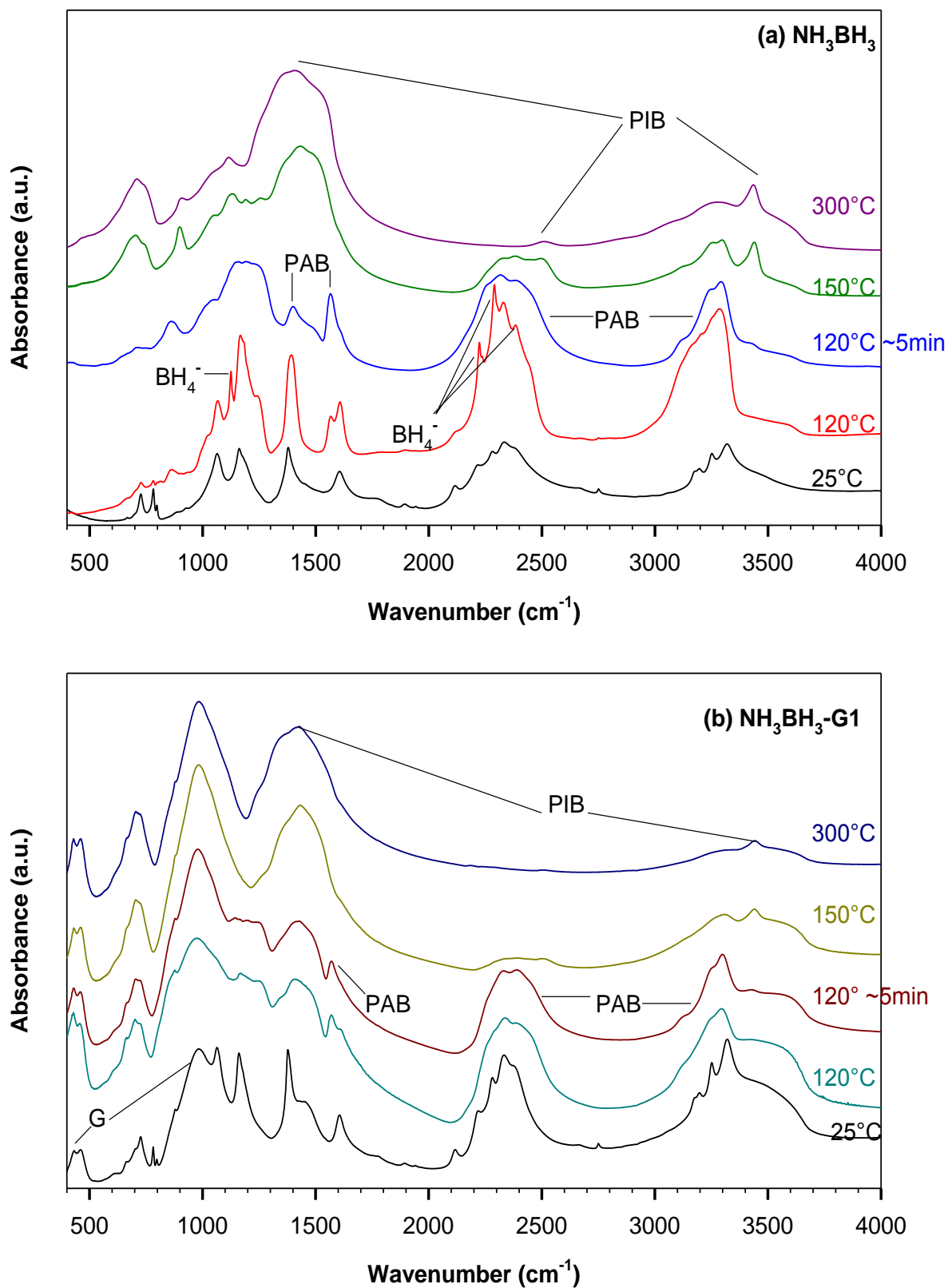
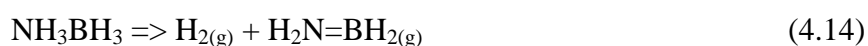


Figure 4.23: IR results of the heating of (a) NH₃BH₃ and (b) NH₃BH₃-G1 under open conditions to different temperatures as denoted. IR spectra of NH₃BH₃ and NH₃BH₃-G1 are shown for comparison.

The melt of NH_3BH_3 pressed in KBr pellets shows IR peaks of BH_4^-/KBr at 1125, 2224, 2290 and 2385 cm^{-1} . IR features of BH_4^- were also observed in TIR using KBr matrix at 120°C.

The foaming observed at 120°C could be related to the liberation of B, N-containing volatiles $\text{NH}_2=\text{BH}_2(\text{g})$ and $\text{B}_3\text{N}_3\text{H}_6(\text{g})$ according to reactions (4.14) and (4.15) [118, 121, 123], respectively .



The IR spectrum of the soft white powder produced upon slightly longer heating at 120°C (5 min) shows principally N-H stretching modes at 3293 and 2350 cm^{-1} , B-H stretching modes at 2318 and 2380 cm^{-1} and NH_2 deformation mode at 1565 cm^{-1} . These can be referred to PAB according to reactions (4.11) and (4.12).

Monomeric aminoborane $\text{H}_2\text{N}=\text{BH}_2(\text{g})$ may also polymerize to PAB [118] (4.16).



Further heating to 150 and 300°C suggest partial and nearly complete reaction to PIB (reaction 4.13) as can be deduced from the NH and BH stretching modes at higher frequencies, 3435 and 2500 cm^{-1} , respectively. The formation of PIB is accompanied by a broadening between 1300 and 1560 cm^{-1} associated to the condensation and polymerization reactions of BN bonds.

Similar decomposition products were obtained for $\text{NH}_3\text{BH}_3\text{-G1}$ samples following the same heating sequence to 120, 150 and 300°C. Handling was, however, much easier since undesired effects as evaporation, foaming and voluminous swelling of the sample observed for NH_3BH_3 do not occur for $\text{NH}_3\text{BH}_3\text{-G}$.

IR spectra of PAB and PIB obtained in the heating experiments under open conditions at 120°C 5 min and 300°C (**Figure 4.23**) are close to those obtained in TIR experiment using NaCl matrix at 140 and 260°C (**Figure 4.22**), respectively. The lower amount of BH in the IR

spectrum of PIB under open conditions compared to the TIR spectrum using NaCl matrix is due to the oxidation of B-H to B-O under air.

4.2.11 Characterization of the dehydrogenation products

The nature of PAB and PIB has not been unequivocally established due to the complexity of their structures (**Figure 4.3**). Therefore, IR spectra reported previously for PAB and PIB are not unique. IR frequencies of PAB obtained in this work are summarized in **Table 4.3** and compared to the IR frequencies of cyclotriborazane (CTB) (BH₂NH₂)₃ and other PAB like-structures as reported in the literature. In **Table 4.4**, IR frequencies of PIB obtained from TIR using NaCl matrix are shown in comparison to other possible decomposition products with unsaturated BN bonds including H₂N=BH₂, B₃N₃H₆ and PIB structures. The IR frequencies of boron nitride BN are also shown. The IR spectra of the well-established structure of aminoborane, borazine and BN are useful for the description of the IR modes of PAB and PIB structures.

Monomeric aminoborane H₂B=NH_{2(g)} is characterized principally by BN stretching mode at 1337 cm⁻¹, B-H symmetric and asymmetric stretching at 2495 and 2564 cm⁻¹, respectively, and N-H symmetric and asymmetric stretching at 3451 and 3534 cm⁻¹, respectively [156]. In the case of PAB, N-H and B-H stretching, as well as NH₂ deformations modes were unequivocally attributed to the bands in the frequency ranges 3200-3400, 2250-2400 and 1150-1600 cm⁻¹, respectively. Nonetheless, the assignment of B-N stretching frequencies was not straightforward. The peak near 1400 cm⁻¹ was labeled as the signature of BN stretching by Kim et al. [155] and Baumann et al. [122]. Ab-initio investigations on the properties and the vibrational spectra of different conformers of PAB [157] predicted the BN stretching mode at 900 cm⁻¹. The peak at 1380 cm⁻¹ was referred to the umbrella of NH₃ terminal groups, with intensity decreasing with increasing oligomer size. This finding was recently supported by Frueh et al. [118] who made the assignment basing on a comparison with IR frequencies of molecular compounds with different BN bond orders. Accordingly, they concluded the BN stretching of PAB at 850 cm⁻¹, between those of NH₃BH₃ and aminoborane.

Table 4.3: IR frequencies obtained in this work for PAB in comparison with literature values for polymers containing single bonds between B and N atoms. HEL (helical) and COIL (coiled) are two possible conformers proposed for PAB.

Ref. [122]	Ref. [157] ^a	Ref. [154] ^b	Ref. [158]	Ref. [157](HEL)	Ref. [157](COIL)	Ref. [118] ^c	Ref. [132] ^c	(BH ₂ NH ₂) ₃ [159]	PAB this work
3425-3197	3330		3320-3220	3380	3350				
		3300						3308	
	3280								3283 (b)
				3230	3250	3250	3270	3260	3253 (b)
				2400					
	2360		2380-2280		2380			2371	2381 (b)
2348		2340							
							2300		2319 (b)
						2250			
1622		1600		1620	1610				
	1550		1575			1556	1562	1562	1564 (m)
1400	1400		1405			1394			1398 (m)
		1380		1370	1380		1380		
								1236	
	1200			1200	1210			1201	1221 (b)
1182		1160					1168		1166 (b)
								1137	
						1119			
1068					1090				
		1040				1035	1036	1051	1047 (sh)
								894	
866	860	850		880		850		826	866 (w)
809, 706									

b: broad, m: medium, sh: shoulder, w: weak

^a estimated from spectra reproduction of ref. [155]

^b shoulders and some very weak peaks are not considered

^c The peaks are estimated from the spectra reproduction

For PIB, the introduction of the π -character shifts the stretching frequencies toward higher wavenumbers. The BN stretching was recorded about of 1400-1500 cm^{-1} , similarly to that of borazine. A detailed description of the IR spectrum of the gas phase of borazine $\text{B}_3\text{N}_3\text{H}_6(\text{g})$ can be found in ref. [160]. NH, BH and BN stretching frequencies appear at 3486, 2526 and 1406-1465 cm^{-1} , respectively.

Table 4.4: IR frequencies obtained in this work for PIB in comparison with literature values for compounds containing π -bonds between B and N atoms. Asterisks denote the peaks that were estimated by reproduction of the IR spectra.

Aminoborane (g) [156]	borazine (g) [160]	BN (hex) [161]	[122]	PIB [118]	PIB this work
3534					
3451	3486				3441 (b)
			3430	3435	
			3264		
2564					
2495	2520			2498	2502 (b)
			2389		
			2291		
1625			1628		
			1571		
	1465				
	1406		1405		1395 (vb)
		1390			
1337				1350	
			1203		
1131				1128*	1129 (w)
	1096				1106 (w)
			1058		
1005	990				
	917.5			914*	899 (w)
		810	871		
			820		
	719				

b: broad, vb: very broad, w: weak

Hexagonal boron nitride BN is characterized principally by two modes: the out-of-plane motion at about 800 cm⁻¹ and the in-plane motion at about 1380 cm⁻¹ (very broad) [161, 162, 163].

4.3 Summary: thermal decomposition routes of NH₃BH₃-G and NH₃BH₃ in KBr and NaCl matrices

The IR bands of BH₄⁻ anions were observed upon the first decomposition step of NH₃BH₃-G and NH₃BH₃ in TIR using KBr matrix and were stabilized up to 400°C. Some indications of BH₄⁻ were also seen in the IR spectrum of the melt isolated after heating NH₃BH₃ under open conditions to 120°C and pressed in KBr pellets. The KBr pellets of the ex-situ dehydrogenation by-products of NH₃BH₃ at 150 and 300°C do not show BH₄⁻ anions and were similar to those obtained in TIR using NaCl matrix at 140 and 260°C, respectively. This indicates the existence of a reaction-intermediate at 110-120°C upon the release of the

first mol of H_2 which may exchange BH_4^- anions with KBr matrix. This is the diammoniate of diborane $[(\text{NH}_3)_2\text{BH}_2]\text{BH}_4$ (DADB). The anionic exchange can be explained by the proximity of the ionic radii of BH_4^- (2.05 Å [164]) and Br^- (1.96 Å [165]). In the case of NaCl matrix, the anionic exchange is less favorable (Cl^- : 1.81 Å [164]). The conversion of NH_3BH_3 to DADB is a dimerization which occurs without loss of hydrogen according to reaction (4.17). It is not a labile equilibrium in the solid phase [166] and occurs very slowly at room temperature [110].



Stowe et al. [120] reported the formation of DADB intermediate during the first decomposition step of NH_3BH_3 to PAB at 88°C basing on NMR ^{11}B studies. The thermal investigations on NH_3BH_3 between 70 and 90°C of Bowden et al. [167] confirmed the formation of a mobile phase (NH_3BH_3^*) and DADB before the release of the first mol H_2 . DSC curves of isothermal treatments of NH_3BH_3 between 20 and 90°C show two exothermic effects well separated in time at 70-80°C which overlap as the temperature increases to 90°C. The mass loss occurs during the second exotherm. In the present work, the DTA curve obtained during linearly heating NH_3BH_3 at 5°C/min (**Figure 4.17**) shows a single broad exothermic effect centered at 120°C indicating that at temperatures above 100°C the two exothermic steps of Bowden et al. [167] corresponding to the formation of NH_3BH_3^* and DADB and the release of the first mol H_2 could not be distinguished anymore. TIR using NaCl matrix does not show IR features of DADB confirming that DADB is unstable at temperatures above 100°C and decomposes immediately to $\text{H}_{2(g)}$ and PAB. This agrees with previous works on the thermal decomposition of DADB [128, 129]. Therefore, the formation of DADB at 110-120°C was indirectly proved by the stabilization effect of KBr on BH_4^- anions. The anionic exchange with KBr causes a partial loss of H_2 in the form of BH_4^- . The remaining structure of the KBr-pellet at 120°C is constituted probably of $[(\text{NH}_3)_2\text{BH}_2]^+$ and/or other oligomeric/polymeric B, N(H)-species which condense above 150°C to polymeric species involving π -character between B and N atoms (**Figure 4.24**). It can be hard said whether the conversion of NH_3BH_3 to DADB is total or partial and whether H_2 is liberated from DADB or from a bimolecular reaction between NH_3BH_3 and DADB. Stowe et al. [120] suggested that once the DADB species is present in the sample, hydrogen release occurs by bimolecular reactions between the un-reacted NH_3BH_3 and the DADB yielding H_2 and PAB precursors at 88°C.

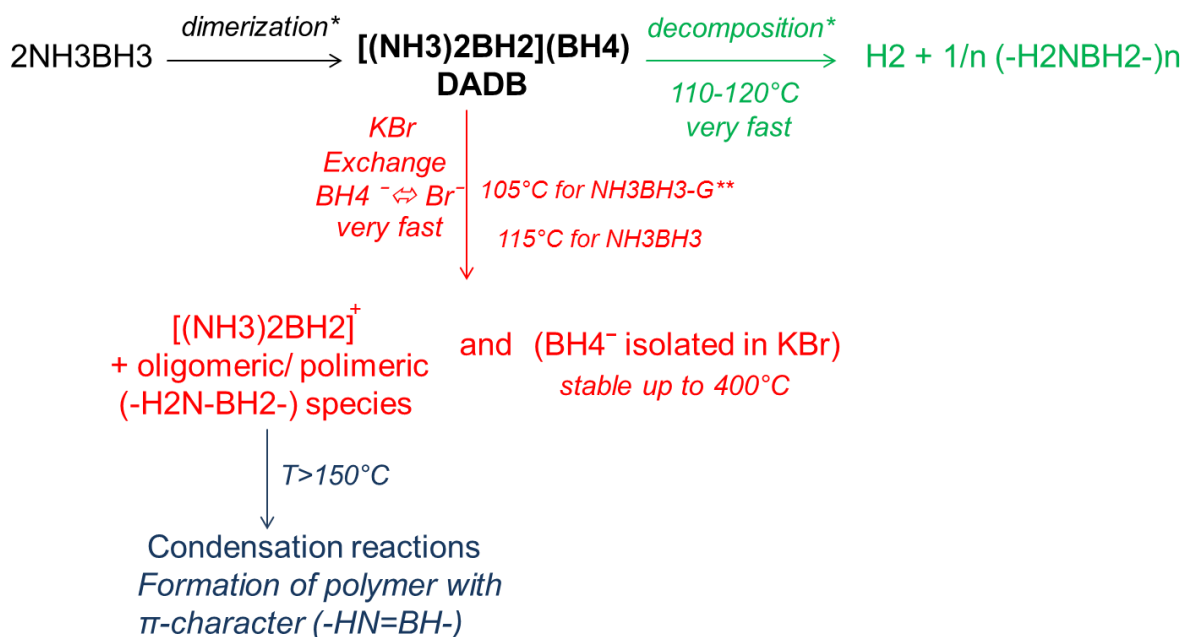


Figure 4.24: Reaction scheme of the decomposition of NH₃BH₃ and NH₃BH₃-G in KBr and formation of BH₄⁻ anions. * It can be hard said whether the conversion of NH₃BH₃ to DADB is total or partial and whether H₂ is liberated from DADB or from a bimolecular reaction of NH₃BH₃ with DADB. ** v₄(BH₄⁻) appears for NH₃BH₃-G at slightly lower temperatures compared to NH₃BH₃.

The thermal behavior of NH₃BH₃-G is summarized in **Figure 4.25** basing on TG/DTA and TIR results. Water of hydration is released between 100 and 150°C. The dehydrogenation path of NH₃BH₃-G is similar to that of NH₃BH₃ and can be described by series of polymerizations and condensations between B, N-chains yielding PAB then PIB structures at about 140 and 160°C according to TIR using NaCl matrix, respectively. The two dehydrogenation steps correspond on the DTA curve of AB-G to the two exotherms centered at 120 and 155°C, respectively. About 105°C a dimerization of NH₃BH₃ to DADB occurs as demonstrated by use of KBr matrix. In the first stages of the decomposition, oligomeric species (as linear dimer of aminoborane LDAB NH₃BH₂NH₂BH₃) could be found which further polymerize to PAB.

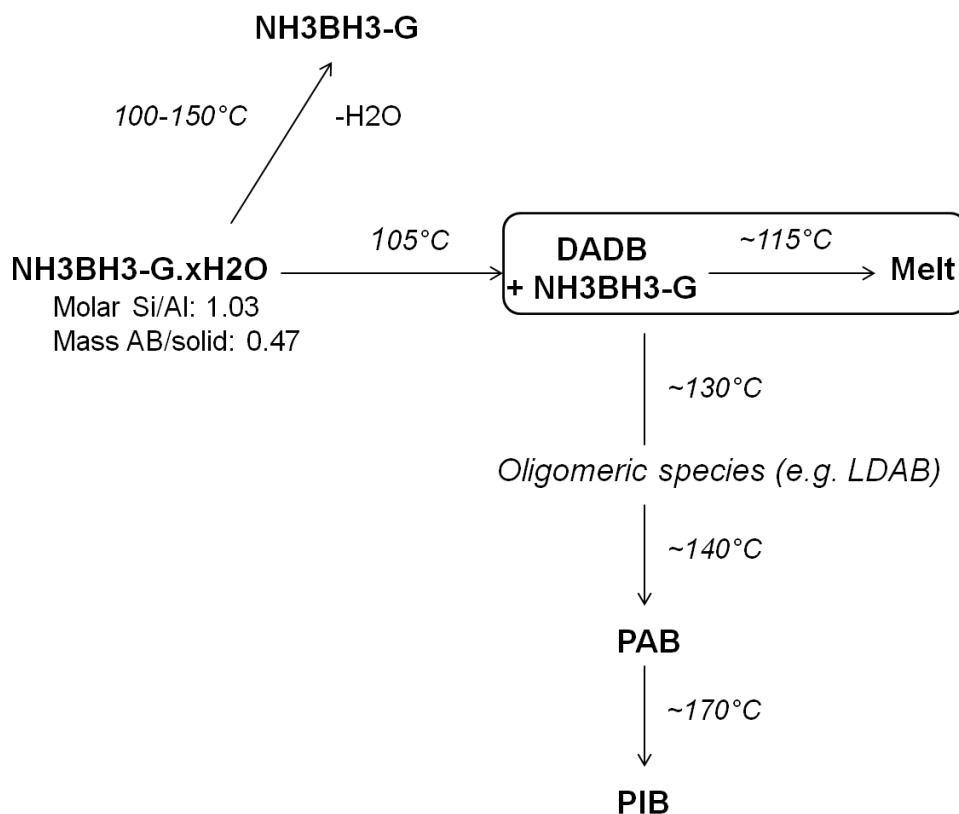


Figure 4.25: Reaction scheme of the thermal decomposition of $\text{NH}_3\text{BH}_3\text{-G}$ composite.

Both NH_3BH_3 and $\text{NH}_3\text{BH}_3\text{-G}$ samples melt at $115\text{-}118^\circ\text{C}$. This is indicated by the endothermic effect peaked at $115\text{-}118^\circ\text{C}$ on the DTA curve and the total disappearance of the IR mode of the dative N-B bond at 780 cm^{-1} in the TIR spectra at 120°C . The melt was significantly reduced for $\text{NH}_3\text{BH}_3\text{-G}$. The heat desorbed during the first exotherm offsets the heat required for NH_3BH_3 melting indicating that hydrogen release from $\text{NH}_3\text{BH}_3\text{-G1}$ sample starts before the melt occurs, at slightly lower temperature compared to NH_3BH_3 . This was further supported by the TIR experiments using KBr in presence of NaNO_3 tracer. The IR peak of BH_4^- at 1123 cm^{-1} (ν_4) and the deformation mode of NH_2 group at 1565 cm^{-1} characteristic of PAB like-structures are detected for $\text{NH}_3\text{BH}_3\text{-G}$ at about 110°C , whereas for NH_3BH_3 at about 120°C .

5. Solid Solutions of BH_4^- in Different Halide AX Matrices ($A = Na, K, Rb; X = Cl, Br, I$)

5.1 State of the art

Nakamori et al. [168, 169] reported a correlation between the first hydrogen desorption temperature (T_d) defined as the temperature of the first desorption peak of the metal borohydrides and the Pauling electronegativity (χ_P) of the metal cations. T_d decreases with increasing χ_P of the cation. An apparent linear relationship was obtained between T_d and χ_P of the cation element for the borohydrides of Na, Li, Mg, Sc, Zr and Zn indicating that χ_P could be considered as an indicator for approximate estimations of the stability of borohydrides. This correlation is applicable for other classes of hydrides as tetra-alanates (AlH_4^-) [170] and hexa-alanates (AlH_6^{3-}) [171], too. In **Figure 5.1**, T_d of the borohydrides of Na, K and Rb is compared with those of the alanates. The cation element of the borohydride/alanate with high χ_P attracts electron density back from BH_4^- and reduces the electron density on the BH_4^-/AlH_4^- destabilizing thus the borohydride/alanate. The lower stability of AlH_4^- in comparison with BH_4^- is due to the lower value of χ_P of Al (1.61) in comparison with χ_P of B (2.04) [13].

Basing on the concept of the cation electronegativity, one approach to affect the thermal stability of the borohydrides is to introduce a metal with high electronegativity through lattice cation substitution. The cation substitution of Na ($\chi_P = 0.93$) and Li ($\chi_P = 0.98$) by Zn ($\chi_P = 1.65$) in $NaBH_4$ and $LiBH_4$ salts, respectively, could be produced by mechanically ball milling with $ZnCl_2$ forming mixed-metal of borohydrides $NaZn(BH_4)_3$, $NaZn_2(BH_4)_5$ and $LiZn_2(BH_4)_5$. These samples are showed to be less thermally stable than their un-substituted patterns [172].

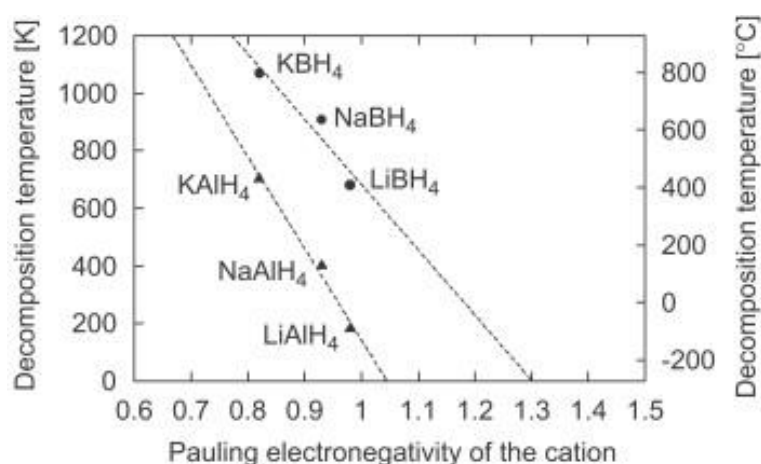


Figure 5.1: Linear correlation between the decomposition temperature (T_d) of the complex hydride (borohydrides and aluminates, respectively) and the Pauling electronegativity (χ_p) of the cation (the figure is taken from ref. [170]).

The anion substitution in the alkali borohydride can also be useful in tuning the thermodynamics of the borohydrides. The mixed hydride-fluoride $\text{Na}_3\text{AlH}_{(6-x)}\text{F}_x$ prepared from NaF, Al and H_2 is destabilized relative to the hydride pure system Na_3AlH_6 [173]. Likewise, first-principles calculations of the decomposition reaction of LiBH_4 with and without fluorine anion F^- suggested that doping the borohydride salt with F^- may result in F^- lattice in the borohydride salt LiBH_4 as well as in the dehydrogenated product LiH yielding favorable thermodynamics modifications [174]. In a more recent study on ball milled samples of NaBH_4 and NaBF_4 , the authors reported a fluorine substitution in the temperature range 200-215°C yielding NaBH_2F_2 . The NaBH_4 - NaBF_4 composite was found to decompose at temperatures lower by at least 100°C in comparison with NaBH_4 [175].

The anion substitution may involve the whole borohydride unit as the substitution of BH_4^- with Cl^- in NaBH_4 [164, 176] and with Br^- [165] and I^- [177] in LiBH_4 . Differential Scanning Calorimetry (DSC) measurements of the produced solid solutions showed the endothermic peaks of the melt as indicator of the thermal stability at higher temperatures compared to the un-substituted borohydride salts suggesting that hydrogen release is not well improved upon these substitutions.

The stabilization/destabilization effect upon the lattice substitutions could be attributed to different types of interactions altered during the ionic exchange. The ionic bonding is effective between the cation element and the BH_4^- group, whereas the bond between B and H atoms within the BH_4^- group has a covalent character [14]. In fact, the interactions on the

BH_4^- anion could be observed by the frequency variations of the BH_4^- related peaks in Raman and IR spectra.

Orimo et al. [20] found that for lithium, sodium and potassium borohydrides, the Raman active stretching ν_1 and bending ν_2 modes decrease in the order ($\nu_2(\text{LiBH}_4) = 1295 \text{ cm}^{-1}$ and $\nu_2'(\text{LiBH}_4) = 1305 \text{ cm}^{-1}$) $>$ ($\nu_2(\text{NaBH}_4) = 1280 \text{ cm}^{-1}$) $>$ ($\nu_2(\text{KBH}_4) = 1240 \text{ cm}^{-1}$) and ($\nu_1(\text{NaBH}_4) = 2325 \text{ cm}^{-1}$) $>$ ($\nu_1(\text{KBH}_4) = 2305 \text{ cm}^{-1}$), whereas the melting temperature (T_m) varies in the opposite direction, $T_m(\text{LiBH}_4) < T_m(\text{NaBH}_4) < T_m(\text{KBH}_4)$. The ν_1 of LiBH_4 was reported at 2293 cm^{-1} and did not follow the afforded relation due to the difference of the crystal system. LiBH_4 adopts an orthorhombic structure (space group $Pcmn$) at room temperature, whereas the other alkali metal (Na, K, Rb and Cs) borohydrides crystallize in a rock salt, face-centered-cubic structure [51].

Renaudin et al. [81] performed a structural study on MBH_4 and MBD_4 salts ($M = \text{Na, K, Rb and Cs}$). Structural parameters were determined using powder X-ray diffraction for the cell parameters and Neutron diffraction for the positions of D atoms. Analyses were conducted at room temperature (295-298 K) and at temperatures below 10 K for the high and low temperature phases, respectively. The Raman and FTIR-ATR spectra were also reported and assigned. The data were found to be in good agreement with Badger's rule showing a linear decrease of the symmetric stretching ν_1 frequencies with increasing the B-D bond length of MBD_4 by increase of the cell parameters.

The Badger's rule was firstly established on diatomic molecules providing a simple linear relation between the force constant of the bond (k_e) and the equilibrium position (r_e) which can be written as:

$$r_e = \left(\frac{1.86 \times 10^5}{k_e} \right)^{\frac{1}{3}} + d_{ij} \quad [178] \quad (5.1)$$

and,

$$r_e = \left(\frac{C_{mn}}{k_e} \right)^{\frac{1}{3}} + d_{mn} \quad [179] \quad (5.2)$$

d_{ij} is a constant which depends on the period in the periodic table of the two atoms constituting the molecule, and C_{mn} and d_{mn} are two constants related to the corresponding groups of the elements in the periodic table. The relation established for diatomic molecules could be also justified for polyatomic molecules [180].

Earlier works on borohydrides using matrix isolation technique reported the IR frequencies of BH_4^- anions in different alkali halides AX [91, 92]. The matrix isolation technique consists of trapping species as isolated entities in an inert solid or matrix where the solute (the polyatomic ion) is dispersed in the matrix in very low amounts, varying typically between 0.01 and 0.5 mol%. Therefore, it is commonly called “impurity” [36]. The broadening of IR absorption bands is due to the direct interactions between similar vibrational groups. The matrix-isolated species have sharp IR bands. The typical half band-width for BH_4^- in the alkali halide lattice is 0.65 cm^{-1} [181]. This effect is referred to the absence of coupling between identical ions in the solid solutions [182]. The local symmetry group of the BH_4^- in different halide matrices ion is found to be T_d and the IR frequencies depend on the particular alkali-halide in which the ion is imbedded [92].

5.2 Results and discussion

In a first approach, the effect of pressing NaBH_4 in halide matrices is investigated. Therefore, equimolar mixtures (molar ratio 1:1) of $\text{NaBH}_4\text{:NaCl}$, $\text{NaBH}_4\text{:NaBr}$ and $\text{NaBH}_4\text{:KBr}$ were pressed in pellets and then characterized by XRD. The results of the thermal treatment of $\text{NaBH}_4\text{:NaCl}$ and $\text{NaBH}_4\text{:NaBr}$ are considered, too. In a second approach, the IR frequencies of the BH_4^- anion in high dilution in halides AX (A = Na, K, Rb; X = Cl, Br, I) are investigated in details.

5.2.1 Solid solution formation in equimolar NaBH_4 : AX pressed pellets

Equimolar mixtures of $\text{NaBH}_4\text{:NaCl}$, $\text{NaBH}_4\text{:NaBr}$ and $\text{NaBH}_4\text{:KBr}$ were hand-mixed and pressed into pellets using a force of 100 kN for few minutes. Afterwards, the pellets were ground into powder. XRD patterns were taken on thin films of the samples using acetone as solvent (“Streupräparat”). Results are shown for the (2 2 0) reflexes in **Figure 5.2** in addition to the X-ray diffractograms of pristine NaBH_4 , NaBr, NaCl and KBr salts.

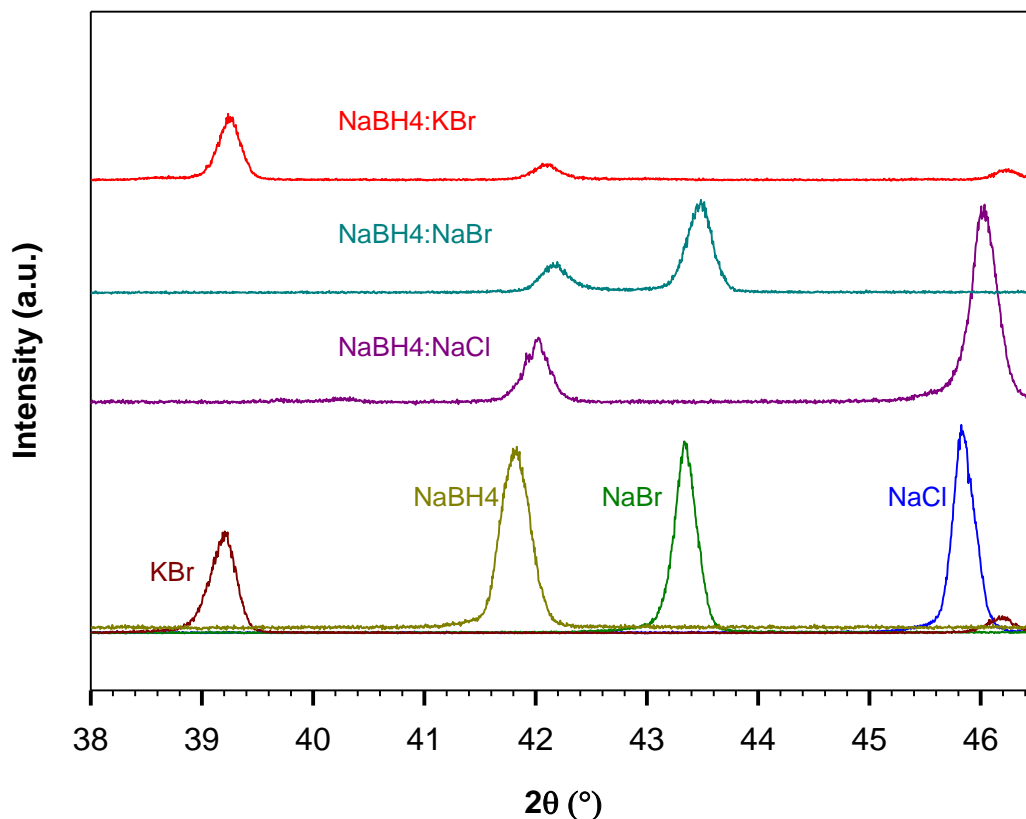


Figure 5.2: XRD patterns of the equimolar mixtures of $NaBH_4:NaBr$, $NaBH_4:NaCl$ and $NaBH_4:KBr$ pressed pellets in the range of the (2 2 0) reflections of the pristine $NaBH_4$, $NaBr$, $NaCl$ and KBr salts

For $NaBH_4:NaCl$ and $NaBH_4:NaBr$ pellets, the $NaBH_4$ index is shifted to higher 2θ by $0.19^\circ 2\theta$ and $0.35^\circ 2\theta$, respectively. Ravensbæk et al. [164] and Olsen et al. [176] showed that the cell parameters of the solid solutions of $NaBH_4$ and $NaCl$ lie between those of $NaBH_4$ and $NaCl$ and vary linearly with the nominal compositions of the solid solutions (Vegard's law). This implies that the (2 2 0) reflexes of the solid solutions occur between the (2 2 0) reflexes of $NaBH_4$ and $NaCl$, respectively. This could be also expected for $NaBH_4:NaBr$ which has not yet been investigated in the literature. Therefore, the shifting of $NaBH_4$ indexes to higher 2θ can be referred to some dissolution of $NaBH_4$ in the halide indicating that $NaBH_4$ salt is more affected by $NaBr$ salt where the ionic radii of the anions are similar (BH_4^- : 2.05 Å [164] and Br^- : 1.96 Å [165]). The reflexes of $NaCl$ and $NaBr$ in the mixture-pellets are shifted by approximately 0.2 and 0.13 to higher 2θ , respectively, due to the use of thin films ("Streupräparate").

In the case of KBr mixture, the NaBH_4 reflex is displaced by $0.26^\circ 2\theta$ to higher 2θ . The indexes of NaBH_4 in the solid solutions of NaBH_4 and KBr are expected to move in the direction of KBr index, i.e in the opposite direction to that observed.

In a further step, The equimolar pellets of $\text{NaBH}_4\text{:NaBr}$ and $\text{NaBH}_4\text{:NaCl}$ were further thermally treated to temperatures between 300 and 375°C for different heating times as indicated in **Table 5.1**.

Table 5.1: List of thermally treated samples

Materials	Molar ratio	Treatment	Notation
$\text{NaBH}_4\text{:NaBr}$	0.5:0.5	300°C 20 h (N_2)	B-0.5- 300° -20h
$\text{NaBH}_4\text{:NaCl}$	0.5:0.5	350°C 20 h (N_2)	C-0.5- 350° -20h
		375°C 20 h (N_2)	C-0.5- 375° -20h
		370°C 68 h (Ar)	C-0.5- 370° -68h

The X-ray diffractogram of the thermally treated $\text{NaBH}_4\text{:NaBr}$ mixture is shown in **Figure 5.3**. The X-ray patterns of pristine NaBH_4 and NaBr salts and the pressed-pellet before the thermal treatment are also shown for comparison.

The XRD pattern of B-0.5- 300° -20h shows reflexes for NaBr but no indication of NaBH_4 . The inset graph is zoomed for the (2 2 0) reflexes between 41.4 and $43.8^\circ 2\theta$. New reflexes are observed at slightly higher 2θ in comparison with NaBH_4 crystal which indicate the dissolution of NaBH_4 and the formation of $\text{Na}(\text{BH}_4)_{(1-x)}\text{Br}_x$. The reflexes of the solid solution are broadened over the whole range between the original reflexes of NaBH_4 and NaBr indicating a wide range of compositions. The total dissolution of NaBH_4 is not reached even after annealing the pellet to 300°C for 20 h.

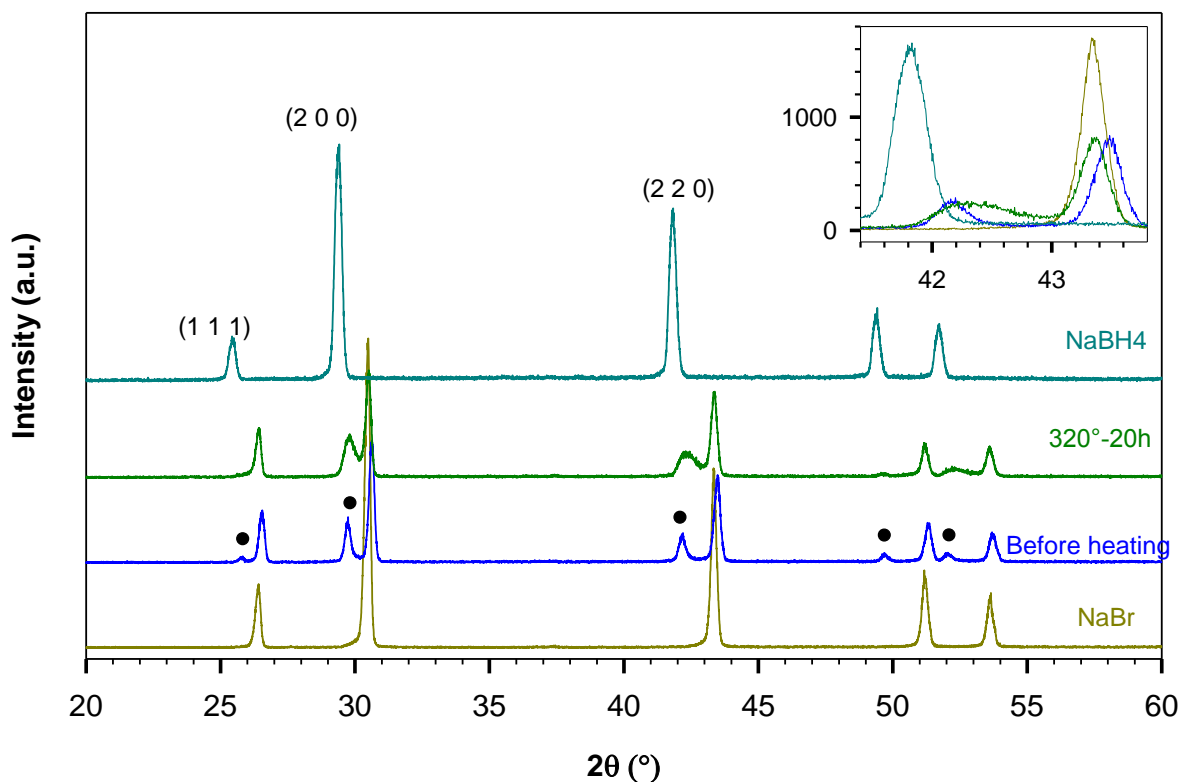


Figure 5.3: X-ray diffractograms of B-0.5-300°-20h in comparison with the diffractograms of the mixture before heating and $NaBH_4$ and $NaBr$ pristine salts. The reflexes of $NaBH_4$ are indexed. Inset graph is zoomed for the (2 0 0) reflection between 41.4 and 43.8° 2θ . Circles denote $Na(BH_4)_{(x-1)}Br_x$ reflexes.

Figure 5.4 shows the X-ray results of $NaBH_4:NaCl$ mixtures. Some peaks related to decomposition by-products were obtained. These are more intense in the samples treated at a higher temperature 375°C compared to 350°C. For comparison, the thermally treated $NaBH_4:NaBr$ pellet does not show decomposition peaks indicating that $NaBH_4$ was already dissolved in $NaBr$ in the pressed-mixture and protected against the decomposition, whereas in the case of $NaCl$, non-dissolved $NaBH_4$ during annealing is decomposed at temperatures above 300°C.

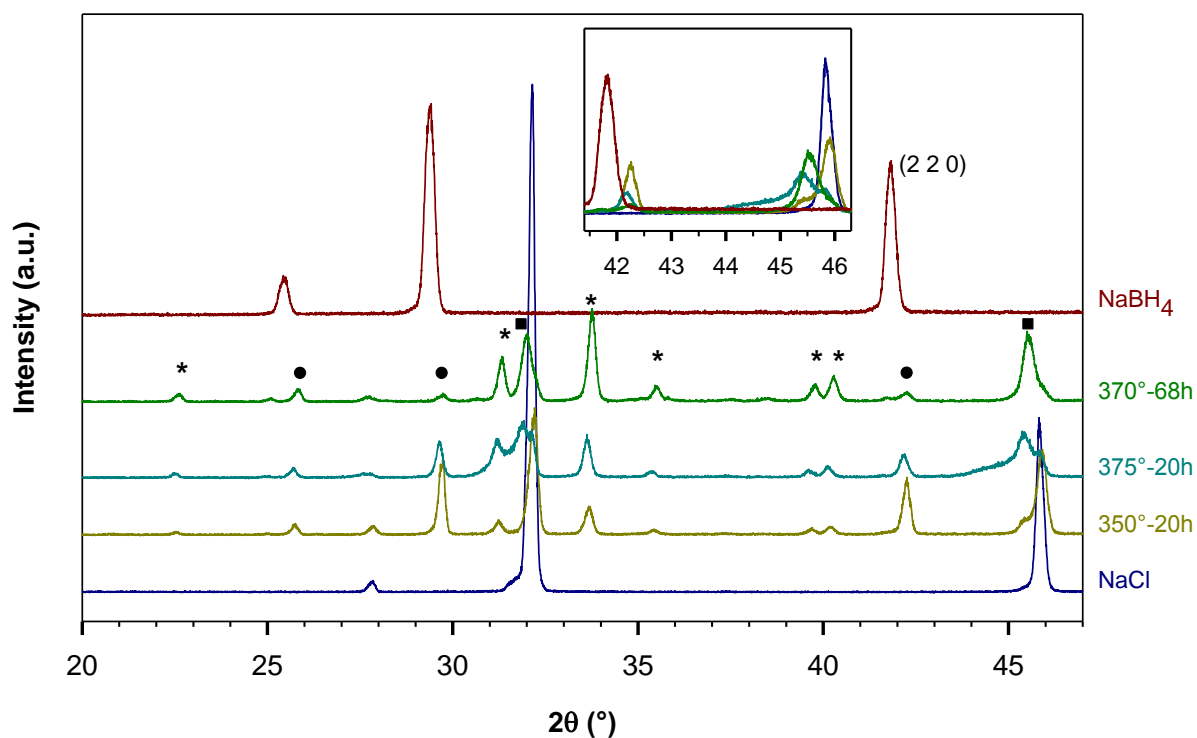
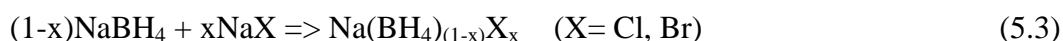


Figure 5.4: X-ray diffractograms of the thermally treated NaBH_4 : NaCl mixtures. Diffractograms of NaBH_4 and NaCl are shown for comparison. Inset graph is zoomed for the (2 2 0) reflections. Circles and squares denote $\text{Na}(\text{BH}_4)_{(1-x)}\text{Cl}_x$ and $\text{Na}(\text{BH}_4)_y\text{Cl}_{(1-y)}$, respectively. Asterisks are for the by-products.

The quality of the diffractograms was not sufficient to refine the X-ray data and to calculate the molar composition of the samples. Therefore data were qualitatively evaluated to give an insight into the anion substitution mechanism by thermal treatment.

In all thermally treated samples, there is no evidence of NaBH_4 at the end of the thermal treatment. The dissolution of NaCl salt is less pronounced since all samples show NaCl reflexes after the thermal treatment even after the long isotherm for 68 h at 370°C .

The NaBH_4 peaks are slightly shifted toward higher 2θ values confirming the formation of $\text{Na}(\text{BH}_4)_{(1-x)}\text{Cl}_x$ according to:



Another type of solid solutions is indicated by the reflexes at slightly lower 2θ than the reflexes of NaCl salt which can be referred to a slight dissolution of NaCl and substitution with BH_4^- . This solid solution is denoted $\text{Na}(\text{BH}_4)_y\text{Cl}_{(1-y)}$.

It can be observed in the inset graph of **Figure 5.4** that the peak intensities of $Na(BH_4)_yCl_{(1-y)}$ and $Na(BH_4)_{(1-x)}Cl_x$ varies in an opposite way. An increase of $Na(BH_4)_yCl_{(1-y)}$ is accompanied with a decrease of XRD peaks of $Na(BH_4)_{(1-x)}Cl_x$ and NaCl. This suggests that $Na(BH_4)_{(1-x)}Cl_x$ and NaCl dissolve into each other to produce $Na(BH_4)_yCl_{(1-y)}$.

In order to get a quantification of the degrees of substitution x and y in $Na(BH_4)_{(1-x)}Cl_x$ and $Na(BH_4)_yCl_{(1-y)}$, respectively, the peak positions of the reflexes (2 2 0) were taken and compared to the results of Olsen et al. [176] who reported the 2θ values of the reflex (2 2 0) for different solid solutions of $NaBH_4$ and NaCl with different nominal compositions. For $Na(BH_4)_{(1-x)}Cl_x$, the (2 2 0) reflexes are shifted to higher 2θ by approximately $0.45^\circ 2\theta$ relative to $NaBH_4$ and those for $Na(BH_4)_yCl_{(1-y)}$ are shifted to lower 2θ by approximately $0.5^\circ 2\theta$ relative to NaCl. These shifts correspond to x and y of approximately 0.1-0.15 and 0.1, respectively.

The molar proportions of $Na(BH_4)_{(1-x)}Cl_x$, $Na(BH_4)_yCl_{(1-y)}$ and NaCl in the samples are strongly affected by the thermal treatment. Higher amounts of $Na(BH_4)_yCl_{(1-y)}$ and respectively lower amounts of NaCl are obtained for the samples annealed to higher temperatures (375° in comparison with $350^\circ C$) and for a longer time (68 h at $370^\circ C$ in comparison with 20 h at $375^\circ C$).

Ravnsbaek et al. [164] obtained $Na(BH_4)_{0.43}Cl_{0.57}$ during the thermal treatment of $NaBH_4:NaCl$ mixture (0.5:0.5) at $300^\circ C$ independently of the heating time. The prolonged heating time promoted, however, the dissolution of NaCl and the formation of $Na(BH_4)_{0.1}Cl_{0.9}$. In the present work the degree of substitutions x and y do not exceed 0.1-0.15 and 0.1, respectively. The difference between the results could be referred to the history of the sample before the thermal treatment. Ravnsbaek et al. [164] ball milled the $NaBH_4:NaCl$ mixture for 2 h before annealing resulting in the composition of 50.3 mol% $Na(BH_4)_{0.1}Cl_{0.9}$ and 49.7 mol% NaCl, whereas in the present work the mixture were only pressed into pellets before the thermal treatment and still contain significant amounts of $NaBH_4$ salt.

5.2.2 Spectra of NaBH₄/KBH₄ in ATR and pressed in various halides

The ATR spectra of as-received NaBH₄ and KBH₄ powders are shown in **Figure 5.5**. The positions of the peak maxima frequencies are in good agreement with values reported by Renaudin et al. [81] as collected in **Table 5.2** together with the given assignments.

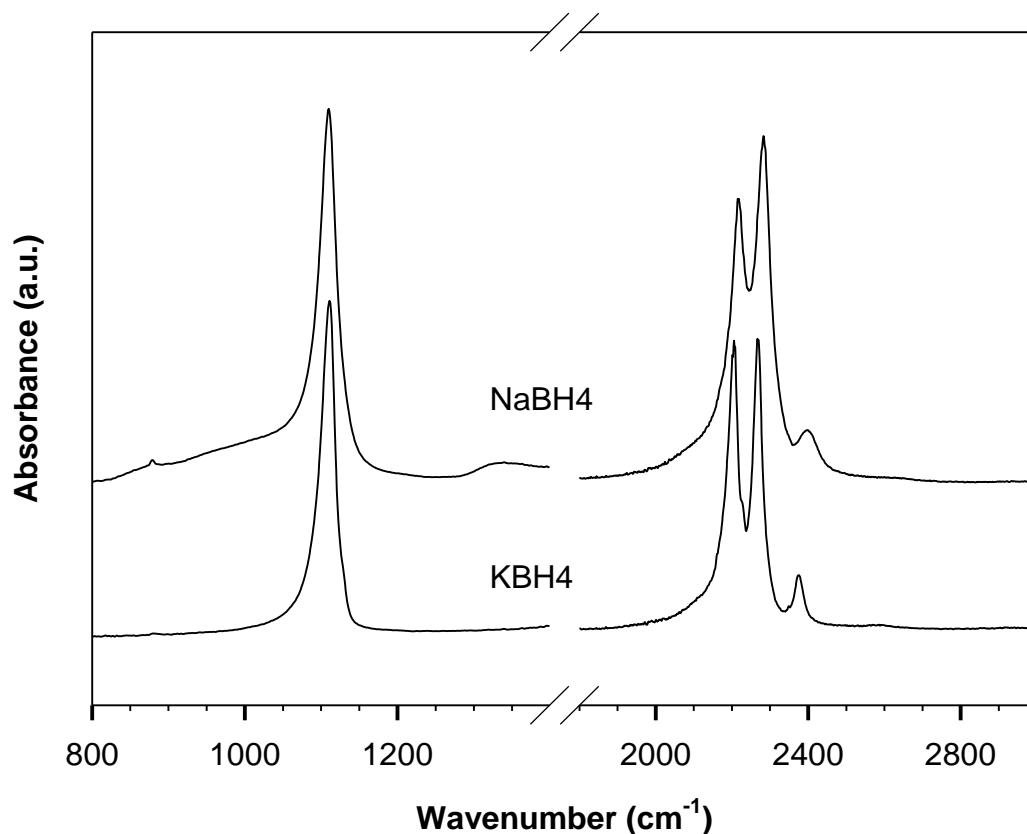


Figure 5.5: FTIR-ATR spectra of the as-received NaBH₄ and KBH₄ samples

It is well known that the bands in the ATR spectra are generally shifted to lower frequencies compared to the transmission spectra caused by the dispersion of the refractive index. This is one reason that the IR peak positions obtained using the standard pressed pellet technique, e.g. in KBr halide shows more or less deviations from peak positions determined using ATR peak positions. A correction of the ATR peak positions can be carried out which depends on a detailed knowledge of the functional dependence of the refractive index in the vicinity of the peak absorption peak.

Another reason for deviations in the peak positions determined in the pressed pellet method is related to a rather uncontrolled anion or cation exchange effect between the probe

and the matrix. This is shown in **Figure 5.6** for $NaBH_4$ in KBr (spectrum b, e). Rather broad and less well determined peak positions are observed for short hand-mixing and short pressing time (less than 30 s). Contrary, good hand-mixing and pressing for 90 s at the same force (100 kN on a pellet of 13 mm diameter is equivalent to a pressure of 754 MPa) reveal much sharper and shifted peak position. The position of the peak maxima are also given in **Table 5.2** for comparison.

Table 5.2: ATR frequencies of $NaBH_4$ and KBH_4 compared to ATR values of Renaudin et al. [81] (values in brackets) in addition to the transmission IR frequencies of $NaBH_4$ in KBr and NaCl pellets.

		ν_4	$2\nu_4$	ν_3	$\nu_2 + \nu_4$
ATR	$NaBH_4$	1110 (1110)	2217 (2217)	2283 (2284)	2397 (2404)
	KBH_4	1111 (1112)	2205 (2208)	2268 (2270)	2375 (2376)
Transmission (pellets)	$NaBH_4/KBr$ (< 30 s pressed)	1120	2220	2299	2398
	$NaBH_4/KBr$ (90 s pressed)	1126	2224	2291	2387
	$NaBH_4/NaCl$	1121	2229	2302	2403

The better mixing and longer pressing time leads to better resolved peaks, e.g. for the isotope effect $^{11}B/^{10}B$ depicted by the shoulders at higher wavenumbers. This better resolution is explained, however, by a higher degree of solution of the BH_4^- -anion into the KBr matrix. In this respect the broader peaks seem to be more representative for $NaBH_4$. This could also be supported by inspection of the spectrum obtained for $NaBH_4$ diluted and pressed into NaCl also shown in **Figure 5.6** (spectrum a). The peaks well coincide with those of $NaBH_4$ in KBr also taken from the typically broader one. Spectra given for $NaBH_4$ in NaBr (d) and KI (e) also show rather sharp peaks but at significant different peak positions. This indicates the effect of a sufficient dilution and incorporation of the BH_4^- -anion in the various halide type lattices.

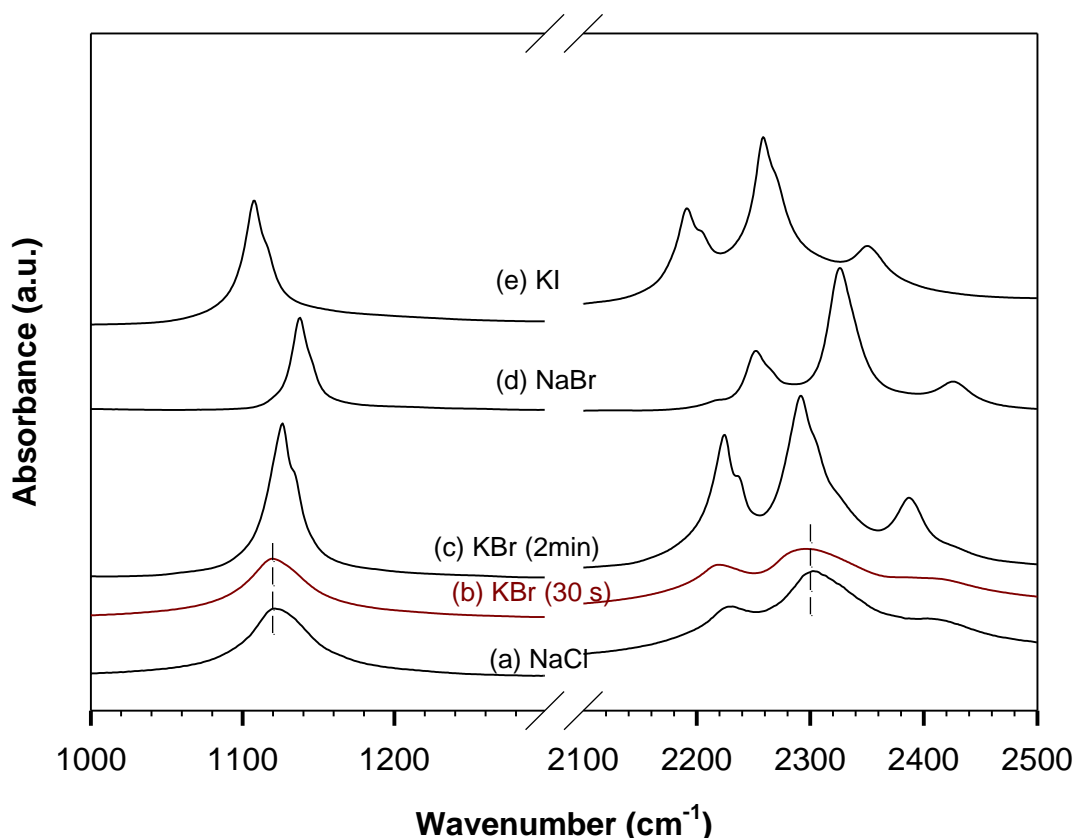


Figure 5.6: Room temperature transmission IR spectra of as-received NaBH_4 in (a) NaCl, in KBr (b) short pressed and (c) long pressed, in (d) NaBr and in (e) KI

It has been reported that the BH_4^- anions could be highly diluted in AX by heating discs constituted of AX and traces of borohydride (NaBH_4 or KBH_4) to temperatures between 500 and 600°C [91]. This effect is demonstrated in **Figure 5.7**. Shown are spectra for NaBH_4 (1 mg) diluted into 200 mg of NaCl and KCl (dashed curves) compared to those after heating to 450°C. For NaBH_4 in NaCl, the IR peaks after the thermal treatment are sharpened and shifted to higher wavenumbers compared to the spectrum taken before the heating. For NaBH_4 diluted and pressed in KCl, the spectrum shows peak splitting indicating the formation of two types of solid solutions with a higher and smaller BH_4^- -anion concentration in KCl, respectively. However, after thermal treatment a more homogeneous dilution of BH_4^- -anions in KCl crystals is obtained.

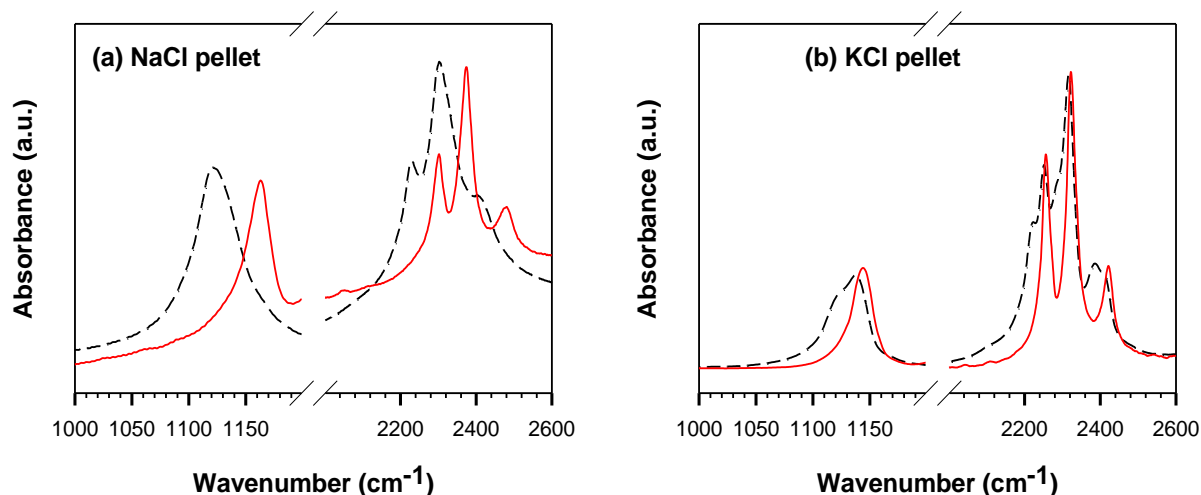


Figure 5.7: IR spectra of $NaBH_4$ diluted in (a) $NaCl$ and (b) KCl pellets before (black dashed lines) and after the thermal treatment to $450^\circ C$ (red solid lines)

5.2.3 TIR of $NaBH_4/NaCl$ pellet

The incorporation of BH_4^- in $NaCl$ was followed in more details using TIR spectroscopy performed from room temperature to $450^\circ C$. Results are shown in **Figure 5.8**.

At room temperature, the IR spectrum reveals a partial hydration of $NaBH_4$ to $NaBH_4 \cdot 2H_2O$ as can be concluded from the presence of H_2O IR libration modes at 572 and 614 cm^{-1} , the H-O-H bending mode at 1625 cm^{-1} and the O-H stretching modes at 3242 , 3476 , 3505 and 3566 cm^{-1} [49]. Crystalline H_2O molecules are released at relatively low temperatures, below $100^\circ C$, without being consumed by $NaBH_4$ since the IR spectrum $120 \Rightarrow 25^\circ C$ does not show new IR peaks.

The IR peaks of BH_4^- at the end of the thermal treatment to $450^\circ C$ appear at 1165 , 2303 , 2375 and 2482 cm^{-1} , for ν_4 , $2\nu_4$, ν_3 and $\nu_2 + \nu_4$, respectively. Interestingly, the overtone $2\nu_4$, the combination mode $\nu_2 + \nu_4$ and the stretching ν_3 modes are displaced by the same amount, 73 , 75 and 73 cm^{-1} , respectively, confirming the conservation of the symmetry T_d and the Fermi resonance of BH_4^- anion in the solid solutions as suggested in ref. [92].

Concurrent to the dilution of BH_4^- in $NaCl$, $NaBH_4$ is partially oxidized to $Na_3B_3O_6$ in agreement with the decomposition peaks observed in the X-ray patterns of the thermally treated $NaBH_4:NaCl$ mixtures (**Figure 5.4**).

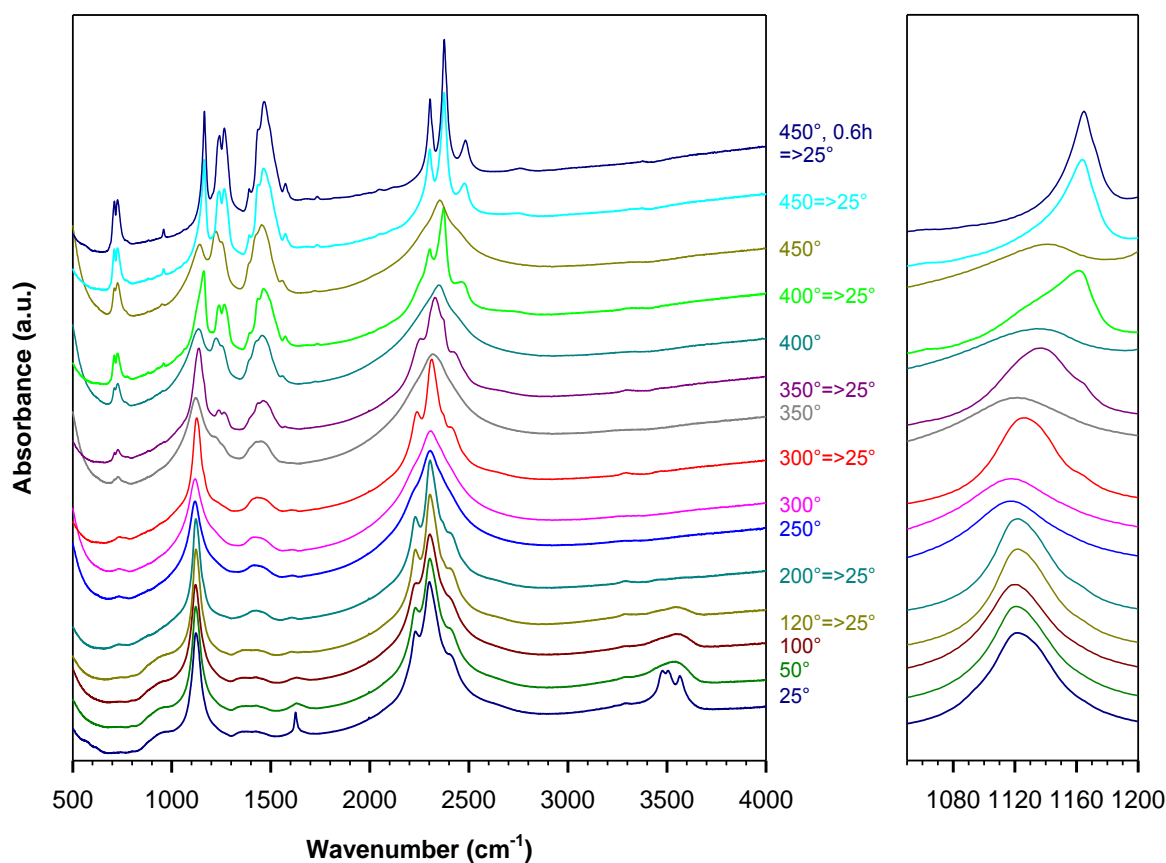


Figure 5.8: TIR spectra of NaBH₄/NaCl pellet. The graph at the left side is zoomed for ν_4 .

The total shifting observed at 450°C for the fundamentals ν_4 and ν_3 occurs in systematic way. A slight peak shifting of 4 and 10 cm⁻¹, respectively, is observed for the IR spectrum cooled down from 300°C (300=>25°C). The fundamentals ν_4 and ν_3 are further shifted between 300 and 350°C by 10 and 19 cm⁻¹, respectively. At 400=>25°C, a shoulder appears near 1165 cm⁻¹ related to ν_4 of BH₄⁻ highly diluted in NaCl. This increases in intensity upon further heating.

For a better resolution of the IR peaks of BH₄⁻, the second derivative (Ψ'') of the TIR spectra cooled down to 25°C were calculated and traced for only ν_4 because of the complexity of the spectral range between 2100 and 2450 cm⁻¹ and the superimposition of many peaks. TIR spectra and the corresponding Ψ'' curves for NaBH₄/KBr pellet are also shown, for comparison (**Figure 5.9**).

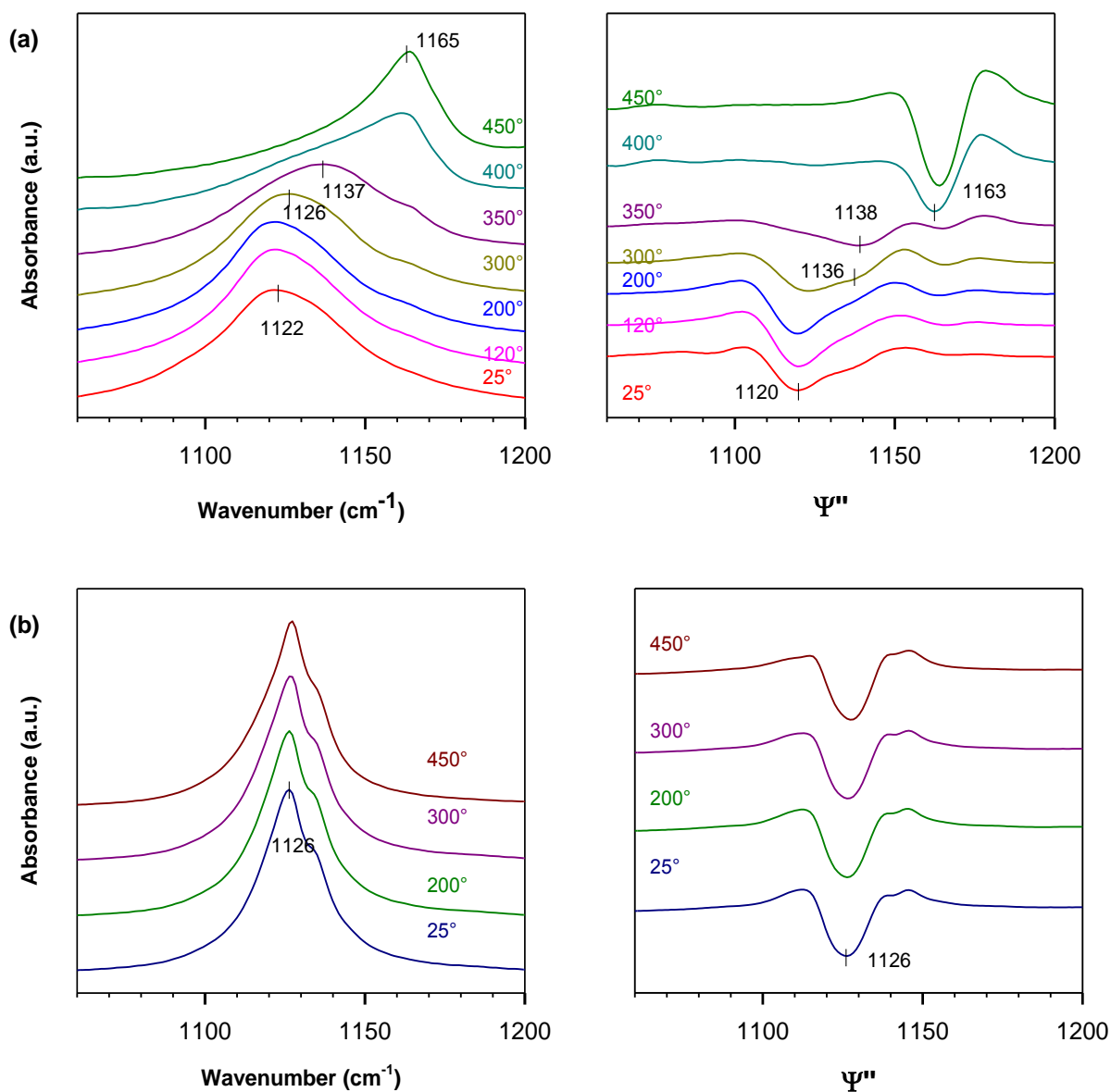


Figure 5.9: TIR spectra of (a) NaBH₄/NaCl for ν_4 and their second derivatives Ψ'' . Results of (b) NaBH₄/KBr are shown for comparison.

For NaBH₄/KBr pellet, the room temperature IR spectrum corresponds to BH₄⁻ highly diluted in KBr. The peak position of ν_4 remains approximately the same at all temperatures, with a maximum at 1126 cm⁻¹ and a shoulder at 1133 cm⁻¹ assigned to the isotopes ¹¹B and ¹⁰B of boron atom in natural abundance, respectively. Ψ'' of all considered TIR spectra show a global minimum at 1126 cm⁻¹ corresponding to the peak maximum in the TIR spectra.

For NaBH₄/NaCl, $\Psi''_{(25^\circ C)}$ shows principally a global minimum at 1120 corresponding to the peak maximum of the IR spectrum at 25°C. The slight peak shifting observed in the

TIR spectrum 300=>25°C is resolved in the second derivative curve $\Psi''_{(300^\circ \Rightarrow RT)}$ to a peak minimum with approximately the same position 1120 as for $\Psi''_{(25^\circ C)}$, and a shoulder at about 1136. The peak minimum is totally shifted to 1138 in $\Psi''_{(350^\circ \Rightarrow RT)}$. This indicates that all NaBH_4 crystals are dissolved and transformed to $\text{Na}(\text{BH}_4)_{(1-x)}\text{Cl}_x$ (reaction 5.3). In $\Psi''_{(400^\circ \Rightarrow 25^\circ C)}$, the minimum is shifted to 1163 indicating further dissolutions in the pellet and incorporation of BH_4^- in NaCl. These observations are in accordance with XRD results of the thermally treated $\text{NaBH}_4:\text{NaCl}$ mixtures revealing in a first step the dissolution of NaBH_4 and slight substitutions with Cl^- yielding $\text{Na}(\text{BH}_4)_{(1-x)}\text{Cl}_x$ followed by further dissolution of the latter in NaCl.

Detailed inspections of **Figure 5.9a** reveal the presence of a shoulder at 1136 in $\Psi''_{(25^\circ C)}$ related to $\text{Na}(\text{BH}_4)_{(1-x)}\text{Cl}_x$. This can be referred to a slight dissolution between the outer layers of NaBH_4 and NaCl during the pellet preparation. The shoulder disappears in $\Psi''_{(200^\circ \Rightarrow RT)}$ and the weak minimum at about 1165 cm^{-1} appears confirming the dissolution of $\text{Na}(\text{BH}_4)_{(1-x)}\text{Cl}_x$ and the incorporation of BH_4^- in NaCl.

5.2.4 BH_4^- -frequency variations dependences on halide parameters

The pellet preparation procedure using a pressure of approximately 754 MPa was sufficient to solve NaBH_4 ($a_0 = 6.16 \text{ \AA}$) in each of NaI ($a_0 = 6.48 \text{ \AA}$), NaBr ($a_0 = 5.97 \text{ \AA}$), KBr ($a_0 = 6.60 \text{ \AA}$) and KI ($a_0 = 7.06 \text{ \AA}$), whereas for NaCl ($a_0 = 5.64 \text{ \AA}$) and KCl ($a_0 = 6.29 \text{ \AA}$), a subsequent annealing to 450°C was necessary to achieve the total solution of BH_4^- in the halide lattice. This can be explained by the smaller effective ionic radius of Cl^- (1.81 Å [164]) compared to BH_4^- (2.05 Å [164]). Contrary, the ionic radii of Br^- (1.96 Å [165]) and I^- (2.20 Å [177]) are close or significantly larger than that of BH_4^- , respectively, facilitating thus the ionic exchange at room temperature by only the pressure effect. The larger cation radius of K^+ compared to Na^+ of the halide lattice may enhance the solution effect as could be suggested from the two type of compositions indicated in the NaBH_4 spectrum in KCl compared to NaBH_4 in NaCl (**Figure 5.7**).

The obtained IR frequencies of BH_4^- in different halide matrices in the limit of high dilution refer to an isolation of BH_4^- in the halide (denominated as i- BH_4^- , “i” for isolated) and are summarized in **Table 5.3**. The IR values for BH_4^- in RbX matrices are taken from ref. [92]. The obtained frequencies for BH_4^- in NaX and KX matrices are in good agreement with those of ref. [91, 92]. The cell parameter (a_0) [183] and the radius ratio of the effective

ionic radius (NaCl structure, coordination number 6) of the cation to the ionic radius of the anion ($R = r^+/r^-$) [184] are also given in **Table 5.3**.

Table 5.3: IR frequencies of $i-BH_4^-$ in different AX lattices. Structural parameters of AX are also given.

AX	IR frequencies of $i-BH_4^-$ in AX				Structural parameters of AX	
	ν_4	$2\nu_4$	ν_3	$\nu_2+\nu_4$	a_0	$R=r^+/r^-$
NaCl	1165	2303	2375	2482	5.6402	0.5635
NaBr	1138	2252	2326	2426	5.9738	0.5204
NaI	1112	2208	2281	2364	6.479	0.4636
KCl	1144	2257	2323	2422	6.290	0.7624
KBr	1127	2226	2293	2390	6.598	0.7041
KI	1107	2191	2258	2350	7.064	0.6273
RbCl	1132	2236	2303	2395	6.582	0.8398
RbBr	1118	2212	2279	2369	6.8768	0.7755
RbI	1104	2181	2250	2335	7.3291	0.6909

It is observed that $\nu_3(i-BH_4^-)$ in NaI and RbBr are similar, 2281 and 2279 cm^{-1} , respectively, while the corresponding a_0 (6.479 Å and 6.877 Å, respectively) and R (0.4636 and 0.7755, respectively) of the halide matrices are very different. Therefore, the frequencies of $\nu_3(i-BH_4^-)$ cannot be interpreted in terms of only the lattice parameter a_0 and the radius ratio R determining the available space for the substituting BH_4^- in AX. Contrary, the IR frequencies of $i-BH_4^-$ are found to depend on the nature of the host matrix, in agreement with ref. [92]. To show this effect more clearly, graphical representations of $\nu_3(i-BH_4^-)$ in function of the structural parameters, a_0 and R of the corresponding AX are given in **Figure 5.10a** and **Figure 5.10b**, respectively.

Approximately linear relationships are observed between $\nu_3(i-BH_4^-)$ and $a_0(AX)$ for the homologous series of halides with same cationic element A (A-series) or with the same anionic element X (X-series). The linearity between $\nu_3(i-BH_4^-)$ and $a_0(AX)$ is valid within each of the defined halide series showing an increase of $\nu_3(i-BH_4^-)$ with decreasing $a_0(AX)$ (**Figure 5.10a**).

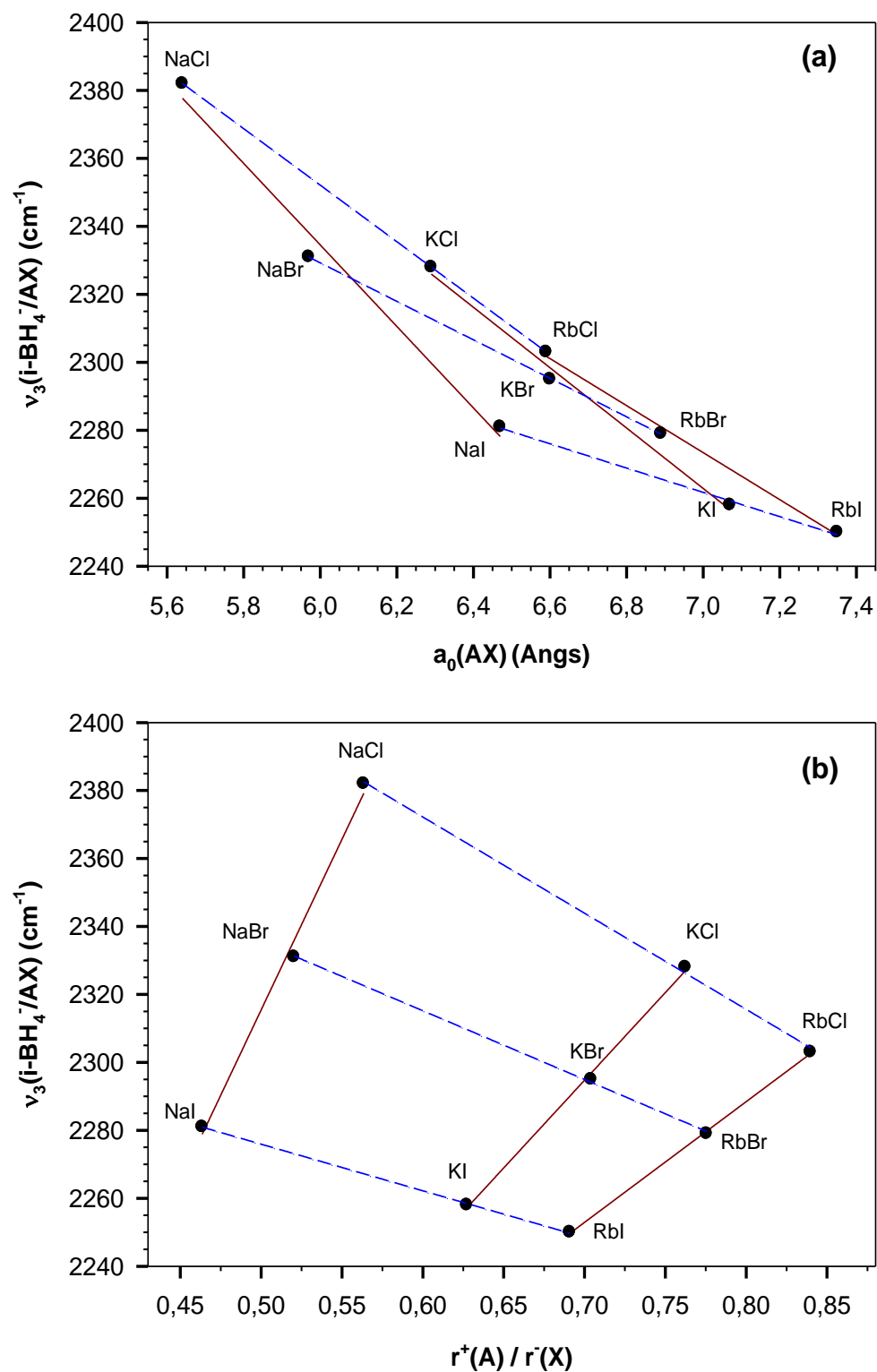


Figure 5.10: Graphical representations of $\nu_3(i-BH_4^-)$ in function of (a) cell parameter a_0 and (b) radius ratio ($R = r^+/r^-$) of the corresponding AX halide. Solid lines represent common cation A-series and dashed lines are for the common anion X-series.

Furthermore, according to **Figure 5.10b**, an increase of $\nu_3(i-BH_4^-)$ is accompanied with an increase of R for the A-series but with a decrease of R for the X-series. This indicates that $\nu_3(i-BH_4^-)$ varies in an opposite direction to the ionic radii of the cations (r^+) and the anions (r^-). Smaller cations and anions tend to increase $\nu_3(i-BH_4^-)$. This still could indicate that increasing the available space for the substituting BH_4^- anion along series with increasing anion size (for e.g. NaCl, NaBr and NaI) is responsible for the decrease of ν_3 . A similar effect is observed for X-series. An increase of the size of the cation along a series (for e.g. I-series: NaI, KI and RbI) is accompanied with an increase of the available space which decreases, thus, $\nu_3(i-BH_4^-)$. This argument fails, however, between different series as alluded above for the case of NaI and RbBr which exhibit similar $\nu_3(i-BH_4^-)$ but completely different available anion spaces. The same is for NaBr and KCl matrices. Therefore, the main factor responsible of frequency variations should not be based on the available space.

The linear relationship established between $\nu_3(i-BH_4^-)$ and $a_0(AX)$ can be presented empirically according to:

$$\nu_3(i-BH_4^-) = \alpha \cdot a_0(AX) + \beta \quad (5.4)$$

where α is the gradient and β is a constant obtained from the linear regressions. These parameters are given in **Table 5.4**. The R^2 values (> 0.98) are satisfactory and indicate the effectiveness of the linear correlations.

Table 5.4: Empirical constants (α and β) of the linear relationship $\nu_3(i-BH_4^-) = \alpha \cdot a_0(AX) + \beta$ for common cation A- series and common anion X-series

A-groups	α ($\text{cm}^{-1} \text{ \AA}^{-1}$)	β (cm^{-1})	R^2
Na-group	-119.9275	3054.0962	0.9848
K-group	-88.8481	2884.8024	0.9928
Rb-group	-69.1765	2757.6490	0.9956
X-groups			
Cl-group	-83.1449	2850.9477	0.9999
Br-group	-56.6220	2668.9545	0.9999
I-group	-35.7190	2511.7233	0.9957

The absolute value of α of the A-series decreases when descending column 1 of the periodic table, i.e. in the order Na-series > K-series > Rb-series. Similarly, the absolute values of α of the X-series decrease when going down column 17, i.e. in the order Cl-series > Br-series > I-series. Assuming that the gradient α of the linear regression gives insight into the rate at which changes are taking place, i.e. how much the variations of $a_0(\text{AX})$ affect the values of $v_3(\text{i-BH}_4^-)$, obtained results suggest that the dependency of $v_3(\text{i-BH}_4^-)$ on $a_0(\text{AX})$ diminishes across column 1 and column 17 of the periodic table, i.e. when increasing the ionic radii of A and X of A-series and X-series, respectively. Furthermore, the absolute values of α of A-series are greater than those of the X-series. Since in a given A-series the anionic element is varying and for a given X-series the cationic element is changing, the obtained results suggest that the anionic element X of AX has more impact on $v_3(\text{i-BH}_4^-)$ than the cationic element A.

The interrelations established between $v_3(\text{i-BH}_4^-)$, $a_0(\text{AX})$ and $R(\text{AX})$ can be extended and discussed in term of other parameters of AX as the negative value of the standard enthalpy of formation ($-\Delta H$ or exothermicity), the fractional ionic character of the bond for AX (I_c) and χ_p of A and X, respectively.

$-\Delta H$ decreases with increasing a_0 of the homologous A-series. Moreover, $-\Delta H$ and I_c increase with increasing $R(\text{AX})$ of A-series and X-series [184]. By combining these correlations with those deduced from **Figure 5.10**, it can be deduced that for the same cationic A-series, $v_3(\text{i-BH}_4^-)$ is positively correlated to $-\Delta H$ and I_c of AX, i.e. an increase of $v_3(\text{i-BH}_4^-)$ is accompanied with an increase of $-\Delta H$ and I_c of AX. For the homologous series with the same anionic element, an inverse correlation lies between $v_3(\text{i-BH}_4^-)$ and $-\Delta H$ and I_c of AX, i.e. an increase of $v_3(\text{i-BH}_4^-)$ is accompanied with a decrease of $-\Delta H$ and I_c of AX (**Figure 5.11**).

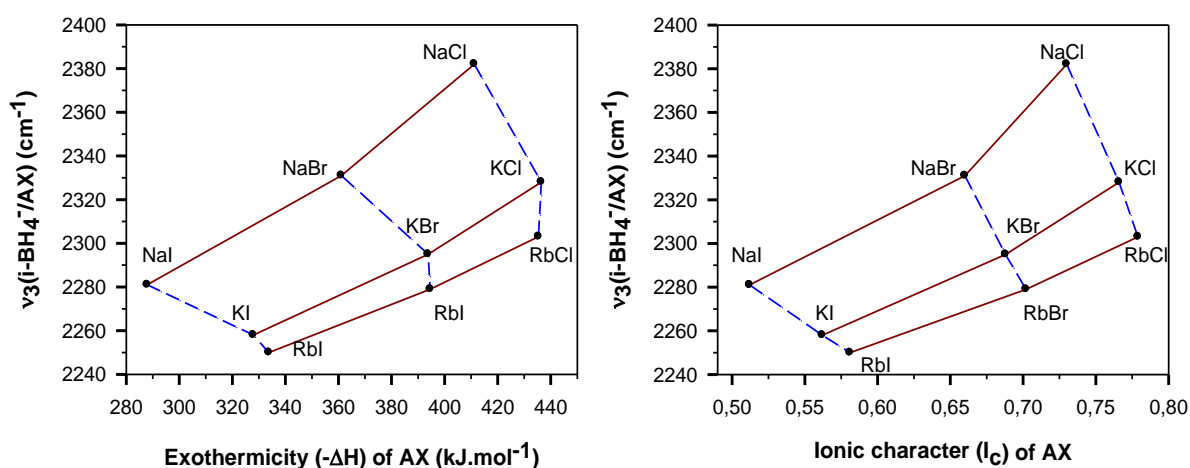


Figure 5.11: Graphical representations of $\nu_3(i-BH_4^-)$ in function of (a) exothermicity $-\Delta H$ of AX and (b) ionic character I_c of the bond for AX halides. Solid lines are for A-series and dashed lines are for X-series.

According to Pauling, χ_P of an atom in a molecule is the power of this atom to attract electrons toward itself [185]. χ_P is dimensionless and varies in an opposite direction to that observed for the ionic radius in the periodic table, i.e. χ_P increases by going from left to right across a period, and decreases by moving down a column. Thus, small cations and anions in homologous A- or X-series have higher χ_P and higher $\nu_3(i-BH_4^-)$.

The size and electronegativities of the cation and anion complexes determine the structure and bonding of the compound [171]. The correlations between $\nu_3(i-BH_4^-)$ and $\chi_P(A)$ and $\chi_P(X)$ for the different series, could provide some information about the stability of the borohydride. A more charge transfer to BH_4^- anion results in stronger B-H bonds stabilizing thus the borohydride [13]. A more electronegative cation destabilizes the borohydride by attracting the electron density toward itself and reducing the electron density in the B-H bonds [168]. For MBH_4 salts the thermal stability increases in the order $NaBH_4 < KBH_4 < RbBH_4 < CsBH_4$ [20] whereas χ_P of the cation increases in the opposite way. At the same time according to the Raman and ATR results of Renaudin et al. [81], the stretching frequencies ν_1 and ν_3 vary in the opposite direction. This indicates an inverse correlation between the stability of the borohydride and ν_3 of BH_4^- anion. Basing on these results, it can be said that in a given X-group where A is changing, an increase of $\nu_3(i-BH_4^-)$ is accompanied with a decrease of the stability. At the same time, $a_0(AX)$, $R(AX)$, $I_c(AX)$ and $-\Delta H(AX)$ decrease.

DSC data reveal stabilization with increasing chloride-substitution in NaBH_4 [176]. Sieverts measurements of the hexagonal $\text{Li}(\text{BH}_4)_{0.5}\text{Br}_{0.5}$ indicate similar H_2 release as for the un-substituted pattern LiBH_4 [165]. This may indicate that the substitution with a more electronegative anion localizes the negative charge on the B-H bond, stabilizing, thus, the borohydride. Therefore, it could be deduced that for the A-series where the anionic element X is varying, an increase of $\nu_3(\text{i-BH}_4^-)$ is accompanied with an increase of the stability. At the same time, $a_0(\text{AX})$ decreases, $R(\text{AX})$, $I_c(\text{AX})$ and $-\Delta\text{H}(\text{AX})$ are increased. Further experiments are still needed to demonstrate the correlations suggested between χ_P of the anion, ν_3 and the thermal stability of the borohydride.

The correlations found between $\nu_3(\text{i-BH}_4^-)$ and the different parameters ($a_0, -\Delta\text{H}$, I_c , R , the effective radii of the cation (r^+) and the anion (r^-), χ_P of the cation and the anion) are summarized in (Table 5.5). The effect on the stability of the borohydride is also indicated.

Table 5.5: Correlations found between $\nu_3(\text{i-BH}_4^-)$ and the different parameters of the AX halide (the cell parameter a_0 , the effective radii of the cation (r^+) and the anion (r^-), the radius ratio $R = r^+/r^-$, the Pauling electronegativity χ_P , the fractional ionic character I_c and the standard enthalpy of formation ΔH). The effect on the stability of BH_4^- is also indicated.

for a given A-group : X is varying	for a given X-group : A is varying
$\nu_3(\text{i-BH}_4^-)$ increases	$\nu_3(\text{i-BH}_4^-)$ increases
$a_0(\text{AX})$ decreases	$a_0(\text{AX})$ decreases
R increases	R decreases
r^- decreases	r^+ decreases
$\chi_P(\text{X})$ increases	$\chi_P(\text{A})$ increases
I_c increases	I_c decreases
$-\Delta\text{H}$ increases	$-\Delta\text{H}$ decreases*
Stability increases	Stability decreases

*non-linear

5.2.5 BH_4^- -frequency variations using empirical experimental models

BH_4^- anion isolated in AX replaces the anion X^- at individual sites in the alkali halide lattice. Several complex empirical functions have been developed to carry out a quantitative evaluation of the frequencies shift of an isolated ion in foreign surroundings. In a general way, the potential function (V') governing the vibration of a molecular ion substituted in NaCl-type cube can be regarded as the sum of the potential function of the free ion (V_F) and the interaction energy (V) arising from the presence of the environment (equation 5.5) [186].

$$V' = V_F + V \quad (5.5)$$

The perturbing potential function has two distinct effects on the considered ion: (i) the second derivatives of the perturbing potential with respect to appropriate symmetry coordinates which represent additional contributions to the effective force constants of the impurity ion and (ii) the first derivatives of the perturbing potential representing the forces which modify the equilibrium internuclear spacing within the ion. Accordingly, the frequency shift of the i th normal mode of the solute is given by:

$$\frac{\Delta v_i}{v_i} = \frac{1}{2ki} \left(\frac{\partial^2 V}{\partial S_i^2} - \frac{3a_{iii}}{a_{ii}} \frac{\partial V}{\partial S_i} - \sum_r \frac{a_{iir}}{a_{rr}} \frac{\partial V}{\partial S_r} \right) \quad (5.6)$$

where ki is the force constant of the i th mode, S_i are the normal co-ordinates and a are the potential constants [187]. For a diatomic ion described by a Morse potential of the form $V_F = D(1 - e^{-\beta\xi})^2$ the equation is reduced to:

$$\frac{\Delta v}{v} = \frac{1}{2k} \left(\frac{\partial^2 V}{\partial \xi^2} + 3\beta \frac{\partial V}{\partial \xi} \right) \quad (5.7)$$

where $\xi = r - r_e$, the change in the internuclear spacing [187, 188]. The perturbing potential can be explicitly expressed based on the classical theory of ionic crystals given by Born and Mayer as the sum of a polarization term (V_p) arising from static or dynamic polarization of the isolated ion or the surrounding lattice, a columbic term (V_c) describing the charge-charge interaction between the solute ion and the supporting alkali halide lattice and a repulsive short-range term (V_s) due to the overlap of electron density of the isolated ion with its

surrounding ions of the lattice [186, 188]. In most cases where the terms of equation (5.7) or its equivalent have been evaluated, it was found that the first derivative term (force multiplied by anharmonicity) dominated the frequency shift calculations [187]. For example, for the cyanide ion CN^- isolated in various alkali halides [188], the authors observed that the frequency shifts calculations are dominated by the repulsive term shortening the CN bond.

An approximately linear relation is obtained between $\nu_3(\text{i-BH}_4^-)$ and the short range lattice energies of AX (**Figure 5.12**). The short lattice energy of AX can be considered as the contribution of the repulsive, dipole-dipole and dipole-quadrupole interaction energies given by the Born-Mayer equation of AX. These values are tabulated in **Table 5.6** and show that the repulsive forces constitute the major part. Similar linear correlations were obtained for the nitrate anion NO_3^- [32] and CN^- [188] embedded in different halide matrices.

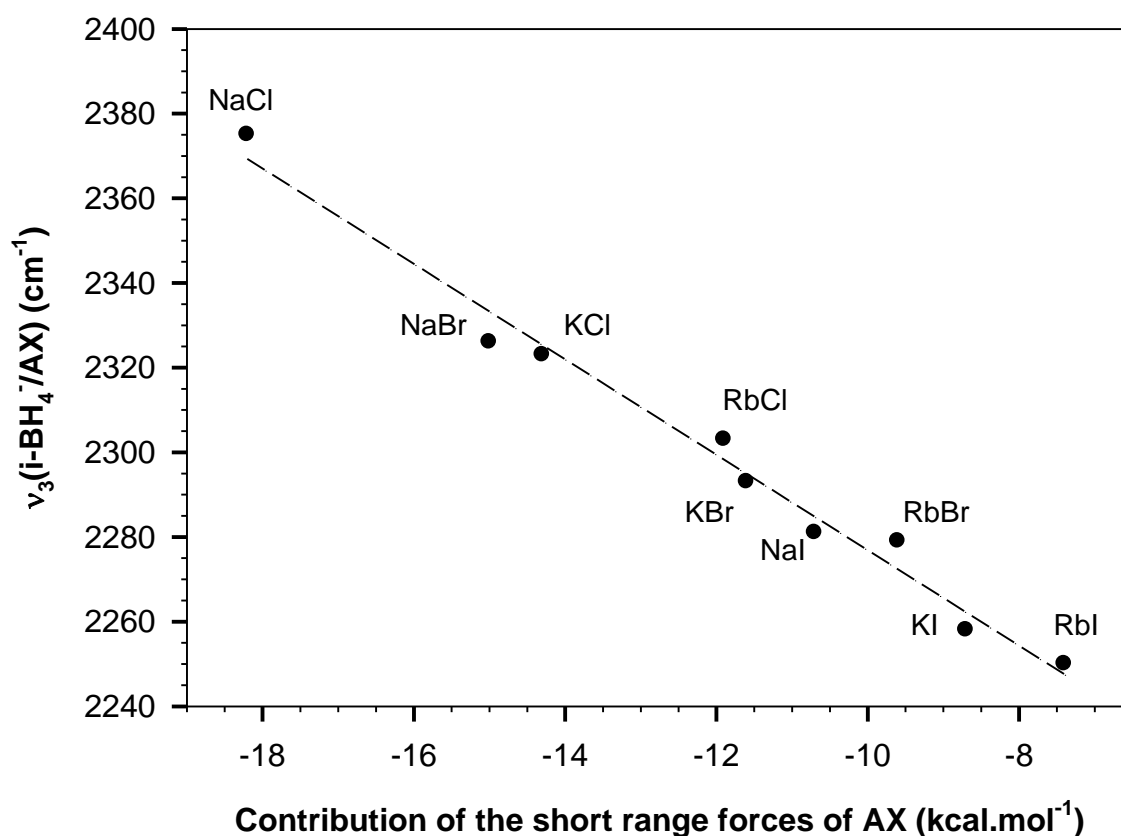


Figure 5.12: Graphical representation of $\nu_3(\text{i-BH}_4^-)$ as a function of the contribution of the short range interaction energies in the corresponding AX. Dashed line is the linear regression.

Table 5.6: Contribution of the short range forces of the alkali halides as given by the Born-Mayer equation (in kg.cal.mol⁻¹) [189]

AX	Repulsive	Dipole-dipole	Dipole-quadrupole	Short range
NaCl	-23.5	5.2	0.1	-18.2
NaBr	-20.6	5.5	0.1	-15
NaI	-17.1	6.3	0.1	-10.7
KCl	-21.5	7.1	0.1	-14.3
KBr	-18.6	6.9	0.1	-11.6
KI	-15.9	7.1	0.1	-8.7
RbCl	-19.9	7.9	0.1	-11.9
RbBr	-17.6	7.9	0.1	-9.6
RbI	-15.4	7.9	0.1	-7.4

Zhang et al. [190] studied the properties of MBH_4 ($M = Na, K, Rb$ and Cs) using first principle calculations (projected augmented plane-wave method). The optimized structures suggest a variation of 0.0068 Å for the B-H distances between $NaBH_4$ and $CsBH_4$. According to the experimental results of Renaudin et al. [81], the B-D distances are diminished by 0.039 Å from $NaBD_4$ to $CsBD_4$ salts. Density functional theory (DFT) calculations at generalized gradient approximation (GGA) level calculations indicated negligible variations of B-H distances for MBH_4 as well as for the solid solutions $Na(BH_4)_{(1-x)}Cl_x$, $Na(BH_4)_{(1-x)}Br_x$ and $Na(BH_4)_{(1-x)}I_x$ for $x = 0.25, 0.5$ and 0.75 . The variations are rather due the effective potential function related to the changes of the neighborhood of BH_4^- [191]. Further experimental and theoretical studies investigating in more details the different solid solutions of BH_4^- are highly recommendable to more clarify the discrepancies between the results of Renaudin et al. [81] and those obtained from first principle calculations [190, 191].

6. Thermal dehydration of Sodium Metaborate Tetrahydrate $\text{NaBO}_2 \cdot 4\text{H}_2\text{O}$

6.1 State of the art

6.1.1 Borates and sodium metaborate compounds

Boron is usually coordinated to oxygen in three- or four-fold coordination forming trigonal planar $(\text{BO}_3)^{3-}$ and tetrahedral $(\text{BO}_4)^{5-}$ primary units, respectively. These fundamental units often polymerize by oxygen-sharing atoms yielding complex varieties of borate anions [192]. Hydration of borates is referred to the presence of crystalline H_2O molecules and/or structural water in the form of hydroxyls $-\text{OH}$ groups. The representation $\text{ABO}_2 \cdot y\text{H}_2\text{O}$ with A being the alkali metal, is commonly used to represent the hydration degree y of the borate including H_2O and $-\text{OH}$ groups.

The thermal dehydration of synthetic and mineral borates produces anhydrous borates. It is a complex process which involves multiple steps including generally the release of crystal water, the removal of $-\text{OH}$ groups (dehydroxylation), amorphization and recrystallization of the anhydrous remains of the structure of the precursor solid [193]. Therefore, the thermal dehydration of borates has been considered as a relevant case for the investigations of reactions which involve amorphization and recrystallization in the solid state phase [194]. For example, the dehydration of lithium borates ($\text{LiBO}_2 \cdot 8\text{H}_2\text{O}$ equivalent to $\text{Li}(\text{H}_2\text{O})_4\text{B}(\text{OH})_4 \cdot 2\text{H}_2\text{O}$, $\text{LiB}_5\text{O}_8 \cdot 5\text{H}_2\text{O}$ equivalent to $\text{Li}(\text{H}_2\text{O})_3\text{B}_5\text{O}_6(\text{OH})_4$ [195]) and potassium borates ($\text{K}_2\text{B}_4\text{O}_7 \cdot 4\text{H}_2\text{O}$ [196]) reveals the formation of amorphous anhydrous products with the same B/Li and B/K ratios as the hydrated lithium and potassium precursors, respectively, which further crystallize upon heating.

The ordering of the release of H_2O and $-\text{OH}$ groups depends generally on the strength of their bonds [193]. The dehydroxylation involves condensation reaction leading to cyclic compounds:



Sodium metaborates $\text{NaBO}_2 \cdot y\text{H}_2\text{O}$ are derivatives of BO_2^- . Five principal different degrees of hydration have been reported until now, with $y = 4, 2, 2/3, 1/3$ and 0. Crystallographic data and molecular structure of the corresponding borate anions are outlined in **Table 6.1** following the references as given.

Tetrahydrate $\text{NaBO}_2 \cdot 4\text{H}_2\text{O}$ and dihydrate $\text{NaBO}_2 \cdot 2\text{H}_2\text{O}$ also described as $\text{NaB}(\text{OH})_4 \cdot 2\text{H}_2\text{O}$ [197] and $\text{NaB}(\text{OH})_4$ [198], respectively, contain the tetrahedral tetrahydroxoborate anion $\text{B}(\text{OH})_4^-$. The unit cells of the tetrahydrate and the dihydrate are shown in **Figure 6.1**. The tetrahydrate contains in addition to $\text{B}(\text{OH})_4^-$ anions two crystallographically distinct molecules of water.

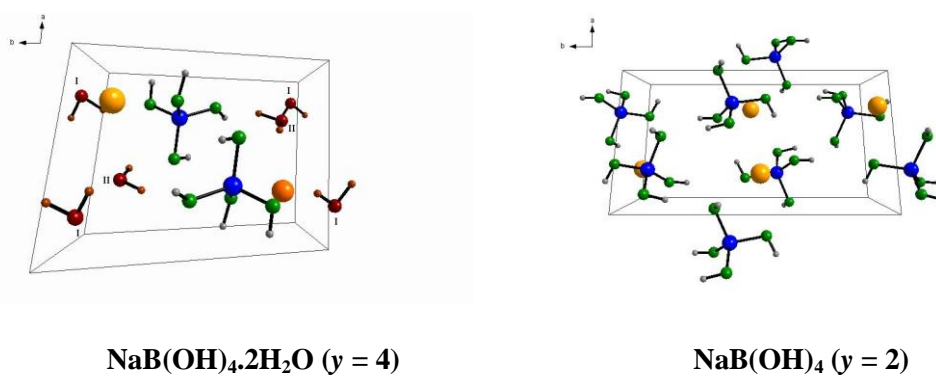
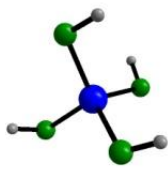
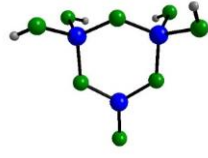
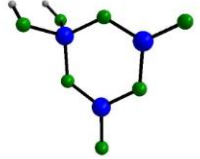
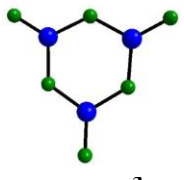


Figure 6.1: Crystal structures of sodium metaborate tetrahydrate and dihydrate (projection along c-axis). I and II denote the two distinct crystallographic molecules of water of the tetrahydrate (Na: orange, B: blue, O: green, H of $\text{B}(\text{OH})_4^-$: gray and H_2O molecules: dark red). I and II denote the two types of crystalline molecular water of the tetrahydrate.

The borate anion in the two-third $\text{NaBO}_2 \cdot 2/3\text{H}_2\text{O}$, the one-third $\text{NaBO}_2 \cdot 1/3\text{H}_2\text{O}$ and the anhydrous NaBO_2 phases consists of 6-membered ring formed by oxygen corner sharing between three boron entities, called triborate anion.

The anhydrous sodium metaborate has the structure formula $\text{Na}_3\text{B}_3\text{O}_6$ and contains $(\text{B}_3\text{O}_6)^{3-}$ anion built of three $(\text{BO}_3)^{3-}$ moieties which consist of a boron atom B three-fold coordinated to three oxygen O atoms [199]. The borate $(\text{B}_3\text{O}_6)^{3-}$ anion occurs in the potassium salt KBO_2 but not in the lithium salt LiBO_2 [200]. The same borate anion with extra-cyclic oxygen being hydroxylated is found in the orthorhombic form of the metaboric acid $\text{B}_3\text{O}_3(\text{OH})_3$ [201].

Table 6.1: Crystallographic data of $\text{NaBO}_{2,y}\text{H}_2\text{O}$ compounds as reported in the literature in addition to the molecular structure of the borate anion (B: blue, O: green, H: gray).

$\text{NaBO}_{2,y}\text{H}_2\text{O}$	Crystallographic data	Borate anion	Ref.
$y = 4$ $\text{NaB}(\text{OH})_4 \cdot 2\text{H}_2\text{O}$	P-1 (triclinic) a= 6.126 Å b= 8.18 Å c= 6.068 Å $\alpha = 67.92^\circ$ $\beta = 110.58^\circ$ $\gamma = 101.85^\circ$	 $\text{B}(\text{OH})_4^-$	[197]
$y = 2$ $\text{NaB}(\text{OH})_4$	$P2_1/a$ (monoclinic) a= 5.886 Å b= 10.566 Å c= 6.146 Å $\beta = 111.60^\circ$		[198]
$y = 2/3$ $\text{Na}_3[\text{B}_3\text{O}_4(\text{OH})_4]$	C1c1 a= 12.8274 Å b= 7.7276 Å c= 6.969 Å $\beta = 98.161^\circ$	 $[\text{B}_3\text{O}_4(\text{OH})_4]^{3-}$	[202]
$y = 1/3$ $\text{Na}_3[\text{B}_3\text{O}_3(\text{OH})_2]$	Pnma a= 8.923 Å b= 7.152 Å c= 9.548 Å	 $[\text{B}_3\text{O}_5(\text{OH})_2]^{3-}$	[203]
$y = 0$ $\text{Na}_3\text{B}_3\text{O}_6$	R-3c a= 11.925 Å c= 6.439 Å	 $(\text{B}_3\text{O}_6)^{3-}$	[199]

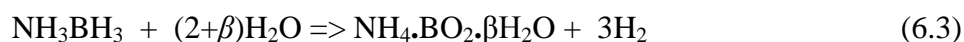
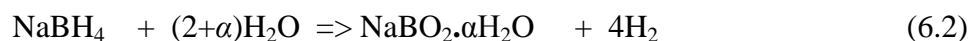
The triborate anion may also contain tetrahedral boron moieties. For example, the one-third phase with the structural formula $\text{Na}_3[\text{B}_3\text{O}_3(\text{OH})_2]$ contains the triborate anion $[\text{B}_3\text{O}_5(\text{OH})_2]^{3-}$ which is formed of two $(\text{BO}_3)^{3-}$ moieties and one $[\text{BO}_2(\text{OH})_2]^{3-}$ corresponding to a boron atom coordinated to two oxygen atoms and two $-\text{OH}$ groups [203]. The two-third phase $\text{Na}_3[\text{B}_3\text{O}_4(\text{OH})_4]$ contains $[\text{B}_3\text{O}_4(\text{OH})_4]^{3-}$ anion formed of two tetrahedral boron $[\text{BO}_2(\text{OH})_2]^{3-}$ entities and one boron triangular group $(\text{BO}_3)^{3-}$ [202].

Other hydration degrees of $\text{NaBO}_2 \cdot y\text{H}_2\text{O}$ including the monohydrate $\text{NaBO}_2 \cdot \text{H}_2\text{O}$ [204] and the hemihydrate $\text{NaBO}_2 \cdot (1/2)\text{H}_2\text{O}$ [204, 205] have been claimed. Even though, XRD patterns of these compounds were given [204], no single phase crystallographic structures were determined. Corazza et al. [203] suggested that the hemihydrate form proposed as $1\text{Na}_2\text{O}:1\text{B}_2\text{O}_3:1\text{H}_2\text{O}$ corresponds in the reality to a molar constitution of 3:3:2 with the structure formula $\text{Na}_3[\text{B}_3\text{O}_5(\text{OH})_2]$ which represents the one-third phase. Recently, Andrieux et al. [206] revised the $\text{NaBO}_2\text{-H}_2\text{O}$ phase diagram and suggested the non-existence of the hemihydrate (1:1:1) and the monohydrate (1:1:2) as stable compounds.

The thermal dehydration of $\text{NaBO}_2 \cdot y\text{H}_2\text{O}$ has been the subject of many previous papers using thermogravimetric analyses [61, 85, 207], in-situ X-ray diffraction [85, 206] and in-situ Raman spectroscopy [85]. Kanturk et al. [207] reported five mass loss steps for $\text{NaBO}_2 \cdot 4\text{H}_2\text{O}$. The two first were assigned to the release of crystal molecular water yielding $\text{NaB}(\text{OH})_4$ below 100°C and the last three steps to the removal of $-\text{OH}$ groups yielding the anhydrous phase near 300°C . Beaird et al. [85] suggested that the thermal decomposition of $\text{NaB}(\text{OH})_4$ initiates near 100°C and yields $\text{NaBO}_2 \cdot 1/3\text{H}_2\text{O}$ around 150°C and then the anhydrous NaBO_2 at much higher temperatures ($T > 250^\circ\text{C}$). Andrieux et al. [206] performed in-situ X-ray diffraction studies on $\text{NaBO}_2 \cdot 4\text{H}_2\text{O}$. The authors observed a swelling of the sample near 100°C preventing the identification of the formed compound. The decomposition of the $y = 2/3$ phase yields the $y = 1/3$ phase followed by the $y = 0$ phase. The $y = 2/3$ phase can be synthetically obtained by subjecting the tetrahydrate to an isotherm at 84°C for 12 h followed by a slow heating ($1^\circ\text{C}/\text{min}$) to 110°C where another isotherm has to be applied for 12 h [202]. A longer isotherm at 110°C (3 days) results in the formation of the $y = 1/3$ phase [206].

6.1.2 Role of $\text{NaBO}_2 \cdot y\text{H}_2\text{O}$ in H_2 release from NaBH_4 and NH_3BH_3

Metaborate compounds constitute the by-products of the hydrolysis reactions of NaBH_4 and NH_3BH_3 according to reactions (6.2) and (6.3), respectively.



α and β are the excess hydration factor and represent the unutilized H_2O in the H_2 release reaction. This notion was introduced by Marrero-Alfonso et al. [61] in their investigations of the hydrolysis of solid NaBH_4 .

In an ideal way, the quantity of water just required to evolve $\text{H}_{2(\text{g})}$ is only considered, i.e. $\alpha = 0$ and $\beta = 0$. This implies that the hydrogen storage capacity of $\text{NaBH}_4\text{-H}_2\text{O}$ and $\text{NH}_3\text{BH}_3\text{-H}_2\text{O}$ systems would be 10.8 and 9.1 wt% hydrogen, respectively. The hydrogen storage capacity is calculated according to [206]:

$$\frac{m(\text{H}_2)}{m(\text{reactants})} \times 100 \quad (6.4)$$

In practical systems, the low solubility of metaborate by-products reduces the storage capacities. For example, in the case of NaBO_2 by-product where only 28 g could be dissolved in 100 g H_2O at 25°C [54], the reaction (6.2) would give only 2.9 wt% hydrogen to keep the system in solution! Consequently, as water enters in the reagents, the amount of hydrogen provided by the reactions (6.2) and (6.3) decreases when α and β increase (**Figure 6.2**). Therefore, minimizing α and β is the key to improve the hydrogen storage capacity of $\text{NaBH}_4\text{-H}_2\text{O}$ and $\text{NH}_3\text{BH}_3\text{-H}_2\text{O}$ systems, respectively [61, 85, 206].

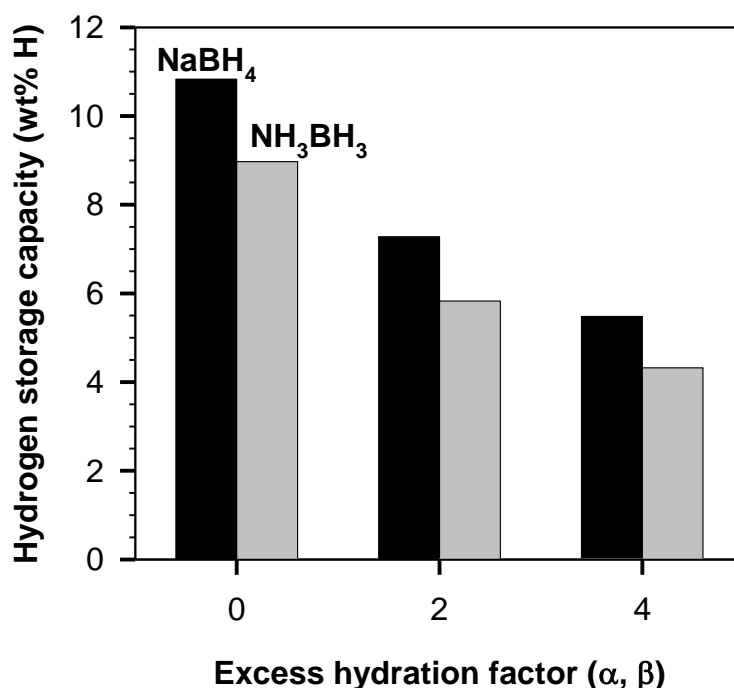
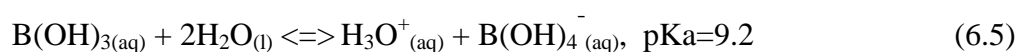


Figure 6.2: Role of the excess hydration factors α and β in the hydrogen storage capacity of $\text{NaBH}_4\text{-H}_2\text{O}$ (black) and $\text{NH}_3\text{BH}_3\text{-H}_2\text{O}$ (gray) systems according to reactions (6.2) and (6.3), respectively (α and β equal to 0, 2 and 4)

The main constituent of the hydrolysate of NH_3BH_3 in presence of a catalyst is the boric acid H_3BO_3 [208]. Boric acid is a weak Lewis acid and is present in water at pH lower than 9. At higher pH the ionized form $\text{B}(\text{OH})_4^-$ is dominant (6.5) [209].



Marrero-Alfonso et al. [61] obtained $\text{NaB}(\text{OH})_4$ from the hydrolysis of solid NaBH_4 with water steam at 110°C regardless of the hydride/water ratio. Therefore, the hydration degree of the metaborate by-product is not a direct function of $\text{H}_2\text{O}/\text{NaBH}_4$ ratio or more precisely of the excess hydration factor α of the reaction (6.2). Even if there is enough water to build the tetrahydrate ($\alpha = 4$), the isolated by-product is the dihydrate and un-reacted water remains unbound. Basing on the refining binary phase diagram $\text{NaBO}_2\text{-H}_2\text{O}$ at ambient pressure of Andrieux et al. [206], the hydrolysis product of NaBH_4 about 103°C might be the $y = 2/3$ phase. Andrieux et al. referred the discrepancy between their results and those of Marrero-Alfonso et al. to the experimental conditions of Marrero-Alfonso et al. as the hydrolysis in a closed reactor which may modify the thermodynamic equilibrium.

Alternatively, the $y = 2/3$ phase could be formed in-situ at 110°C but is further rehydrated to NaB(OH)_4 upon cooling down. Furthermore, the attempts of Andrieux et al. to crystallize the $y = 2/3$ solid in equilibrium with its saturated borate solution failed, even though according to the $\text{NaBO}_2\text{-H}_2\text{O}$ phase diagram, the binary phase domain liquid + $\text{NaBO}_2\cdot(2/3)\text{H}_2\text{O}$ could be achieved between 103 and 131.6°C. A metastable gel was instead obtained.

From this literature survey, the mechanism of dehydration of sodium metaborate tetrahydrate and dihydrate still needs further clarifications. Particularly interesting is the temperature range between 100 and 150°C where the decomposition of NaB(OH)_4 and the condensation to the tetraborate anion take place. The objective of this chapter is to contribute to a better understanding of the dehydration mechanism. This knowledge is paramount in the field of hydrolysis of NaBH_4 and NH_3BH_3 for H_2 release. Therefore, the thermal decomposition of the tetrahydrate was refined using thermogravimetric, in-situ X-ray diffraction and TIR experiments performed from room temperature to 400°C. TG/DTA analyses were carried out using different heating rates, 5, 2 and 1°C/min. The role of the flowing gas on the thermal dehydration was also investigated. The different dehydration products were isolated and characterized using XRD, IR and Raman.

6.2 Results and discussion

6.2.1 Characterization of the commercial $\text{NaBO}_2\cdot 4\text{H}_2\text{O}$ sample

The commercial sample of sodium metaborate tetrahydrate $\text{NaBO}_2\cdot 4\text{H}_2\text{O}$ was checked using IR spectroscopy and X-ray diffraction (using $0.03^\circ 2\theta/\text{s}$) (**Figure 6.3**). For the preparation of the IR pellet, the tools were dried at 120°C and then cooled down to room temperature to prevent any dehydration of the tetrahydrate sample. Obtained IR frequencies (**Figure 6.3a**) are in good agreement with those reported earlier for $\text{NaB(OH)}_4\cdot 2\text{H}_2\text{O}$ [89, 210]. A description of the IR modes is presented in section 6.2.5. The XRD patterns of the commercial sample confirm the tetrahydrate in addition to traces of NaB(OH)_4 .

To determine the proportion of the dihydrate in the commercial sample, three different samples were heated under He to 400°C for a total dehydration. The mass of each sample was taken before and after the thermal treatment. All thermally treated samples suggested mass losses of 50-51 % slightly lower than the theoretical loss of 52.23 % corresponding to 4 mol H_2O ($y = 4$). The obtained mass losses are equivalent to y of 3.83-3.91 which correspond to mixtures of 95.7-97.6 % tetrahydrate and 4.3-2.4 % dihydrate.

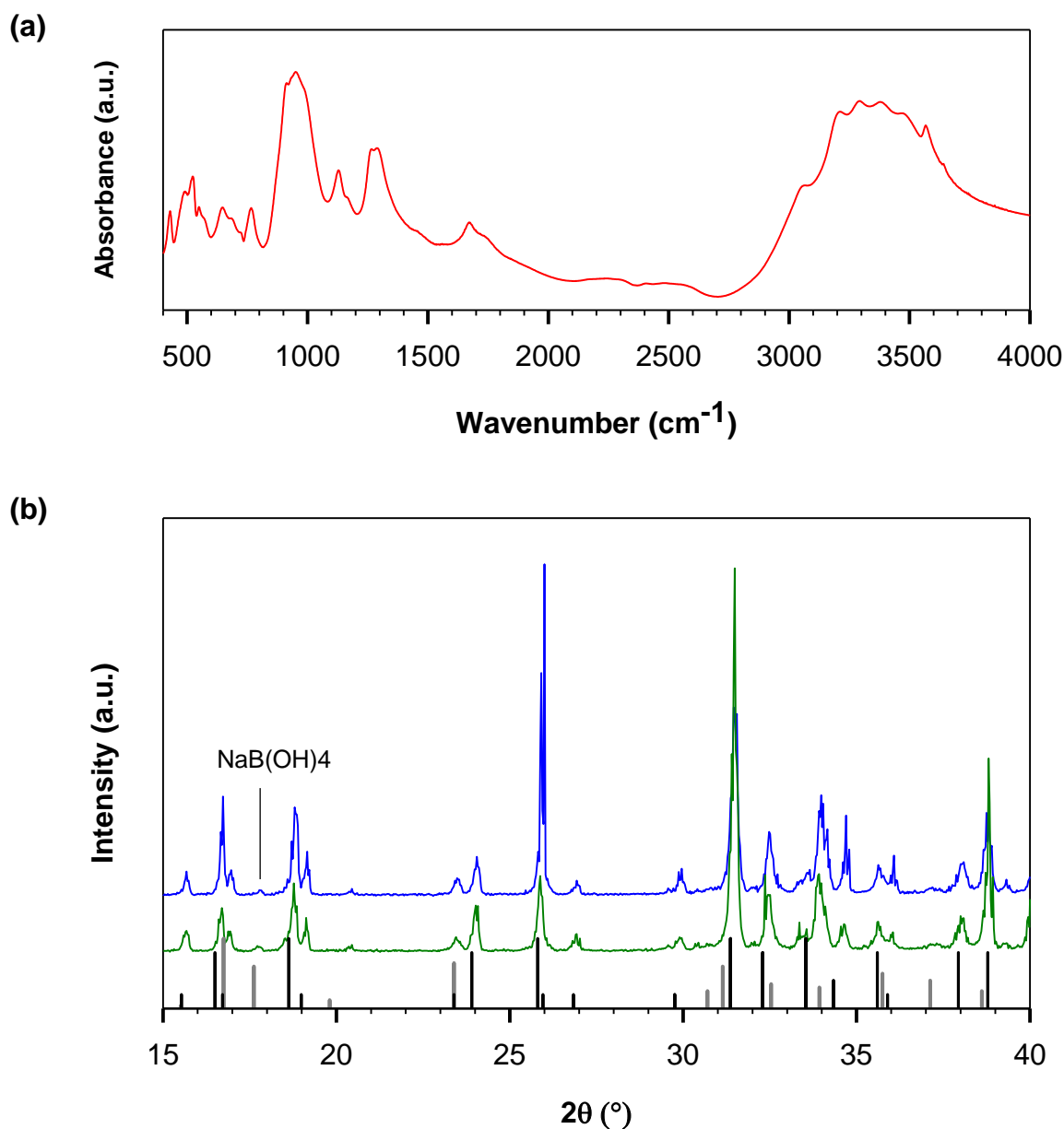


Figure 6.3: Characterization of the commercial sample of $\text{NaBO}_2 \cdot 4\text{H}_2\text{O}$. (a) IR spectrum and (b) X-ray patterns for two measurements. For comparison reflexes of $\text{NaBO}_2 \cdot 4\text{H}_2\text{O}$ (black bars) and $\text{NaBO}_2 \cdot 2\text{H}_2\text{O}$ (gray bars) references are shown.

6.2.2 TG/DTA analyses

Commercial samples of $\text{NaBO}_2 \cdot 4\text{H}_2\text{O}$ were subjected to different TG/DTA analyses from room temperature to 400°C. Different heating rates and flowing gases were considered. **He//novac//5** and **He//vac//5** denote the samples heated under He at 5°C/min without and with pre-evacuation before the heating run, respectively. The thermal treatment under He was also conducted on pre-evacuated samples at 2 and 1°C/min. These experiments are denoted

He//vac//2 and **He//vac//1**, respectively. To check the role of the flowing gas, the thermal decomposition of the tetrahydrate was carried out under synthetic air on pre-evacuated samples of $\text{NaBO}_2 \cdot 4\text{H}_2\text{O}$ at $5^\circ\text{C}/\text{min}$ (denoted **air//vac//5**) and at $1^\circ\text{C}/\text{min}$ (denoted **air//vac//1**). Information about the thermal treatments is given in **Table 6.2**.

Table 6.2: Information about the thermal treatments of the commercial $\text{NaBO}_2 \cdot 4\text{H}_2\text{O}$ sample.
 $\text{ML}_{\text{tot-curv}}$ is the total loss indicated on the TG curve and y_i is the equivalent mol of water.
 $\text{ML}_{\text{tot-calc}}$ is the total loss obtained by subtracting the mass of the crucible and the sample after the thermal treatment from that before the thermal treatment.

Experiment	Thermal treatment parameters	$\text{ML}_{\text{tot-curv}}(\%)$ y_i	$\text{ML}_{\text{tot-calc}}(\%)$	Principal mass loss steps
He//novac//5	He Without pre-evacuation $5^\circ\text{C}/\text{min}$	47.592 % 3.64	51	$y_i \Rightarrow y=2$: 23.19% (1.77mol) $y=2 \Rightarrow y=1/3$: 19.89% (1.52mol) $y=1/3 \Rightarrow y=0$: 4.5% (0.34mol)
He//vac//5	He With pre-evacuation $5^\circ\text{C}/\text{min}$	37.52 % 2.87	50.91	$y_i \Rightarrow y=2$: 12.15% (0.93mol) $y=2 \Rightarrow y=1/3$: 20.62% (1.58mol) $y=1/3 \Rightarrow y=0$: 4.81% (0.36mol)
He//vac//2	He With pre-evacuation $2^\circ\text{C}/\text{min}$	31.408 % 2.41	51	$y_i \Rightarrow y=2$: 5.84% (0.45mol) $y=2 \Rightarrow y=1/3$: 21.199% (1.62mol) $y=1/3 \Rightarrow y=0$: 4.303% (0.33mol)
He//vac//1	He With pre-evacuation $1^\circ\text{C}/\text{min}$	31.677 % 2.42	50.81	$y_i \Rightarrow y=2$: 6.063% (0.46mol) $y=2 \Rightarrow y=1/3$: 21.003% (1.61mol) $y=1/3 \Rightarrow y=0$: 4.674% (0.36mol)
air//vac//5	air With pre-evacuation $5^\circ\text{C}/\text{min}$	41.04 % 3.14		$y_i \Rightarrow y=2$: 15.837% (1.21mol) $y=2 \Rightarrow y=1/3$: 20.675% (1.58mol) $y=1/3 \Rightarrow y=0$: 4.68 % (0.36mol)
air//vac//1	air With pre-evacuation $1^\circ\text{C}/\text{min}$	30.039 % 2.3		$y_i \Rightarrow y=2$: 5.711% (0.44mol) $y=2 \Rightarrow y=1/3$: 20.119% (1.54mol) $y=1/3 \Rightarrow y=0$: 4.207% (0.32mol)

Effect of pre-evacuation/non-pre-evacuation

TG/DTA results of **He//vac//5** and **He//novac//5** experiments are shown in **Figure 6.4**.

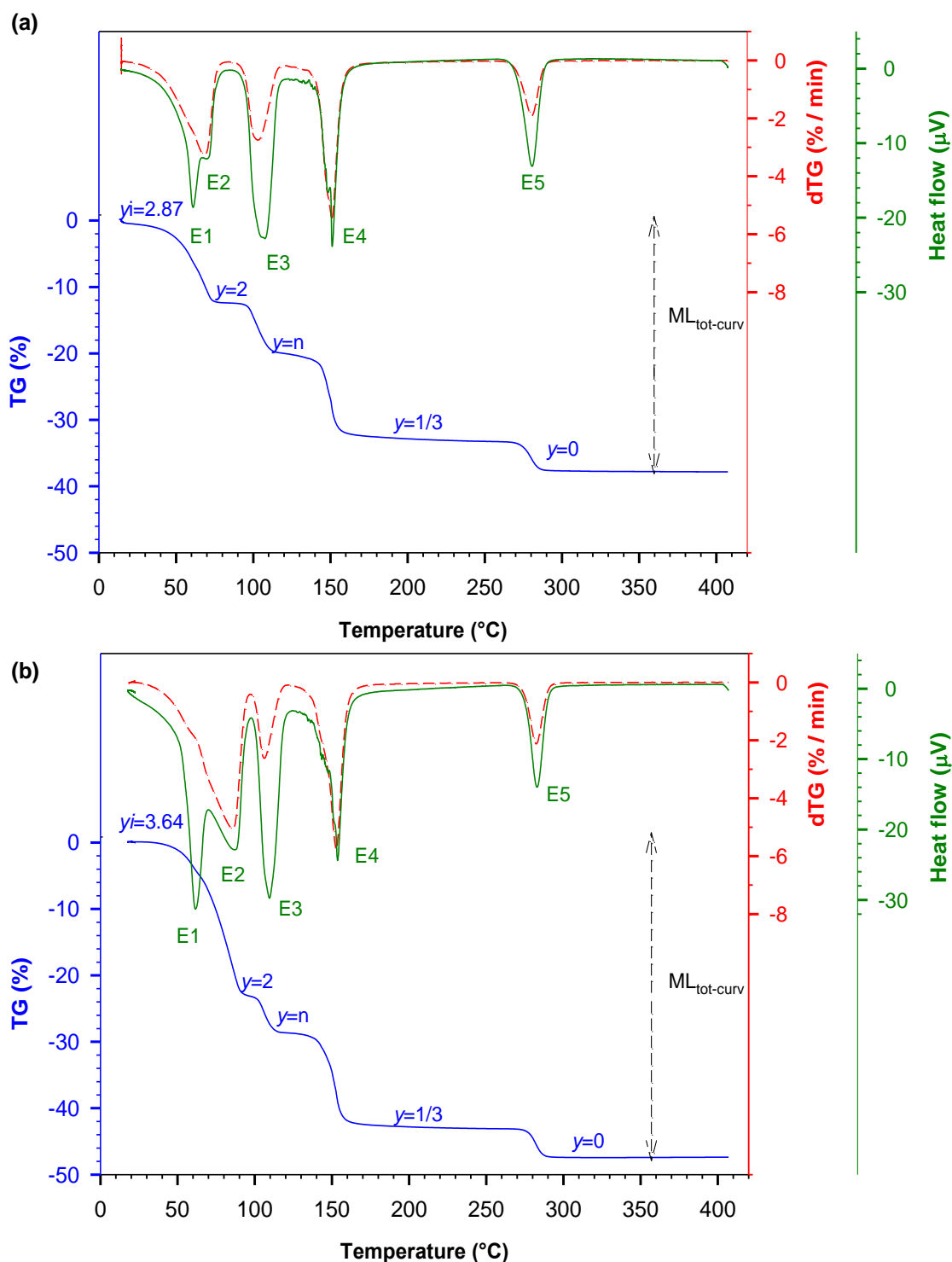


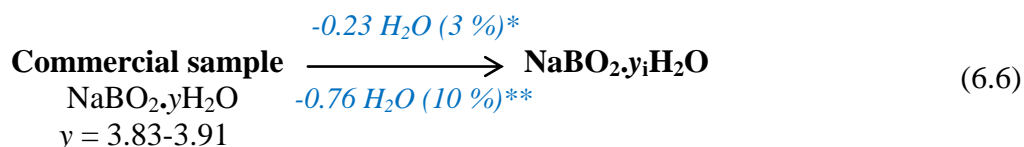
Figure 6.4: TG (solid blue lines), dTG (dashed red lines) and DTA (green solid lines) results for (a) He//vac//5 and (b) He//novac//5. The phases of the plateaus of the TG curves and the endotherms (E1-E5) are indicated.

The total mass losses on the TG curve are 37.52 % and 47.592 % for the pre-evacuated and the non-pre-evacuated samples, respectively. The mass loss evidenced by the TG curve is

denoted $ML_{\text{tot-curv}}$. The total mass losses were also calculated by subtracting the mass of the crucible and the sample after TG from that before the thermal treatment. Total mass losses obtained in this way are denoted $ML_{\text{tot-calc}}$ and are found to be 50.91 % for He//vac//5 and 51 % for He//nonvac//5.

The difference of $ML_{\text{tot-curv}}$ between the two experiments indicates that the samples have different fraction of water at the beginning of data acquisition. Assuming that the theoretical mass loss of 4 mol H_2O corresponds to a total mass loss of 52.23 %, the obtained values for $ML_{\text{tot-curv}}$ suggest that the hydration degrees of the samples at the beginning of data acquisition (denoted y_i) are approximately 3.64 for He//novac//5 and 2.87 for He//vac//5. The difference is approximately 10 % (equivalent to 0.77 mol H_2O) and is not related to the composition of the start commercial material used since $ML_{\text{tot-calc}}$ values are similar for both experiments. It is rather due to the history of the sample before the TG run. Since the only difference between the two experiments is the pre-evacuation of the sample in the TG apparatus before the thermal treatment for He//vac//5, it can be said that a significant amount of water is lost during pre-evacuation without being recorded and seen on the TG curves. There is a difference between the values of $ML_{\text{tot-curv}}$ and $ML_{\text{tot-calc}}$ for the non-pre-evacuated sample, too. This is about 3 % (0.23 mol H_2O) and indicates that a slight amount of water is lost under inert atmosphere without being recorded and seen on the TG curve. This could occur during the stabilization time of 10 min which is necessary for the equipment before starting to heat. Therefore, it can be said that the tetrahydrate commercial sample loses about 10 % H_2O during pre-evacuation in addition to 3 % during the stabilization time under He.

The unseen losses (about 13 % for the pre-evacuated sample and 3 % for the non-pre-evacuated sample) are part of crystal molecular water since structural water of sodium metaborates is stronger bonded to the system in the form of $-OH$ groups (6.6).



* loss during the stabilization time

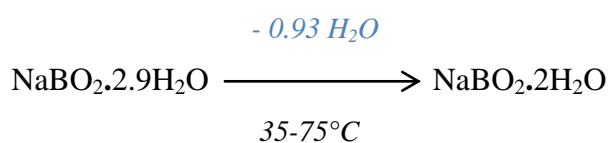
** loss during the pre-evacuation of the sample before the TG run

Mass losses initiate near 50°C and are completed about 300°C. The TG curves shows four plateaus centered at 85, 125, 210 and 310°C, respectively, indicating the formation of four different decomposition phases.

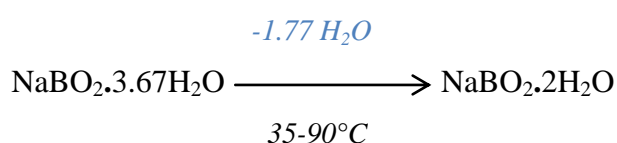
The DTA curves show five principal endothermic peaks denoted E1, E2, E3, E4 and E5 centered at about 60, 70-80, 105-110, 150 and 280°C, respectively. All endothermic effects were accompanied by more or less dehydration as can be concluded from a comparison of DTA and dTG curves.

The first plateau at 80-90°C corresponds to E1 and E2 and is accompanied with a mass loss of 12.15 % (equivalent to 0.93 mol H_2O) for He//vac//5, and 23.19 % (1.77 mol H_2O) for He//novac//5. These values suggest the formation of the $y = 2$ phase according to:

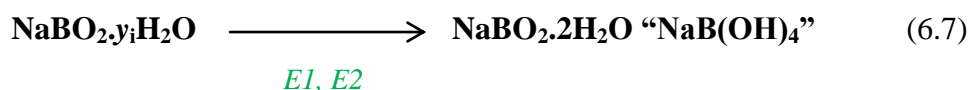
For He//vac//5:



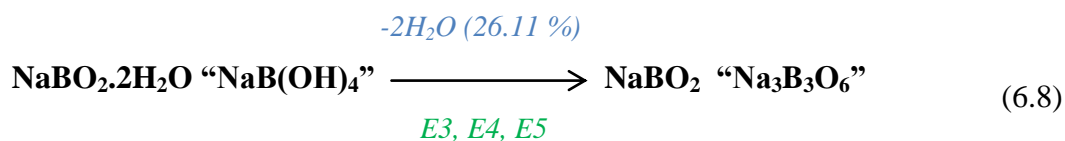
For He//novac//5:



In a more general way:



Between 100 and 300°C, mass losses of 25.4 and 24.58 % were observed for the pre-evacuated and the non-pre-evacuated samples, respectively, nearly close to the theoretical value of 26.1 % corresponding to the release of 2 mol H_2O and the formation of the anhydrous NaBO_2 . Thus, the plateau on the TG curve above 300°C is for the $y = 0$ phase and the three endotherms E1, E2 and E3 are related to the release of structural water (-OH groups) (6.8).

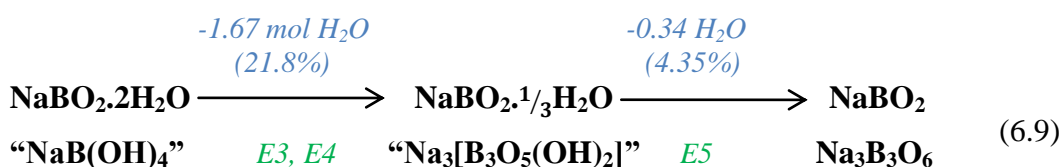


The given value is the theoretical loss

The fact that the mass loss corresponding to the dehydration reaction (6.8) is the same for both experiments, He//vac//5 and He//novac//5, and nearly close to the theoretical loss of 2 mol H₂O confirms that the unseen losses discussed above (reaction 6.6) are part of the crystal molecular water.

The reactions described in (6.7) and (6.8) support previous works suggesting that crystal molecular water is released below 100°C yielding NaB(OH)₄ which further dehydrates at higher temperatures in a stepwise fashion yielding the anhydrous metaborate at 300°C [206, 207].

Between 90 and 200°C, mass losses of 20.62 % (1.58 mol H₂O) and 19.89 % (1.52 mol H₂O) are observed for He//vac//5 and He//novac//5, respectively, which are close to the theoretical loss of 1.67 mol H₂O corresponding to the dehydration of the $y = 2$ to the $y = 1/3$ phases. The last dehydration step between 200 and 300°C is accompanied by mass losses of 4.81 % (0.36 mol H₂O) for the pre-evacuated sample and 4.5 % (0.34 mol H₂O) for the non-pre-evacuated sample, which are near of the theoretical loss of 0.34 mol H₂O corresponding to the dehydration of the $y = 1/3$ to the anhydrous $y = 0$ phases. Therefore, the TG-plateaus at 210 and 300°C can be assigned to the $y = 1/3$ and the $y = 0$ phases, respectively, and the endotherms E3 and E4 to the dehydration of the $y = 2$ to the $y = 1/3$ phases and E5 to the dehydration of the $y = 1/3$ to the $y = 0$ phases (reaction 6.9).



The given values are for the theoretical losses.

The plateau on the TG curve at 125°C indicates that the dehydration of the $y = 2$ to the $y = 1/3$ occurs through the formation of an intermediary phase. The only reported stable phase that may occur between the $y = 2$ and the $y = 1/3$ phases is the $y = 2/3$ phase [202]. Nonetheless, the obtained mass losses between 90 and 123°C, 5.6 % (0.43 mol H₂O) for the pre-evacuated and 7.87 % (0.6 mol H₂O) for the non-pre-evacuated samples, are too far from the theoretical loss of 1.34 mol H₂O corresponding to the dehydration of the $y = 2$ to the $y = 2/3$ phases. Beaird et al. [85] were not able to see the $y = 2/3$ phase during the thermal dehydration of NaB(OH)₄ even at slow heating rate (1°C/min). Therefore, the plateau at

115-130°C corresponding to E3 on the DTA curve indicates a new phase denoted as $y = n$. This dehydrates further to the $y = 1/3$ phase (E4) (reaction 6.10).



Further inspections of **Figure 6.4** suggest that E1 and E2 are sufficiently separated in He//novac//5 where y_i is higher. E1 is much more endothermic than E2, while E1 is correlated to a small shoulder on the dTG curve indicating a weak dehydration. This can be interpreted by structural endothermic changes (represented by E1) followed by the removal of the crystal molecular water (E2). Likewise, the high endothermicity of E3 accompanying the formation of the $y = n$ phase could not be referred to only the mass loss evidenced by TG and dTG curves.

Role of the heating rate

TG/DTA of pre-evacuated samples of $\text{NaBO}_2 \cdot 4\text{H}_2\text{O}$ performed under He using heating rates of 2 and 1°C/min (He//vac//2 and He//vac//1, respectively) are shown in **Figure 6.5** in comparison with He//vac//5.

The calculated values for the total mass losses $\text{ML}_{\text{tot-calc}}$ at 2 and 1°C/min were 51 and 50.81 %, respectively, close to those obtained at 5°C/min for He//vac//5 and He//novac//5. These are different from the total mass losses indicated on the TG curves $\text{ML}_{\text{tot-curv}}$ which are equal to 31.408 % at 2°C/min and 31.677 % at 1°C/min corresponding to y_i of 2.41 and 2.42, respectively, and are lower than that obtained at 5°C/min ($y_i = 2.87$).

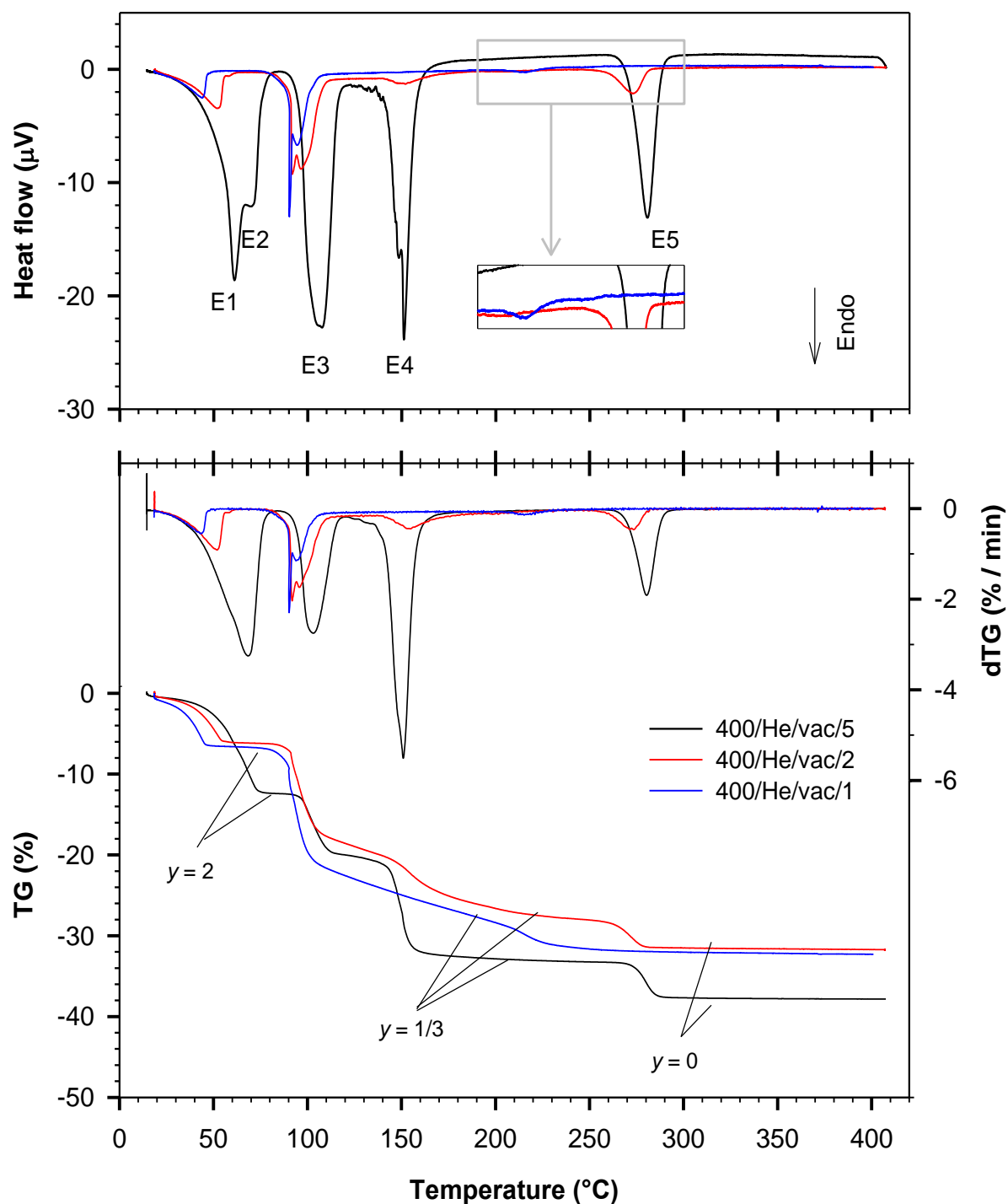


Figure 6.5: TG/DTA results of He//vac//2 and He//vac//1 in comparison with He//vac//5

The samples lose between 30 and 50°C about 5.84 % (0.45 mol H₂O) for He//vac//2 and 6.063 % (0.46 mol H₂O) for He//vac//1. These values can be referred to the formation of the $y = 2$ phase (reaction 6.7). At 5°C/min, this dehydration was accompanied with a higher mass loss (12.15 %). The dehydration of structural water between 100 and 300°C yields mass

losses of 25.337 % and 25.491 % for He//vac//2 and He//vac//1, respectively, close to that obtained at 5°C/min (25.42 %) and assigned to the formation of the anhydrous phase (reaction 6.8). Since all samples He//vac//5, He//vac//2 and He//vac//1 were evacuated the same, obtained results suggest that the unseen loss of the crystal molecular water due to the dehydration of the tetrahydrate during the stabilization time at room temperature under inert gas becomes more significant at slow heating rates yielding lower values for y_i . As a result, the endotherms E1 and E2 merge into a single broad endotherm at 2 and 1°C/min.

At 2°C/min, the TG curve shows a mass loss of 4.303 % (0.33 mol H_2O) between 240 and 300°C nearly close to the theoretical value characteristic of the dehydration of the $y = 1/3$ to the $y = 0$ phases (E5, reaction 6.9). At 1°C/min this dehydration can be assigned to the mass loss of 4.674 % (0.36 mol H_2O) observed between 191 and 270°C.

The individual steps of the dehydration of the $y = 2$ to the $y = 1/3$ phases are affected by the heating rate used. As the heating rate decreases from 5 to 2°C/min, the intermediary phase ($y = n$) between the $y = 2$ and the $y = 1/3$ phases is accompanied by more dehydration and it overlaps with the $y = 1/3$ phase. At 1°C/min, the $y = n$ and $y = 1/3$ phases could not be separated anymore.

It is well known that DTA curves are influenced by the heating rates. At higher heating rates, the peaks grow in intensity and move to higher temperatures. Furthermore, the DTA peaks are broadened as a function of temperature. In the present case, DTA peaks are reduced and slightly shifted to lower temperatures with decreasing the heating rate from 5 to 2°C/min. At 1°C/min, E5 appears as a very weak peak at 215°C and E4 is not detectable anymore.

At 2 and 1°C/min E3 is resolved in two endotherms peaked at 96°C and a sharper one at 91°C, respectively. The TG curve at 1°C/min shows an abrupt decrease at 90-95°C accompanied with a mass loss of 14.3 % (1.09 mol H_2O) followed by a subsequent mass loss of 6.82 % (0.53 mol H_2O) long-tailed in the temperature range between 105 to 210°C. The sharp endotherm at 91°C indicate a structural endothermic phenomenon accompanying the dehydration of the $y = 2$ to the $y = n$ phases.

As a consequence, the dehydration of the dihydrate to the one-third is affected by the heating rate used. It proceeds through the formation of a new intermediary stage ($y = n$) which could be better isolated at high heating rates. The formation of the $y = n$ phase may involve a

structural endothermic effect due to the sharp endotherm resolved at slow heating rates. The hydration degree of the intermediary stage $y = n$ is not stable and depends on the heating rate used. At slow heating rates it is less hydrated and overlap with the $y = 1/3$ phase.

Role of the flowing gas

To check the effect of the flowing gas on the thermal dehydration mechanism, TG/DTA measurements were carried out under synthetic air on pre-evacuated commercial tetrahydrate samples to 400°C using two different heating rates 5°C/min (air//vac//5) and 1°C/min (air//vac//1). Results are shown in **Figure 6.6**. For comparison, the measurements performed under He on pre-evacuated samples at 5 and 1°C/min are also shown.

TG curves show mass losses $ML_{\text{tot-curv}}$ of 41.04 and 30.039 % for air//vac//5 and air//vac//1, respectively. Similarly to the investigations under He, the unseen loss of crystal water in the pre-evacuated samples during the stabilization time increases at 1°C/min compared to 5°C/min.

At 5°C/min under synthetic air, the $y = 2$ phase is correlated on the TG curve to a small variation of the slope near 100°C. Indeed, the mass loss between 100 and 300°C is 25.27 %, equivalent approximately to 2 mol H₂O confirming the dehydration of the $y = 2$ to the $y = 0$ phases according to the reaction (6.8). On the DTA curve, E2 is peaked at 95°C, at higher temperatures compared to the measurement under He. Otherwise, no substantial difference concerning the dehydration of structural water between the two flowing gases could be observed. The sample loses between 260 and 300°C about 4.68 % which can be referred to the dehydration of the $y = 1/3$ to the $y = 0$ phases (E5, 6.9). Interestingly, the dehydration of the $y = 2$ to the $y = n$ phases between 100 and 120°C is accompanied with a mass loss of 5.13 % nearly close to that obtained under He (5.6 %). The corresponding endotherm E3 is highly endothermic and could not be described by only the dehydration indicated on the dTG curve confirming that an additional endothermic structural process takes place along with the dehydration of the $y = 2$ to the $y = n$ phase.

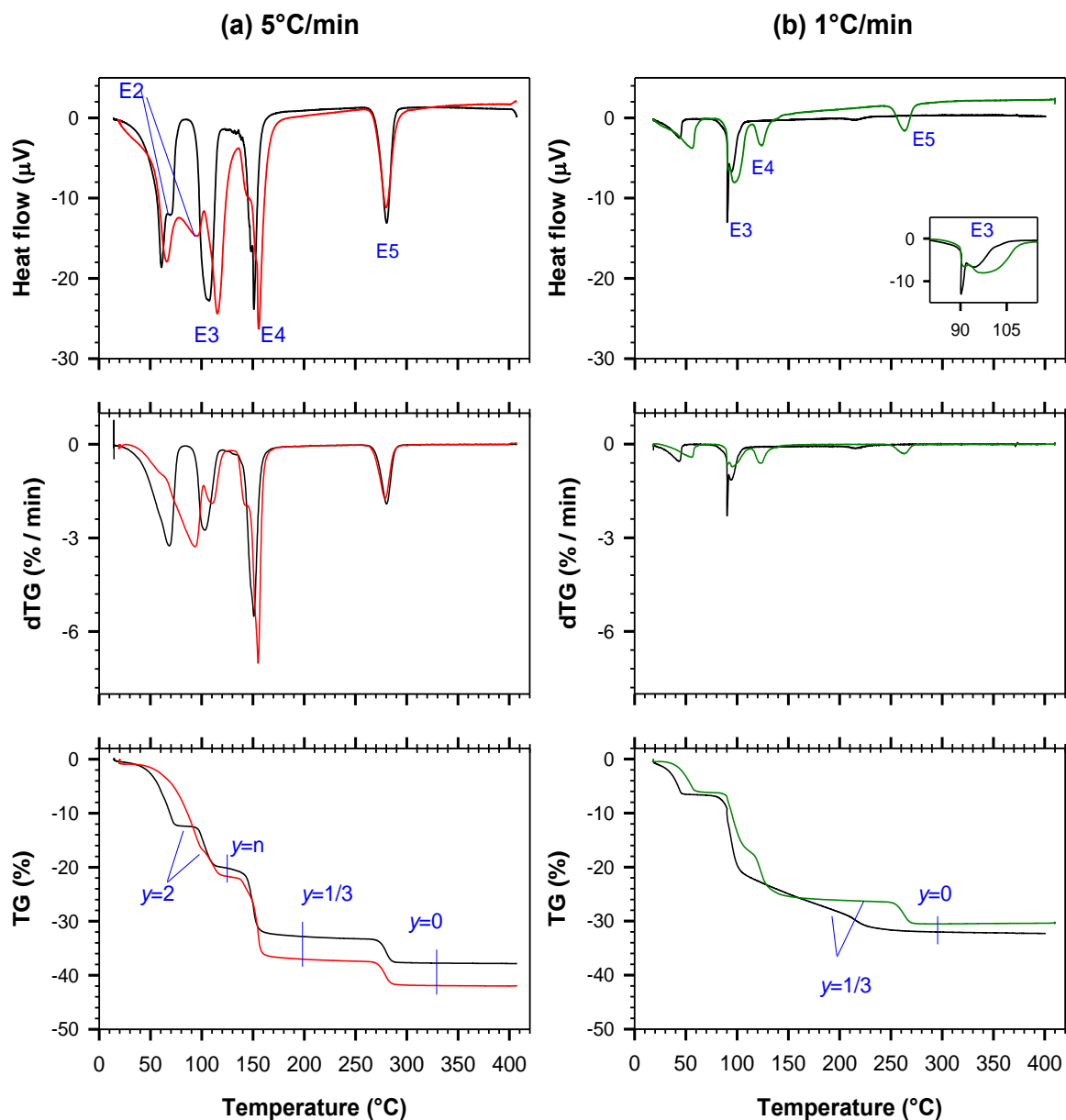


Figure 6.6: TG, dTG and DTA results of (a) air//vac//5 (red lines) in comparison with He//vac//5 (black) and (b) air//vac//1 (green) in comparison with He//vac//1 (black)

At 1°C/min, the sample under air loses between 50 and 300°C 24.34 % assigned to the reaction (6.8) describing the dehydration of the $y = 2$ to the $y = 0$ phases. Between 230 and 300°C, the loss is 4.207 % and corresponds to the dehydration of the $y = 1/3$ to the $y = 0$ phases (E5, reaction 3.9). Similarly to He//vac//1, the $y = n$ overlap with the $y = 1/3$ phases under synthetic air and E3 shows an additional sharp endotherm at 91°C.

6.2.3 In-situ X-ray diffraction

Basing on TG/DTA results, the different dehydrated phases $y = 2, n, 1/3$ and 0 could be better separated at relatively fast heating rates regardless of the considered atmosphere. Therefore, in-situ X-ray investigations of the thermal dehydration of the commercial tetrahydrate sample were carried out at $10^{\circ}\text{C}/\text{min}$ under N_2 flowing. Patterns were collected at key temperatures determined from TG/DTA analyses. During the acquisition time of 5 min, the temperature of the sample was maintained constant. The measurements were firstly performed from room temperature to 400°C . Data were taken in steps of $\Delta 2\theta = 0.02^{\circ}2\theta$ and a time/step of 0.12 s (**Figure 6.7**).

A slight heating to 50°C results in the disappearance of the peaks of the tetrahydrate and the appearance of the main reflections of the dihydrate which persist up to 100°C . In this temperature range TG/DTA analyses show two endotherms E1 and E2 (reaction 6.7). The observation of only the dihydrate pattern suggests that the end-products of E1 and E2 are crystallographically identical to $\text{NaB}(\text{OH})_4$. Furthermore, E1 is highly endothermic and is accompanied with only a weak dehydration, whereas the majority of crystalline H_2O molecules are released upon E2. Therefore it can be said that the phase resulting from E1 is constituted of $\text{NaB}(\text{OH})_4$ in addition to some external water and could be denoted as $\text{NaB}(\text{OH})_{4+y'}\text{H}_2\text{O}$ with $2 < y' < 4$.

At 110°C , the XRD peaks of $\text{NaB}(\text{OH})_4$ are attenuated and the pattern indicates the formation of an X-ray amorphous phase. Around 180°C very weak peaks are observed at $29.73, 34.21, 37.46$ and $41.38^{\circ}2\theta$ but could not be identified because of the low intensity. Near 200°C , weak peaks related to anhydrous NaBO_2 appear at $28.91, 32.63, 34.29$ and $40.52^{\circ}2\theta$ which gradually increase in intensity with increasing the temperature.

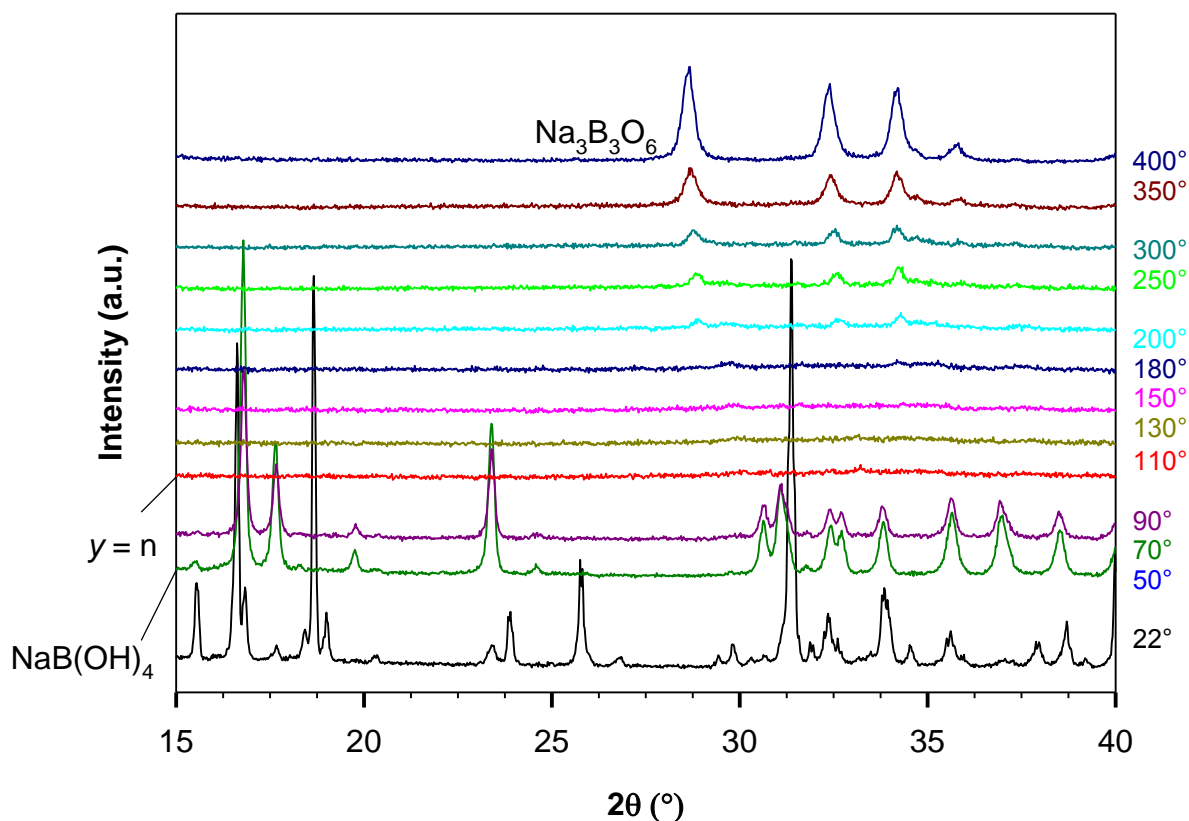


Figure 6.7: In-situ X-ray patterns of the thermal dehydration of $\text{NaBO}_2 \cdot 4\text{H}_2\text{O}$ using 0.12 s per step from room temperature to 400°C

The structural changes between 90 and 200°C were investigated using a higher time/step of 0.7 s. Results between 90 and 200°C are shown in **Figure 6.8**.

The pattern at 110°C exhibits a broad bump between 27 and 38°2θ in addition to the presence of some very weak peaks between 40 and 50°2θ. The patterns between 150 and 200°C can be principally indexed to the $y = 1/3$ phase with low crystallinity. Some other unidentified peaks were also observed. The $y = 2/3$ phase can be excluded since its main reflexes at 33.153 and 17.885°2θ [202] are not present.

The in-situ X-ray results indicate that the intermediary phase $y = n$ between the $y = 2$ and the $y = 1/3$ phases corresponding to E3 on the DTA curves is amorphous. It dehydrates upon further heating to the $y = 1/3$ phase (E4) which in turn dehydrates further to the $y = 0$ phase (E5).

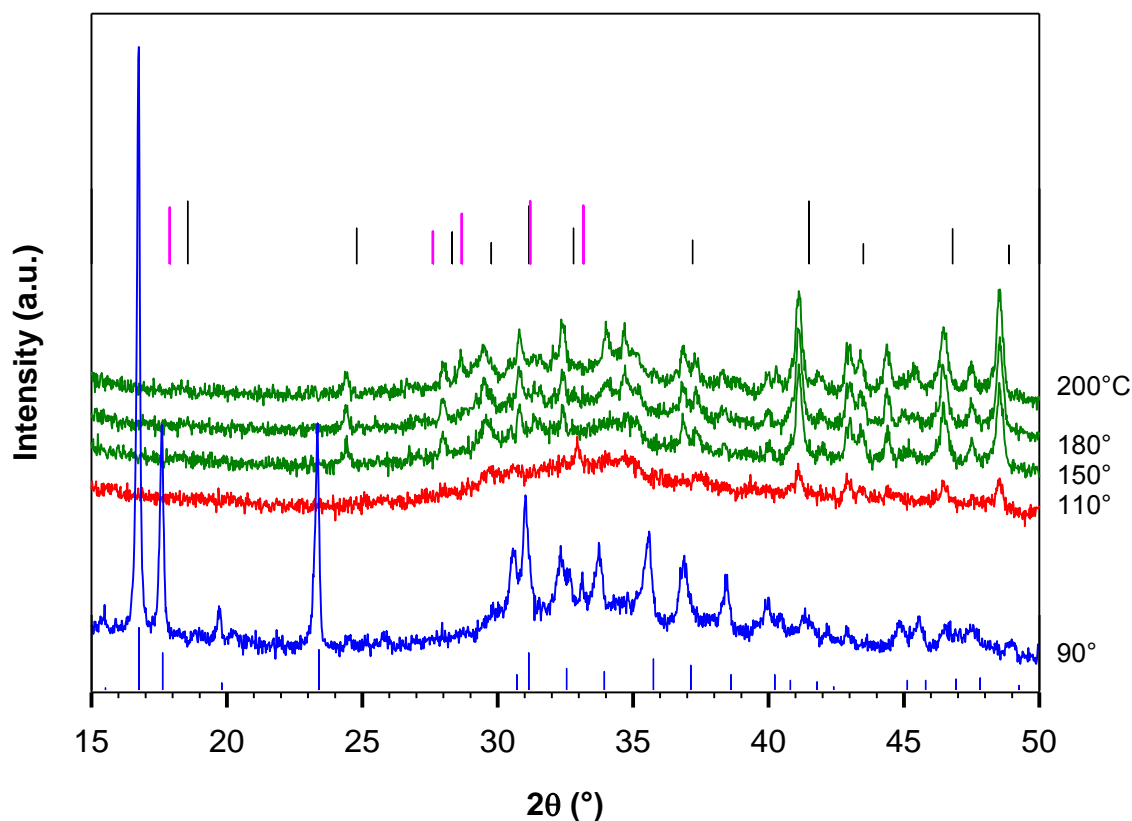


Figure 6.8: In-situ X-ray patterns obtained from the thermal dehydration of $\text{NaBO}_2 \cdot 4\text{H}_2\text{O}$ using 0.7 s per step between 90 and 200°C. The main reflexes of NaB(OH)_4 , $\text{NaBO}_2 \cdot (1/3)\text{H}_2\text{O}$ ($I \geq 30\%$, black bars) and $\text{NaBO}_2 \cdot (2/3)\text{H}_2\text{O}$ ($I \geq 50\%$, pink bars) are overlaid for comparison.

Beaird et al. [85] identified the one-third and the anhydrous phases from the thermal dehydration of $\text{NaBO}_2 \cdot 2\text{H}_2\text{O}$. However, they did not observe a non-crystalline phase ($y = n$) between the $y = 2$ and the $y = 1/3$ phases. This can be explained by the slow heating rate of 1°C/min and the long acquisition time of 4 h used in their study.

6.2.4 TIR

TIR investigations of the thermal dehydration mechanism can be divided into two parts. The first is for the dehydration of crystal molecular water below 100°C using a tetrahydrate/KBr pellet. The second investigates the condensation reaction of NaB(OH)_4 to $\text{Na}_3\text{B}_3\text{O}_6$ using $\text{NaB(OH)}_4/\text{KBr}$. Therefore, the commercial tetrahydrate sample was heated at 70°C for 20 h to eliminate molecular water of hydration. The obtained sample consisting of NaB(OH)_4 was then pressed in two KBr pellets. One was linearly heated to 400°C at

10°C/min, and for the other pellet the heating run was altered by an isotherm at 160°C for 43 h.

TIR spectra of $\text{NaBO}_2 \cdot 4\text{H}_2\text{O}$ from room temperature to 85 °C are shown in **Figure 6.9**.

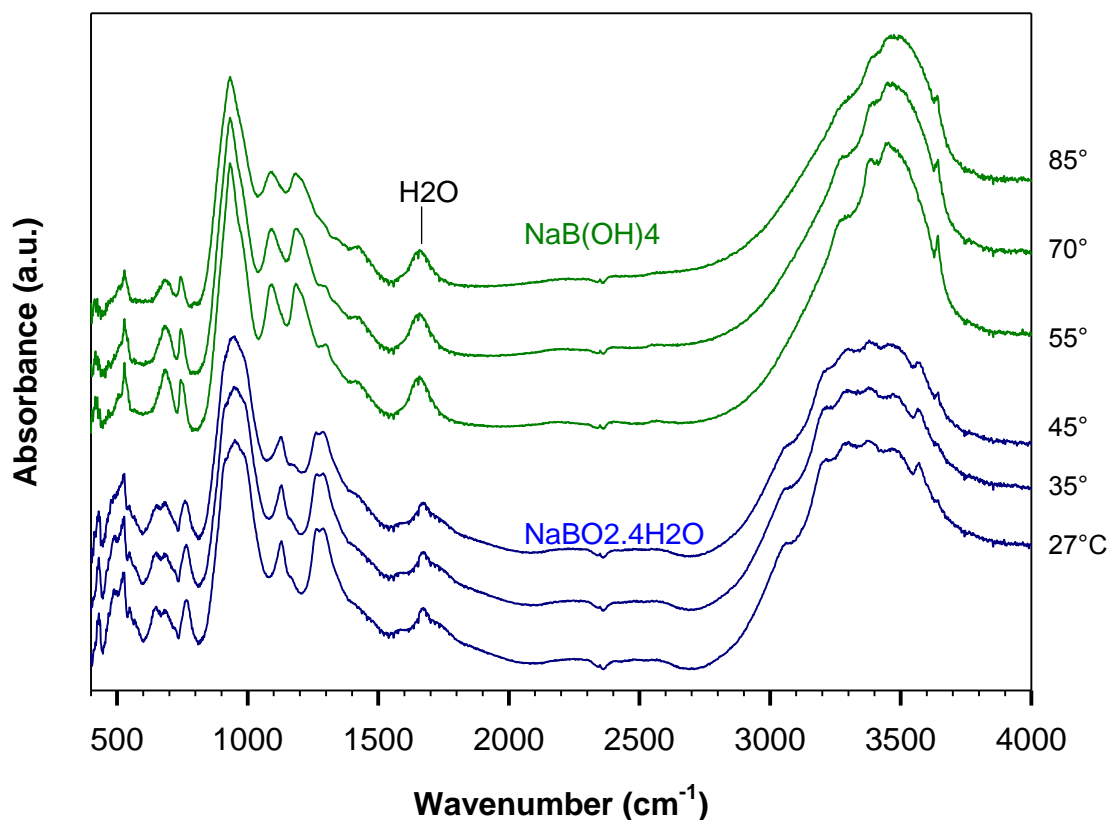


Figure 6.9: TIR of $\text{NaBO}_2 \cdot 4\text{H}_2\text{O}$ from room temperature to 90°C

The spectra taken at 27, 35 and 45°C show the typical peaks of $\text{NaBO}_2 \cdot 4\text{H}_2\text{O}$ phase [210] with the lattice vibrations principally at 429, 492, 525, 549, 647, 684, 766, 947, 1130, 1265 and 1288 cm^{-1} . The H_2O bending vibration is split into two main peaks with maxima at 1673 and 1711 cm^{-1} . The OH-related band is broad and includes at least seven OH peaks in the range between 2765 and 3740 cm^{-1} . Block and Perloff [197] reported two distinct crystallographic water molecules (**Figure 6.1**) and proposed a hydrogen bonding network constituted of eight crystallographic distinct hydrogen bonds.

The spectra taken at 55, 70 and 85°C show the typical peaks of $\text{NaB}(\text{OH})_4$ crystal [88] in agreement with the X-ray patterns taken between 50 and 90°C which are indexed to $\text{NaB}(\text{OH})_4$ (**Figure 6.7**). The IR lattice vibrations of $\text{NaB}(\text{OH})_4$ are peaked at 528, 684, 743,

933, 1084, 1181 and 1298 cm^{-1} . The OH absorption bands are also changed showing three peaks at 2382, 3385, 3438 and 3640 cm^{-1} . The peak at 1658 cm^{-1} indicates that H_2O molecules go into the KBr pellet. This peak decreases in intensity during heating from 55 to 85°C.

The TIR spectrum at 55°C confirms the presence of a phase isomorphous to $\text{NaB}(\text{OH})_4$ which contains in addition unbound water molecules ($\text{NaB}(\text{OH})_{4+y}\text{H}_2\text{O}$). This phase is formed in the first stages of the thermal dehydration (E1). Water of hydration are further released without crystallographic changes in the structure (E2) yielding $\text{NaB}(\text{OH})_4$. The transition of the tetrahydrate to the $\text{NaB}(\text{OH})_{4+y}\text{H}_2\text{O}$ phase is accompanied with profound changes in the H_2O and OH-related bands.

The dehydration of structural during linearly heating $\text{NaB}(\text{OH})_4/\text{KBr}$ pellet to 400°C is demonstrated in **Figure 6.10**.

Above 100°C, $\text{NaB}(\text{OH})_4$ peaks are attenuated. At 115°C, the IR spectrum shows broad IR bands at 820-1090 cm^{-1} and 1200-1415 cm^{-1} indicating the formation of an amorphous phase in agreement with the in-situ X-ray results for the $y = n$ phase. These peaks are assigned to vibrations involving boron tetra-coordinated (tetrahedral) and tri-coordinated (planar) to oxygen atoms, $\text{B}_4\text{-O}$ and $\text{B}_3\text{-O}$ groups, respectively [211].

The amorphous phase remains up to 200°C. Upon further heating, the IR bands of BO_4 between 900 and 1000 cm^{-1} decrease and those of BO_3 groups at about 1200-1500 cm^{-1} increase. At about 330°C the IR absorption bands of OH groups between 3000 and 3700 cm^{-1} disappear. The IR spectrum shows principally absorption peaks at 705, 723, 1230, 1260 and 1440 cm^{-1} assigned to the anhydrous crystalline $\text{Na}_3\text{B}_3\text{O}_6$ [91].

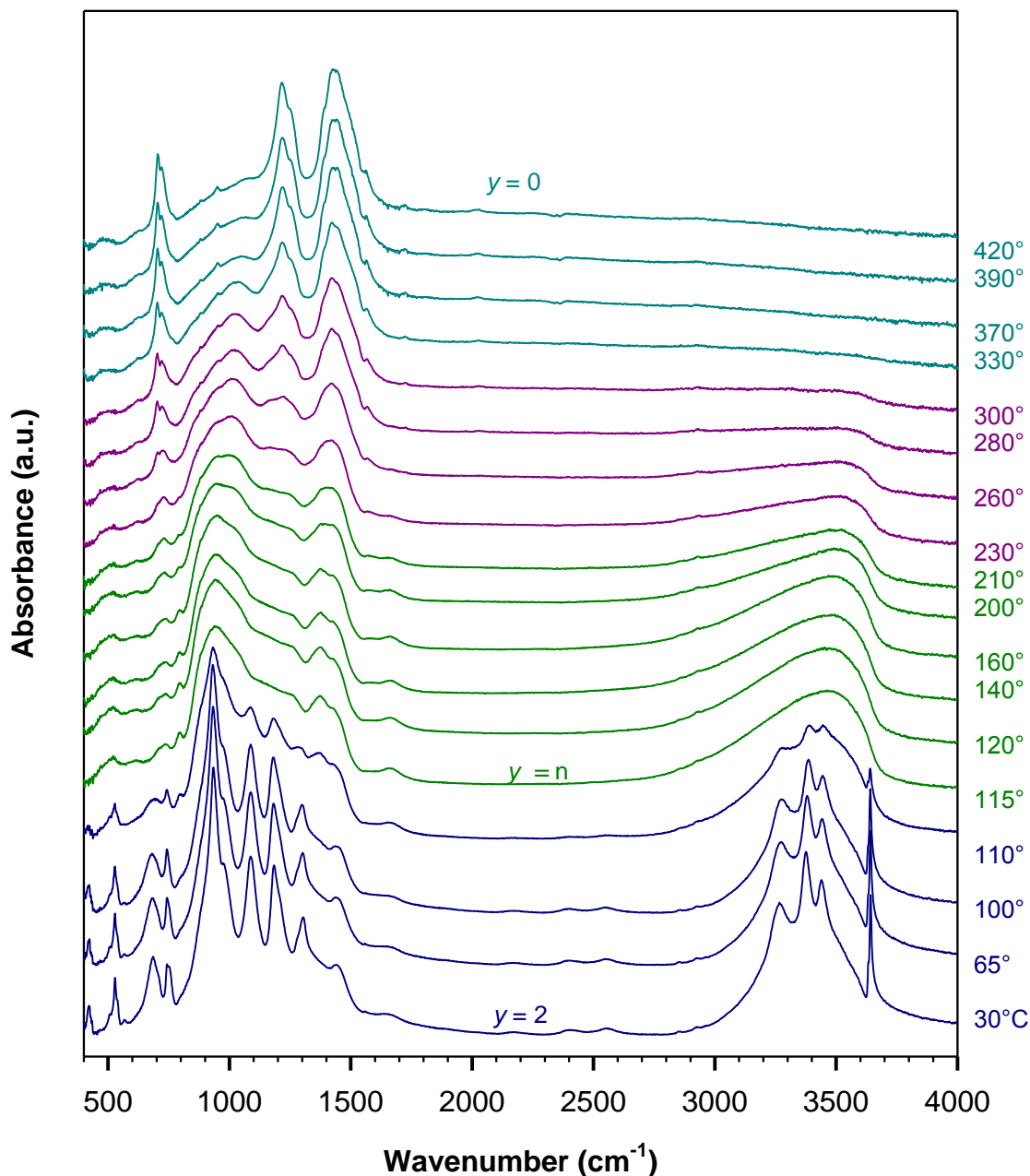


Figure 6.10: TIR of $\text{NaB}(\text{OH})_4$ linearly heated from room temperature to 420°C

The formation of the one-third phase, as expected from TG/DTA and in-situ X-ray analyses, was not observed in this TIR run. Therefore, TIR investigations from room temperature to 400°C were also conducted by applying a long isotherm at 160°C . Results are shown in **Figure 6.11**.

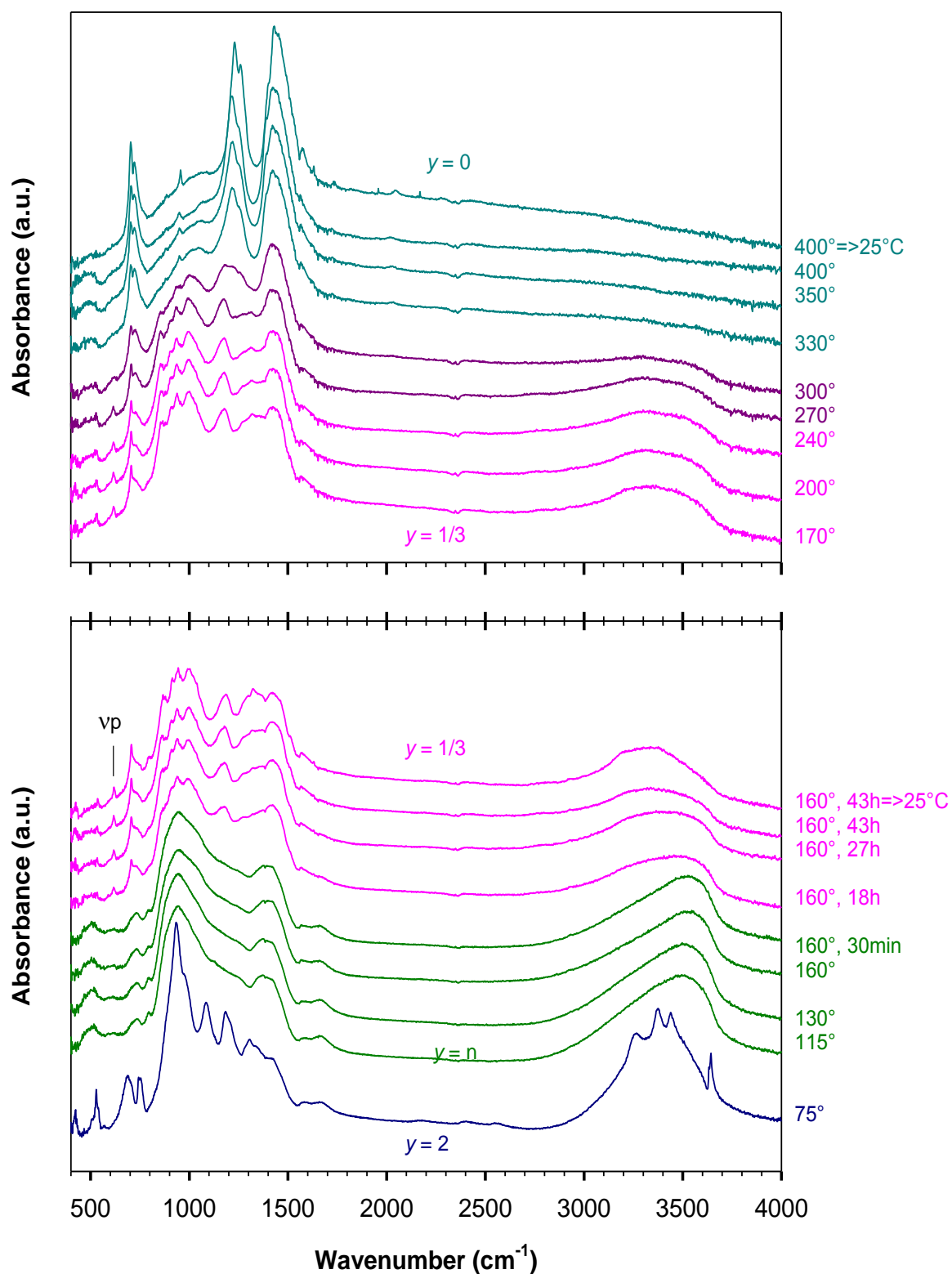


Figure 6.11: TIR of $\text{NaB}(\text{OH})_4$ to 400°C using isothermals conditions at 160°C

The decomposition of the $y = 2$ to the $y = n$ phases occurs about 115°C as deduced from the disappearance of the IR bands of $\text{NaB}(\text{OH})_4$ and the appearance of principally two

broad IR bands centered at 950 and 1380 cm^{-1} , respectively. The TIR spectrum at 160°C shows broad IR bands similar to those at 115°C. After the long isotherm at 160°C, the broad bands are sharpened into a fine structure. Interestingly, the peak at 617 cm^{-1} can be attributed to the symmetric pulse vibration ν_p of a triborate ion containing tetrahedral and planar boron units [89, 212]. Thus, the corresponding TIR spectrum can be assigned to the $y = 1/3$ phase which remains stable after 16 h at 160°C.

TG/DTA analysis at 5°C/min suggested the $y = 1/3$ phase over a wide temperature range from 180 to 260°C. The fact that a long isotherm was needed in the TIR experiment to obtain the IR spectrum of the $y = 1/3$ phase could be referred to the matrix effect retarding the cyclization and the crystallization of the structure in a polyborate ring rather than affecting the dehydration. Indeed, the integral intensity of the OH stretching band calculated between 2867 and 3805 cm^{-1} shows a decrease of 46 % between the IR spectrum at room temperature and that obtained at 160°C after 27 h. This decrease matches in the TIR with linear heating (**Figure 6.10**) the variation of the integral intensity of OH band between the IR spectra at room temperature and that taken at 205°C. However, the TIR spectrum taken at 205°C in the linear heating shows relatively broad IR bands and a very weak peak at 620 cm^{-1} corresponding to the triborate ring pulse vibration.

The one-third phase remains stable up to 270°C. At higher temperatures, the IR bands of $\text{Na}_3\text{B}_3\text{O}_6$ increase in intensity.

6.2.5 Characterization of the dehydration products

The different metaborate phases could be isolated and characterized in runs of $\text{NaBO}_2 \cdot 4\text{H}_2\text{O}$ samples heated under N_2 to 70°C, 70°C for 20 h, 120°C, 120°C for 30 min, 120°C for 2 h and 400°C for 5 h. End-products were collected and characterized using powder X-ray diffraction, IR and Raman spectroscopy.

The first experiment (denoted exp.a) was carried out to 70°C for 20 h. Heating the commercial sample to 120°C at 5°C/min (exp.b) yielded a gel-like phase. This experiment was repeated in the same manner (exp.b'). The gels were immediately isolated and subjected to XRD and IR measurements. The IR spectra were taken by simply mixing 1-2 drops of the gel in approximately 200 mg KBr. In another experiments, the gel was maintained at 120°C for 20 min (exp.c) and 2 h (exp.d), respectively. Exp.e is for the isotherm performed at 400°C

for 5 h. It is worth noting that the cyclic phases ($y = 1/3$ and $y = 0$) were not stable for long term at ambient conditions. Characterizations were made directly after the thermal treatments.

X-ray patterns of the end-products of exp.a-e are depicted in **Figure 6.12**. The obtained pattern for the isotherm at 70°C (exp.a) can be assigned to the dihydrate phase. The long heating time of 20 h was applied to get all H₂O molecules out of the sample since according to in-situ X-ray diffraction results the first two steps of the thermal dehydration of NaBO₂·4H₂O corresponding to E1 and E2, respectively (reaction 6.7), have similar X-ray patterns.

The gel-like phase isolated at 120°C (exp.b and exp.b') is amorphous. The prolonged heating of the gel at 120°C (for 20 min in exp.c and for 2 h in exp.d) yields the $y = 1/3$ phase. The thermal treatment at 400°C for 5 h (exp.e) produces the anhydrous $y = 0$ phase. The obtained results are in good agreement with in-situ X-ray results and confirm that between the $y = 2$ and $y = 1/3$ phases an amorphous phase occurs. The different thermal treatments and the corresponding phases are summarized in **Table 6.3**.

Table 6.3: Thermal treatments of NaBO₂·4H₂O and end-products

Exp.	Thermal treatment	End-product
a	70°C, 20 h	NaB(OH) ₄
b	120°C	Gel, non-crystalline
b'	Repetition of exp. (b)	Gel, non-crystalline
c	120°C, 20 min	Na ₃ [B ₃ O ₅ (OH) ₂]
d	120°C, 2 h	Na ₃ [B ₃ O ₅ (OH) ₂]
e	400°C, 5 h	Na ₃ B ₃ O ₆

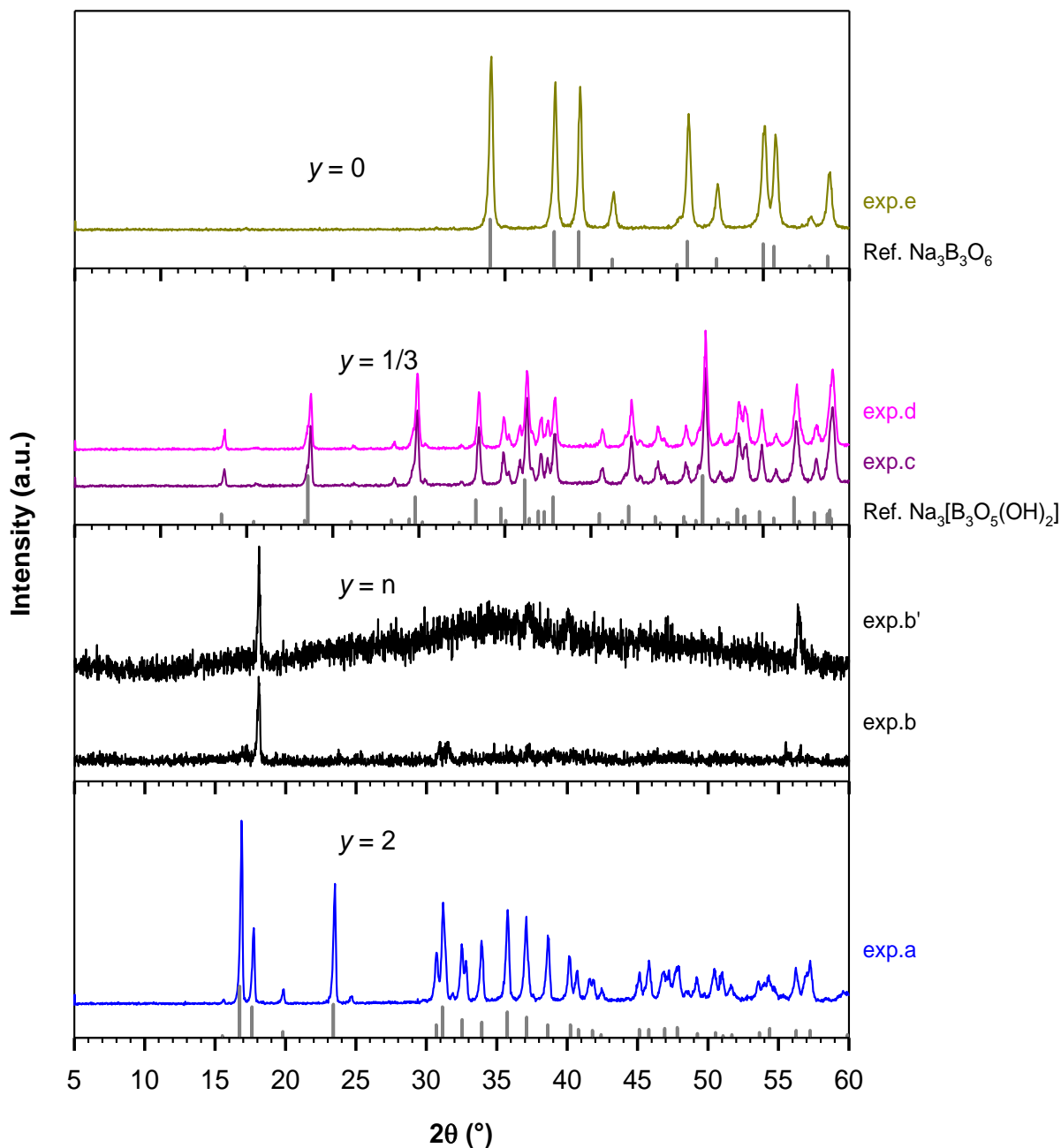


Figure 6.12: X-ray patterns of the end-products of exp.a-e. When necessary, a comparison with a reference pattern is given (vertical bars).

IR spectra of exp.a-e are shown in **Figure 6.13**. Raman spectra are shown for the dihydrate (exp.a), the one-third (exp.d) and the anhydrous (exp.e) phases in **Figure 6.14**.

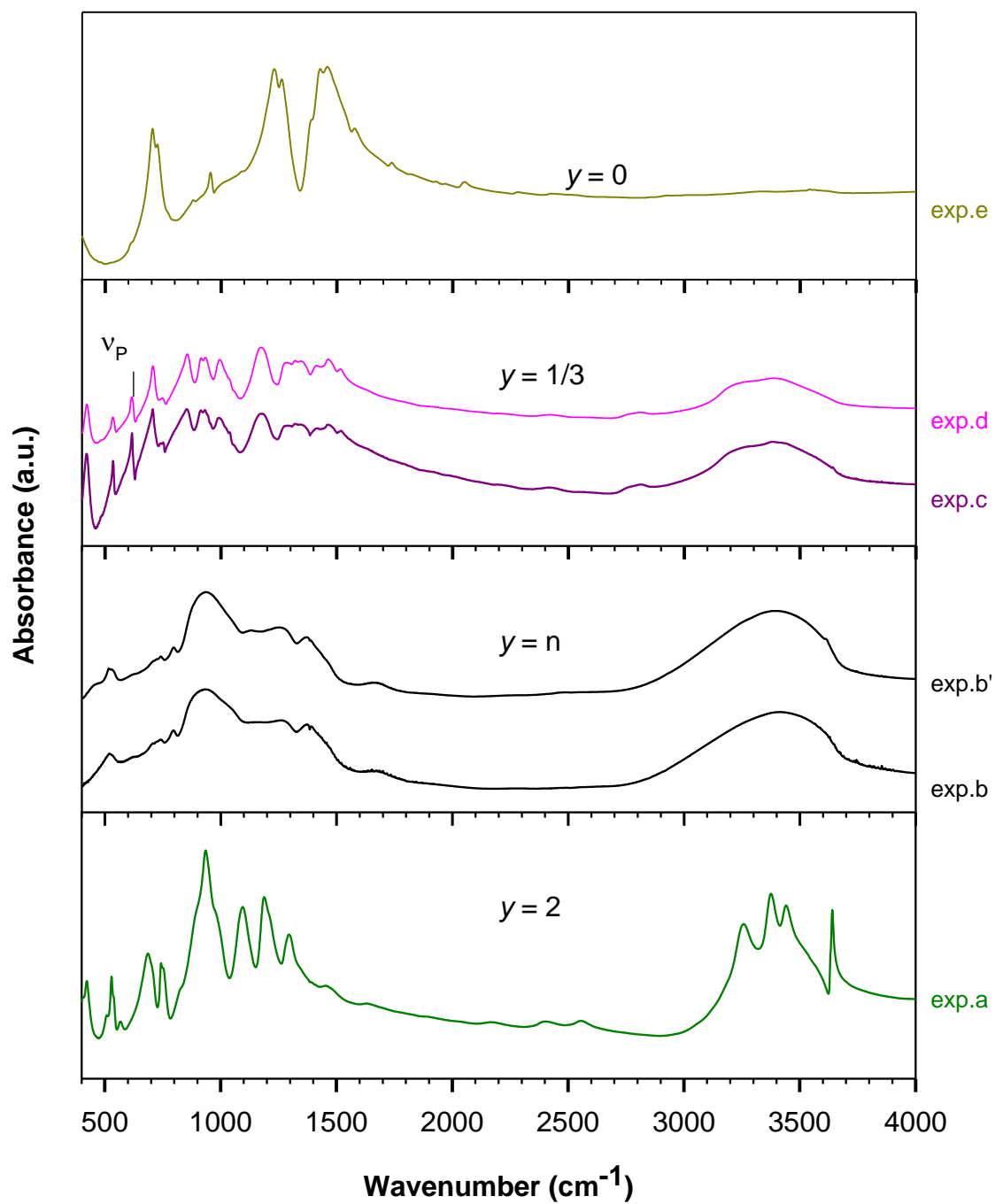


Figure 6.13: IR spectra of the end-products of exp.a-e

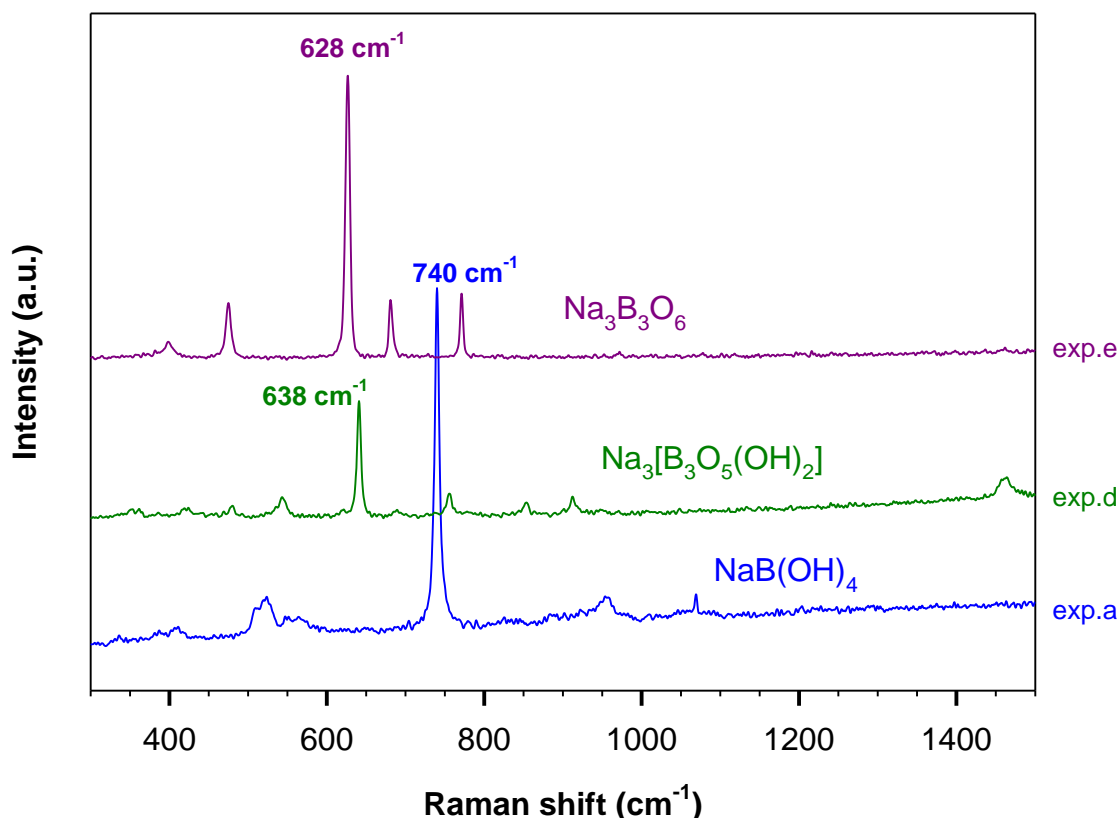


Figure 6.14: Raman spectra of the dihydrate (exp.a), the one-third (exp.d) and the anhydrous (exp.e) phases. The peak positions of the primary peak of each phase are indicated.

The obtained IR spectra for the $y = 2$ (exp.a), the gel $y = n$ (exp.b and exp.b'), the $y = 1/3$ (exp.c and exp.d) and the $y = 0$ (exp.e) phases are similar to those obtained using TIR experiment.

An aqueous solution of $\text{B}(\text{OH})_4^-$ exhibits the asymmetric ν_3 (IR) and the symmetric ν_1 (Raman) stretching modes at 958 cm^{-1} and 744 cm^{-1} , respectively [213]. The IR spectra of $\text{NaBO}_2 \cdot 4\text{H}_2\text{O}$ and $\text{NaBO}_2 \cdot 2\text{H}_2\text{O}$ were described by Kessler [210] and Kessler and Lehmann [88], respectively. One would assume that IR and Raman peaks at similar frequencies could be assigned and described the same. Accordingly, the IR and Raman peaks in the spectral range $900\text{-}950$ and $740\text{-}770 \text{ cm}^{-1}$ are for the asymmetric (ν_3) and symmetric stretching (ν_1) of the $\text{B}_4\text{-O}$ bond, respectively. The peaks between 1090 and 1290 cm^{-1} are assigned to the deformation or in-plane bending mode of BOH groups. The bands appearing between 600 and 700 cm^{-1} are referred to $\gamma(\text{B-OH})$ mode, the deformation vibration perpendicular to the plane of B-OH grouping. The IR bands between 500 and 600 cm^{-1} are assigned to the bending ν_4 mode of $\text{B}_4\text{-O}$. Jun et al. [89] assigned the Raman peak of the tetrahydrate at 579 cm^{-1} to

$\gamma(\text{B-OH})$ rather than ν_4 mode. IR and Raman modes of $\text{NaBO}_2 \cdot 4\text{H}_2\text{O}$ and $\text{NaBO}_2 \cdot 2\text{H}_2\text{O}$ are summarized in **Table 6.4**.

Table 6.4: Experimental IR frequencies and Raman shifts of $\text{NaB(OH)}_4 \cdot 2\text{H}_2\text{O}$ and NaB(OH)_4 in comparison with literature

$\text{NaB(OH)}_4 \cdot 2\text{H}_2\text{O}, y = 4$		$\text{NaB(OH)}_4, y = 2$				Assignment
IR		IR		Raman		
Exp.	Ref. [210]	Exp.	Ref. [88]	Exp.	Ref. [85]	
2800-3600	3200-3600	3640	3640			Stretching of OH
		3442	3390			
		3377	3350			
		3258	3260			
1670	1680					Bending of HOH
1288	1286	1297	1290			Deformation or in-plane bending of B-O-H
1265	1266					
		1188	1185			
1162	1166					
1130	1129					
		1085	1090			
953	1006-916			1070	1072	Asymmetrical stretching of $\text{B}_4\text{-O}$ (ν_3)
912		934	930	954	952	
766	768					Symmetrical stretching of $\text{B}_4\text{-O}$ (ν_1)
		742	740	740	740	
		684	685			$\gamma\text{B-OH}$
678						
647	646					
549	549	565	565	564	579	Bending of $\text{B}_4\text{-O}$ (ν_4)
			535			
524	525	528	527	524	527	
		508	506	510	510	
492	491					
					466	
				411	410	

$\text{B}_4\text{-O}$ denotes the bond of B tetrahedrally coordinated to O

The IR region of O-H stretching in NaB(OH)_4 reveals a strong broad band with three peaks at 3443, 3376 and 3258 cm^{-1} , respectively, and a single sharp band at 3640 cm^{-1} . This is consistent with the crystal structure of NaB(OH)_4 where three of the $-\text{OH}$ groups (including H(1), H(2) and H(3)) participate to hydrogen bonding network but not H(4) [198].

The IR spectra of exp.b and exp.b' are similar and consist principally of broad B-O bands centered at 936, 1250 and 1360 cm^{-1} that can be assigned to the stretching of $\text{B}_4\text{-O}$, the

bending of B-OH and the stretching of $\text{B}_3\text{-O}$, respectively [89, 211]. This indicates that the $y = n$ phase includes short ranges of tetrahedral BO_4 and planar BO_3 boron moieties with the content of fourfold BO_4 is greater than that of BO_3 .

Under ambient conditions, the gel dries progressively and forms a white powder identified as $\text{NaB}(\text{OH})_4$ (*results not shown*) due to the uptake of sufficient water from the atmosphere.

A prolonged heating of the gel at 120°C or a slight increase in the temperature leads to the $y = 1/3$ phase. Beaird et al. [85] reported the Raman spectrum of the $y = 1/3$ phase. To our knowledge, no IR spectrum has been reported to date. A primary peak of the one-third phase is the symmetric pulse ν_p of the triborate anion containing BO_3 and BO_4 groups which appears at 617 and 638 cm^{-1} in the IR and Raman spectra, respectively [89, 212]. The peak assignment is made based on the IR and Raman spectra reported for other borate compounds containing triborate rings of planar and tetrahedral boron moieties as $\text{K}_3[\text{B}_3\text{O}_4(\text{OH})_4] \cdot 2\text{H}_2\text{O}$ and the hexaborate compounds [89, 212]. The obtained IR frequencies and Raman shifts with a plausible description are presented in **Table 6.5**.

The experimental IR frequencies and Raman shifts obtained for $\text{Na}_3\text{B}_3\text{O}_6$ (exp.e) are in good agreement with those reported previously in the literature (**Table 6.6**). The free ion $(\text{B}_3\text{O}_6)^{3-}$ has D_{3h} symmetry. The corresponding irreducible representation of the internal vibrational modes can be written as: $\Gamma_{\text{vib}} = 3\text{A}_1' (\text{R}) + 2\text{A}_2' (\text{inactive}) + 5\text{E}' (\text{R, IR}) + 2\text{A}_2'' (\text{IR}) + 2\text{E}'' (\text{R})$. The species A_1' , A_2' and E' represent the in-plane vibrations and the species A_2'' and E'' the out-of-plane vibrations [214]. The occurrence of boron atom in natural isotopical abundance causes a lowering of the D_{3h} symmetry to C_{2v} . For example, the IR doublet observed near 700 cm^{-1} is replaced by a single band for isotopically pure ^{10}B or ^{11}B [91]. Raman bands were assigned according to Chryssikos et al. [214]. Beaird et al. [85] reported a Raman peak at 1078 cm^{-1} which was observed neither in our work nor in the work of Chryssikos et al.. Only the species A_2'' and E' are infrared active. The IR doublet at about 700 cm^{-1} could be attributed to the ring out-of-plane bending mode of the metaborate ring [91, 215, 216]. The other IR bands at higher frequencies are for the asymmetrical stretching B-O modes of E' [217]. According to Hisatsune and Suarez [91], the single peak at 950 cm^{-1} is not influenced by isotopical changes and could be assigned to the stretching of the extra B-O⁻ bond and the two IR doublets at 1400 and 1222 cm^{-1} are related to the ring stretching modes.

Table 6.5: IR frequencies and Raman shifts of $\text{Na}_3\text{B}_3\text{O}_5(\text{OH})_2$ in comparison with Raman results of the literature

$y = 1/3, \text{Na}_3\text{B}_3\text{O}_5(\text{OH})_2$			Assignment
IR	Raman		
Exp.	Exp.	Ref. [85]	
3050-3700			Stretching of OH
1518			Asymmetrical stretching of $\text{B}_3\text{-O}^-$
1465	1462		
1415			Asymmetrical stretching of $\text{B}_3\text{-O}$
1334			
1287			In-plane bending of $\text{B}_4\text{-O-H}$
1174			
	1078	1079	
1037			Asymmetrical stretching of $\text{B}_4\text{-O}$
990			
931			Symmetrical stretching of $\text{B}_3\text{-O}$
914	911	908	
855	851	847	Symmetrical stretching of $\text{B}_4\text{-O}$
	754	757	Out-of-plane bending of $\text{B}_3\text{-O}$
706			
	638	636	Symmetric pulse vibration of the ring
617			
535	542	543	
	477	476	Bending of $\text{B}_4\text{-O}$
421	422	420	
	352	359	

$\text{B}_4\text{-O}$ denotes the bond of B tetrahedrally coordinated to O

$\text{B}_3\text{-O}$ denotes the bond of B tri-coordinated to O

Table 6.6: IR frequencies and Raman shifts of $\text{Na}_3\text{B}_3\text{O}_6$, in comparison with literature

$y=0, \text{Na}_3\text{B}_3\text{O}_6$					Assignment
IR		Raman			
Exp.	Ref. [91]	Exp.	Ref. [85]	Ref. [214]	
		1575	1571	1575	Stretching of B-O^- (A_1')
		1552	1547	1554	
1458	1466				E' : ring stretching
1428	1436				
1261	1264				E' : ring stretching
1230	1241				
955	950				E' : stretching of B-O^-
		770	755	770	
					Ring breathing (A_1')
722	724				A_2'' : ring out-of- plane bending
705	708				
		680	683	682	Out-of-plane bending of the ring (E'')
		626	628	627	
		475	476	475	Ring breathing A_1' In-plane bending of $\text{B}_3\text{-O}$ (E')
		399	402	309	

$\text{Na}_3\text{B}_3\text{O}_6/\text{KBr}$ pellet heated above 500°C under vacuum reveals a decomposition of $(\text{B}_3\text{O}_6)^{3-}$ ring to linear BO_2^- anions (**Figure 6.15**). The IR spectrum shows two pairs of very sharp peaks about 600 and 2000 cm^{-1} assigned to the bending ν_2 and the stretching ν_3 modes, respectively. The high frequency peak of each pair is due to ^{10}B isotope [36, 91, 93]. Under high resolution, each peak of the doublet near 2000 cm^{-1} shows a lower frequency weak component which disappears for the spectra cooled to liquid nitrogen. These are at 1950 and 2019 cm^{-1} and could be explained as hot bands of the high frequency fundamental [91].

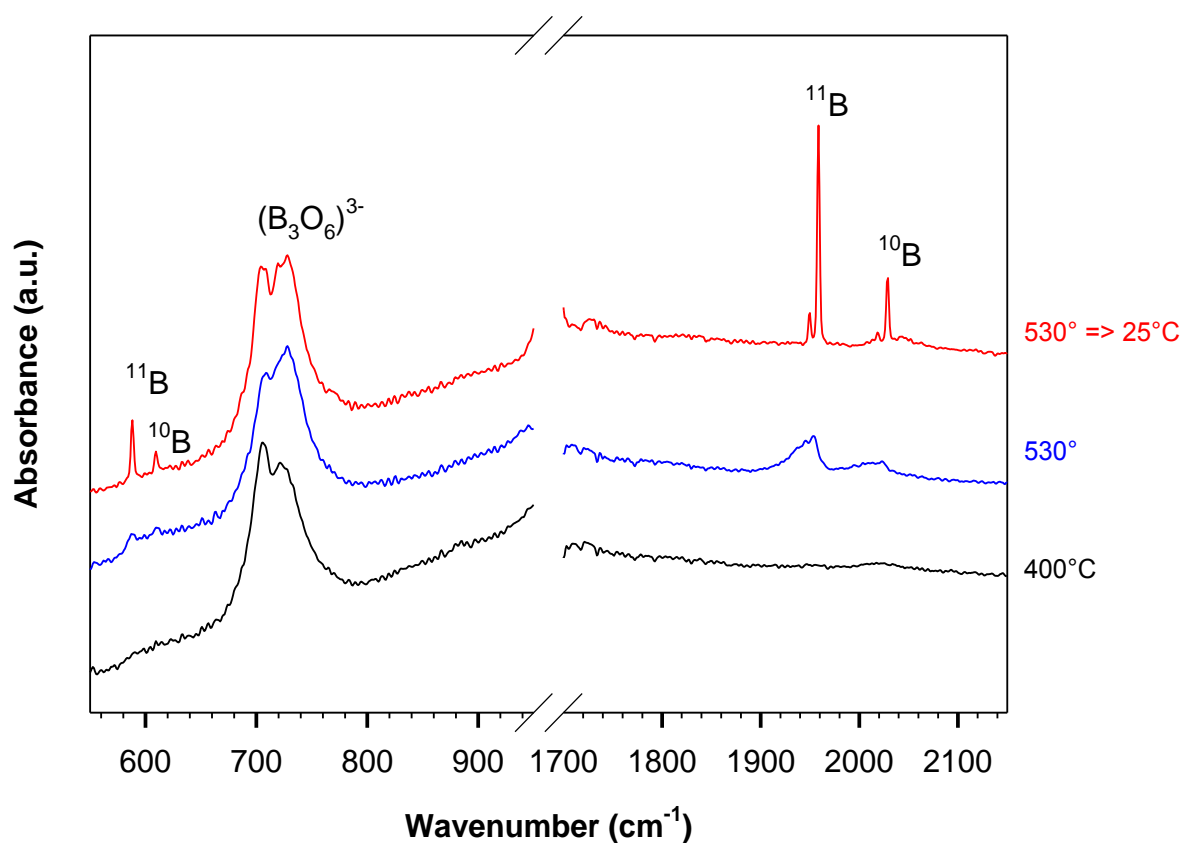


Figure 6.15: TIR spectra of the decomposition of the metaborate ring $(\text{B}_3\text{O}_6)^{3-}$ to the linear BO_2^- molecule

6.3 Summary: dehydration path of $\text{NaBO}_2 \cdot 4\text{H}_2\text{O}$

The thermal dehydration path of $\text{NaBO}_2 \cdot 4\text{H}_2\text{O}$ to NaBO_2 , as reported in the literature and as obtained in this work, is schematized in **Figure 6.16**.

Kanturk et al. [207] reported the dehydration of $\text{NaBO}_2 \cdot 4\text{H}_2\text{O}$ to $\text{NaB}(\text{OH})_4$ for temperatures below 100°C and the further dehydration of the latter to $\text{Na}_3\text{B}_3\text{O}_6$ near 300°C . Andrieux et al. [202] obtained $\text{NaBO}_2 \cdot 2/3\text{H}_2\text{O}$ in the isothermal treatment of $\text{NaBO}_2 \cdot 4\text{H}_2\text{O}$ at 110°C for 12 h. The $y = 2/3$ decomposes to the $y = 1/3$ which dehydrates in turn to the $y = 0$ phases [206]. Beaird et al. [85] observed the dehydration of the $y = 2$ to the $y = 1/3$ followed by the formation of the $y = 0$ phases.

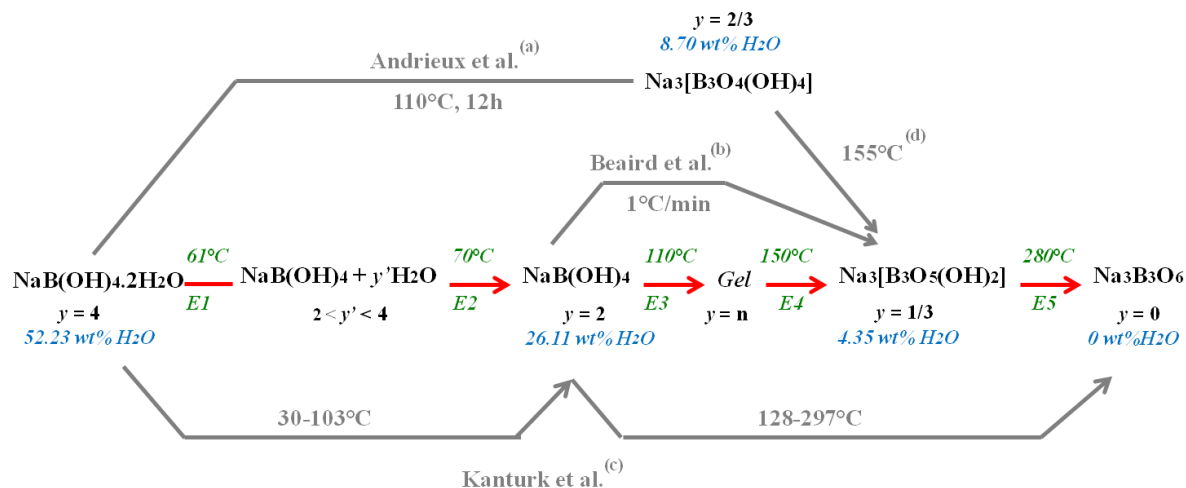


Figure 6.16: The thermal dehydration path of $\text{NaBO}_2 \cdot 4\text{H}_2\text{O}$ according to this work (red path) in comparison with those reported previously in the literature (gray paths). The dehydration temperatures are given according to TG He//vac//5. For each metaborate phase, the hydration degree y and the content of water (wt% H_2O) are given. ^(a) ref. [202], ^(b) ref. [85], ^(c) ref. [207], ^(d) ref. [206].

The present work presents a more complete picture of the thermal dehydration of the $y = 4$ to the $y = 0$ phases and reports the formation of a new gel type phase for the first time. The dehydration process of $\text{NaBO}_2 \cdot 4\text{H}_2\text{O}$ occurs in five main steps; all correspond principally to endothermic effects on the DTA curves. The first two endotherms (E1 and E2) occur below 100°C and correspond to the release of crystal molecular water and the formation of NaB(OH)_4 ($y = 2$). The last three endotherms above 100°C (E3, E4 and E5) are for the removal of structural water present in the sample in the form of $-\text{OH}$ groups via series of dehydration-condensation reactions yielding anhydrous sodium metaborate $\text{Na}_3\text{B}_3\text{O}_6$ ($y = 0$) near 300°C . At $5^\circ\text{C}/\text{min}$ under He, the five endothermic peaks E1, E2, E3, E4 and E5 occur at about 61 , 70 , 110 , 150 and 280°C , respectively.

E1 and E2 result in similar X-ray patterns isomorphous to NaB(OH)_4 . E1 is highly endothermic and is accompanied with a slight dehydration. The major amount of molecular water is released upon E2. The phases of E1 and E2 could be better differentiated using TIR. TIR spectra taken between 27 and 45°C show typical IR peaks of $\text{NaB(OH)}_4 \cdot 2\text{H}_2\text{O}$. The H_2O bending vibration is split in two main peaks with maxima at 1673 and 1711 cm^{-1} and the OH-related band is broad and includes at least seven OH peaks in the range between 2765 and 3740 cm^{-1} . The structure of $\text{NaB(OH)}_4 \cdot 2\text{H}_2\text{O}$ has been determined by Block and Perloff [197] basing on direct methods using three-dimensional $\text{Cu K}\alpha$ single crystal. The authors could not determine precisely the position of H atoms and proposed the hydrogen bonding network

considering the shortest oxygen to oxygen distances. Two crystallographic distinct H_2O molecules and more than eight crystallographic distinct hydrogen bonding of the type OH-OH (between $\text{B}(\text{OH})_4$ anions) and OH- H_2O (between $\text{B}(\text{OH})_4$ and H_2O) were reported. Na is in a distorted six-coordination. Each Na is coordinated to two $-\text{OH}$ of two different $\text{B}(\text{OH})_4^-$ groups and four water molecules. The coordination environment of $\text{B}(\text{OH})_4^-$ anion in $\text{NaB}(\text{OH})_4 \cdot 2\text{H}_2\text{O}$ is shown in **Figure 6.17a**. The hydrogen bonding network in $\text{NaB}(\text{OH})_4 \cdot 2\text{H}_2\text{O}$ is traced between the oxygen atoms. At 55°C , profound changes occur particularly in the OH- and H_2O -related IR bands. The TIR spectrum at 55°C has the IR features of $\text{NaB}(\text{OH})_4$. The OH absorption exhibits a strong broad band with three peaks at 3443 , 3376 and 3258 cm^{-1} , respectively, and a single sharp peak at 3640 cm^{-1} , consistent with the crystal structure of $\text{NaB}(\text{OH})_4$ as described by Csetenyi et al. [198]. The $\text{B}(\text{OH})_4^-$ anions are interconnected in three dimensions via hydrogen bonding involving H(1), H(2) and H(3) but not H(4). Na is in a distorted six-coordinated environment. Each Na is in contact with four distinct $\text{B}(\text{OH})_4^-$ anions (**Figure 6.17b**). In addition, the TIR spectrum shows H_2O bending absorption at 1658 cm^{-1} . This indicates the formation of a phase containing the dihydrate in addition to “external” molecular water and could be denoted as $\text{NaB}(\text{OH})_{4+y} \cdot y' \text{H}_2\text{O}$ with $2 < y' < 4$. Further heating to 85°C results only in a decrease of the intensity of the H_2O bending mode. It can be therefore concluded that during E1, $\text{NaB}(\text{OH})_4 \cdot 2\text{H}_2\text{O}$ undergoes structural re-arrangement to $\text{NaB}(\text{OH})_{4+y} \cdot y' \text{H}_2\text{O}$. The hydrogen bonding network between $\text{B}(\text{OH})_4^-$ and the crystal molecular water of $\text{NaB}(\text{OH})_4 \cdot 2\text{H}_2\text{O}$ is disrupted and $\text{B}(\text{OH})_4^-$ anions are placed in a similar way to that of the dihydrate $\text{NaB}(\text{OH})_4$. Water of hydration ($y' \text{H}_2\text{O}$) remains “unbound” to $\text{NaB}(\text{OH})_4$ and is further released upon E2.

The thermal decomposition of $\text{NaB}(\text{OH})_4$ yields an X-ray amorphous phase ($y = n$) near 100°C (E3) which dehydrates further to the $y = 1/3$ (E4) followed by the dehydration to the $y = 0$ (E5) phases at about 300°C . The $y = n$ phase could be better separated from the $y = 1/3$ phase at high heating rates ($5^\circ\text{C}/\text{min}$). The hydration degree n is lower at 2 and $1^\circ\text{C}/\text{min}$ compared to $5^\circ\text{C}/\text{min}$. This phase was isolated at 120°C under N_2 using a heating rate of $5^\circ\text{C}/\text{min}$ and consists of a gel exhibiting broad IR bands peaked at 936 and 1360 cm^{-1} . These can be assigned to the stretching vibrations of BO_4 and BO_3 groups, respectively; with the content of fourfold BO_4 units could be estimated to be twice as large as BO_3 polyhedra according to the IR absorption intensity. The ageing of the gel at ambient conditions yields a white powder identified as $\text{NaB}(\text{OH})_4$ due to the uptake of sufficient water from the atmosphere.

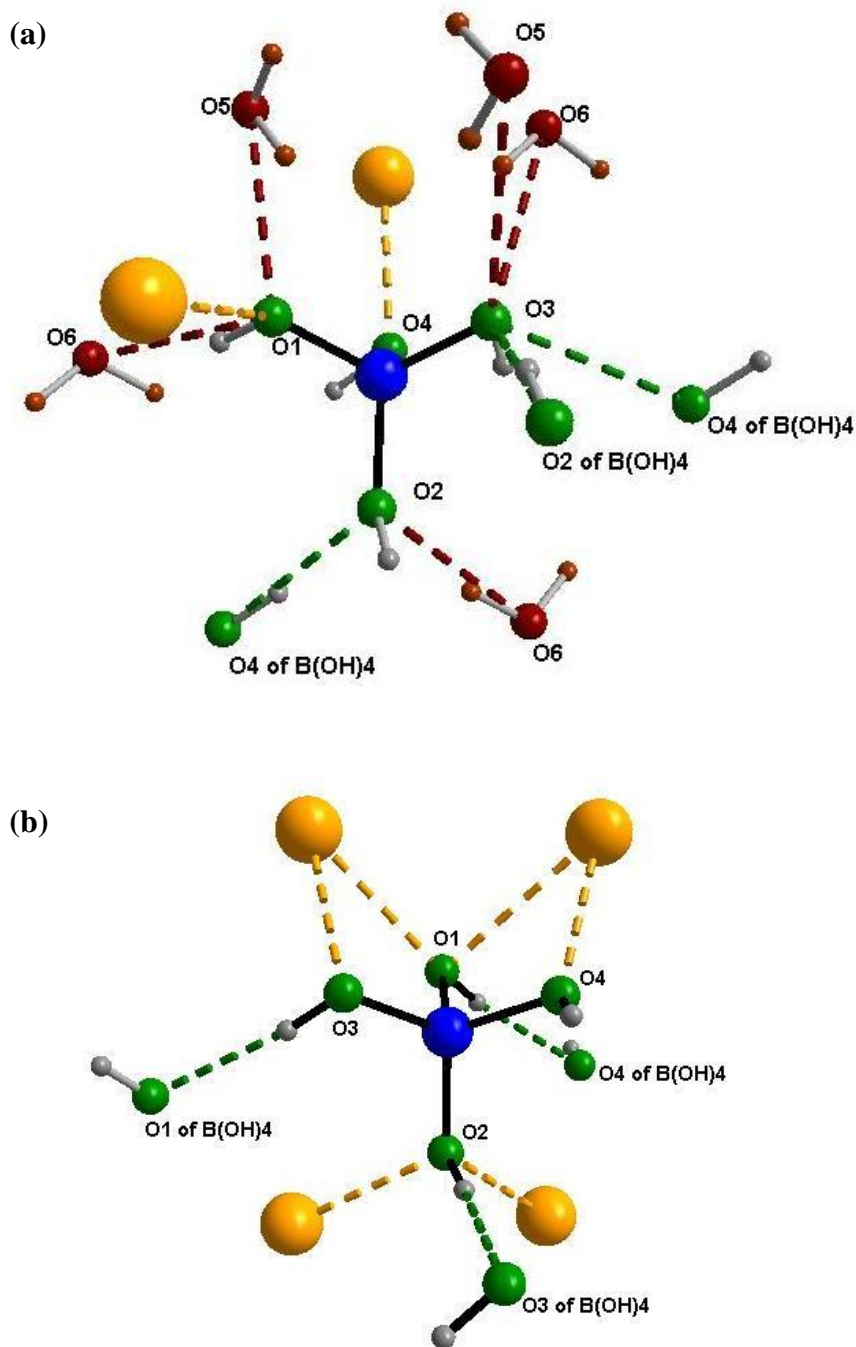


Figure 6.17: Coordination of B(OH)_4^- anion in (a) $\text{NaB(OH)}_4 \cdot 2\text{H}_2\text{O}$ and (b) NaB(OH)_4 crystals including sodium atoms and hydrogen bonds. The hydrogen bonding network in $\text{NaB(OH)}_4 \cdot 2\text{H}_2\text{O}$ is traced between oxygen atoms. (Na: yellow, B: blue; O and H of B(OH)_4^- : green and gray, respectively; H_2O molecules: dark red)

The gel is produced from the decomposition and dehydration of NaB(OH)_4 rather than its melting. At slow heating rates (2 and $1^\circ\text{C}/\text{min}$), the endotherm E3 corresponding to the formation of the gel from NaB(OH)_4 is resolved into two endotherms peaked at 96°C and a

sharper one at 91°C , respectively (**Figure 6.5**). Both are accompanied with dehydration as indicated on the dTG curves.

In a first approach, the gel formation could be referred to an amorphization which could explain the high endothermicity of E3 on the DTA curves (**Figure 6.4** and **Figure 6.6**). The gel crystallizes further to the $y = 1/3$ and then the $y = 0$ phases along with the dehydration process. By this way, the heat absorbed for the dehydration offsets the heat desorbed for the crystallization, i.e. the exothermic peaks of the crystallization overlap with the endothermic peaks of the dehydration on the DTA curves. It has been reported that the thermal dehydration of many borates ($\text{LiBO}_2 \cdot 8\text{H}_2\text{O}$ [195], $\text{LiB}_5\text{O}_8 \cdot 5\text{H}_2\text{O}$ [195] and $\text{K}_2\text{B}_4\text{O}_7 \cdot 4\text{H}_2\text{O}$ [196]) is accompanied with amorphization yielding amorphous anhydrous products which crystallize after completing the thermal dehydration process. For $\text{LiB}_2\text{O}_3(\text{OH}) \cdot \text{H}_2\text{O}$, in-situ X-ray patterns during the thermal dehydration reveals an intermediary amorphous phase which crystallizes along with the dehydration to the anhydrous crystalline $\text{Li}_2\text{B}_4\text{O}_7$. The corresponding DSC curve shows only endotherms related to the dehydration process [218, 219].

A different approach to explain the removal of $-\text{OH}$ groups from $\text{NaB}(\text{OH})_4$ is that the gel formation could be due to the condensation of water vapor evolved by the thermal dehydration and the dissolution of the solid reactant into the condensed water at the surface. This is based on the work of Koga et al. [196] who observed aggregated fine powders during the thermal dehydration of $\text{K}_2\text{B}_4\text{O}_7 \cdot 4\text{H}_2\text{O}$ using SEM photographs at different stages of the dehydration. The TG curve of $\text{K}_2\text{B}_4\text{O}_7 \cdot 4\text{H}_2\text{O}$ taken between 30 and 520°C under N_2 flowing shows a rapid mass decrease followed by a decelerating gradual mass loss in a wide temperature range. A similar trend was observed in this thesis for $\text{NaBO}_2 \cdot 4\text{H}_2\text{O}$ between 80 and 250°C at $1^\circ\text{C}/\text{min}$ under He (**Figure 6.5**). The rapid loss could be referred to the gel formation and the decelerating mass loss to the dehydration of the gel powders. The present approach implies that the dehydration of the $y = 2$ to the $y = 1/3$ phases includes dissolution and evaporation which are both in this case endothermic processes.

The anhydrous solid residues of the TG analyses performed on pre-evacuated and non-pre-evacuated samples of $\text{NaBO}_2 \cdot 4\text{H}_2\text{O}$ heated to 400°C at $5^\circ\text{C}/\text{min}$ (He//vac//5 and He//novac//5 experiments) and at $1^\circ\text{C}/\text{min}$ (He//vac//1) discussed in section 6.2.2 were collected and pressed in KBr pellets. All pellets were prepared in the same manner. Results are shown in **Figure 6.18**. The IR spectrum corresponding to TG analysis at $1^\circ\text{C}/\text{min}$ for a

non-pre-evacuated $\text{NaBO}_2 \cdot 4\text{H}_2\text{O}$ sample is also shown. This experiment is denoted He//novac//1 (TG results are not shown).

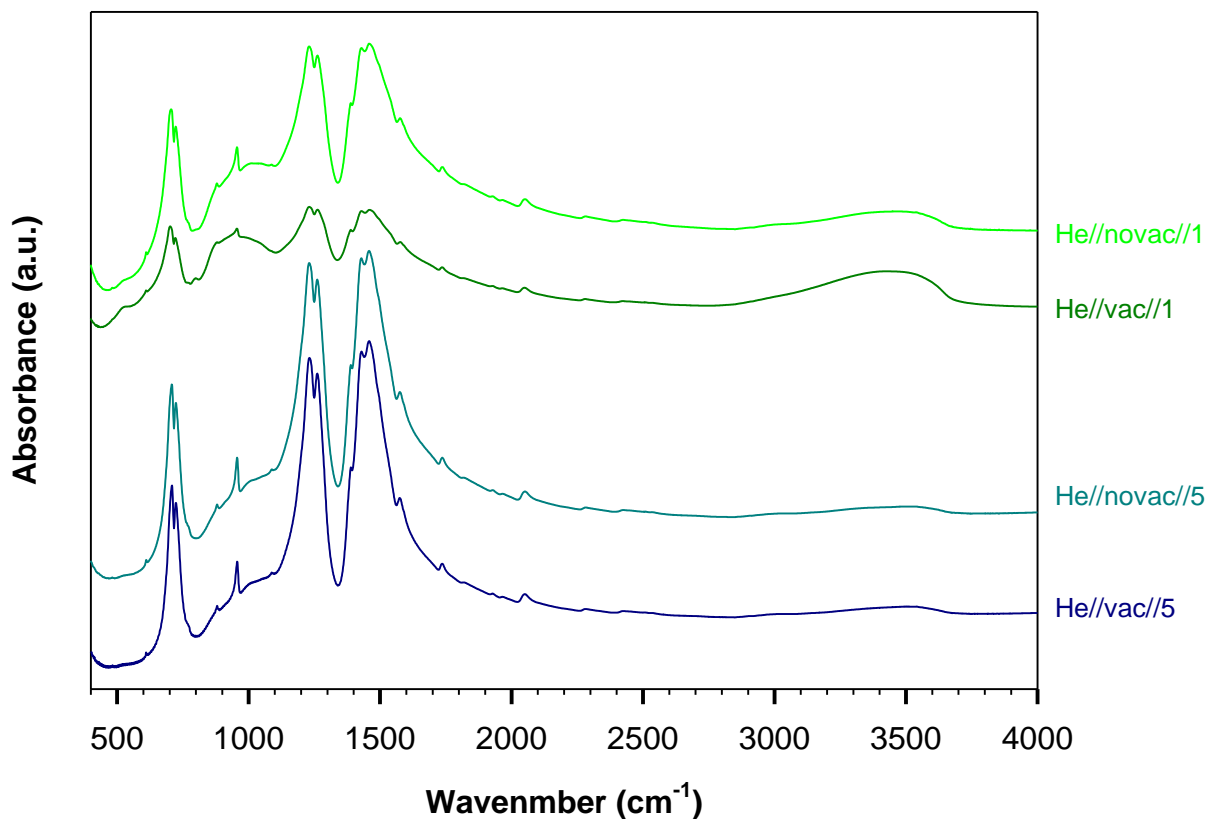


Figure 6.18: IR spectra of the anhydrous samples after TG analyses of pre-evacuated and non-pre-evacuated $\text{NaBO}_2 \cdot 4\text{H}_2\text{O}$ samples under He at 5 and 1°C/min (TG experiments are He//vac//5, He//novac//5, He//vac//1 and He//novac//1).

The IR spectra corresponding to the TG analyses at 5°C/min reveal strong and sharp peaks. Whereas at 1°C/min, the IR spectra exhibit a weak broadening at 900-1000 cm^{-1} and broader IR bands for $\text{Na}_3\text{B}_6\text{O}_6$ in addition to OH stretching band, indicating a rapid re-hydration and decomposition of the anhydrous samples. This could be interpreted by a large number of defects resulting from the slow dehydration of $\text{NaB}(\text{OH})_4$ at slow heating rates. The TG curve at 1°C/min indicates that the dehydration of the gel powders is decelerating and takes place over a wide temperature range. At 5°C/min, the gel dehydrates rapidly and could be better separated from the $y = 1/3$ phase. The rapid dehydration of the gel minimizes the defects and leads to $y = 1/3$ and $y = 0$ phases with better crystallinity.

The gel phase is obtained during the hydrolysis reaction of NaBH_4 with neutral $\text{H}_2\text{O}_{(l)}$ at 80°C (chapter 3, section 3.2.1). Marrero-Alfonso et al. [60] obtained 95 % hydrogen from the reaction of $\text{NaBH}_{4(s)}$ with $\text{H}_2\text{O}_{(g)}$ at 115°C without any need of catalyst, and 54% H_2 for the hydrolysis at 140°C . In this study, it is shown that the metaborate build a gel-like phase at $110\text{-}120^\circ\text{C}$ which could enhance the permeability of the reactant batch to $\text{H}_2\text{O}_{(g)}$ molecules and favor its diffusion in the NaBH_4 bulk leading to high H_2 yield. Whereas at 140°C , the gel dehydrates to $\text{Na}_3[\text{B}_3\text{O}_5(\text{OH})_2]$ crystal which hampers the diffusion of H_2O in the bulk material resulting in low H_2 yields.

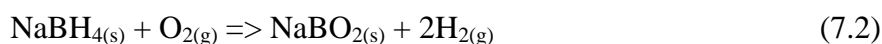
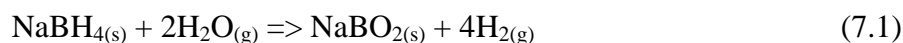
Further works on the mechanism of formation of the gel and its further crystallization to the one-third phase using surface exploring techniques as SEM are highly recommendable.

7. Conclusion and Outlook

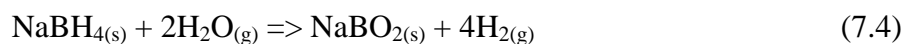
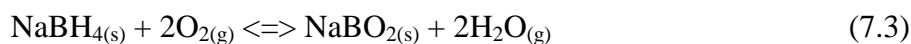
H₂ release of solid state NaBH₄ and role of metaborate by-products

NaBH₄ slightly subjected to ambient conditions forms NaBH₄·2H₂O. Crystalline water is released between 40 and 60°C without reaction with NaBH₄.

Under He, NaBH₄ is stable to 400°C. In presence of traces of H₂O or O₂, NaBH₄ reacted to Na₃B₃O₆ (*or* NaBO₂) between 300 and 400°C, releasing H₂ according to reactions (7.1) and (7.2), respectively.



The reaction with O_{2(g)} initiates at about 230°C for a dried NaBH₄ sample by pre-evacuating previous to the temperature treatment and proceeds in three main exothermic steps peaked on the dTG curve at 240, 272 and 306°C, respectively. For a non-pre-evacuated sample, the reaction is retarded by 10°C and is explained by a relatively higher effective water partial pressure in the sample. Therefore, it can be assumed that the reaction of NaBH₄ with O₂ produces in a first stage H₂O according to reaction (7.3). This reaction may form NaBO₂ or other intermediate. Water produced reacts further with NaBH₄ *or the intermediate* releasing H₂ (7.4).



In this way, the reaction (7.2) describes only the net effect. The reaction-step for water production (7.3) is an equilibrium, which can be displaced with a variation of the effective water partial pressure in the sample.

The reaction of NaBH₄ with H₂O_(g) to Na₃B₃O₆ is observed for temperatures above 300°C. At lower temperatures no decomposition of NaBH₄ with water vapor loaded in the atmosphere could be observed. In this temperature range TIR conducted under vacuum on

NaBH_4 using NaNO_3 indicates some H_2 release, which becomes more pronounced above 300°C along with the oxidation reaction of NaBH_4 to $\text{Na}_3\text{B}_3\text{O}_6$. The formation of $\text{Na}_3\text{B}_3\text{O}_6$ includes probably a transient species due to some indications of a weak but significant peak in the TIR spectra taken between 200 and 300°C at 1575 cm^{-1} assigned to a vibration involving boron B sp^2 hybridized and oxygen atoms.

The role of H_2O in the hydrogen release of NaBH_4 still needs further clarifications. This concerns the retardation effect on the reaction of NaBH_4 with O_2 and the H_2 release observed between 200 and 300°C under vacuum without decomposition of NaBH_4 .

The thermal stability of sodium metaborate compounds $\text{NaBO}_2 \cdot y\text{H}_2\text{O}$ was investigated in details to give more insights into the decomposition of NaBH_4 with $\text{H}_2\text{O}/\text{O}_2$. The thermal dehydration of $\text{NaB}(\text{OH})_4 \cdot 2\text{H}_2\text{O}$ (or $\text{NaBO}_2 \cdot 4\text{H}_2\text{O}$, $y = 4$) can be described in five main steps as follows:

- Disruption of the dihydrogen bonding network between crystalline H_2O molecules and $\text{B}(\text{OH})_4^-$ anions of the tetrahydrate and rearrangement of $\text{B}(\text{OH})_4^-$ anions in a similar way to that of the dihydrate ($y = 2$). The resulting phase corresponds to $\text{NaB}(\text{OH})_4$ in addition to “external” water of hydration and is denoted $\text{NaB}(\text{OH})_{4+y'} \cdot \text{H}_2\text{O}$ ($2 < y' < 4$)
- Release of molecular water ($y' \text{H}_2\text{O}$) and formation of $\text{NaB}(\text{OH})_4$ ($y = 2$)
- Dehydration of $\text{NaB}(\text{OH})_4$ to an amorphous gel-like phase formed of tetrahedral BO_4 and planar BO_3 groups
- Dehydration-crystallization of the gel to $\text{Na}_3[\text{B}_3\text{O}_5(\text{OH})]_2$ ($y = 1/3$)
- Dehydration of the one-third phase to $\text{Na}_3\text{B}_3\text{O}_6$ ($y = 0$)

All these steps correspond to endothermic effects peaked on the DTA curve taken at 5°C under He at 61, 86, 109, 154 and 283°C , respectively.

The reaction of NaBH_4 with neutral H_2O at room temperature leads to $\text{NaB}(\text{OH})_4$ and un-reacted NaBH_4 . Additional water of hydration remains unbound to the dihydrate by-product ($\text{NaB}(\text{OH})_{4+y'} \cdot \text{H}_2\text{O}$). At 80°C , the reaction yields after a prolonged heating time (more than 24 h) the gel phase. At temperatures above 300°C , NaBH_4 reacts with $\text{H}_2\text{O}/\text{O}_2$ to $\text{Na}_3\text{B}_3\text{O}_6$. **Figure 7.1** summarizes the thermal H_2 release path using NaBH_4 between 20 and 400°C in comparison with the dehydration path of sodium metaborate compounds.

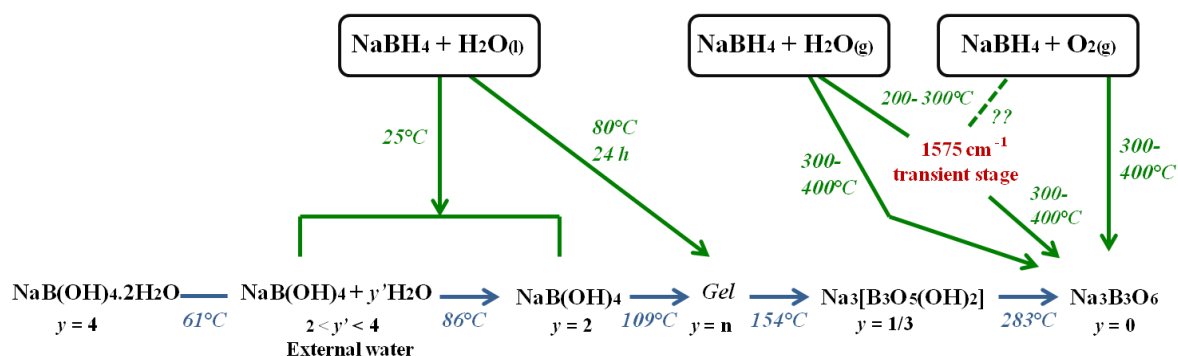


Figure 7.1: The thermal path for H_2 release using NaBH_4 between 20 and 400°C (green arrows) in comparison with the dehydration path for $\text{NaBO}_2 \cdot 4\text{H}_2\text{O}$ (blue arrows), as obtained in this thesis. The net reaction of NaBH_4 with O_2 is considered. Further experiments are needed to verify whether the transient species at 1575 cm^{-1} may occur from the reaction of NaBH_4 with O_2 between 200 and 300°C.

No decomposition of NaBH_4 to the one-third phase between 200 and 300°C could be observed. Instead, a weak peak at 1575 cm^{-1} is observed as transient state to $\text{Na}_3\text{B}_3\text{O}_6$. This may indicate a new reaction path for H_2 release using NaBH_4 between 200 and 300°C which is different from the decomposition path to $\text{Na}_3\text{B}_3\text{O}_6$ observed at temperatures above 300°C according to reactions (7.1) and (7.2). This may pose new insights in the research field of hydrogen storage using NaBH_4 . One approach, hydrogen release between 200 and 300°C may involve a poorly catalytic effect of NaBH_4 for the thermal production of hydrogen from water. The released O_2 adsorbs on NaBH_4 and reacts further to $\text{Na}_3\text{B}_3\text{O}_6$ (reactions 7.1 and 7.2). Other scenarios could not be excluded.

Further work including systematic variations of the partial pressures of H_2O and O_2 on NaBH_4 films heated between 20 and 400°C with characterization of the metaborate by-product and analysis of the evolved gas phase are highly recommendable.

H_2 release from NH_3BH_3 and $\text{NH}_3\text{BH}_3\text{-G}$ composites

$\text{NH}_3\text{BH}_3\text{-G}$ behaves similarly to NH_3BH_3 upon heating. Foaming and undesirable B, N-containing gases observed during the dehydrogenation of NH_3BH_3 salt can be avoided for $\text{NH}_3\text{BH}_3\text{-G}$. Both melt at about 115-118°C as indicated on the DTA curves. The dehydrogenation can be described by series of polymerizations and condensations reactions of B, N-chains yielding in a first step PAB ($-\text{H}_2\text{N}-\text{BH}_2-$)_n at about 140°C characterized by single bonds between B and N atoms, and in a second step PIB ($-\text{HN}=\text{BH}-$)_n at about 170°C characterized by the π -character between the BN bonds. The formation of PAB goes through

the diammoniate of diborane DADB $[(\text{NH}_3)_2\text{BH}_2]\text{BH}_4$ intermediate. This was indirectly proven in the TIR experiments using KBr matrix which favors the anionic exchange between DADB and KBr stabilizing thus the BH_4^- anions in the matrix. Short oligomeric species as linear dimer of aminoborane LDAB $\text{NH}_3\text{BH}_2\text{NH}_2\text{BH}_3$ could be found in the early stages of the condensation-dehydrogenation reactions.

Further optimization procedures of $\text{NH}_3\text{BH}_3\text{-G}$ composite including the variation of the molar Si/Al ratio, the mass ratio $\text{NH}_3\text{BH}_3/\text{sample}$, the drying procedure...are desirable for an optimization of H_2 release.

Solid solution of BH_4^-

The IR frequencies observed after room temperature pressing of NaBH_4 in halide matrices are affected by more or less strong ion exchange effects between the halide and the borohydride. For NaBH_4 in NaBr, NaI, KBr and KI pellets, respectively, the IR frequencies refer to BH_4^- highly diluted in AX. For NaBH_4 in NaCl and KCl pellets the solution of BH_4^- in AX occurs after thermal treatment to 450°C . This is accompanied by shifting of the BH_4^- related peaks to higher frequencies. The high dilution of BH_4^- anion in the halide refers to an isolation of BH_4^- in AX ($i\text{-BH}_4^-$). The impact of the halide ionic surrounding on BH_4^- anion is discussed in terms of the IR frequencies of $i\text{-BH}_4^-$. Systematic variations are observed between $\nu_3(i\text{-BH}_4^-)$ and different structural parameters of AX including the cell parameter, the cation to anion ratio, enthalpie, ionic character of the halide and Pauling electronegativity of the cations and anions. The correlations are applicable to homologous series of AX possessing the same cationic A element (A-series: Na-, K-, Rb-series) or the same anionic X element (X-series: Cl-, Br and I-series). It is observed that small cations and anions produces deeper changes in $\nu_3(i\text{-BH}_4^-)$. Furthermore, $\nu_3(i\text{-BH}_4^-)$ is strongly affected by the nature of the anion X rather than the cation A. The correlations are extended to include the thermal stability of the borohydride. Within X-group, an increase of $\nu_3(i\text{-BH}_4^-)$ is accompanied by a decrease of the thermal stability of the borohydride. Whereas, within A-group, an increase of $\nu_3(i\text{-BH}_4^-)$ is expected to be accompanied by an increase of the thermal stability. For X-group, an increase of the Pauling electronegativity of the cation reduces the electronic density on BH_4^- destabilizing thus the borohydride, whereas for A-group, an increase of the Pauling electronegativity of the anions would increase the electronic density on BH_4^- due to the increased repulsive interactions yielding to a stabilization of the borohydride.

A more regular linear relation is found between $\nu_3(\text{i-BH}_4^-)$ and the contribution of the short range interactions energies of AX. This indicates that the frequency variations are strongly influenced by the repulsive forces between BH_4^- and the nearest neighbors.

The effect of cation electronegativity on the thermal stability of the borohydride is well discussed in the literature (for e.g. ref. [168]). Further experiments are needed to demonstrate the effect of anion electronegativity on the thermal stability of the borohydride.

V. Literature

- [1] G. Walker, *Solid-state Hydrogen Storage: Materials and Chemistry*, Woodhead Publishing Ltd, 2008.
- [2] M. B. Ley, L. H. Jepsen, Y.-S. Lee, Y. W. Cho, J. M. Bellosta von Colbe, M. Dornheim, M. Rokni, J. O. Jensen, M. Sloth, Y. Filinchuk, J. E. Jørgensen, F. Besenbacher and T. R. Jensen, "Complex Hydrides for Hydrogen Storage – New Perspectives," *Mater. Today*, vol. 17, pp. 122-128, 2014.
- [3] C. Liu, F. Li, L.-P. Ma and H.-M. Cheng, "Advanced Materials for Energy Storage," *Adv. Mater.*, vol. 22, pp. E28-E62, 2010.
- [4] N. C. Smythe and J. C. Gordon, "Ammonia Borane as a Hydrogen Carrier: Dehydrogenation and Regeneration," *Eur. J. Inorg. Chem.*, pp. 509-521, 2010.
- [5] T. K. Mandal and D. H. Gregory, "Hydrogen Storage Materials: Present Scenarios," *Annu. Rep. Prog. Chem., Sect. A*, vol. 105, pp. 21-54, 2009.
- [6] P. Benard and R. Chahine, "Storage of Hydrogen by Physisorption on Carbon and Nanostructured Materials," *Scripta Mater.*, vol. 56, pp. 803-808, 2007.
- [7] T. Umegaki, J.-M. Yan, X.-B. Zhang, H. Shioyama, N. Kuriyama and Q. Xu, "Boron- and Nitrogen-Based Chemical Hydrogen Storage Materials," *Int. J. Hydrogen Energy*, vol. 34, pp. 2303-2311, 2009.
- [8] C. W. Hamilton, R. T. Baker, A. Staubitz and I. Manners, "B–N Compounds for Chemical Hydrogen Storage," *Chem. Soc. Rev.*, vol. 38, pp. 279-293, 2009.
- [9] L. H. Jepsen, M. B. Ley, Y.-S. Lee, Y. W. Cho, M. Dornheim, J. O. Jensen, Y. Filinchuk, J. E. Jørgensen, F. Besenbacher and T. R. Jensen, "Boron–Nitrogen Based Hydrides and Reactive Composites for Hydrogen Storage," *Mater. Today*, vol. 17, pp. 129-135, 2014.
- [10] A. Karkamkar, S. M. Kathmann, G. K. Schenter, D. J. Heldebrant, N. Hess, M. Gutowski and T. Autrey, "Thermodynamic and Structural Investigations of Ammonium Borohydride, a Solid with a Highest Content of Thermodynamically and Kinetically Accessible Hydrogen," *Chem. Mater.*, vol. 21, pp. 4356-4358, 2009.
- [11] U. B. Demirci and P. Miele, "Sodium Borohydride versus Ammonia Borane, in Hydrogen Storage and Direct Fuel Cell Applications," *Energy Environ. Sci.*, vol. 2, pp. 627-637, 2009.
- [12] A. D'Ulivo, "Chemical Vapor Generation by Tetrahydroborate(III) and Other Borane Complexes in Aqueous Media A Critical Discussion of Fundamental Processes and Mechanisms Involved in Reagent Decomposition and Hydride Formation," *Spectrochim. Acta B*, vol. 59, pp. 793-825, 2004.

- [13] A. Züttel, A. Borgschulte and S.-I. Orimo, "Tetrahydroborates as New Hydrogen Storage Materials," *Scripta Mater.*, vol. 56, pp. 823-828, 2007.
- [14] P. Vajeeston, P. Ravindran, A. Kjekshus and H. Fjellvag, "Structural Stability of Alkali Boron Tetrahydrides ABH_4 ($A = Li, Na, K, Rb, Cs$) from First Principle Calculation," *J. Alloys Compd.*, vol. 387, p. 97-104, 2005.
- [15] H. I. Schlesinger, H. C. Brown, A. E. Finholt, J. R. Gilbreath, H. R. Hoekstra and E. K. Hyde, "Sodium Borohydride, its Hydrolysis and its Use as a Reducing Agent and in the Generation of Hydrogen," *J. Am. Chem. Soc.*, vol. 75, pp. 215-219, 1953.
- [16] A. M. Soldate, "Crystal Structure of Sodium Borohydride," *J. Am. Chem. Soc.*, vol. 69, pp. 987-988, 1947.
- [17] "<http://www.hydrogen.energy.gov/>," [Online].
- [18] U. B. Demirci, O. Akdim and P. Miele, "Ten-Year Efforts and a No-Go Recommendation for Sodium Borohydride for On-Board Automotive Hydrogen Storage," *Int. J. Hydrogen Energy*, vol. 34, pp. 2638-2645, 2009.
- [19] J. Mao and D. H. Gregory, "Recent Advances in the Use of Sodium Borohydride as a Solid State Hydrogen Store," *Energies*, vol. 8, pp. 430-453, 2015.
- [20] S. Orimo, Y. Nakamori and A. Züttel, "Material Properties of MBH_4 ($M = Li, Na, and K$)," *Mater. Sci. Eng., B*, vol. 108, pp. 51-53, 2004.
- [21] J. Urgnani, F. J. Torres, M. Palumbo and M. Baricco, "Hydrogen Release from Solid State $NaBH_4$," *Int. J. Hydrogen Energy*, vol. 33, pp. 3111-3115, 2008.
- [22] P. Wang, "Solid-State Thermolysis of Ammonia Borane and Related Materials for High-Capacity Hydrogen Storage," *Dalton Trans.*, vol. 41, p. 4296-4302, 2012.
- [23] T. B. Marder, "Will We Soon Be Fueling our Automobiles with Ammonia-Borane?," *Angew. Chem. Int. Ed.*, vol. 46, p. 8116 - 8118, 2007.
- [24] C. H. Rüscher, L. Schomborg, A. Schulz and J. C. Buhl, "Basic Research on Geopolymer Gels for Production of Green Binders and Hydrogen Storages," *In Developments in strategic materials and computational design IV* (eds W. M. Kriven, J. Wang, Y. Zhou, A. L. Gyekenyesi, S. Kirihara and S. Widjaja John), Wiley & Sons, Inc., Hoboken, NJ, USA, vol. 34, pp. 97-114, 2013.
- [25] L. Schomborg, C. H. Rüscher, J. C. Buhl and F. Kiesel, " $NaBH_4$ Geopolymer Composites," *International Conference on Advanced Ceramics and Composites January 27-31, 2014 Daytona Beach, Florida ICACC*, 2014.
- [26] L. Schomborg, Z. Assi, J.-C. Buhl, C. H. Rüscher and M. Wark, "Ammonia Borane Geopolymer (AB-G) Composite," *In Developments in Strategic Ceramic Materials: A Collection of Papers Presented at the 39th International Conference on Advanced Ceramics and Composites* (eds W. M. Kriven, J. Wang, D. Zhu and T. Fischer), John

- Wiley & Sons, Inc., Hoboken, NJ, USA, 2015.
- [27] P. Duxson, A. Fernandez-Jimenez, J. L. Provis, G. C. Lukey, A. Palomo and J. S. J. van Deventer, "Geopolymer Technology: the Current State of the Art," *J. Mater. Sci.*, vol. 42, p. 2917–2933, 2007.
- [28] H. Kamarudin, A. M. Mustafa Al Bakri, M. Binhussain, C. M. Ruzaidi, M. Luqman, C. Y. Heah and Y. M. Liew, "Preliminary Study on Effect of NaOH Concentration on Early Age Compressive Strength of Kaolin-Based Green Cement," *International Conference on Chemistry and Chemical Process ICCCP, Singapore*, vol. 10, pp. 18-24, 2011.
- [29] "https://shop.perkinelmer.com/content/TechnicalInfo/TCH_FTIRATR.pdf," [Online].
- [30] C. H. Rüscher, "Chemical Reactions and Structural Phase Transitions of Sodalites and Cancrinites in Temperature Dependent Infrared (TIR) Experiments," *Micropor. Mesopor. Mat.*, vol. 86, pp. 58-68, 2005.
- [31] K. Nakamoto, *Infrared and Raman Spectra of Inorganic and Coordination Compounds, Part A: Theory and Applications in Inorganic Chemistry*, sixth edition, New Jersey: Wiley, 2009.
- [32] A. Strasheim and K. Buijs, "Infrared Absorption of Nitrate Ions Dissolved in Solid Alkali Halides," *J. Chem. Phys.*, vol. 34, pp. 691-692, 1961.
- [33] R. Metselaar and J. V. D. Elskens, "Lattice Vibrations of Solid Solutions; Infrared Absorption Spectra of Nitrate Ions in Alkali Halides," *Phys. Rev.*, vol. 165, pp. 359-375, 1968.
- [34] A. Maki and J. C. Decius, "Vibrational Spectrum of Cyanate Ion in Various Alkali Halide Lattices," *J. Chem. Phys.*, vol. 31, pp. 772-782, 1959.
- [35] D. L. Bernitt, K. O. Hartman and I. C. Hisatsune, "Infrared Spectra of Isotopic Bicarbonate Monomer Ions," *J. Chem. Phys.*, vol. 42, pp. 3553-3558, 1965.
- [36] H. W. Morgan and P. A. Staats, "Infrared Spectra of Dilute Solid Solutions," *J. Appl. Phys.*, vol. 33, pp. 364-366, 1962.
- [37] J. C. Buhl, L. Schomborg and C. H. Rüscher, "Tetrahydroborate Sodalite Nanocrystals: Low Temperature Synthesis and Thermally Controlled Intra-Cage Reactions for Hydrogen Release of Nano- and Micro Crystals," *Micropor. Mesopor. Mat.*, vol. 132, pp. 210-218, 2010.
- [38] J. C. Buhl, L. Schomborg and C. H. Rüscher, "Enclosure of Sodium Tetrahydroborate (NaBH₄) in Solidified Aluminosilicate Gels and Microporous Crystalline Solids for Fuel Processing," in *Hydrogen Storage*, J. Liu ed., INTECH ISBN 978-953-51-0371-6, free online editons, pp. 49-90, 2012.
- [39] V. Narayanamurti, W. D. Seward and R. O. Pohl, "Rotational Degrees of Freedom of Molecules in Solids. II. The Nitrite Ion in Alkali Halides," *Phys. Rev.*, vol. 148, pp. 481-

- 493, 1966.
- [40] M. J. Harris, E. K. H. Salje and B. K. Güttler, "An Infrared Spectroscopic Study of the Internal Modes of Sodium Nitrate: Implications for the Structural Phase Transition," *J. Phys.: Condens. Matter*, vol. 2, pp. 5517-5527, 1990.
- [41] G. S. Bumrah and R. M. Sharma, "Raman Spectroscopy – Basic principle, Instrumentation and Selected Applications for the Characterization of Drugs of Abuse," *Egypt. J. Forensic Sci.*, www.sciencedirect.com, 2015.
- [42] J. S. Kasper, L. V. McCarty and A. E. Newkirk, "Sodium Borohydride--Disodium Diborane," *J. Am. Chem. Soc.*, vol. 71, p. 2583, 1949.
- [43] H. I. Schlesinger, H. C. Brown, H. R. Hoekstra and L. R. Rapp, "Reactions of Diborane with Alkali Metal Hydrides and their Addition Compounds. New Syntheses of Borohydrides. Sodium and Potassium Borohydrides," *J. Am. Chem. Soc.*, vol. 75, pp. 199-204, 1953.
- [44] H. I. Schlesinger, H. C. Brown and A. E. Finholt, "The Preparation of Sodium Borohydride by the High Temperature Reaction of Sodium Hydride with Borate Esters," *J. Am. Chem. Soc.*, vol. 75, pp. 205-209, 1953.
- [45] Y. Wu, J. C. Brady, M. T. Kelly, J. V. Ortega and J. L. Snover, "Synthesis of Sodium Borohydride for Energy Applications," *Prepr. Pap.-Am. Chem. Soc., Div. Fuel Chem.*, vol. 48, pp. 938-939, 2003.
- [46] S. C. Abrahams and J. Kalnajs, "The Lattice Constants of the Alkali Borohydrides and the Low-Temperature Phase of Sodium Borohydride," *J. Chem. Phys.*, vol. 22, pp. 434-436, 1954.
- [47] P. Fischer and A. Züttel, "Order-Disorder Phase Transition in NaBD₄," *Mater. Sci. Forum*, Vols. 443-444, pp. 287-290, 2004.
- [48] Y. Filinchuk, A. V. Talyzin, D. Chernyshov and V. Dmitriev, "High-Pressure Phase of NaBH₄: Crystal Structure from Synchrotron Powder Diffraction Data," *Phys. Rev. B*, vol. 76, p. 092104, 2007.
- [49] Y. Filinchuk and H. Hagemann, "Structure and Properties of NaBH₄·2H₂O and NaBH₄," *Eur. J. Inorg. Chem.*, pp. 3127-3133, 2008.
- [50] R. L. Davis and C. H. L. Kenard, "Structure of Sodium Tetradeuteroborate, NaBD₄," *J. Solid State Chem.*, vol. 59, pp. 393-396, 1985.
- [51] Y. Filinchuk, D. Chernyshov and V. Dmitriev, "Light Metal Borohydrides: Crystal Structures and Beyond," *Z. Kristallogr.*, vol. 223, pp. 649-659, 2008.
- [52] V. G. Minkina, S. I. Shabunya, V. I. Kalinin, V. V. Martynenko and A. L. Smirnova, "Stability of Alkaline Aqueous Solutions of Sodium Borohydride," *Int. J. Hydrogen Energy*, vol. 37, pp. 3313-3318, 2012.

- [53] S. C. Amendola, S. L. Sharp-Goldman, M. S. Janjua, N. C. Spencer, M. T. Kelly, P. J. Petillo and M. Binder, "A Safe, Portable, Hydrogen Gas Generator Using Aqueous Borohydride Solution and Ru Catalyst," *Int. J. Hydrogen Energy*, vol. 25, pp. 969-975, 2000.
- [54] Y. Kojima, K.-i. Suzuki, K. Fukumoto, M. Sasaki, T. Yamamoto, Y. Kawai and H. Hayashi, "Hydrogen Generation Using Sodium Borohydride Solution and Metal Catalyst Coated on Metal Oxide," *Int. J. Hydrogen Energy*, vol. 27, pp. 1029-1034, 2002.
- [55] A. M. F. R. Pinto, D. S. Falcão, R. A. Silva and C. M. Rangel, "Hydrogen Generation and Storage from Hydrolysis of Sodium Borohydride in Batch Reactors," *Int. J. Hydrogen Energy*, vol. 31, p. 1341-1347, 2006.
- [56] B. H. Liu and Z. P. Li, "A Review: Hydrogen Generation from Borohydride Hydrolysis Reaction," *J. Power Sources*, vol. 187, p. 527-534, 2009.
- [57] U. B. Demirci, O. Akdim, J. Andrieux, J. Hannauer, R. Chamoun and P. Miele, "Sodium Borohydride Hydrolysis as Hydrogen Generator: Issues, State of the Art and Applicability Upstream from a Fuel Cell," *Fuel Cells*, vol. 10, pp. 335-350, 2010.
- [58] R. Retnamma, A. Q. Novais and C. M. Rangel, "Kinetics of Hydrolysis of Sodium Borohydride for Hydrogen Production in Fuel Cell Applications: A Review," *Int. J. Hydrogen Energy*, vol. 36, pp. 9772-9790, 2011.
- [59] G. Y. Moon, S. S. Lee, K. Y. Lee, S. H. Kim and K. H. Song, "Behavior of Hydrogen Evolution of Aqueous Sodium Borohydride Solutions," *Ind. Eng. Chem.*, vol. 14, p. 94-99, 2008.
- [60] E. Y. Marrero-Alfonso, J. R. Gray, T. A. Davis and M. A. Matthews, "Hydrolysis of Sodium Borohydride with Steam," *Int. J. Hydrogen Energy*, vol. 32, pp. 4717-4722, 2007.
- [61] E. Y. Marrero-Alfonso, J. R. Gray, T. A. Davis and M. A. Matthews, "Minimizing Water Utilization in Hydrolysis of Sodium Borohydride: The Role of Sodium Metaborate Hydrates," *Int. J. Hydrogen Energy*, vol. 32, pp. 4723-4730, 2007.
- [62] J. Andrieux, U. B. Demirci, J. Hannauer, C. Gervais, C. Goutaudier and P. Miele, "Spontaneous Hydrolysis of Sodium Borohydride in Harsh Conditions," *Int. J. Hydrogen Energy*, vol. 36, pp. 224-233, 2011.
- [63] R. E. Davis, E. Bromels and C. L. Kibby, "Boron Hydrides. 111. Hydrolysis of Sodium Borohydride in Aqueous Solution," *J. Am. Chem. Soc.*, vol. 84, pp. 885-892, 1962.
- [64] R. E. Davis and C. G. Swain, "General Acid Catalysis of the Hydrolysis of Sodium Borohydride," *J. Am. Chem. Soc.*, vol. 82, p. 5949-5950, 1960.
- [65] R. E. Mesmer and W. L. Jolly, "The Hydrolysis of Aqueous Hydroborate," *Inorg. Chem.*, vol. 1, p. 608-612, 1962.

- [66] M. M. Kreevoy and J. E. C. Hutchins, " H_2BH_3 as an Intermediate in Tetrahydridoborate Hydrolysis," *J. Am. Chem. Soc.*, vol. 94, p. 6371–6376, 1972.
- [67] G. A. Olah, P. W. Westerman, Y. K. Mo and G. Klopman, "Electrophilic Reactions at Single Bonds. VII. Hydrogen-Deuterium Exchange Accompanying Protolysis (Deuterolysis) of Borohydride and Aluminum Hydride Anions with Anhydrous Strong Acids," *J. Am. Chem. Soc.*, vol. 94, p. 7859–7862, 1972.
- [68] P. Li, G. Henkelman, J. A. Keith and J. K. Johnson, "Elucidation of Aqueous Solvent-Mediated Hydrogen-Transfer Reactions by Ab-Initio Molecular Dynamics and Nudged Elastic-Band Studies of NaBH_4 Hydrolysis," *J. Phys. Chem. C*, vol. 118, p. 21385–21399, 2014.
- [69] J. A. Gardiner and J. W. Collat, "Kinetics of the Stepwise Hydrolysis of Tetrahydroborate Ion," *J. Am. Chem. Soc.*, vol. 87, p. 1692–1700, 1965.
- [70] W. L. Jolly and R. E. Mesmer, "Exchange of Hydrogen between Water and the Hydroborate Anion," *J. Am. Chem. Soc.*, vol. 83, p. 4470–4471, 1961.
- [71] P. R. Girardot and R. W. Parry, "Isotopic Exchange between D_2O and NaBH_4 ," *J. Am. Chem. Soc.*, vol. 73, p. 2368–2368, 1951.
- [72] K. A. Grice, M. C. Groenenboom, J. D. A. Manuel, M. A. Sovereign and J. A. Keith, "Examining the Selectivity of Borohydride for Carbon Dioxide and Bicarbonate Reduction in Protic Conditions," *Fuel*, vol. 150, p. 139–145, 2015.
- [73] G. Guella, C. Zanchetta, B. Patton and A. Miotello, "New Insights on the Mechanism of Palladium-Catalyzed Hydrolysis of Sodium Borohydride from ^{11}B NMR Measurements," *J. Phys. Chem. B*, vol. 110, pp. 17024–17033, 2006.
- [74] G. Guella, B. Patton and A. Miotello, "Kinetic Features of the Platinum Catalyzed Hydrolysis of Sodium Borohydride from ^{11}B NMR Measurements," *J. Phys. Chem. C*, vol. 111, pp. 18744–18750, 2007.
- [75] J. A. Gardiner and J. W. Collat, "The Hydrolysis of Sodium Tetrahydroborate. Identification of an Intermediate," *J. Am. Chem. Soc.*, vol. 86, p. 3165–3166, 1964.
- [76] J. Goubeau and H. Kallfass, "Die Reaktion Natriumborhydrid und Wasser," *Z. anorg. allg. Chem.*, vol. 299, p. 160–169, 1959.
- [77] F. T. Wang and W. L. Jolly, "Kinetic Study of the Intermediates in the Hydrolysis of the Hydroborate Ion," *Inorg. Chem.*, vol. 11, p. 1933–1941, 1972.
- [78] P. Martelli, R. Caputo, A. Remhof, P. Mauron, A. Borgschulte and A. Züttel, "Stability and Decomposition of NaBH_4 ," *J. Phys. Chem. C*, vol. 114, p. 7173–7177, 2010.
- [79] D. Cakır, G. A. de Wijs and G. Brocks, "Native Defects and the Dehydrogenation of NaBH_4 ," *J. Phys. Chem. C*, vol. 115, p. 24429–24434, 2011.

- [80] O. Friedrichs, A. Remhof, S.-J. Hwang and A. Züttel, "Role of $\text{Li}_2\text{B}_{12}\text{H}_{12}$ for the Formation and Decomposition of LiBH_4 ," *Chem. Mater.*, vol. 22, p. 3265–3268, 2010.
- [81] G. Renaudin, S. Gomes, H. Hagemann, L. Keller and K. Yvon, "Structural and Spectroscopic Studies on the Alkali Borohydrides MBH_4 ($M = \text{Na}, \text{K}, \text{Rb}, \text{Cs}$)," *J. Alloys Compd.*, vol. 375, p. 98–106, 2004.
- [82] K. B. Harvey and McQuaker, "Infrared and Raman Spectra of Potassium and Sodium Borohydride," *Can. J. Chem.*, vol. 49, pp. 3272–3281, 1971.
- [83] M. I. Memon, W. F. Sherman and G. R. Wilkinson, "The Raman Spectra of BH_4^- and BD_4^- Isolated in Alkali Halides at 80 K," *J. Raman Spectrosc.*, vol. 13, pp. 96–99, 1982.
- [84] M. I. Memon, W. F. Sherman and G. R. Wilkinson, "Fermi Resonances in the Raman Spectra of Alkali Halide/ BH_4^- ," *J. Mol. Struct.*, vol. 115, pp. 213–216, 1984.
- [85] A. M. Beaird, P. Li, H. S. Marsh, W. A. Al-Saidi, J. K. Johnson, M. A. Matthews and C. T. Williams, "Thermal Dehydration and Vibrational Spectra of Hydrated Sodium Metaborates," *Ind. Eng. Chem. Res.*, vol. 50, pp. 7746–7752, 2011.
- [86] C. J. H. Schutte, "The Infra-red Spectrum of Thin Films of Sodium Borohydride," *Spectrochim. Acta*, vol. 16, pp. 1054–1059, 1960.
- [87] P. Carbonnière and H. Hagemann, "Fermi Resonances of Borohydrides in a Crystalline Environment of Alkali Metals," *J. Phys. Chem. A*, vol. 110, pp. 9927–9933, 2006.
- [88] G. Kessler and H.-A. Lehmann, "IR-Spektroskopische Untersuchungen an Boraten. I. Natrium(1:1:4)-borathydrat," *Z. Anorg. Allg. Chem.*, vol. 338, pp. 179–184, 1965.
- [89] L. Jun, X. Shuping and G. Shiyang, "FT-IR and Raman Spectroscopic Study of Hydrated Borates," *Spectrochim. Acta*, vol. 51A, pp. 519–532, 1995.
- [90] Z. Assi, L. Schomborg and C. H. Rüscher, "Investigations of the Thermally Induced Hydrogen Release of NaBH_4 , NH_3BH_3 and their Geopolymer Composites," in *the 40th International Conference and Expo on Advanced Ceramics and Composites*, 2016.
- [91] I. C. Hisatsune and N. H. Suarez, "Infrared Spectra of Metaborate Monomer and Trimer Ions," *Inorg. Chem.*, vol. 3, pp. 168–174, 1964.
- [92] J. A. A. Ketelaar and C. J. H. Schutte, "The Borohydride ion (BH_4^-) in a Face-Centred Cubic Alkali-Halide Lattice," *Spectrochim. Acta*, vol. 17, pp. 1240–1243, 1961.
- [93] T. R. Burkholder and L. Andrews, "Reactions of Boron Atoms with Molecular Oxygen. Infrared Spectra of BO , BO_2 , B_2O_2 , B_2O_3 , and BO_2^- in Solid Argon," *J. Chem. Phys.*, vol. 95, pp. 8697–8709, 1991.
- [94] B. Pachaly and R. West, "Synthesis of a 1,3-Dioxa-2,4-diboretane: an Oxoborane," *J. Am. Chem. Soc.*, vol. 107, pp. 2987–2988, 1985.

- [95] M. G. Walawalkar, "Multiple Bonds Continue to Fascinate Chemists: Discovery of Stable Si≡Si and B=O Bonds," *Curr. Sci.* 2005, 89, 606–607, vol. 89, pp. 606-607, 2005.
- [96] H. H. E. Pietsch, M. Fechtelkord and J. C. Buhl, "The Formation of Unusually Twofold Coordinated Boron in a Sodalite Matrix," *J. Alloy. Compd.*, vol. 257, pp. 168-174, 1997.
- [97] K. O. Hartman and I. C. Hisatsune, "The Kinetics of Formate Ion Pyrolysis in Alkali Halide Matrices," *J. Phys. Chem.*, vol. 70, p. 1281–1287, 1966.
- [98] I. C. Hisatsune, T. Adl, E. C. Beahm and R. J. Kempf, "Matrix Isolation and Decay Kinetics of Carbon Dioxide and Carbonate Anion Free Radicals," *J. Phys. Chem.*, vol. 74, p. 3225–3231, 1970.
- [99] K. O. Hartman and I. C. Hisatsune, "The Kinetics of Calcium Formate Pyrolysis in Potassium Bromide Matrix," *J. Phys. Chem.*, vol. 69, p. 583–589, 1965.
- [100] K. O. Hartman and I. C. Hisatsune, "Infrared Spectrum of Carbon Dioxide Anion Radical," *J. Chem. Phys.*, vol. 44, pp. 1913-1918, 1966.
- [101] J. Zhang and J. W. Lee, "Production of Boron-Doped Porous Carbon by the Reaction of Carbon Dioxide with Sodium Borohydride at Atmospheric Pressure," *Carbon*, vol. 53, pp. 216-221, 2013.
- [102] J. Schiffer and D. F. Hornig, "On a Reported New Form of Ice," *J. Chem. Phys.*, vol. 35, pp. 1136-1137, 1961.
- [103] E. W. Hughes, "The Crystal Structure of Ammonia-Borane, H₃NBH₃," *J. Am. Chem. Soc.*, vol. 78, pp. 502-503, 1956.
- [104] M. E. Bowden, G. J. Gainsford and W. T. Robinson, "Room-Temperature Structure of Ammonia Borane," *Aust. J. Chem.* 2007, vol. 60, pp. 149-153, 2007.
- [105] C. F. Hoon and E. C. Reynhardt, "Molecular Dynamics and Structures of Amine Boranes of the Type R₃N.BH₃: I. X-Ray Investigation of H₃N.BH₃ at 295 K and 110 K," *J. Phys. C: Solid State Phys.*, vol. 16, pp. 6129-6136, 1983.
- [106] W. T. Klooster, T. F. Koetzle, P. E. M. Siegbahn, T. B. Richardson and R. H. Crabtree, "Study of The N-H...H-B Dihydrogen Bond Including the Crystal Structure of BH₃NH₃ by Neutron Diffraction," *J. Am. Chem. Soc.*, vol. 121, pp. 6337-6343, 1999.
- [107] P. Wang and X.-d. Kang, "Hydrogen-Rich Boron-Containing Materials for Hydrogen Storage," *Dalton Trans.*, p. 5400–5413, 2008.
- [108] C. R. Miranda and G. Ceder, "Ab Initio Investigation of Ammonia-Borane Complexes for Hydrogen Storage," *J. Chem. Phys.*, vol. 126, pp. 184703-1-11, 2007.
- [109] P. V. Ramachandran and P. D. Gagare, "Preparation of Ammonia Borane in High Yield and Purity, Methanolysis, and Regeneration," *Inorg. Chem.*, vol. 46, pp. 7810-7817,

- 2007.
- [110] S. G. Shore and R. W. Parry, "Chemical Evidence for the Structure of the Diammoniate of Diborane.II.The Preparation of Ammonia-Borane," *J. Am. Chem. Soc.*, vol. 80, pp. 8-12, 1958.
- [111] S. G. Shore and R. W. Parry, "The Crystalline Compound Ammonia-borane, H_3NBH_3 ," *J. Am. Chem. Soc.*, vol. 77, pp. 6084-6085, 1955.
- [112] M. Chandra and Q. Xu, "A High-Performance Hydrogen Generation System: Transition Metal-Catalyzed Dissociation and Hydrolysis of Ammonia-Borane," *J. Power Sources*, vol. 156, pp. 190-194, 2006.
- [113] M. Chanra and Q. Xu, "Dissociation and Hydrolysis of Ammonia-Borane with Solid Acids and Carbon Dioxide: An Efficient Hydrogen Generation System," *J. Power Sources*, vol. 159, pp. 855-860, 2006.
- [114] Q. Xu and M. Chandra, "Catalytic Activities of Non-Noble Metals for Hydrogen Generation from Aqueous Ammonia-Borane at Room Temperature," *J Power Sources*, vol. 163, pp. 364-370, 2006.
- [115] H. C. Kelly and V. B. Marriott, "Reexamination of the Mechanism of Acid-Catalyzed Amine-Borane Hydrolysis. The Hydrolysis of Ammonia-Borane," *Inorg. Chem.*, vol. 18, pp. 2875-2878, 1979.
- [116] F. H. Stephens, R. T. Baker, M. H. Matus, D. J. Grant and D. A. Dixon, "Acid Initiation of Ammonia-Borane Dehydrogenation for Hydrogen Storage," *Angew. Chem. Int. Ed.*, vol. 46, p. 746-749, 2007.
- [117] D. Choi, A. J. Karkamkar, S. T. Autrey and C. L. Aardahl, "Process and Composition for Controlling Foaming in Bulk Hydrogen Storage and Releasing Materials". US Patent Patent US20090302269 A1, December 2009.
- [118] S. Frueh, R. Kellett, C. Mallery, T. Molter, W. S. Willis, C. King'ondou and S. L. Suib, "Pyrolytic Decomposition of Ammonia Borane to Boron Nitride," *Inorg. Chem.*, vol. 50, pp. 783-792, 2011.
- [119] M. Bowden, T. Kemmitt, W. Shaw, N. Hess, J. Linehan, M. Gutowski, B. Schmid and T. Autrey, "Mechanistic Studies of Hydrogen Release from Solid Amine Borane Materials," *Proceedings Materials Research Society Symposium, San Francisco, CA*, April 17-19, 2006.
- [120] A. C. Stowe, W. J. Shaw, J. C. Linehan, B. Schmid and T. Autrey, "In Situ Solid State ^{11}B MAS-NMR Studies of the Thermal Decomposition of Ammonia Borane: Mechanistic Studies of the Hydrogen Release Pathways from a Solid State Hydrogen Storage Material," *Phys. Chem. Chem. Phys.*, vol. 9, pp. 1831-1836, 2007.
- [121] F. Baitalow, J. Baumann, G. Wolf, K. Jaenicke-Rößler and G. Leitner, "Thermal Decomposition of B-N-H Compounds Investigated by Using Combined Thermoanalytical Methods," *Thermochim. Acta*, vol. 391, p. 159-168, 2002.

- [122] J. Baumann, F. Baitalow and G. Wolf, "Thermal Decomposition of Polymeric Aminoborane (H_2BNH_2)_x under Hydrogen Release," *Thermochimica Acta*, vol. 430, pp. 9-14, 2005.
- [123] G. Wolf, J. Baumann, F. Baitalow and F. P. Hoffmann, "Calorimetric Process Monitoring of Thermal Decomposition of B-N-H Compounds," *Thermochim. Acta*, vol. 343, pp. 19-25, 2000.
- [124] Z. Li, G. Zhu, G. Lu, S. Qiu and X. Yao, "Ammonia Borane Confined by a Metal-Organic Framework for Chemical Hydrogen Storage: Enhancing Kinetics and Eliminating Ammonia," *J. Am. Chem. Soc.*, vol. 132, pp. 1490-1491, 2010.
- [125] D. R. Schultz and R. W. Parry, "Chemical Evidence for the Structure of the Diammoniate of Diborane. I. Evidence for the Borohydride Ion and for the Dihydro-diammineboron(III) Cation," *J. Am. Chem. Soc.*, vol. 80, pp. 4-8, 1958.
- [126] H. I. Schlesinger and A. B. Burg, "Hydrides of Boron. VIII. The Structure of the Diammoniate of Diborane and its Relation to the Structure of Diborane," *J. Am. Chem. Soc.*, vol. 60, pp. 290-299, 1938.
- [127] G. W. Schaeffer, M. D. Adams, F. J. Koenig and S. J. Koenig, "On the Alkali Metal Salts Derived from the Diammoniate of Diborane," *J. Am. Chem. Soc.*, vol. 78, pp. 725-728, 1956.
- [128] M. Bowden, D. J. Heldebrant, A. Karkamkar, T. Proffen, G. K. Schenter and T. Autrey, "The Diammoniate of Diborane: Crystal Structure and Hydrogen Release," *Chem. Commun.*, vol. 46, pp. 8564-8566, 2010.
- [129] Z. Fang, J. Luo, X. Kang, H. Xia, S. Wang, W. Wen, X. Zhou and P. Wang, "Facile Solid-Phase Synthesis of the Diammoniate of Diborane and its Thermal Decomposition Behavior," *Phys. Chem. Chem. Phys.*, vol. 13, pp. 7508-7513, 2011.
- [130] D. W. Himmelberger, L. R. Alden, M. E. Bluhm and L. G. Sneddon, "Ammonia Borane Hydrogen Release in Ionic Liquids," *Inorg. Chem.*, vol. 48, p. 9883-9889, 2009.
- [131] R. K. Ahluwalia, J. K. Peng and T. Q. Hua, "Hydrogen Release from Ammonia Borane Dissolved in an Ionic Liquid," *Int. J. Hydrogen Energy*, vol. 36, pp. 15689-15697, 2011.
- [132] J. Zhang, Y. Zhao, D. L. Akins and J. W. Lee, "Thermal Decomposition and Spectroscopic Studies of Preheated Ammonia Borane," *J. Phys. Chem. C*, vol. 114, pp. 19529-19534, 2010.
- [133] D. J. Heldebrant, A. Karkamkar, N. J. Hess, M. Bowden, S. Rassat, F. Zheng, K. Rappe and T. Autrey, "The Effects of Chemical Additives on the Induction Phase in Solid-State Thermal Decomposition of Ammonia Borane," *Chem. Mater.*, vol. 20, pp. 5332-5336, 2008.
- [134] D. W. Himmelberger, C. W. Yoon, M. E. Bluhm, P. J. Carroll and L. G. Sneddon,

- "Base-Promoted Ammonia Borane Hydrogen-Release," *J. Am. Chem. Soc.*, vol. 131, pp. 14101-14110, 2009.
- [135] W. C. Ewing, A. Marchione, D. W. Himmelberger, P. J. Carroll and L. G. Sneddon, "Syntheses and Structural Characterizations of Anionic Borane-Capped Ammonia Borane Oligomers: Evidence for Ammonia Borane H₂ Release via a Base-Promoted Anionic Dehydropolymerization Mechanism," *J. Am. Chem. Soc.*, vol. 133, p. 17093–17099, 2011.
- [136] B. L. Conley, D. Guess and T. J. Williams, "A Robust, Air-Stable, Reusable Ruthenium Catalyst for Dehydrogenation of Ammonia Borane," *J. Am. Chem. Soc.*, vol. 133, p. 14212–14215, 2011.
- [137] P.-Z. Li, A. Aijaz and Q. Xu, "Highly Dispersed Surfactant-Free Nickel Nanoparticles and Their Remarkable Catalytic Activity in the Hydrolysis of Ammonia Borane for Hydrogen Generation," *Angew. Chem. Int. Ed.*, vol. 51, p. 6753–6756, 2012.
- [138] X.-B. Zhang, J.-M. Yan, S. Han, H. Shioyama and Q. Xu, "Magnetically Recyclable Fe@Pt Core-Shell Nanoparticles and Their Use as Electrocatalysts for Ammonia Borane Oxidation: The Role of Crystallinity of the Core," *J. Am. Chem. Soc.*, vol. 131, p. 2778–2779, 2009.
- [139] C. A. Jaska, K. Temple, A. J. Lough and I. Manners, "Rhodium-Catalyzed Formation of Boron–Nitrogen Bonds: A Mild Route to Cyclic Aminoboranes and Borazines," *Chem. Commun.*, p. 962–963, 2001.
- [140] Z. Tang, X. Chen, H. Chen, L. Wu and X. Yu, "Metal-Free Catalysis of Ammonia–Borane Dehydrogenation/Regeneration for a Highly Efficient and Facilely Recyclable Hydrogen-Storage Material," *Angew. Chem. Int. Ed.*, vol. 52, p. 5832–5835, 2013.
- [141] A. Gutowska, L. Li, Y. Shin, C. M. Wang, X. S. Li, J. C. Linehan, R. S. Smith, B. D. Kay, B. Schmid, W. Shaw, M. Gutowski and T. Autrey, "Nanoscaffold Mediates Hydrogen Release and the Reactivity of Ammonia Borane," *Angew. Chem. Int. Ed.*, vol. 44, pp. 3578-3582, 2005.
- [142] T. Zhang, X. Yang, S. Yang, D. Li, F. Cheng, Z. Tao and J. Chen, "Silica Hollow Nanospheres as New Nanoscaffold Materials to Enhance Hydrogen Releasing from Ammonia Borane," *Phys. Chem. Chem. Phys.*, vol. 13, p. 18592–18599, 2011.
- [143] M. Asadi, A. Nemati, R. Naghizadeh, K. Arzani and J. Fahim, "Effect of Temperature and Activator Molar of Na₂O to SiO₂ in the Process of Synthesis and Microstructure of Cement Geopolymer," *Journal of Advanced Materials and Processing*, vol. 1, pp. 3-9, 2013.
- [144] K. A. Komnitsas, "Potential of Geopolymer Technology towards Green Buildings and Sustainable Cities," *Proc. Eng.*, vol. 21, pp. 1023-1032, 2011.
- [145] J. Smith, K. S. Seshadri and D. White, "Infrared Spectra of Matrix Isolated BH₃-NH₃, BD₃-ND₃ and BH₃-ND₃," *J. Mol. Spectrosc.*, vol. 45, pp. 327-337, 1973.

- [146] N. J. Hess, M. E. Bowden, V. M. Parvanov, C. Mundy, S. M. Kathmann, G. K. Schenter and T. Autrey, "Spectroscopic Studies of the Phase Transition in Ammonia Borane: Raman Spectroscopy of Single Crystal NH_3BH_3 as a Function of Temperature from 88 to 330 K," *J. Chem. Phys.*, vol. 128, p. 034508, 2008.
- [147] S. Xie, Y. Song and Z. Liu, "In-situ High-Pressure Study of Ammonia Borane by Raman and IR Spectroscopy," *Can. J. Chem.*, vol. 87, pp. 1235-1247, 2009.
- [148] R. Custelcean and Z. A. Dreger, "Dihydrogen Bonding under High Pressure: A Raman Study of BH_3NH_3 Molecular Crystal," *J. Phys. Chem. B*, vol. 107, pp. 9231-9235, 2003.
- [149] P. Jash, K. Meaux and T. Trenary, "Transmission Infrared Spectroscopy of Ammonia Borane," *Journal of Undergraduate Research*, vol. 5, 2012.
- [150] J. Goubeau and E. Ricker, "Borinhydrazin und seine Pyrolyseprodukte," *Z. anorg. allg. Chem.*, vol. 310, p. 123-142, 1961.
- [151] D. G. Allis, M. E. Kosmowski and B. S. Hudson, "The Inelastic Neutron Scattering Spectrum of $\text{H}_3\text{B:NH}_3$ and the Reproduction of its Solid-State Features by Periodic DFT," *J. Am. Chem. Soc.*, vol. 126, pp. 7756-7757, 2004.
- [152] B. Peng and J. Chen, "Ammonia Borane as an Efficient and Lightweight Hydrogen Storage Medium," *Energy Environ. Sci.*, vol. 1, pp. 479-483, 2008.
- [153] J. S. Wang and R. A. Geanangel, " ^{11}B NMR Studies of the Thermal Decomposition of Ammonia-Borane in Solution," *Inorg. Chim. Acta*, vol. 148, pp. 185-190, 1988.
- [154] R. Komm, R. A. Geanangel and R. Liepens, "Synthesis and Studies of Poly(aminoborane), $(\text{H}_2\text{NBH}_2)_x$," *Inorg. Chem.*, vol. 22, pp. 1684-1686, 1983.
- [155] D.-P. Kim, K.-T. Moon, J.-G. Kho, J. Economy, C. Gervais and F. Babonneau, "Synthesis and Characterization of Poly-(Aminoborane) as a New Boron Nitride," *Polym. Adv. Technol.*, vol. 10, pp. 702-712, 1999.
- [156] J. D. Carpenter and B. S. Ault, "Infrared Matrix Isolation Characterization of Aminoborane and Related Compounds," *J. Phys. Chem.*, vol. 95, p. 3502-3506, 1991.
- [157] D. Jacquemin, E. A. Perpète, V. Wathélet and J.-M. André, "Ab Initio Investigation of the Structures and Properties of Polyaminoborane," *J. Phys. Chem. A*, vol. 108, p. 9616-9624, 2004.
- [158] D. L. Denton, A. D. Johnson, C. W. Hickam, R. K. Bunting and S. G. Shore, "Boron-Nitrogen Chemistry—II. Poly (Aminoborane)," *J. Inorg. Nucl. Chem.*, pp. 1037-1038, 1975.
- [159] A. T-Raissi and N. Mohajeri, "Hydrogen Storage and Recovery in Ammonia Borane Complex," *NASA Hydrogen Research at Florida Universities*, pp. 147-151, 2006.
- [160] K. Niedenzu, W. Sawodny, H. Watanabe, J. W. Dawson, T. Totani and W. Weber, "The

- Vibrational Spectrum of Borazine," *Inorg. Chem.*, vol. 6, p. 1453–1461, 1967.
- [161] F. A. Miler and C. H. Wilkins, "Infrared Spectra and Characteristic Frequencies of Inorganic Ions," *Anal. Chem.*, vol. 24, p. 1253–1294, 1952.
- [162] D. M. Hoffman, G. L. Doll and P. C. Eklund, "Optical Properties of Pyrolytic Boron Nitride in the Energy Range 0.05–10 eV," *Phys. Rev. B*, vol. 30, pp. 6051–6056, 1984.
- [163] D.-P. Kim, C. G. Cofer and J. Economy, "Fabrication and Properties of Ceramic Composites with a Boron Nitride Matrix," *J. Am. Ceram. Soc.*, vol. 78, pp. 1546–1552, 1995.
- [164] D. B. Ravnsbæk, L. H. Rude and T. R. Jensen, "Chloride Substitution in Sodium Borohydride," *J. Solid State Chem.*, vol. 184, p. 1858–1866, 2011.
- [165] L. H. Rude, O. Zavorotynska, L. M. Arnbjerg, D. B. Ravnsbæk, R. A. Malmkjær, H. Grove, B. C. Hauback, M. Baricco, Y. Filinchuk, F. Besenbacher and T. R. Jensen, "Bromide Substitution in Lithium Borohydride, LiBH₄-LiBr," *Int. J. Hydrogen Energy*, vol. 36, p. 15664–15672, 2011.
- [166] E. Mayer, "Conversion of Dihydridodiammineboron(III) Borohydride to Ammonia-Borane without Hydrogen Evolution," *Inorg. Chem.*, vol. 12, p. 1954–1955, 1973.
- [167] M. Bowden, T. Autrey, I. Brown and M. Ryan, "The Thermal Decomposition of Ammonia Borane: A Potential Hydrogen Storage Material," *Curr. Appl. Phys.*, vol. 8, p. 498–500, 2008.
- [168] Y. Nakamori, K. Miwa, A. Ninomiya, H. Li, N. Ohba, S.-i. Towata, A. Züttel and S.-i. Orimo, "Correlation between Thermodynamical Stabilities of Metal Borohydrides and Cation Electronegativities: First-Principles Calculations and Experiments," *Phys. Rev. B*, vol. 74, p. 045126, 2006.
- [169] Y. Nakamori, H.-W. Li, K. Kikuchi, M. Aoki and K. Miwa, "Thermodynamical Stabilities of Metal-Borohydrides," *J. Alloys Compd.*, Vols. 446–447, pp. 296–300, 2007.
- [170] T. Matsunaga, F. Buchter, K. Miwa, S. Towata, S. Orimo and A. Züttel, "Magnesium Borohydride: A New Hydrogen Storage Material," *Renew. Energ.*, vol. 33, p. 193–196, 2008.
- [171] J. Graetz, "New Approaches to Hydrogen Storage," *Chem. Soc. Rev.*, vol. 38, pp. 73–82, 2009.
- [172] D. Ravnsbæk, Y. Filinchuk, Y. Cerenius, H. J. Jakobsen, F. Besenbacher, J. Skibsted and T. R. Jensen, "A Series of Mixed-Metal Borohydrides," *Angew. Chem.*, vol. 121, p. 6787–6791, 2009.
- [173] H. W. Brinks, A. Fossdal and B. C. Hauback, "Adjustment of the Stability of Complex Hydrides by Anion Substitution," *J. Phys. Chem. C*, vol. 112, pp. 5658–5661, 2008.

- [174] L. Yin, P. Wang, Z. Fang and H. Cheng, "Thermodynamically Tuning LiBH_4 by Fluorine Anion Doping for Hydrogen Storage: A Density Functional Study," *Chem. Phys. Lett.*, vol. 450, p. 318–321, 2008.
- [175] L. H. Rude, U. Filsø, V. D'Anna, A. Spyratou, B. Richter, S. Hino, O. Zavorotynska, M. Baricco, M. H. Sørby, B. C. Hauback, H. Hagemann, F. Besenbacher, J. Skibsted and T. R. Jensen, "Hydrogen–Fluorine Exchange in NaBH_4 – NaBF_4 ," *Phys.Chem. Chem. Phys.*, vol. 15, pp. 18185-18194, 2013.
- [176] J. E. Olsen, M. H. Sørby and B. C. Hauback, "Chloride-Substitution in Sodium Borohydride," *J. Alloys Compd.*, vol. 509, p. L228–L231, 2011.
- [177] L. H. Rude, E. Groppo, L. M. Arnbjerg, D. B. Ravnsbæk, R. A. Malmkjær, Y. Filinchuk, M. Baricco, F. Besenbacher and T. R. Jensen, "Iodide Substitution in Lithium Borohydride, LiBH_4 – LiI ," *Int. J. Hydrogen Energy*, vol. 509, p. 8299– 8305, 2011.
- [178] R. M. Badger, "A Relation between Internuclear Distances and Bond Force Constants," *J. Chem. Phys.*, vol. 2, pp. 128-131, 1934.
- [179] R. M. Badger, "The Relation between Internuclear Distances and the Force Constants of Diatomic Molecules," *Phys. Rev.*, vol. 48, pp. 284-285, 1935.
- [180] R. M. Badger, "The Relation between the Internuclear Distances and Force Constants of Molecules and its Application to Polyatomic Molecules," *J. Chem. Phys.*, vol. 3, pp. 710-714, 1935.
- [181] W. C. Price, W. F. Sherman and G. R. Wilkinson, "Infra-red Studies on Polyatomic Ions Isolated in Alkali-Halide Lattices," *Spectrochim. Acta*, vol. 16, pp. 663-676, 1960.
- [182] J. A. A. Ketelaar and J. V. d. Elskens, "Frequency Shifts in the Infrared Absorption Spectrum of Complex Ions in Solid Solution," *J. Chem. Phys.*, vol. 30, pp. 336-337, 1959.
- [183] "The Inorganic Crystal Structure Database (ICSD)".
- [184] A. Nasar, "Correlation between Standard Enthalpy of Formation, Structural Parameters and Ionicity for Alkali Halides," *J. Serb. Chem. Soc.*, vol. 78, p. 241–253, 2013.
- [185] J. Hinze, "The Concept of Electronegativity of Atoms in Molecules," *Theoretical and Computational Chemistry*, vol. 6, pp. 189-212, 1999.
- [186] J. I. Bryant and G. C. Turrell, "Infrared Spectra of the Azide Ion in Alkali-Halide Lattices," *J. Chem. Phys.*, vol. 37, pp. 1069-1077, 1962.
- [187] W. F. Sherman and G. R. Wilkinson, "Infrared and Raman Studies on the Vibrational Spectra of Impurities in Ionic and Covalent Crystals," in *Vibrational Spectroscopy of Trapped Species*, edited by H. E. Hallam, New York, Wiley, 1973, p. 245.

- [188] G. R. Field and W. F. Sherman, "Cyanide Ion—Environmental Perturbation of its Vibrational and Rotational Motion when Isolated in Alkali Halides," *J. Chem. Phys.*, vol. 47, pp. 2378-2389, 1967.
- [189] F. Seitz, *The Modern Theory of Solids*, New York: Mc-Graw Hill Book Company, Inc., 1940.
- [190] X.-D. Zhang, Z.-F. Hou, Z.-Y. Jiang and Y.-Q. Hou, "Elastic Properties of MBH_4 ($M = Na, K, Rb, Cs$)," *Physica B*, vol. 406, p. 2196–2199, 2011.
- [191] T. Bredow, A. G. Schneider and A. C. Ulpe, Mulliken Center for Theoretical Chemistry, Institut für Physikalische und Theoretische Chemie, Universität Bonn, Personal Communications.
- [192] W. G. Woods, "An Introduction to Boron: History, Sources, Uses, and Chemistry," *Environ. Health Perspect.*, vol. 102, pp. 5-11, 1994.
- [193] L. Stoch and I. Waclawska, "Thermal Decomposition of Hydrated Borates. Part 3. Structural Mechanism of Thermal Decomposition of Borates," *Thermochim. Acta*, vol. 215, pp. 273-279, 1993.
- [194] M. Touboul, N. Penin and G. Nowogrocki, "Borates: a Survey of Main Trends Concerning Crystal-Chemistry, Polymorphism and Dehydration Process of Alkaline and Pseudo-Alkaline Borates," *Solid State Sci.*, vol. 5, pp. 1327-1342, 2003.
- [195] M. Touboul and E. Betourne, "Dehydration Process of Lithium Borates," *Solid State Ionics*, vol. 84, pp. 189-197, 1996.
- [196] N. Koga, T. Utsuoka and H. Tanaka, "Thermal Dehydration of Dipotassium Tetraborate Tetrahydrate and Crystallization of Amorphous Dehydration Product," *J. Therm. Anal. Cal.*, vol. 80, pp. 71-75, 2005.
- [197] S. Block and A. Perloff, "The Direct Determination of the Crystal Structure of $NaB(OH)_4 \cdot 2H_2O$," *Acta Cryst.*, vol. 16, pp. 1233-1238, 1963.
- [198] L. G. Csetenyi, F. P. Glasser and R. A. Howie, "Structure of Sodium Tetrahydroxyborate," *Acta Cryst.*, vol. C49, pp. 1039-1041, 1993.
- [199] M. Marezio, H. A. Plettinger and W. H. Zachariasen, "The Bond Lengths in the Sodium Metaborate Structure," *Acta Cryst.*, vol. 16, pp. 594-595, 1963.
- [200] W. H. Zachariasen, "The Crystal Structure of Lithium Metaborate," *Acta Cryst.*, vol. 17, pp. 749-751, 1964.
- [201] C. L. Christ and J. R. Clark, "A Crystal-Chemical Classification of Borate Structures with Emphasis on Hydrated Borates," *Phys. Chem. Minerals*, vol. 2, pp. 59-87, 1977.
- [202] J. Andrieux, C. Goutaudier, L. Laversenne, E. Jeanneau and P. Miele, "Synthesis, Characterization, and Crystal Structure of a New Trisodium Triborate,

- $\text{Na}_3[\text{B}_3\text{O}_4(\text{OH})_4]$," *Inorg. Chem.*, vol. 49, p. 4830–4835, 2010.
- [203] E. Corazza, S. Menchetti and C. Sabelli, "The Crystal Structure of $\text{Na}_3[\text{B}_3\text{O}_5(\text{OH})_2]$," *Acta Cryst.*, vol. B31, pp. 1993-1997, 1975.
- [204] R. Bouaziz, "Contribution à l'Etude Radiocristallographique de Quelques Borates de Lithium et de Sodium," *Bull. Soc. Chim. Fr.*, vol. 7, p. 1451, 1962.
- [205] N. P. Nies and R. W. Hulbert, "Solubility Isotherms in the System Sodium Oxide-Boric Oxide-Water," *J. Chem. Eng. Data*, vol. 12, pp. 303-313, 1967.
- [206] J. Andrieux, L. Laversenne, O. Krol, R. Chiriach, Z. Bouajila, R. Tenu, J. J. Counioux and C. Goutaudier, "Revision of the $\text{NaBO}_2\text{-H}_2\text{O}$ Phase Diagram for Optimized Yield in the H_2 Generation through NaBH_4 Hydrolysis," *Int. J. Hydrogen Energy*, vol. 37, pp. 5798-5810, 2012.
- [207] A. Kanturk, M. Sari and S. Piskin, "Synthesis, Crystal Structure and Dehydration Kinetics of $\text{NaB}(\text{OH})_4 \cdot 2\text{H}_2\text{O}$," *Korean J. Chem. Eng.*, vol. 25, pp. 1331-1337, 2008.
- [208] G. Moussa, R. Moury, U. B. Demirci and P. Miele, "Borates in Hydrolysis of Ammonia Borane," *Int. J. Hydrogen Energy*, vol. 38, pp. 7888-7895, 2013.
- [209] H. K. Atiyeh and B. R. Davis, "Separation of Sodium Metaborate from Sodium Borohydride Using Nanofiltration Membranes for Hydrogen Storage Application," *Int. J. of Hydrogen Energy*, vol. 32, pp. 229-236, 2007.
- [210] G. Kessler, "IR-Spektroskopische Untersuchungen an Boraten. III. Besondere Merkmale der IR-Spektren einiger Kristalliner Tetrahydroxoborate," *Z. Anorg. Allg. Chem.*, vol. 343, pp. 25-38, 1966.
- [211] C. E. Weir and R. A. Schroeder, "Infrared Spectra of the Crystalline Inorganic Borates," *J. Res. Nat. Bur. Stand.*, vol. 68A, pp. 465-487, 1964.
- [212] Z. Lixia, Y. Tao, W. Jiang and G. Shiyang, "FT-IR and Raman Spectroscopic Study of Hydrated Rubidium (Cesium) Borates and Alkali Double Borates," *Russ. J. Inorg. Chem.*, vol. 52, pp. 1786-1792, 2007.
- [213] S. Pinchas and J. Shamir, "Anomalous Behavior of ^{18}O Labeled Compounds. VI. The Vibrational Spectra of Isotopic Metaborates," *J. Chem. Phys.*, vol. 56, pp. 2017-2019, 1972.
- [214] G. D. Chryssikos, J. A. Kapoutsis, A. P. Patsis and E. I. Kamitsos, "A Classification of Metaborate Crystals Based on Raman Spectroscopy," *Spectrochim. Acta*, vol. 47A, pp. 1117-1126, 1991.
- [215] J. L. Parsons, "Vibrational Spectra of Orthorhombic Metaboric Acid," *J. Chem. Phys.*, vol. 33, pp. 1860-1866, 1960.
- [216] H. D. Fisher, W. J. Lehmann and I. Shapiro, "Trifluoroboxine: Preparation, Infrared

- Spectrum and Structure," *J. Phys. Chem.*, vol. 65, pp. 1166-1168, 1961.
- [217] K. Wu and S.-Y. Lee, "Ab Initio Calculations on Normal Mode Vibrations and the Raman and IR Spectra of the $[\text{B}_3\text{O}_6]^{3-}$ Metaborate Ring," *J. Phys. Chem. A*, vol. 101, pp. 937-940, 1997.
- [218] N. Koga, J. M. Criado and H. Tanaka, "A Kinetic Aspect of the Thermal Dehydration of Dilithium Tetraborate Trihydrate," *J. Therm. Anal. Cal.*, vol. 67, pp. 153-161, 2002.
- [219] M. Touboul and E. Betourne, "LiB₂O₃(OH).H₂O as Precursor of Lithium Boron Oxide LiB₂O₃.5: Synthesis and Dehydration Process," *Solid State Ionics*, pp. 340-345, 1993.

VI. Curriculum Vitae

PERSONAL INFORMATION

Name	Zeina Assi	Nationality	Lebanese
Date of birth	01.01.1987	email	zeina.assi@hotmail.de

RESEARCH INTERESTS

- Chemical hydrides as hydrogen (energy) storage materials
- Boron based-materials
- Spectroscopy as supporting method in structure determination

WORK EXPERIENCE AND INTERNSHIPS

Since Nov. 2011	Research assistant at the institute of Mineralogy LUH, Hanover, Germany
2008 - 2009	Student research assistant Faculty of Science, Lebanese University, Inorganic chemistry group

EDUCATION

Since Nov. 2011	PhD student at the institute of Mineralogy (DAAD Scholarship) LUH, Hanover, Germany
<i>(Dec. 2011 - Sep. 2012)</i>	<i>“Home office”, Maternity leave (Birth of my daughter in Dec. 2011)</i>
April 2011 - Sep. 2011	Intensive German course (A2, B1, B2, C1) Goethe-Institut, Göttingen, Germany
2008 - 2009	“Master de Recherche (M2R)”, option: Inorganic Chemistry (overall grade: 84.34% “sehr gut”, rank: 1/7) Topic: Extraction of the heavy metal cations from aqueous solutions using new anionic derivatives of hydroborates Doctoral School of Science and Technology, Lebanese University, Hadath-Beyrouth , Lebanon
2004 - 2008	Diploma “Maitrise-es Sciences”, option: General Chemistry Faculty of Science , Lebanese University, Lebanon
2003 - 2004	Baccalauréat scientifique, option: life science Collège Notre Dames des Soeurs Antonines, Nabatieh, Lebanon

ADDITIONAL SKILLS

Language: Arabic (mother tongue), French (bilingual), English (fluent), German (good skills)

Software: MS office, Opus, SigmaPlot, Diamond, GULP (basic)

Analytical methods: Infrared spectroscopy, Raman spectroscopy, X-ray diffraction,
Thermogravimetry, Differential thermos analytics.

VII. List of Publications

Publications

D. Naoufal, Z. Assi, E. Abdelhai, G. Ibrahim, O. Yazbeck, A. Hachem, H. Abdallah, M. El Masri, "The Reaction of Closo-diazononahydrodecaborate $[1-N_2B_{10}H_9]^-$ with Bidentate Diamino Ligands L: A New Route to Dicaige Derivatives $[B_{10}H_9LB_{10}H_9]^{2-}$," *Inorg. Chim. Acta*, vol. 383, pp. 33-37 (2012).

L. Schomborg, Z. Assi, J.-C. Buhl, C.H. Rüscher, M. Wark, "Ammonia Borane Geopolymer (AB-G) Composite," *A Collection of Papers Presented at the 39th International Conference on Advanced Ceramics and Composites (eds W. M. Kriven, J. Wang, D. Zhu and T. Fischer)*, John Wiley & Sons, Inc., Hoboken, NJ, USA (2015).

C. H. Rüscher, L. Schomborg, Z. Assi, J.-C. Buhl, "NH₃BH₃ and NaBH₄ Enclosed in Geopolymers and Zeolites," *in the 11th Conference on Ceramic Materials and Components for Energy and Environmental Applications* (2015).

Z. Assi, L. Schomborg, C.H. Rüscher, "Investigations of the Thermally Induced Hydrogen Release of NaBH₄, NH₃BH₃ and their Geopolymer Composites," *in the 40th International Conference and Expo on Advanced Ceramics and Composites*, accepted paper (2016).

Z. Assi, A. G. Schneider, A. C. Ulpe, T. Bredow, C. H. Rüscher, "Frequency Variation of IR Active Modes of the BH₄-Anion Dispersed in Halides AX, A = Na, K; X = Cl, Br, I, and of MBH₄ with M = Na, K, Rb, Cs," *in progress*.

Abstracts

Z. Assi, C.H. Rüscher, "Thermogravimetric, Temperature Dependant Infrared and XRD Investigations on NaBO₂.xH₂O system," *in the 22nd Annual Conference of the German Crystallographic Society* (2014). *Talk*

Z. Assi, C. H. Rüscher, "Investigation of Sodium Borohydride NaBH₄ in Different Halide matrices (NaX): Hydrogen Release Reactions and New Compositions of the Type Na[BH₄]_xX_(1-x), (X = Cl, Br, I)," *in the 23rd Annual Conference of the German Crystallographic Society* (2015). *Talk*

C. H. Rüscher, W. M. Kriven, L. Schomborg, Z. Assi, H. Tchakoute, J. Temuujin, F. Jirasit, L. Lohaus, J. C. Buhl, "Geopolymers, Substitutions to Portland-Cement and Hosting Hydrogen Storage Materials," *in Geoberlin* (2015).

L. Schomorg, Z. Assi, J. C. Buhl, M. Wark, C.H. Rüscher, "Sodium-Borontetrahydride and Ammonia-Borane Encapsulated in Sodalites and Recrystallized in Zeolite Precursor Materials". *Poster*